UNIVERSITÀ DEGLI STUDI DELL'AQUILA
DIPARTIMENTO DI INGEGNERIA CIVILE, EDILE-ARCHITETTURA, AMBIENTALE

Dottorato di Ricerca in Ingegneria Civile, Edile-Architettura, Ambientale

Curriculum Ingegneria Civile ed Ambientale

XXXVII ciclo

Studio delle caratteristiche meccaniche di calcestruzzi a elevate prestazioni, a elevata resistenza, leggeri, fibro-rinforzati o con additivi innovativi

SSD CEAR-06/A

Dottorando

Giuliano Aretusi

Coordinatore del corso

Prof. Federico De Matteis

Tutor

Prof. Francesco dell'Isola

a.a. 2024/2025

Modeling of high-performance, high-strength, lightweight, fiber-reinforced concretes, or concretes with innovative additives

Giuliano Aretusi

Prof. Francesco dell'Isola

Modeling of high-performance, high-strength, lightweight, fiber-reinforced concretes, or concretes with innovative additives

Giuliano Aretusi
Candidate ID number: 282875

Department of Civil, Construction-Architectural and Environmental Engineering-DICEAA
University of L'Aquila

Copyright © 2025, Giuliano Aretusi. All rights reserved.

Material for which the author is the copyright owner cannot be used without the written permission of the author. The permission to reproduce copyright protected material does not extend to any material that is copyright of a third party; authorization to reproduce such material must be obtained from the copyright owners concerned. This thesis has been typeset by LaTeX and phdiceaa class.

Website: http://diceaa.univaq.it/

[Blank page]

Acknowledgements

I would like to express my deepest gratitude to my supervisors, Professor Francesco dell'Isola and Professor Ivan Giorgio, for their invaluable guidance, support, and encouragement throughout my doctoral journey. Their expertise, insights, and dedication have been instrumental in shaping this research.

Professor Francesco dell'Isola's profound knowledge and inspiring mentorship provided a strong foundation for my work. His ability to guide me through complex challenges with patience and clarity was truly remarkable.

I am equally grateful to Professor Ivan Giorgio for his insightful feedback, constructive criticism, and unwavering support. His attention to detail and thoughtful guidance helped me refine my research and achieve my academic goals.

I feel incredibly fortunate to have had the opportunity to learn from and collaborate with such distinguished scholars. Their passion for research and commitment to excellence have not only enriched my academic experience but also motivated me to pursue knowledge with integrity and curiosity.

Thank you both for believing in me and for being an essential part of this achievement.

[Blank page]

Abstract

In this thesis, a generalized 1D model is introduced to efficiently describe internal friction phenomena that can be observed in cementitious materials assuming small displacements and strains undergoing slow dynamic cyclic loads without inducing damage growth. The key idea is to exploit an extension of the Timoshenko model for plane bending beams. The modified beam model, inspired by micromorphic continua, includes a new kinematic descriptor. This descriptor represents the average sliding relevant to a density of micro-cracks, which is assumed to remain constant over time. It was assumed that the microcrack density would not increase under small deformation, indicating no damage growth. Due to the rough surfaces of the micro-faces of such a distribution of micro-cracks, both elastic deformation and frictional dissipation are considered, similar to what happens for the fingers of joints with a tooth saw profile. The system of governing second-order differential equations is obtained using a variational approach and standard boundary conditions. A generalized version of the principle of virtual work is used to derive these equations. This includes contributions from: (i) variation of the inner elastic energy due to the linear elasticity of the sound material and the reversible deformation of the asperities inside the micro-cracks in a nonlinear way; (ii) virtual work of external actions consistent with the beam model, such as distributed transversal forces and moments per unit lengths; and (iii) the dissipation due to friction specified through a smooth Rayleigh potential, which consider a nonlinear dependence of viscous and Coulomb types on the sliding rate. We carry out 1D finite element analyses using Comsol Multiphysics to simulate structural elements subjected to three and four-point bending tests with alternating loading cycles. The dissipation of energy is assessed by varying the model parameters, and the predictions are in agreement with preliminary data from an experimental campaign. Afterward, the model is updated to allow for the storage of stretching or compressive energy within the beam. Furthermore, a parametric study was conducted to vary the friction force amplitude, revealing its impact on dissipated energy. The study highlighted a non-monotonic relationship between friction force amplitude and dissipated energy, with an optimal value maximizing dissipation. Overall, the model provided insights into the mechanics of cement-based materials, particularly regarding dissipation, which is essential for understanding their behavior in structural applications. Finally, the model was further developed by investigating the possibility of using a friction force characterized by an evolutionary law instead of a static constitutive relationship. This dynamic friction term is based on a well-known model for dry fric-

tion in solids developed by P. R. Dahl. Here, the friction force relies solely on the sliding displacement and evolves over time, exhibiting elastoplastic behavior. The proposed model takes into account the mechanical energy transfer between bending and shear distortion in the beam with the sliding at the microcracks. Numerical simulations of the kinematic descriptors and dissipative cycles using the Finite Element Method are also provided to assess the predictive abilities of the model. Two digressions are also made on two aspects that are very important in the design of concrete buildings: a study on the modeling to be employed in case of environmental loading due to earthquakes and some aspects of delamination in composites made of fiber-reinforced concrete. The current understanding in geophysics and civil engineering suggests that linear models may not adequately describe earthquakes and the propagation of seismic waves due to significant soil deformation. A study aims to demonstrate this inadequacy by analyzing a two-dimensional body with a non-linear strain energy in a piecewise homogeneous domain resembling the Aterno River Valley. Numerical predictions support the idea that non-linear models provide closer predictions to experimental evidence compared to linear models. An analytical model for studying delamination in composite cantilever beams is proposed. It uses cohesive zone models to simulate the degradation process at the connection. The model highlights the crucial role of interface layer strength in maintaining the structural integrity of composites. It offers a refined analytical approach to studying delamination, providing insights into beam deflection, shear stress, and axial force distribution, which is important for improving the design and analysis of composite structures.

Keywords: Enhanced Timoshenko beam model, 1D continua with microstructure, Micro-cracks, Cementitious materials, Dissipated energy, Friction, Hysteresis cycles.

[Blank page]

Sommario

In questa tesi, viene introdotto un modello generalizzato 1D per descrivere in modo efficiente i fenomeni di attrito interno osservabili nei materiali cementizi, assumendo piccoli spostamenti e deformazioni soggetti a carichi ciclici dinamici lenti senza crescita del danno.

L'idea chiave è quella di sfruttare un'estensione del modello di Timoshenko per travi in flessione piana. Il modello di trave modificato, ispirato ai continui micromorfici, include un nuovo descrittore cinematico. Questo descrittore rappresenta lo scorrimento medio associato a una densità di microfessure, che si assume rimanere costante nel tempo. Si suppone che la densità di microfessure non aumenti in presenza di piccole deformazioni, indicando l'assenza di crescita del danno. A causa delle superfici irregolari delle micro-facce associate a questa distribuzione di microfessure, vengono considerate sia la deformazione elastica sia la dissipazione per attrito, analogamente a quanto avviene per le giunzioni degli incastri con profilo a pettine.

Il sistema di equazioni differenziali del secondo ordine che governa il modello è ottenuto utilizzando un approccio variazionale e condizioni al contorno standard. Per derivare queste equazioni si utilizza una versione generalizzata del principio dei lavori virtuali, che include contributi derivanti da: (i) la variazione dell'energia elastica interna dovuta all'elasticità lineare del materiale integro e alla deformazione reversibile delle asperità all'interno delle microfessure in modo non lineare; (ii) il lavoro virtuale delle azioni esterne compatibili con il modello di trave, come forze trasversali distribuite e momenti per unità di lunghezza; e (iii) la dissipazione dovuta all'attrito, specificata attraverso un potenziale di Rayleigh, che considera una dipendenza non lineare di tipo viscoso e di Coulomb rispetto alla velocità di scorrimento.

Vengono condotte analisi agli elementi finiti in 1D utilizzando Comsol Multiphysics per simulare elementi strutturali sottoposti a test di flessione a tre e quattro punti con cicli di carico alternati. La dissipazione di energia viene valutata variando i parametri del modello e le previsioni sono in accordo con dati preliminari di una campagna sperimentale.

Successivamente, il modello viene aggiornato per consentire l'immagazzinamento di energia di trazione o compressione all'interno della trave. Inoltre, è stato condotto uno studio parametrico per variare l'ampiezza della forza d'attrito, evidenziando il suo impatto sulla dissipazione di energia. Lo studio ha mostrato una relazione non monotona tra l'ampiezza della forza d'attrito e l'energia dissipata, con un valore ottimale che massimizza la dissipazione. Nel complesso, il modello ha fornito approfondimenti sulla mec-

canica dei materiali a base cementizia, in particolare per quanto riguarda la dissipazione, essenziale per comprenderne il comportamento nelle applicazioni strutturali.

Infine, il modello è stato ulteriormente sviluppato esaminando la possibilità di utilizzare una forza d'attrito caratterizzata da una legge evolutiva invece di una relazione costitutiva statica. Questo termine di attrito dinamico è basato su un noto modello per l'attrito nei solidi sviluppato da P. R. Dahl. Qui, la forza d'attrito dipende esclusivamente dallo spostamento di scorrimento ed evolve nel tempo, mostrando un comportamento elasto-plastico. Il modello proposto tiene conto del trasferimento di energia meccanica tra la flessione e la distorsione a taglio della trave con lo scorrimento nelle microfessure. Vengono inoltre fornite simulazioni numeriche dei descrittori cinematici e dei cicli dissipativi utilizzando il metodo degli elementi finiti per valutare le capacità predittive del modello.

Sono inoltre svolte due digressioni su due aspetti di grande importanza nella progettazione di edifici in calcestruzzo: uno studio sulla modellazione da adottare in caso di carichi ambientali dovuti ai terremoti e l'altro su alcuni aspetti della delaminazione nei compositi in calcestruzzo fibrorinforzato. Le attuali conoscenze in geofisica e ingegneria civile suggeriscono che i modelli lineari potrebbero non descrivere adeguatamente i terremoti e la propagazione delle onde sismiche a causa delle significative deformazioni del suolo. Nel primo studio si propone di dimostrare questa inadeguatezza analizzando un corpo bidimensionale con un'energia di deformazione non lineare in un dominio omogeneo a tratti che ha una conformazione simile alla Valle del fiume Aterno. Le previsioni numeriche supportano l'idea che i modelli non lineari forniscono previsioni più vicine all'evidenza sperimentale rispetto ai modelli lineari. Nel secondo studio viene inoltre proposto un modello analitico per lo studio della delaminazione nelle travi a sbalzo composite. Esso utilizza modelli di zona coesiva per simulare il processo di degrado al collegamento. Il modello evidenzia il ruolo cruciale della resistenza dello strato d'interfaccia nel mantenimento dell'integrità strutturale dei compositi. Offre un approccio analitico raffinato per lo studio della delaminazione, fornendo approfondimenti sulla deflessione della trave, sugli sforzi di taglio e sulla distribuzione della forza assiale, aspetti fondamentali per migliorare la progettazione e l'analisi delle strutture composite.

[Blank page]

Contents

1 Introduction **1**

1.1 Advances in Research on Improving the Performance of Concrete 2

1.2 Aim of the study 7

2 A simple extension of Timoshenko beam model to describe dissipation in cementitious elements **9**

3 A dissipation model for concrete based on an enhanced Timoshenko beam **32**

4 An enhanced beam model incorporating a hysteresis-based solid friction damping mechanism for cementitious materials **57**

5 Non-linear effects in seismic waves in high energy earthquakes **76**

6 An analytical model for debonding of composite cantilever beams under point loads **109**

7 Conclusions **133**

8 List of Publications **135**

Introduction

Concrete, a composite material composed primarily of cement, water, aggregates (such as sand and gravel), and sometimes admixtures, has been a cornerstone of construction for centuries. Its significance as a building material is rooted in its versatile properties, which make it indispensable for a wide range of construction applications, from simple residential structures to complex infrastructure projects. The use of concrete dates back to ancient times, with early examples found in ancient Roman architecture, such as the Pantheon and the Colosseum. The durability and longevity of these structures underscore the material enduring importance. The development of Portland cement in the 19th century revolutionized concrete production, allowing for more consistent and stronger materials, thus expanding its applicability and popularity worldwide. Concrete mechanical properties, including its high compressive strength, make it an ideal material for constructing load-bearing structures. Its ability to withstand substantial compressive forces allows it to support massive weights, making it a preferred material for foundations, bridges, and high-rise buildings. Moreover, the tensile strength of concrete, though relatively low, can be significantly enhanced by reinforcement with steel bars (rebar), resulting in reinforced concrete—a material with high resilience against both compressive and tensile stresses. Concrete is known for its exceptional durability, which contributes to the long lifespan of structures. It is resistant to fire, weathering, and chemical attack, which is crucial for infrastructure that needs to endure harsh environmental conditions. The material ability to improve over time through a process known as autogenous healing, where micro-cracks can self-heal in the presence of moisture and unhydrated cement particles and in the absence of tensile stress, further adds to its durability. One of the key advantages of concrete is its versatility. It can be cast into virtually any shape, allowing for innovative architectural designs and the construction of complex forms that would be challenging to achieve with other materials. Concrete can be produced with varying densities and strengths, making it suitable for a broad spectrum of applications, from lightweight panels for in-

sulation to high-strength formulations for industrial floors and heavy-duty pavements. While concrete is a crucial material in modern construction, its production, particularly the manufacture of cement, is associated with significant environmental impacts. Cement production is a major source of carbon dioxide (CO_2) emissions, contributing to global climate change. The industry is actively researching and developing greener alternatives, such as supplementary cementitious materials (SCMs), carbon capture technologies, and the use of recycled aggregates, to reduce the carbon footprint of concrete. Concrete is an economically viable material due to its abundance, affordability, and the relatively low cost of raw materials. The scalability of concrete production allows for mass production, making it accessible for large-scale infrastructure projects as well as smaller residential applications. Its long lifespan also reduces the need for frequent repairs and replacements, offering cost savings over the long term. Concrete remains one of the most important building materials in modern construction due to its unparalleled combination of strength, durability, versatility, and economic viability. While environmental challenges associated with concrete production need to be addressed, ongoing advancements in sustainable practices are paving the way for more eco-friendly concrete solutions. As the construction industry continues to evolve, concrete will undoubtedly remain a foundational material, crucial to building the infrastructure of the future.

1.1 Advances in Research on Improving the Performance of Concrete

Ongoing research in concrete technology is driving the development of materials with enhanced performance, sustainability, and functionality. A concise list of pertinent topics related to concrete-based materials is presented below, highlighting the numerous research lines that delve into this building material of paramount importance (see the categorized mind map 1.1 as a summary).

High-Performance Concrete (HPC) represents a significant advancement over traditional concrete, offering superior mechanical properties and durability. Research into HPC focuses on optimizing the mix design, including the use of high-quality materials and advanced admixtures, to achieve higher strength, better workability, and enhanced durability. HPC typically incorporates silica fume, fly ash, and superplasticizers, which reduce the water-to-cement ratio and enhance the concrete microstructure, leading to improved performance under both compressive and tensile stresses.

Ultra-High-Performance Concrete (UHPC) is an advanced form of

concrete that exhibits compressive strengths exceeding 150 MPa and remarkable durability. Current research in UHPC involves the use of steel or organic fibers to improve its tensile strength and toughness, making it nearly impermeable to water and other aggressive agents. The development of UHPC is driven by the need for materials that can withstand extreme conditions, such as those encountered in high-rise buildings, bridges, and structures exposed to severe environmental stressors.

Self-Healing Concrete is an innovative material designed to automatically repair micro-cracks that form over time. This capability is achieved through various mechanisms, such as the incorporation of microcapsules containing healing agents (e.g., epoxy resins) or bacteria that precipitate calcium carbonate when exposed to moisture. Research in this field is focused on optimizing the healing efficiency, longevity, and cost-effectiveness of self-healing concrete, with the goal of extending the lifespan of structures and reducing maintenance costs.

Nanotechnology is increasingly being applied to improve the properties of concrete at the molecular level. The addition of nanoparticles, such as nano-silica, nano-titania, or carbon nanotubes, can enhance the microstructure of concrete, leading to improved strength, durability, and resistance to environmental degradation. Researchers are investigating the optimal types and amounts of nanoparticles that can be incorporated into concrete mixtures to maximize these benefits without compromising workability or cost.

Sustainable Concrete Materials. The environmental impact of concrete, particularly its carbon footprint, has prompted significant research into sustainable alternatives. One major focus is the development of low-carbon or carbon-neutral cement, such as those incorporating supplementary cementitious materials (SCMs) like fly ash, slag, and calcined clay. Another area of research is the utilization of waste materials, such as recycled concrete aggregates and industrial by-products, to reduce the demand for virgin materials. Additionally, researchers are exploring the use of bio-based and geopolymer cements, which have the potential to significantly lower greenhouse gas emissions compared to traditional Portland cement.

Smart Concrete integrates sensors and other technologies to monitor the structural health of buildings and infrastructure in real-time. These sensors can measure various parameters, such as strain, temperature, humidity, and crack formation, allowing for predictive maintenance and early intervention to prevent structural failures. Research in

smart concrete is expanding to include self-sensing capabilities, where the concrete itself can detect changes in its condition without the need for external sensors. This is achieved through the incorporation of conductive materials, such as carbon fibers, which alter their electrical properties in response to stress or damage.

3D-Printed Concrete. 3D printing technology is revolutionizing the construction industry, with concrete being one of the primary materials used in this process. Research in 3D-printed concrete focuses on developing printable mixtures that can set quickly while maintaining sufficient workability. This technology enables the creation of complex, customized structures with high precision and minimal waste. Current research efforts are directed at improving the material performance, including its strength, durability, and surface finish, as well as optimizing the printing process for faster and more efficient construction.

Geopolymer Concrete is a sustainable alternative to traditional Portland cement-based concrete, made from aluminosilicate-rich materials like fly ash or slag. Research into geopolymer concrete focuses on understanding and improving its mechanical properties, durability, and long-term performance. Geopolymers have a lower carbon footprint and higher resistance to chemical attack and heat, making them particularly suitable for applications in harsh environments. Ongoing research aims to optimize the mix designs and curing processes to make geopolymer concrete a viable mainstream construction material.

Recycled Aggregate Concrete. The use of recycled aggregates derived from demolished concrete structures is an important area of research aimed at improving the sustainability of concrete. Studies focus on the effects of incorporating different percentages of recycled aggregates on the mechanical properties, workability, and durability of concrete. Advances in processing techniques and the development of admixtures that can enhance the performance of recycled aggregate concrete are key areas of focus. These efforts aim to reduce the consumption of natural resources and minimize waste in the construction industry.

Computer aided design (CAD) and computational tools play a crucial role in enhancing the performance of concrete, both in terms of material optimization and structural design. These technologies have revolutionized the way engineers and researchers approach concrete design, leading to more efficient, precise, and innovative solutions. Through the use of advanced modeling, simulation, and optimization

tools, engineers and researchers can enhance the performance of concrete, reduce its environmental impact, and ensure the longevity and safety of concrete structures. As computational power and techniques continue to evolve, their application in concrete technology is likely to expand, leading to even greater advancements in the field.

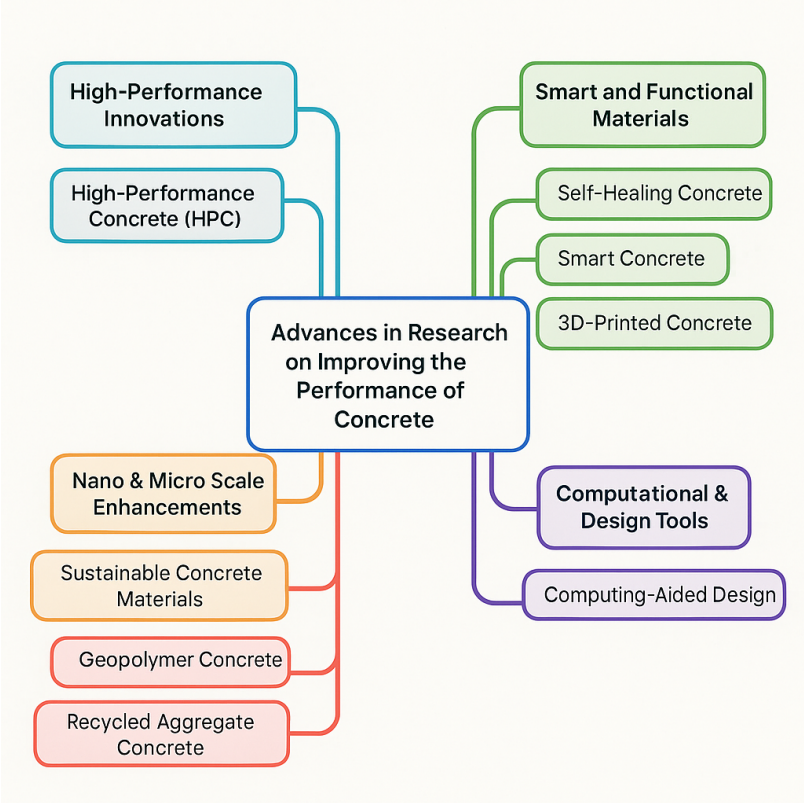


Figure 1.1. Categorized mind map: Advances in Research on Improving the Performance of Concrete.

Below is an exploration of how computer aided design contributes to improving concrete performance.

Optimization of Mix Design. Computational tools are used to optimize the mix design of concrete, ensuring the best possible balance between strength, durability, workability, and cost. Techniques such as Artificial Intelligence (AI), Machine Learning (ML), and genetic algorithms can analyze vast datasets to determine the optimal proportions of cement, water, aggregates, and admixtures. These tools help in: i) Predicting the properties of various concrete mixes without the need for extensive physical testing. ii) Tailoring mixes to specific environmental conditions or structural requirements. iii) Reducing the use of materials, such as cement, which has a high carbon footprint, by finding optimal alternatives that maintain or improve performance.

Finite Element Analysis (FEA) is widely used in the structural analysis of concrete. It involves creating detailed simulations of concrete structures to predict how they will behave under various loads and environmental conditions. FEA allows for: i) Modeling complex geometries and material behaviors, including non-linear stress-strain relationships, cracking, and creep. ii) Assessing the performance of reinforced concrete structures, including the interaction between concrete and steel reinforcement. iii) Identifying potential failure points and optimizing the design to improve safety and performance. iv) Evaluating the effects of various load conditions, such as seismic events, wind loads, and thermal stresses, leading to more resilient structures.

3D Modeling and Simulation. Advanced 3D modeling software is used to visualize and simulate concrete structures before they are built. This allows for: i) Precise design of complex architectural forms, which can be challenging to achieve with traditional methods. ii) Simulation of the construction process, including the flow and setting of concrete, which helps in planning and avoiding potential issues on-site. iii) Virtual testing of different design scenarios, enabling the selection of the most efficient and effective solutions. iv) Integration with Building Information Modeling (BIM) systems to ensure that all aspects of the structure, including materials, load-bearing elements, and sustainability features, are cohesively designed.

Machine Learning for Predictive Modeling (ML) is increasingly used to predict the long-term performance of concrete. By analyzing historical data and real-time inputs, ML models can forecast: i) The durability and lifespan of concrete structures under varying environmental conditions. ii) The development of cracks or other forms of deterioration, allowing for proactive maintenance. iii) The impact of different mix designs on the concrete mechanical properties over time. iv) Optimization of curing processes and schedules, which is critical for achieving desired strength and durability.

Topological Optimization involves using algorithms to find the most efficient material distribution within a given design space. In concrete construction, this can lead to: i) Reduced material usage without compromising structural integrity, leading to cost savings and lower environmental impact. ii) Innovative design solutions, such as lightweight, yet strong, structures that use concrete in non-traditional forms. iii) Customized structures with optimized load paths, which are particularly beneficial in 3D printing of concrete.

Data-Driven Maintenance and Monitoring. Computing tools are also essential in the maintenance and monitoring of concrete structures.

Techniques such as: i) Digital twins, where a virtual model of a physical structure is continuously updated with real-time data from sensors embedded in the concrete. This enables predictive maintenance and the early detection of potential issues. ii) Big data analytics, which can process vast amounts of data from multiple structures to identify trends and correlations, improving overall safety and performance. iii) Automated inspection systems using drones or robots equipped with cameras and sensors to assess the condition of concrete structures, reducing the need for manual inspections.

Climate and Environmental Impact Simulations. Computational tools are used to simulate the environmental impact of different concrete mixes and construction methods. These simulations help in: i) Designing concrete structures that are resilient to climate change-related factors such as temperature fluctuations, increased rainfall, and more frequent extreme weather events. ii) Assessing the life-cycle carbon footprint of concrete structures, enabling designers to choose low-carbon materials and methods that meet sustainability goals. iii) Modeling the potential impacts of future environmental scenarios on the performance and durability of concrete structures, leading to designs that are better prepared for long-term challenges.

From high-performance and self-healing concretes to innovations in nanotechnology and smart materials, these advancements are paving the way for more resilient, efficient, and environmentally friendly construction practices. As these technologies continue to evolve, they hold the promise of transforming the future of the built environment, addressing both the technical challenges and the environmental concerns associated with traditional concrete.

1.2 Aim of the study

The microstructure of concrete can be conceptualized as a matrix composed of a solid phase made up of cement and aggregates (characterized by a specific grain size and distribution). If this material were examined at the microstructure level, one would notice cracks (micro-cracks) naturally present in the concrete and generated mainly during the curing processes of the material characterized by temperature differences and chemical phenomena. These "micro-cracks" have the ability to influence the behavior of the concrete even at the macroscopic level. The proposed model takes exactly this aspect into consideration. The presence of micro-cracks has been schematized, idealizing them as having a shape similar to that of a coin (coin-shaped micro-cracks) and a random distribution/orientation.

This first premise is necessary to justify the possibility of making advantageous simplifications in the calculation models without sacrificing the ability to describe the phenomena of interest adequately. It has already been observed in the literature that a concrete sample subjected to cyclic (load-unload) compression tests (with low compressive load) can dissipate energy. In fact, if one looks at the plots of these tests, one can see how the two load and unload curves have a non-linear trend, and although close, they are not perfectly superimposable. This dissipation is caused precisely by the phenomena triggered by the applied stress, which, by bringing the faces of the micro-cracks into contact, allows the friction responsible for internal dissipation to be generated. The idea behind the research is to develop a 1D model of this material within the scope of generalized continua to be used as an evaluation tool to improve its performance. A possible way of improvement, for example, could be the use of fillers that can help maximize the internal dissipation of the material while minimizing any decrease in the mechanical resistance of the material. By using a possible micro-macro identification, the effect of these micro-fillers can be understood, and it will be possible to proceed to improve the performance of the concrete through numerical simulations in a first phase and then validate the results experimentally. It will be necessary to search for additives that, by their nature, are suitable for this purpose, preferring, in principle, those with characteristics that allow to generate more friction and, therefore, obtain a greater dissipation, for example, through the use of particles with a high specific surface.

A simple extension of Timoshenko beam model to describe dissipation in cementitious elements

---

Chapter abstract

This chapter extends the Timoshenko model for plane beams to describe dissipative mechanisms in cementitious materials under small displacements and strains. Inspired by micromorphic continua, the modified beam model introduces a kinematic descriptor representing average sliding within a time-invariant micro-crack density. Elastic deformation and frictional dissipation are considered for rough micro-crack surfaces, akin to saw-tooth joint profiles. The governing second-order differential equations are derived via a variational approach using a generalized virtual work principle in the Hamilton–Rayleigh framework. This includes: (i) inner elastic energy variation from material elasticity and nonlinear asperity deformation; (ii) virtual work of external forces and moments; and (iii) frictional dissipation modeled through a smooth Rayleigh potential with nonlinear viscous and Coulomb effects. 1D finite element simulations in COMSOL Multiphysics analyze structural elements under cyclic three- and four-point bending. Energy dissipation is studied by varying model parameters, showing agreement with preliminary experimental data. This approach provides a quantitative tool for assessing hysteresis cycles, aiding the design of cementitious materials.
Published in *Zeitschrift für angewandte Mathematik und Physik*, 2025

Z. Angew. Math. Phys. (2024) 75:166
© 2024 The Author(s)
https://doi.org/10.1007/s00033-024-02304-w

Zeitschrift für angewandte Mathematik und Physik ZAMP



A simple extension of Timoshenko beam model to describe dissipation in cementitious elements

Giuliano Aretusi, Christian Cardillo, Antonello Salvatori, Ewa Bednarczyk and Roberto Fedele

Abstract. In this paper, an extension of the Timoshenko model for plane beams is outlined, with the aim of describing, under the assumption of small displacements and strains, a class of dissipative mechanisms observed in cementitious materials. In the spirit of micromorphic continua, the modified beam model includes a novel kinematic descriptor, conceived as an average sliding relevant to a density of micro-cracks not varying along time. For the pairs of rough surfaces, in which such a distribution of micro-cracks is articulated, both an elastic deformation and a frictional dissipation are considered, similarly to what occurs for the fingers of the joints having a tooth saw profile. The system of governing differential equations, of the second order, is provided by a variational approach, endowed by standard boundary conditions. To this purpose, a generalized version of the principle of virtual work is used, in the spirit of Hamilton–Rayleigh approach, including as contributions: (i) the variation of the inner elastic energy, generated by the linear elasticity of the sound material and, in a nonlinear way, by the mutual, reversible deformation of the asperities inside the micro-cracks; (ii) the virtual work of the external actions consistent with the beam model, i.e., the distributed transversal forces and the moments per unit lengths; besides these two contributions, constituting the conservative part of the system, (iii) the dissipation due to friction specified through a smooth Rayleigh potential, entering a nonlinear dependence of viscous and Coulomb type on the sliding rate. Through a COMSOL Multiphysics® implementation, 1D finite element analyses are carried out to simulate structural elements subjected to three- and four-point bending tests with alternating loading cycles. The dissipation of energy is investigated at varying the model parameters, and the predictions turn out to be in agreement with preliminary data from an experimental campaign. The present approach is expected to provide a valuable tool for the quantitative and comparative assessment of the hysteresis cycles, favoring the robust design of cementitious materials.

Mathematics Subject Classification. 74K10, 74B20, 74A60, 65M60.

Keywords. Enhanced Timoshenko beam model, 1D continua with microstructure, Micro-cracks, Cementitious materials, Dissipated energy, Friction, Hysteresis cycles.

1. Introduction

Concrete is a multiphase and multiscale composite material that plays a fundamental and pivotal role in shaping our built environment, providing stability, durability, and versatility in a wide range of construction projects. Research in concrete technology is crucial to promote sustainability, enhance safety, and hence turns out to be of prominent interest for the construction industry. Concrete properties stem from its highly heterogeneous microstructure, including constituents of diverse typologies with various sizes and shapes which are subjected to chemical-physical processes not only during curing but along the entire service life, depending on the water-to-cement ratio and other possible additives as well as on the environmental conditions (in primis the history of temperature and of relative humidity, but also the possible diffusion of aggressive compounds). At the macroscale, the mechanical behavior of concrete results to be extremely complex, characterized by the superposition of an instantaneous response, which can be modeled by nonlinear elasticity, plasticity and damage, leading to hysteresis under cyclic loading,

Published online: 24 August 2024

and of deferred phenomena, such as shrinkage and creep. A network of very small cracks, not visible by eyes, is usually present in concrete as a consequence of the cement hydration, shrinkage and loading.

The most recent research topics on concrete concern the study of supplementary cementitious materials, also of nanometer size, the long-term chemical physical deterioration processes and self-healing provisions. Materials like fly ash, slag and silica fume can be added to concrete, in order to improve some of its features and reduce its carbon footprint [1–3], contributing to more sustainable and environmentally friendly construction practices. As an alternative, the mechanical properties and the longevity of the material can be enhanced also by incorporating nanomaterials, see, e.g., [4,5]. Nanoparticles are much smaller in size than conventional concrete constituents, and hence they fill in the gaps between larger particles, improving packing and the overall strength with it, and reducing permeability and porosity. Furthermore, nanomaterials such as nano-silica or nanotubes have a high surface-to-volume ratio [6], allowing for a better bonding with cement particles and favoring the chemical reactivity. Nanomaterials can contribute to mitigate early-age cracking in concrete by reducing the heat of hydration, controlling the formation of micro-cracks and improving the curing process. After decades of services life, chemical physical processes, such as the alkali silica reaction and the sulfate attack, promoted by specific ions already present in the constituents or diffusing from outside, accomplices the environmental conditions, can cause local swelling phenomena in the concrete elements endowed by cracking, with a correlated decrease in mechanical stiffness and strength, see e.g. [7–10]. Research on self-healing concrete focuses on strategies to repair cracks autonomously, mimicking the behavior of biological tissues, such as bone (see, e.g., [11–13]). Key aspects of this research are the development of healing agents that react and seal the crack, such as bacteria, polymers or organic and inorganic materials. At the same time, concrete-based materials with ultra-high-performance are being conceived, characterized by exceptional strength and durability, e.g., see [14–16].

In this scenario, computer simulations and digital modeling can play an increasing role in designing and optimizing the concrete structures, allowing one to carry out virtual tests very rapidly and at low costs, and contributing to a better understanding of the complex mechanisms which turn out to be multiphase and multiscale. This knowledge allows researchers for a more sustainable design, reduced construction costs, improved safety, enhanced durability, ultimately leading to better-engineered structures [17–21]. Moreover, due to a widespread use of cementitious materials in civil engineering, macroscopic models are supposed to be used also by not specialized personnel, implemented in commercial software, and hence they must be conceived as a compromise between simplicity and accuracy, hopefully including a low number of parameters to identify.

From a modeling perspective, the behavior of concrete poses numerous challenges. Crucial issues concern its nonlinear behavior [22–26] even under small strains, the dissipative effects stemming from its microstructure in both elastic and plastic regime [27–31], and the evolution of cracks [32]. Recent studies have explored innovative approaches using material particles akin to swarm robotics, offering promising computational efficiency [33,34]. As an alternative to Cauchy media, generalized continua have been investigated, see e.g. [35–41]. Among them, Cosserat-type models account for the presence of stiff aggregates, and higher gradient continua can address strong heterogeneities (see, e.g., [42–47]). Furthermore, due to the presence of voids generated during the curing process and of micro-cracks, concrete can be treated as a porous material (see, e.g., [48–50]). In particular, micro-cracks affect concrete behavior by introducing asymmetry in its mechanical response and generating internal friction under cyclic loads.

In modeling the hysteresis cycles, commonly adopted viscous models rest on a linearization of the dissipative actions. Alternatively, Coulomb-type friction between bumpy surfaces in the micro-cracks can be used, providing a response nearly independent of the frequency. Rheological models and thermodynamic frameworks with diffusive internal variables are also employed to address dissipation in solid materials.

Finally, it is important to acknowledge ongoing research efforts related to plasticity and damage evolution [51–53]. Variational formulations are favored for their logical consistency and ability to minimize unnecessary assumptions [54–57].

This work aims at investigating from the numerical standpoint the role played in concrete beams by the existing micro-cracks as a possible source of dissipation, especially during cyclic loading. To this purpose, an enhanced version of the Timoshenko beam model is proposed [58,59], inspired by a 3D continuum formulation endowed with a Coulomb-like dissipation potential (see, e.g., [60,61]), which turns out to predict more effectively the hysteresis cycles under moment and shear actions. The paper is organized as follows. Section 2 is devoted to the postulation of the elastic energy and of a Rayleigh dissipation potential for the beam and to the variational deduction of the governing equations. Details for the finite element implementation in COMSOL Multiphysics are outlined in Sect. 3. In Sect. 4, numerical results are discussed, at varying the model parameters. Section 4 outlines the pros and cons of the proposed approach and presents future developments.

A punctualization about the notation. Since a 1D description is considered in what follows, for the sake of brevity the first spatial derivative with respect to the x-coordinate of a function $a(x,t)$ is denoted by the symbol $a' = \partial a/\partial x$, while $\dot{a} = \partial a/\partial t$ indicates the first derivative of the same function with respect to time t. This notation is extended in a consistent way to the higher order derivatives.

2. Beam model with micro-slips and friction

Let us consider a 1D model of a cementitious structural element in the plane xy, lying along the x-axis in its undeformed configuration and whose length is indicated by L. For the sake of simplicity, we will not introduce a curvilinear abscissa, although the results to be discussed hold for any curved plane beam. As well known, in the standard Timoshenko model, the cross sections remain plane during the deformation process but the orthogonality assumption between the longitudinal beam line and the cross section is not retained: the effect of shear, implying also warping, is accounted for by an equivalent rotation with respect to the neutral axis. Hence, the cross section can translate and rotate around the neutral axis. We assume that at the considered scale a random distribution of micro-cracks variously oriented is in place [62]. Let us introduce a further kinematic descriptor aiming to describe, as a volume average, sliding between pairs of rough surfaces inside the micro-cracks, see, e.g., [29]. Neglecting the axial strain, the complete set of kinematic descriptors is constituted of the three functions $v(x)$, $\varphi(x)$ and $\gamma(x)$, representing in turn the transverse displacement (along y) of the beam longitudinal axis and hence of the centroid, the cross section rotation around the neutral axis and an average relative sliding between the pairs of faces constituting the distribution of micro-cracks. Under small displacements, rotations and strains, the current configuration of the beam is specified by the vector map $\boldsymbol{\chi}_t$ depending on the generic abscissa $x \in [0, L]$ and on the time variable t, as illustrated in Fig. 1. By symbols

$$\boldsymbol{\chi}_t(x) := \begin{cases} \boldsymbol{r}(t) \equiv (x, y = v(x,t)) \\ \varphi = \varphi(x,t) \\ \gamma = \gamma(x,t) \end{cases} . \tag{1}$$

Vector $\boldsymbol{r}(x,t)$ specifies the position of the cross section centroid along the loading history, and $\varphi(x,t)$ [rad] and $\gamma(x,t)$ [L] indicate the slope of the cross section and the average microscopic sliding in the sense explained above.

To seek the equilibrium configuration, a generalized version of the principle of virtual work is considered herein. This principle states that, for any virtual perturbation of the equilibrium configuration, the virtual variation of the elastic energy within the system, say $\delta\mathcal{W}^{\text{el}}$, must equal the virtual work made by the external forces acting on the system plus any other virtual dissipation, indicated in turn by $\delta\mathcal{W}^{\text{ext}}$ and

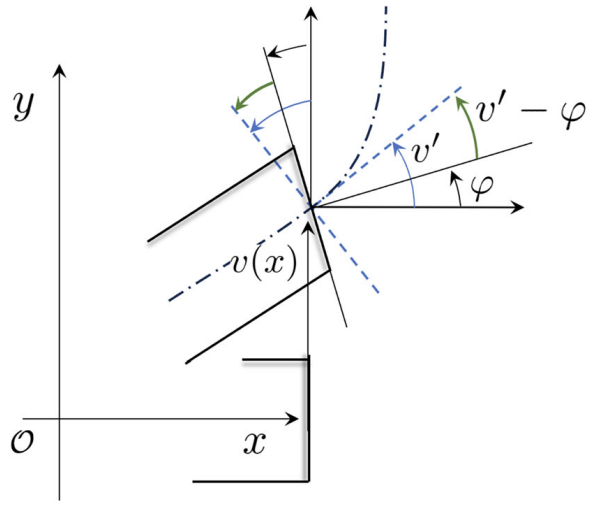


FIG. 1. Macroscopic kinematic descriptors of the beam

$\delta\mathcal{D}^{\,\mathrm{diss}}$. One has

$$\delta\mathcal{W}^{\,\mathrm{el}}(t) = \delta\mathcal{W}^{\,\mathrm{ext}}(t) + \delta\mathcal{D}^{\,\mathrm{diss}}(t), \tag{2}$$

for each time instant t. Quasi-static conditions are assumed herein, neglecting the inertial effects. We postulate the following expression of the elastic energy based on the above mentioned kinematic fields, namely

$$\begin{aligned}\mathcal{W}^{\,\mathrm{el}} = &\int_0^L \frac{1}{2}\mathrm{k}_b\,(\varphi')^2\,\mathrm{d}x + \int_0^L \frac{1}{2}\mathrm{k}_s\,(v'-\varphi)^2\,\mathrm{d}x \\ &+ \int_0^L \frac{1}{2}\mathrm{k}_{m1}\,\gamma^2\,\mathrm{d}x + \int_0^L \frac{1}{4}\mathrm{k}_{m2}\,\gamma^4\,\mathrm{d}x - \int_0^L \alpha_b\,\gamma\,\varphi'\,\mathrm{d}x - \int_0^L \alpha_s\,\gamma\,(v'-\varphi)\,\mathrm{d}x\ .\end{aligned} \tag{3}$$

The arguments of the integrals represent an energy density (per unit length), i.e. with the dimension of a force: the material parameters have the meaning of generalized stiffnesses. In particular, symbols k_b [FL^2], k_s [F], k_{m1} [$\mathrm{F/L}^2$] and k_{m2} [$\mathrm{F/L}^4$] denote direct stiffnesses associated with diverse deformation mechanisms, while α_b and α_s (in turn with dimensions [F] and [F/L]) govern their coupling. Parameters k_{m1} and k_{m2} control the energy stored by the micro-cracks. From the theoretical standpoint, the stored energy of Eq. (3) must be positive defined and strictly convex, to ensure existence and uniqueness of the minimum point. As well known, for quadratic forms these two properties coincide. If we neglect for a while the quartic contribution of the micro-slip, the coefficient matrix of the quadratic form Eq. (3) can be easily specified. Through the Sylvester's theorem, the admissible set of parameters can be specified through the constraints $\mathrm{k}_b > 0$, $\mathrm{k}_s > 0$, $\mathrm{k}_b\,\mathrm{k}_s\mathrm{k}_{m1} > \mathrm{k}_s\,\alpha_b^2 + \mathrm{k}_b\,\alpha_s^2$. All these parameters can be estimated on the basis of suitable experimental data, or through a micro–macro identification strategy, see e.g. [63–67]. Furthermore, if we assume both the coefficients of the micro-slips k_{m1} k_{m2} to be nonnegative, the nonlinear elastic contribution corresponding to the average micro-slip turns out to be positive defined and strictly convex, exhibiting two coinciding real minimum points in the origin and other two complex conjugates. If we image to integrate such a polynomial expression in γ, the odd terms cannot be included since they would provide non-symmetric contributions to the elastic energy, which in this circumstance does not appear mechanically based.

The first two contributions of the energy in Eq. (3), representing bending and shear, coincide with those of the standard Timoshenko model. The first two addends along the second row, which exhibit a polynomial dependence (quadratic and quartic) on γ, govern the amount of elastic energy stored by the pairs of surfaces constituting the distribution of micro-cracks. In fact, from a geometric standpoint, the lips of a micro-crack, which exhibit bumps or asperities, interact with each other. When these asperities come into contact, similarly to the teeth of a saw profile, they can bend like cantilevers, and hence, their relative sliding induces a fully reversible amount of deformation energy. Experimental studies, see, e.g., [68], stated that in cement-based materials sliding of micro-cracks can induce a macroscopic nonlinear response, even under small displacements and strains. The last two contributions of Eq. (3) govern the mutual energy between the beam bending and the relative slip of the asperities within the micro-cracks, as well as between the macroscopic shear distortion of the beam and the asperity deformation. To clarify this concept, let us indicate by $\mathbf{n}$ and $\mathbf{m}$ the unit vectors normal and tangential to an ideally flat micro-crack. Locally, one would expect that the Cauchy stress component $\sigma_{nm} = \boldsymbol{\sigma} : \mathbf{n} \otimes \mathbf{m}$ were responsible for the relative sliding of the opposite surfaces, while the stress component $\sigma_{nn} = \boldsymbol{\sigma} : \mathbf{n} \otimes \mathbf{n}$, if compressive, caused the unilateral closure of that crack and an increase in the frictional dissipation as stated by Coulomb. Due to the random orientation of the micro-cracks within the bulk, we reasonably expect that both the shear action and the bending moment contribute to such a relative sliding, i.e. to σ_{nm}, although not everywhere one has $\sigma_{nn} < 0$ and the frictional dissipation occurs. Therefore, we assume that coupling occurs between the micro-slips and both the shear deformation and the bending curvature.

By differentiating the energy in Eq. (3) with respect to the kinematic descriptors, we obtain the dual generalized stresses of the beam

$$
\begin{aligned}
M(x,t) &= \frac{\partial \mathcal{W}^{\mathrm{el}}}{\partial\, \varphi'} = \mathrm{k}_b \varphi' - \alpha_b \gamma \ , \quad T(x,t) = \frac{\partial \mathcal{W}^{\mathrm{el}}}{\partial\, (v' - \varphi)} = \mathrm{k}_s\, (v' - \varphi) - \alpha_s \gamma, \\
\mathfrak{T}(x,t) &= \frac{\partial \mathcal{W}^{\mathrm{el}}}{\partial\, \gamma} = \mathrm{k}_{m1}\, \gamma + \mathrm{k}_{m2}\, \gamma^3 - \alpha_b\, \varphi' - \alpha_s\, (v' - \varphi) \\
&= \left(\mathrm{k}_{m1} - \frac{\alpha_b^2}{\mathrm{k}_b} - \frac{\alpha_s^2}{\mathrm{k}_s} \right) \gamma + \mathrm{k}_{m2}\, \gamma^3 - \frac{\alpha_b}{\mathrm{k}_b}\, M - \frac{\alpha_s}{\mathrm{k}_s}\, T \ .
\end{aligned}
\tag{4}
$$

The virtual work made by the inner forces is straightforwardly computed by the first variation of the elastic energy (3) as:

$$
\begin{aligned}
\delta \mathcal{W}^{\mathrm{el}} = & \int_0^L \mathrm{k}_b \varphi'\, \delta\varphi'\, \mathrm{d}x + \int_0^L \mathrm{k}_s\, (v' - \varphi)\, \delta\, (v' - \varphi)\ \mathrm{d}x \\
& + \int_0^L \mathrm{k}_{m1} \gamma\, \delta\gamma\, \mathrm{d}x + \int_0^L \mathrm{k}_{m2} \gamma^3\, \delta\gamma\, \mathrm{d}x + \\
& - \int_0^L \alpha_b\, (\varphi'\, \delta\gamma + \gamma\, \delta\varphi')\ \mathrm{d}x - \int_0^L \alpha_s\, [(v' - \varphi)\ \delta\gamma + \gamma\ (\delta v' - \delta\varphi)]\ \mathrm{d}x\,,
\end{aligned}
\tag{5}
$$

where symbol $'$ denotes as usual the derivative with respect to the spatial coordinate x. Integrating by parts and applying the fundamental lemma of the integral calculus (as 1D counterpart of the divergence theorem), the contributions of the internal elastic energy can be grouped on the basis of the kinematic

descriptor appearing as test function,

$$\delta\mathcal{W}^{\rm el} = -\int_0^L \Big[\ (\mathrm{k}_b\varphi')' + \mathrm{k}_s\,(v'-\varphi) - (\alpha_b\gamma)' - \alpha_s\gamma\ \Big]\,\delta\varphi\,\mathrm{d}x + \big[(\mathrm{k}_b\varphi' - \alpha_b\gamma)\ \delta\varphi\big]_0^L$$
$$+\int_0^L \Big[\ \mathrm{k}_{m1}\gamma + \mathrm{k}_{m2}\gamma^3 - \alpha_b\,\varphi' - \alpha_s\,(v'-\varphi)\ \Big]\,\delta\gamma\,\mathrm{d}x +$$
$$-\int_0^L \Big\{\ \Big[\mathrm{k}_s\,(v'-\varphi)\ \Big]' - (\alpha_s\,\gamma)'\ \Big\}\delta v\,\mathrm{d}x + \Big[\ \Big\{\mathrm{k}_s\,(v'-\varphi) - \alpha_s\gamma\ \Big\}\delta v\ \Big]_0^L\,, \tag{6}$$

being as usual $[a(x)]_0^L = a(L) - a(0)$. The above equations describes the conservative part of the system. To simulate the dissipation mechanisms at the macroscale due to microscopic tangential slip with friction, in the spirit of Hamilton–Rayleigh principle a dissipation potential is introduced, see, e.g., [69]. A nonnegative Rayleigh function can be postulated as follows:

$$\mathfrak{R}(x,t) = \frac{\zeta}{\eta}\,\ln\left[\cosh(\eta\,\dot\gamma)\right]\,|\varphi'|\ \geq 0\,, \tag{7}$$

having the dimension of a power density, namely [F/t]. Symbol $\dot\gamma$ [L/t] denotes as usual the time derivative of the average slip in argument, being the product $\eta\,\dot\gamma$ non-dimensional, and ζ has dimension [F]. By differentiating the Rayleigh potential $\mathfrak{R}$ in Eq. (7) with respect to the average slip rate $\dot\gamma$, by changing the sign we obtain the dual friction force density, exerted between the opposite faces of the micro-cracks

$$\tau_{\rm diss} = -\frac{\partial\,\mathfrak{R}}{\partial\,\dot\gamma} = -\zeta\ \tanh\left[\eta\,\dot\gamma\right]\ |\varphi'|\,, \tag{8}$$

having dimension [F/L]. As anticipated in Eq. (2), we can take into account the virtual work carried out by the friction force density at the level of the micro-cracks, as follows:

$$\delta\mathcal{D}^{\rm diss}(t) = -\int_0^L \mathrm{d}x\ \zeta|\varphi'(x,t)|\tanh[\,\eta\,\dot\gamma(x,t)]\,\delta\gamma\ . \tag{9}$$

Basically, any friction force can be described through a standard Coulomb behavior. However, due to the non-Lipschitz continuity of the forcing term, including the signum function, the uniqueness of the solution would be lost. To overcome this drawback, the hyperbolic function $\tanh[\eta\,\dot\gamma]$, with asymptotes ±1 for $\eta\dot\gamma \to \pm\infty$, can be utilized to mimic the Coulomb behavior while avoiding the aforementioned issue, assuming η sufficiently large, see e.g. [70,71]. This approach turns out to work effectively in a variety of applications: moreover, it introduces a viscous behavior for small velocities $\dot\gamma$, which plays a stabilization role in several contexts, without mentioning that η can be tuned on the basis of the experimental data. The appearance in Eq. (9) of the derivative of the cross section rotation in absolute value, $|\varphi'|$, is related to the fact that, by increasing the bending curvature, compressive states become more significant at least in one part of the cross section, favoring the closure of the micro-cracks. The intensity of the friction force is governed also by the parameter ζ, independent of the term $|\varphi'|$. For a comprehensive description of the dissipation in a Lagrangian approach, the reader is referred to [69,72].

The external virtual work, including the distributed forces b_y in the y-direction and the moment per unit length μ, is expressed as:

$$\delta\mathcal{W}^{\rm ext}(t) = \int_0^L \mathrm{d}x\ b_y(x,t)\,\delta v + \int_0^L \mathrm{d}x\ \mu(x,t)\,\delta\varphi$$
$$+\,F_{y0}(t)\,\delta v(0,t) + W_0(t)\,\delta\varphi(0,t) + F_y(t)\,\delta v(L,t) + W_L(t)\,\delta\varphi(L,t)\ \ ,\ \forall\,t, \tag{10}$$

where concentrated vertical forces F_y and moments W can be applied at both the ends of the beam, at each instant t. We remark that Eq. (6) cannot provide any boundary condition for γ since this variable does not appear under a spatial derivative.

By substituting into Eqs. (2) the expressions in Eqs. (6), (9) and (10), by the fundamental lemma of the variational calculus the governing equations in strong form are as follows

$$\begin{cases} -\left[\mathrm{k}_s\,(v'-\varphi)\right]' + (\alpha_s\,\gamma)' = -T' = b_y(x,t) \\ \quad \mathrm{k}_{m1}\gamma + \mathrm{k}_{m2}\gamma^3 - \alpha_b\,\varphi' - \alpha_s\,(v'-\varphi) = \mathfrak{T} = -\zeta|\varphi'|\tanh[\,\eta\,\dot{\gamma}] \\ -\left[(\mathrm{k}_b\varphi')' + \mathrm{k}_s\,(v'-\varphi) - (\alpha_b\gamma)' - \alpha_s\gamma\right] = -M' - T = \mu(x,t) \end{cases} . \tag{11}$$

to hold $\forall\, x \in]0, L[$ and $\forall\, t$. At the beam ends, with abscissae $x = 0$ and $x = L$, values of $v(0,t)$, $v(L,t)$ and $\varphi(0,t)$, $\varphi(L,t)$ can be prescribed (essential boundary conditions), or, dually, the history of the shear force $T(0,t)$, $T(L,t)$ and of the bending moment $M(0,t)$, $M(L,t)$ (natural boundary conditions) in equilibrium with the external loading Eq. (10). Initial conditions at $t = 0$ must be considered, assuming for instance $v(x,0) = \varphi(x,0) = \gamma(x,0) = 0$, $\forall\, x \in]0, L[$.

The above equalities in Eq. (11), endowed by the boundary and the initial conditions, represent a system of nonlinear partial differential equations dependent on space and time, i.e., within the strip $[0, L] \times [0, t]$. The second equation from above includes first order derivatives as maximum order, and exhibits a nonlinear dependence on the micro-crack slip γ, which appears at the maximum power 3, and on time also, through the slip rate $\dot{\gamma}$. The remaining equations are linear in the derivatives: In the first equation, an equivalent or effective distributed transversal loading can be considered, equal to $b_y - (\alpha_s\gamma)'$, while in the last equation an equivalent or effective moment per unit length can be specified, namely $\mu - (\alpha_b\gamma)' - (\alpha_s\gamma)$. If we assume the coupling stiffnesses α_b and α_s to vanish, the second equation becomes decoupled from the remaining ones and the standard Timoshenko beam model is retrieved.

It is worth noting that the average micro-slips can affect both the shear action and the bending moment: it acts like a microrotation of the generic cross section. If we differentiate the constitutive relationships for the shear actions and the bending moment in Eq. (4), in the absence of distributed loading one obtains

$$T' = \mathrm{k}_s\,(v'' - \varphi') - \alpha_s\gamma', \qquad M' = \mathrm{k}_b\varphi'' - \alpha_b\gamma'\,. \tag{12}$$

Hence, at locations where the moment is constant with the abscissa and the shear action T is null, namely $M = c$ and $T = 0$, one has

$$\mathrm{k}_s\,(v' - \varphi) = \alpha_s\gamma, \qquad \mathrm{k}_b\varphi'' = \alpha_b\gamma'\,. \tag{13}$$

Concentrated jumps in the diagram of the shear action cause cusps in the plots of γ (with right and left derivatives tending to $\pm\infty$), while angular points for T or M cause angular points in turn for $v' - \varphi$ and γ, and for φ' and γ.

3. Virtual tests

To assess the dissipative behavior of a cementitious material under small displacements and strains, we make reference to standard experimental configurations under bending, commonly referred to as three-point and four-point bending tests. The sample has a rectangular parallelepiped shape, with sides $d \times d \times L$, and is placed on two supports located symmetrically with respect to the beam center, at a distance ℓ from each other: a vertical force is applied at the center, for the three-point test, or at two specific locations on the top for the four-point bending test (see Figs. 2, 3). Due to the presence of unilateral constraints, exclusively alternating (i.e. pulsating, with non-null mean value) loading cycles have been applied, besides a monotonic history. The preliminary numerical exercises discussed in what follows are intended to provide a basis for the model validation, and the reference for an experimental campaign on course.

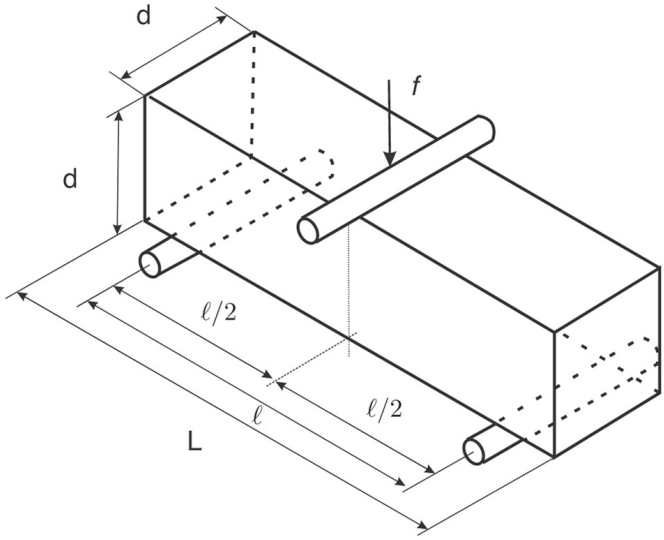


Fig. 2. Experimental configuration for three-point bending test and sample geometry

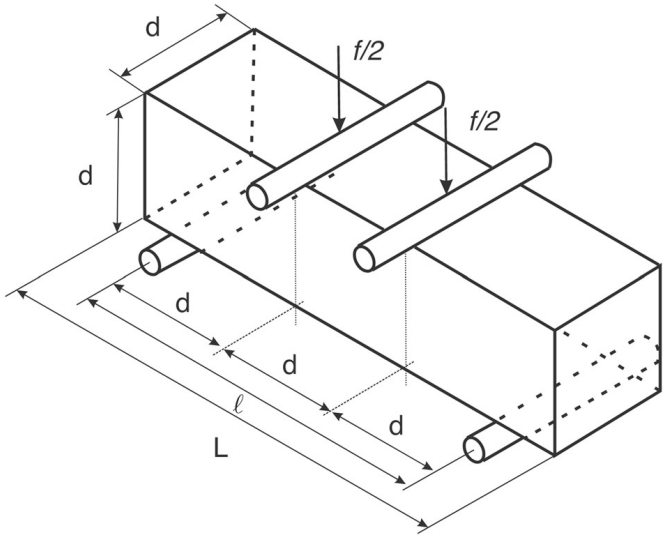


Fig. 3. Experimental configuration for the four-point bending, and sample geometry

The 1D finite element analyses are carried out by the commercial software COMSOL Multiphysics® [73], which enables the direct implementation of the weak formulation Eq. (2) through a package for partial differential equations. Since the proposed model includes the first gradient of the three kinematic descriptors, see Eq. (5), it represents a higher order model of first grade: hence, C^0 conformity at for the finite element discretization is sufficient, guaranteed by standard Lagrangian quadratic polynomials as shape functions. The adopted discretization consists of 121 quadratic finite elements, each one including three nodes, corresponding to 720 overall degrees of freedom when considering the nodal values for the three fields and the constraints. An implicit time integration scheme has been utilized, referred to as backward differentiation formula (BDF) method. For further details on the numerical implementation even under geometric nonlinearity, we forward the interested reader to [74–79].

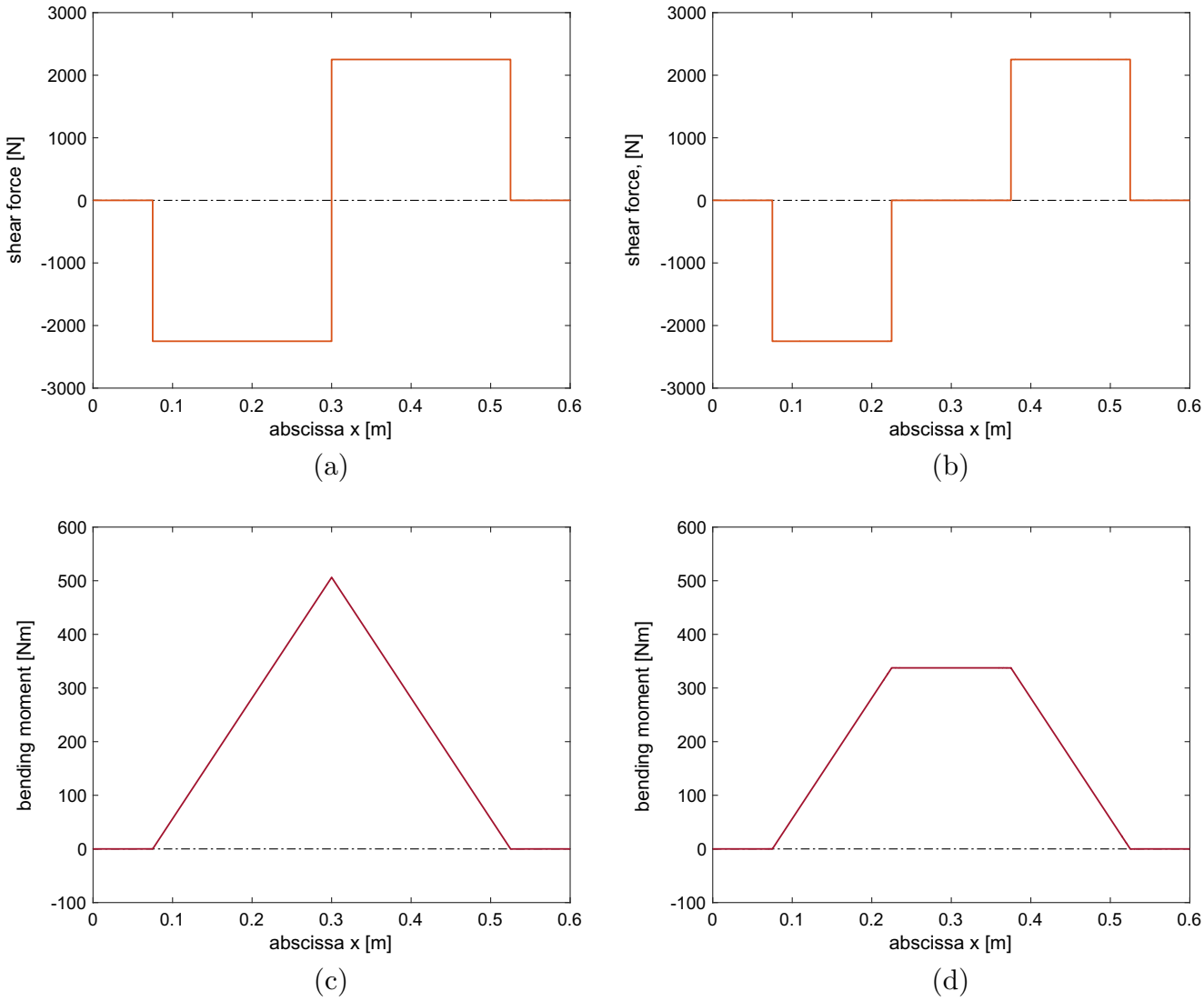


FIG. 4. Profiles of the shear force T, in (**a**) and (**b**), and of the bending moment M, in (**c**) and (d), concerning the three-point bending test (first column) and the four-point bending configuration (second column)

We have assumed Young's modulus E=31.45 (GPa), and Poisson ratio $\nu = 0.15$. The standard bending stiffness can be retrieved as $\mathrm{k}_b = E\,J$, being J the second inertia moment of the cross section, while for the shear stiffness one has $\mathrm{k}_s = 5/6\,G_c\,d^2$, where $G_c = E/[2\,(1+\nu)]$ is the shear modulus. The set of parameter values needed for the simulations is reported in the synoptic Table 1. Alternatively, these parameters can be identified through micro–macro-approaches, or on the basis of experimental data through the minimization of a suitable discrepancy norm. Instead of lengthy minimization procedures requiring numerous forward analyses, artificial neural networks (ANN), once trained and tested on the basis of synthetic data corrupted by noise, can provide very rapidly at negligible cost the solution of the inverse problem in terms of parameter estimates, see, e.g., [80–84]. As external loading an alternating force with a sinusoidal trend was considered, namely

$$f(t) = \frac{F_0}{2}\Big[\,1 - \cos\left(2\pi f_q\,t\right)\,\Big]\,. \tag{14}$$

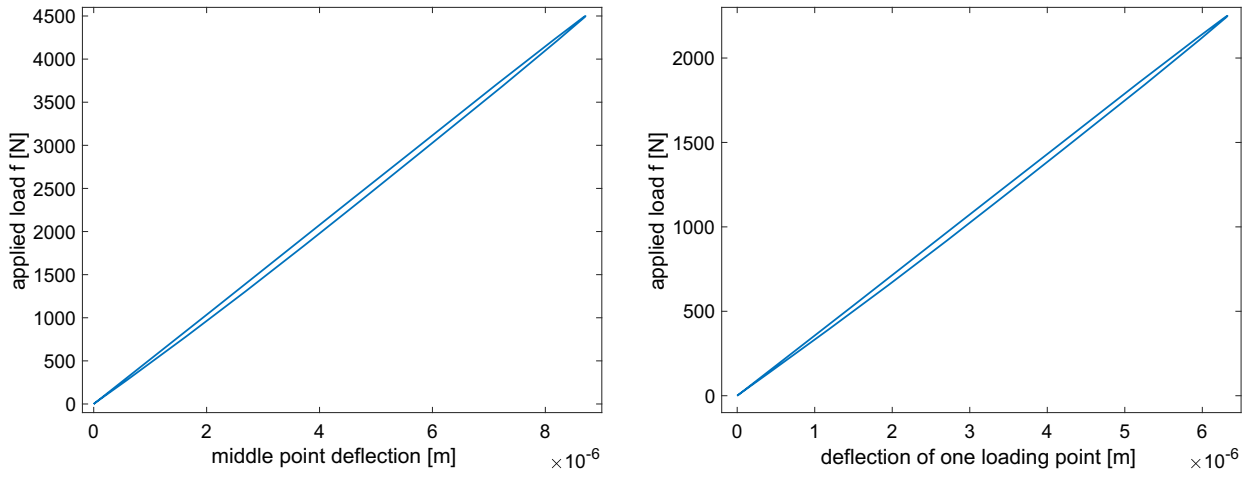


FIG. 5. Hysteresis cycle under three-point bending test, in (**a**), and four-point bending test, in (**b**). Beam geometry and model parameters are assumed as in Table 1

The amplitude was assumed as $F_0 = 4.5$ (kN) for the three-point bending test, and one half of it for the four-point bending configuration. The frequency f_q was set to 10 (Hz).

3.1. Discussion of the results

In this section, the response of the proposed beam model is analyzed critically and comparatively when subjected to three- and four-point bending tests. Parameters, assumed as in Table 1, have been selected by trial and error to fit preliminary data on plain concrete samples. Moreover, we assess the resulting dissipation during cyclic loading.

The diagrams of the generalized stresses of the beam, namely the bending moment M and the shear action T, evaluated at the force peak, are drawn in Fig. 4: those in the first column concern the three-point bending test and those in the second column the four-point bending configuration. All of them can be computed on the basis of equilibrium conditions in the isostatic structural schemes.

Figure 5 shows a complete hysteresis cycle, consisting of a loading and an unloading branch, in terms of vertical force and displacement of the application point for the two configurations. The dissipated energy, corresponding to the area within the cycle for the three-point bending test, and to the double of it for the four bending configuration (in which two identical forces are applied), has been computed by numerical quadrature: the energy loss amounts to 6.212×10^{-4} (J) and to 4.445×10^{-4} (J) for three- and four-point bending tests, respectively.

The spatial profile of the three kinematical descriptors is depicted in Fig. 6: they are evaluated at the force peak, corresponding to the time instant $t = 0.05$ (s). Along the beam axis, run by abscissa x, we report the transverse displacement v (i.e., the deformed configuration), the slope of the cross section φ, and the average sliding at the level of the micro-cracks γ. In the synoptical view of Fig. 6, arranged as a 3×2 matrix, the first column concerns the three-point bending test, the second column the four-point configuration. In the first row, showing the vertical displacement profiles, the location of the hinges is marked by circles $\circ$ along the curve, while the loading application points are marked by rhombs $\diamond$. By visual inspection, spatial profiles of the variables v and φ coincide with those expected by the standard Timoshenko model. For the assigned parameter set of Table 1, the intensity of average micro-slip γ

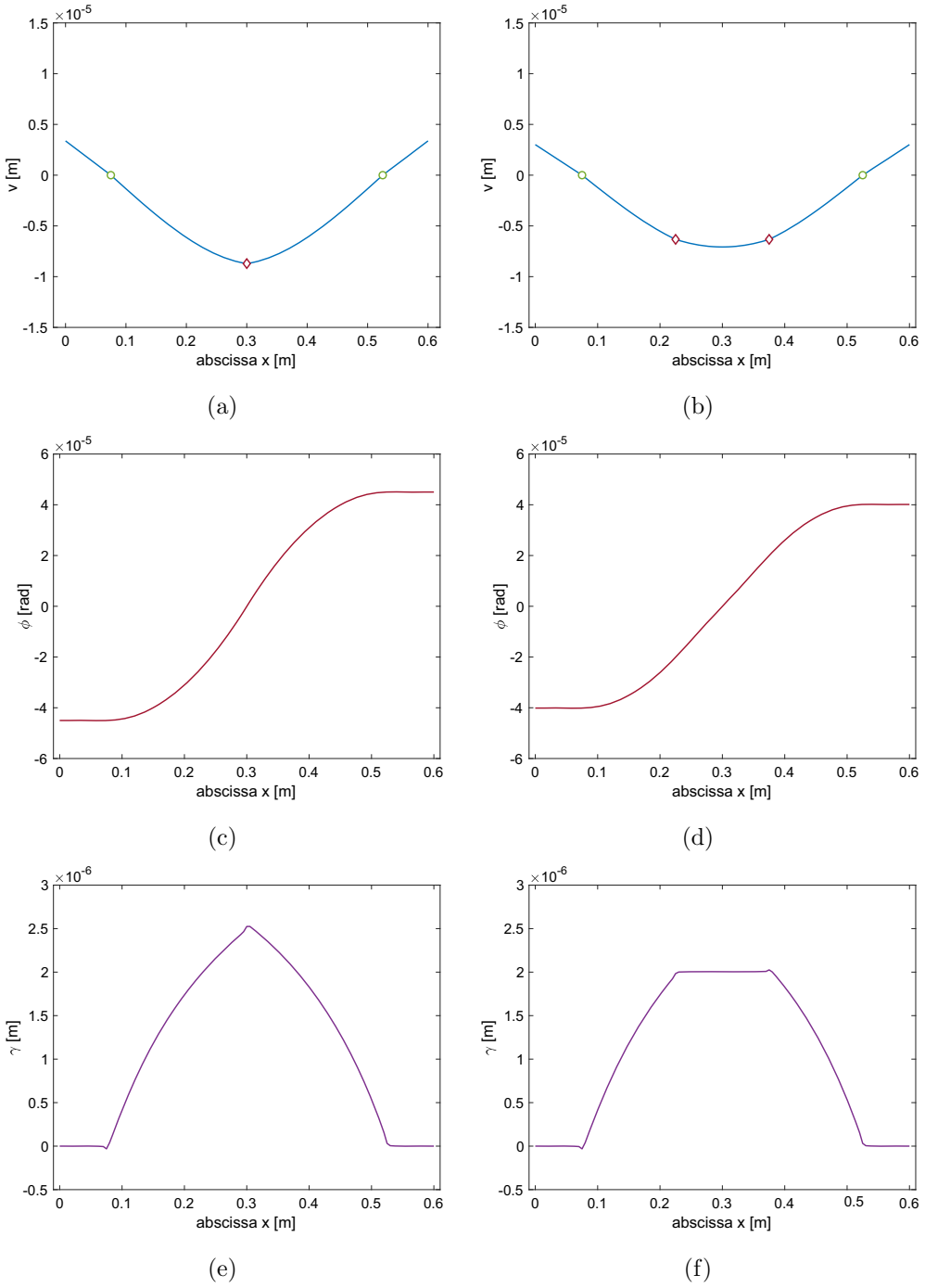


FIG. 6. Three point bending (in the first column) and four-point bending configurations (in the second column). Profiles along the beam axis, evaluated at the force peak (time instant $t = 0.05$ (s)), of the three field variables: the transverse displacement, v, (**a**) and (**b**); the slope of the cross section, φ, (**c**) and (**d**); and the relative sliding at the level of micro-cracks, γ, (**e**) and (**f**). In plots (**a**) and (**b**), the locations of the supports are marked by circles $\circ$, while the application points of the force by rhombs $\diamond$

approximately follows the profile of the bending moment. Moreover, the plot of γ exhibits angular points and cusps at locations where the shear action undergoes jumps.

Table 1. *Beam geometry and model parameters used as a reference in the numerical exercises*

Geometry		
d	L	ℓ
150 (mm)	600 (mm)	450 (mm)
Material parameters		
k_b	k_s	k_{m1}
1.33×10^6 (N m^2)	2.56×10^8 (N)	7.5×10^8 (N/m^2)
k_{m2}	α_b	α_s
1.00×10^8 (N/m^4)	8.05×10^6 (N)	0.5×10^7 (N/m)
ζ	η	E_c
2.95×10^8 (N)	225 (s/m)	31.45 (GPa)

To favor a huge comprehension of the proposed model, Figs. 7 and 8 depict the time histories of the relative micro-slip γ and of the density of friction force $\tau_{\text{diss}} = -\zeta|\varphi'|\tanh[\eta\dot{\gamma}]$, evaluated at the application point of the external force for both the test configurations. It is worth noting that the time response of these quantities is nonlinear with respect to the evolution of the loading multiplier, varying according to the law in Eq. (14).

To assess the role played by the amplitude of the friction force, we have run several analyses by scaling the parameter ζ in Eq. (8) through a factor q. Figure 9 shows the energy lost by the system along one complete cycle at varying the scale factor through the values $q = (0.25, 0.5, 1, 2, 4)$. As a result, we have obtained for the dissipated energy values in the interval $[3.1 \times 10^{-4}, 6.2 \times 10^{-4}]$ (J) for the three-point bending test, and slightly smaller values, within the interval $[1.9 \times 10^{-4}, 4.7 \times 10^{-4}]$ (J), for the four-point configuration. The dotted lines indicate regression curves fitting these data, relevant to each test configuration. The observed trends are qualitatively similar, revealing the presence of a maximum of the dissipated energy. This behavior typically denotes the presence of two conflicting features. In fact, on the one hand, when the amplitude of the friction force density is low, there is less dissipation within a hysteresis cycle. On the other hand, if the amplitude of the friction force exceeds a threshold, the average relative sliding inside the distribution of micro-cracks cannot increase, and with it the dissipation necessarily decreases. Therefore, it is possible to select a value of the friction coefficient as the point which maximizes the dissipated energy.

To assess the role played by the coupling parameters, we have increase the value of the coefficient α_b in Table 1 by 30% and 60%. Figure 10 shows the hysteresis cycles predicted by the finite element analyses for the selected configurations. In particular, for the three-point bending test, starting from 6.212×10^{-4} (J) the dissipated energy is increased up to 0.0011 (J) and 0.0019 (J), respectively. Similarly, in the four-point configuration, for the same percentage increment of the parameter α_b, starting from 4.445×10^{-4} (J) the dissipated energy is increased up to 8.136×10^{-4} (J) and 0.0014 (J), in the order for the two levels of considered increase.

The same analysis has been carried out for the coupling coefficient α_s. However, since this coefficient affects less the overall behavior, the changes in percentage observed with respect to the reference set of parameters are negligible. In the case of the three-point bending test, the 30% increase in this coupling stiffness results into an energy loss of 6.215×10^{-4} (J), and a 60% increase causes a dissipation of 6.219×10^{-4} (J). In the four-point bending test, a 30% increase corresponds to an energy loss of 4.449×10^{-4} (J), while the 60% increase gives rise to a dissipation of 4.453×10^{-4} (J). After that, we increased the value of α_s by five times. Firstly, we have obtained hysteresis cycles very close to those provided by the reference parameters of Table 1, confirming that the impact of α_s is less significant with respect to α_b. The energy loss for the three-point and four-point bending configurations amounts to 6.314×10^{-4} (J) and 4.534×10^{-4} (J), respectively. Secondly, analyzing the distribution of the average sliding γ at the peak, as shown in Fig. 11, due to the linear coupling between γ and the shear deformation $(v' - \varphi)$, one can easily recognize an increase of the average sliding in one side of the beam and the opposite behavior

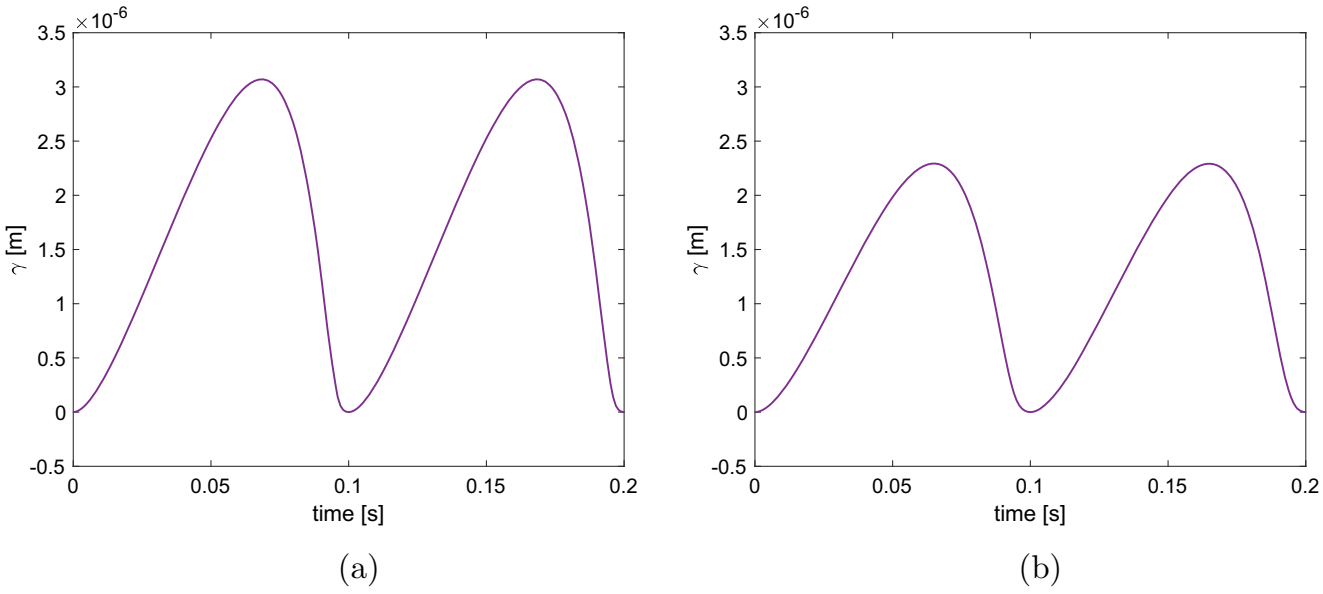


FIG. 7. Time history of the micro-slip γ for the three-point bending test evaluated at the middle point, in (**a**), and for the four-point bending test evaluated at one loading point, in (**b**)

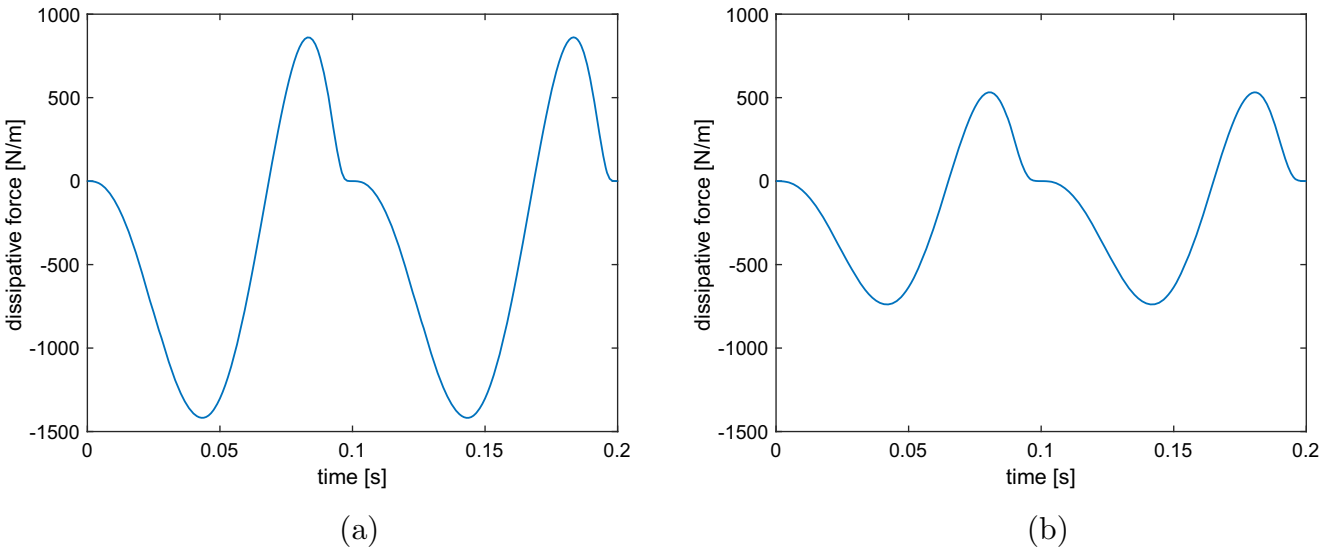


FIG. 8. Time history of the friction force density, $\tau_{\text{diss}} = -\zeta|\varphi'|\tanh[\eta\dot{\gamma}]$, evaluated at the middle point of the beam in the three-point bending configuration, in (**a**), and at one of the force application points for the four-point bending test, in (**b**)

in the remaining part, so that the distribution of the average sliding of micro-cracks turns out to be not symmetric. This asymmetric behavior can be noticed also for the distribution of the dissipated power density, as reported in Fig. 12.

Let us consider the stiffness k_{m2}, multiplying γ^4 in the expression of elastic energy Eq. (3). Figure 13 shows the hysteresis cycles corresponding to $k_{m2} = 0$ (N/m^4) (subfigures (a) and (b)) and $k_{m2} = 1 \times 10^{20}$ (N/m^4) (subfigures (c) and (d)). The first and second column of the composite figure correspond in the order to the three-point and to the four-point bending test. When we set $k_{m2} = 0$ (N/m^4), we obtain

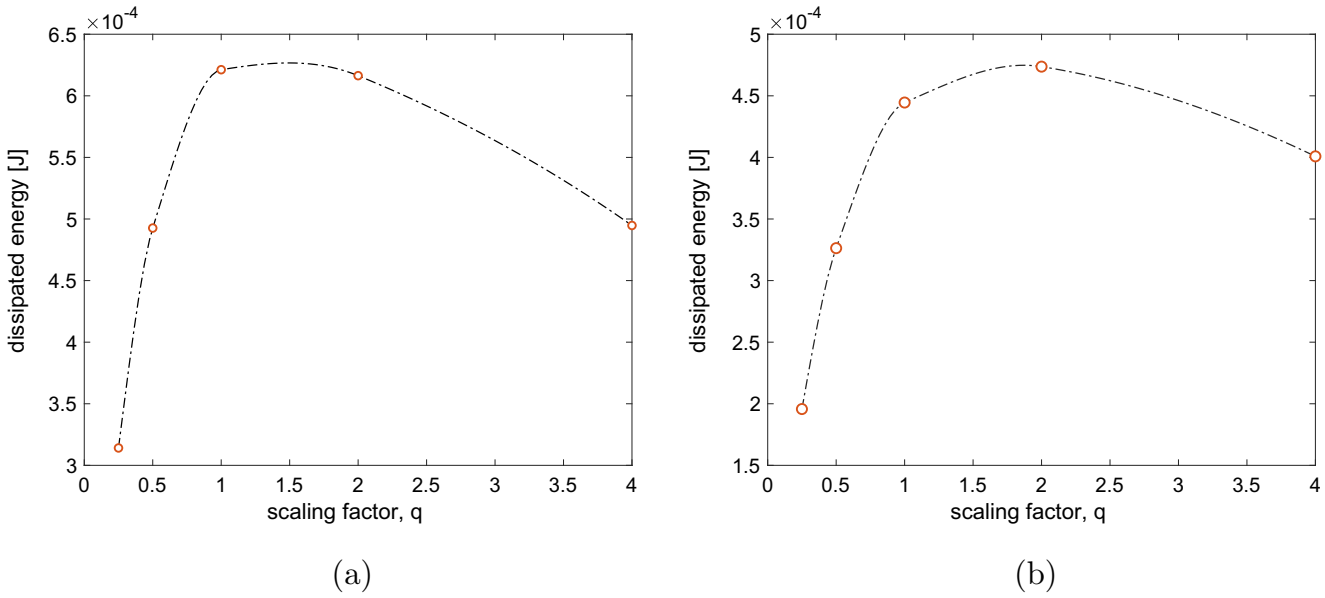


FIG. 9. Dissipated energy at varying the scaling factor q (multiplying parameter ζ), for the three-point bending test, in (**a**), and for the four-point configuration, in (**b**). The dashed line indicate a regression curve, interpolating the results of the simulations marked by red circles ∘

for the three-point bending test an energy loss of 6.212×10^{-4} (J), while for the four-point bending test the dissipated energy per cycle amount to 4.445×10^{-4} (J), almost unchanged with respect to the above mentioned cases, with parameters corresponding to Table 1. By setting $\mathrm{k}_{m2} = 1 \times 10^{20}$ (N/m^4), for the three-point bending test the energy loss in the loading–unloading cycle amounts to 3.423×10^{-4} (J), while for the four-point configuration equals 2.605×10^{-4} (J). Thus, a higher stiffness of the asperities inside the micro-cracks leads to a substantial decrease of the dissipation.

4. Closing remarks and future prospects

In this study, a novel beam model especially suitable for cementitious structural elements is outlined, which generalizes the standard Timoshenko beam by a high order strategy. In the mechanical formulation, an additional kinematic descriptor has been considered, which represents an average sliding between the pairs of rough surfaces constituting a density of micro-cracks. Such a distributions of micro-cracks, randomly oriented within the beam volume, is assumed to remain constant during the entire loading process. The additional field variable, rooted in the meso-structure, generates both an elastic energy and a nonlinear dissipation, defined through a smooth Rayleigh potential which induces a Coulomb-like friction force with a viscous dependence on the rate of deformation. The expression of the stored energy associated with these micro-slips has been enriched up to include a quartic term, and represents the conservative part of the system. The coefficients weighting the diverse contributions are subjected to constraints, deduced by the Sylvester criterion, to guarantee positive definition and strict convexity of the energy functional. This formulation, deduced by a variational approach based on the principle of virtual work in the spirit of Hamilton–Rayleigh approach, provides a simple but effective framework to describe dissipative mechanisms in cementitious elements, which imply an energy loss during cycling loading. The response of the extended Timoshenko beam can be described through a system of three nonlinear partial different equations, depending on space and time, endowed by boundary and initial conditions: at the beam ends, one can prescribe the history of the transversal displacement and of the rotation of the cross

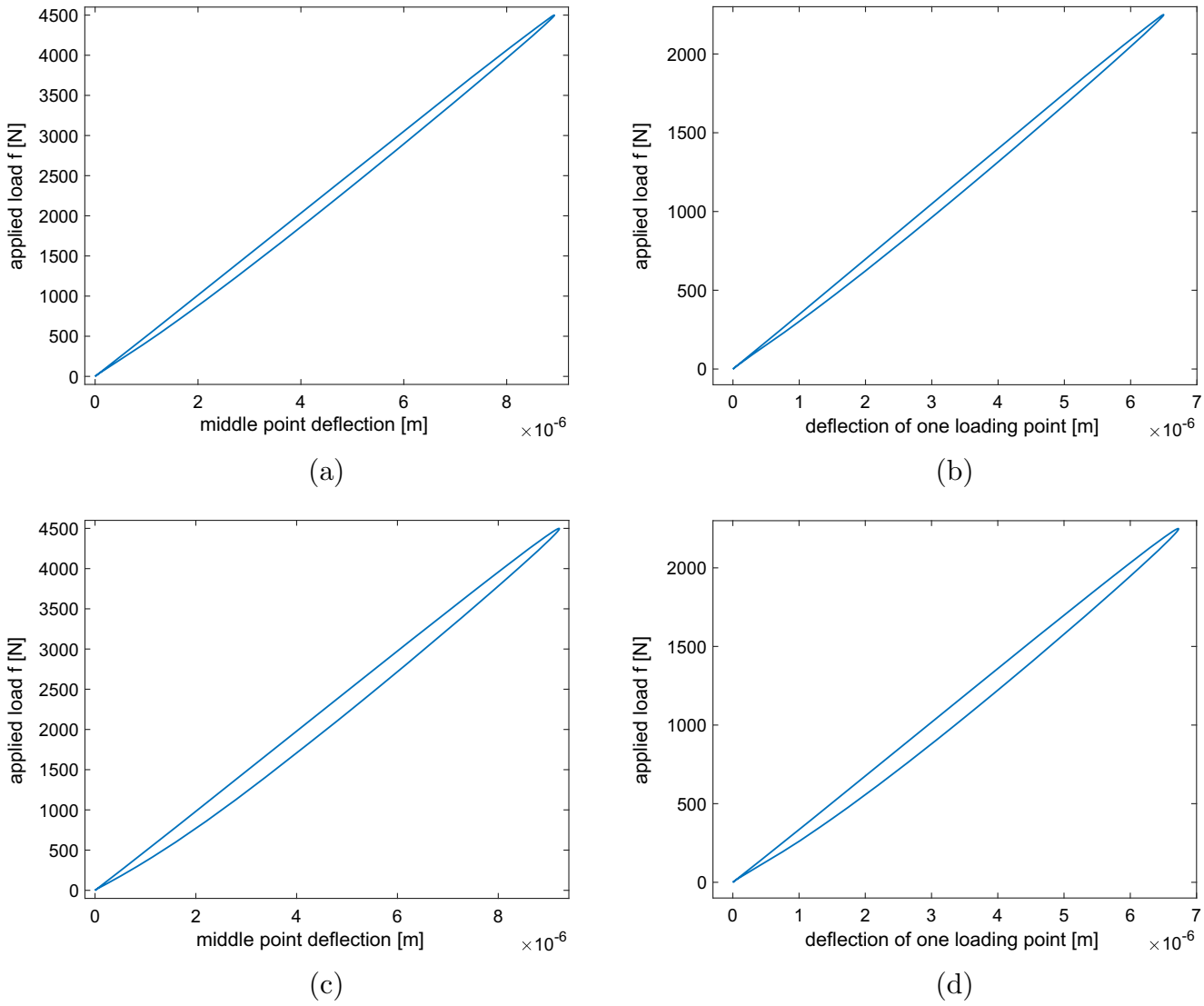


FIG. 10. Hysteresis cycles in the three-point bending test, when scaling the coupling stiffness α_b by factors 1.3 and 1.6, in (**a**) and (**c**), respectively, and in the four-point bending test, in (**b**) and (**d**) with the same scaling

section (but not the average sliding), or, alternatively, of their dual actions, while at the initial time instant the three fields are assumed to be null along the entire beam.

Starting from the weak formulation of this model, 1D finite element analyses have been carried out by COMSOL Multiphysics®, describing the three-point and the four-point bending tests as reference configurations under alternating cycles. At varying the governing parameters, the extended beam model turns out to describe in a satisfactory manner hysteresis cycles, in agreement with literature data (see, e.g., [85,86]) and with preliminary experiments carried out by the authors on plain concrete samples. The nonlinear relationship between the amplitude of the frictional force and the energy loss during the hysteresis cycles has been investigated, revealing the existence of a critical intensity at which the dissipation is maximized.

The proposed model is expected to provide useful insights for the optimal design of cementitious structural elements, particularly in those applications where both the energy dissipation and the mechanical stiffness represent critical factors. For instance, in the seismic structural design, building materials must

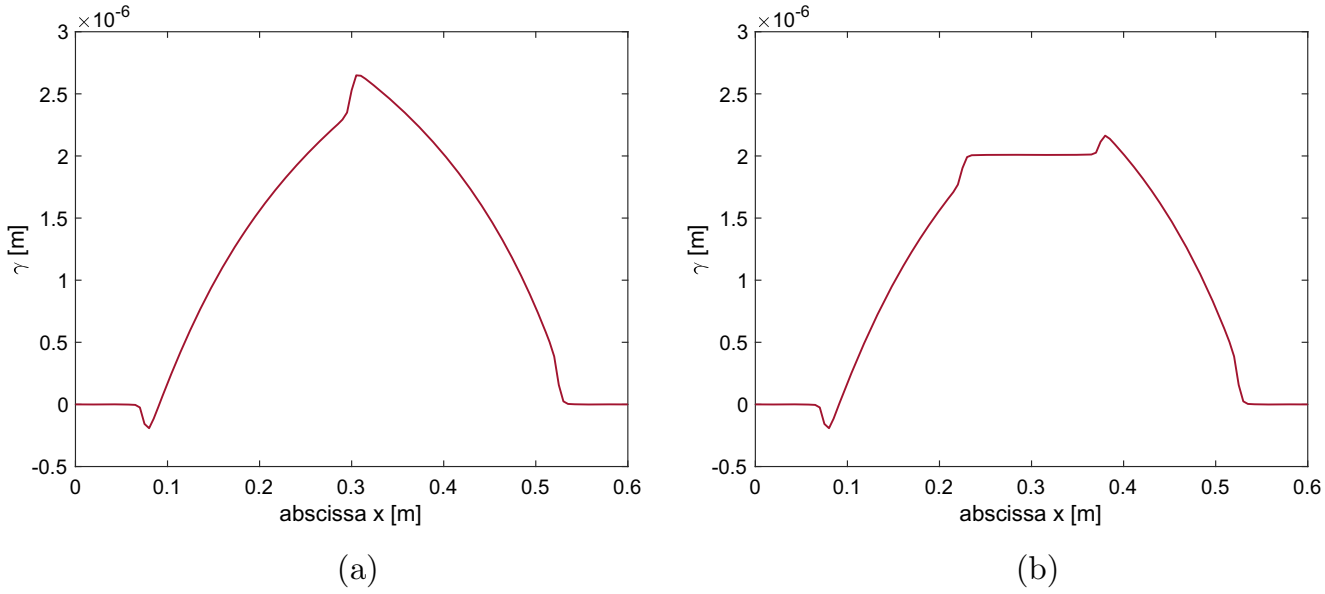


FIG. 11. Distribution of the micro-crack average sliding γ along the beam for the three-point bending test, in (**a**), and for the four-point configuration, in (**b**), relevant to $\alpha_s = 2.5 \times 10^7$ (N/m). For this value of α_s, the profile of γ turns out to be non-symmetric with respect to the center of the beam, exhibiting a stronger dependence on the sign of the shear action T

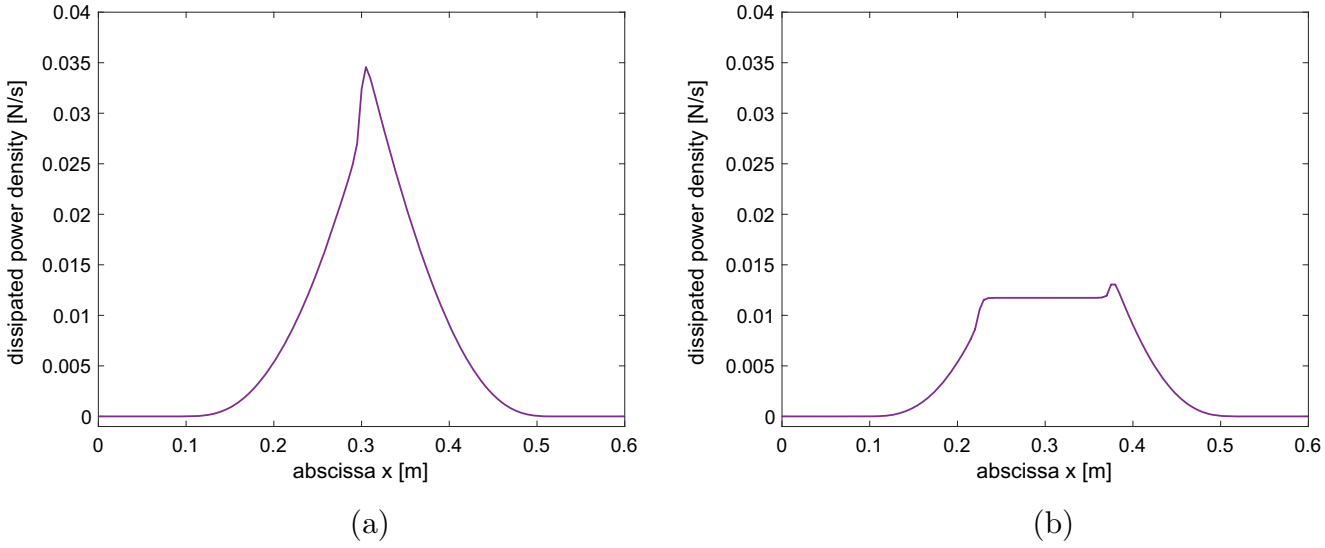


FIG. 12. Distribution of the dissipated power density $\mathfrak{R}$ for the three-point bending test, in (**a**), and for the four-point configuration, in (**b**), relevant to $\alpha_s = 2.5 \times 10^7$ (N/m). For this value of α_s, the distribution of the power density turns out to be non-symmetric with respect to the center of the beam, exhibiting a stronger dependence on the sign of the shear action T

be able of dissipating the highest amount of energy without decreasing the mechanical stiffness; analogous considerations can be referred to structures subjected to dynamic impact. The present formulation allows one to compare the dissipation capabilities of cementitious elements, for instance, at varying the typology and the percentage of additives.

As a possible improvement, the interactions among the micro-cracks can be investigated on a statistical basis, deducing the energy dissipated by friction. As discussed in [87,88], for moderate crack densities, the interaction effects inside the population of cracks can be approximated assuming that the influence of the

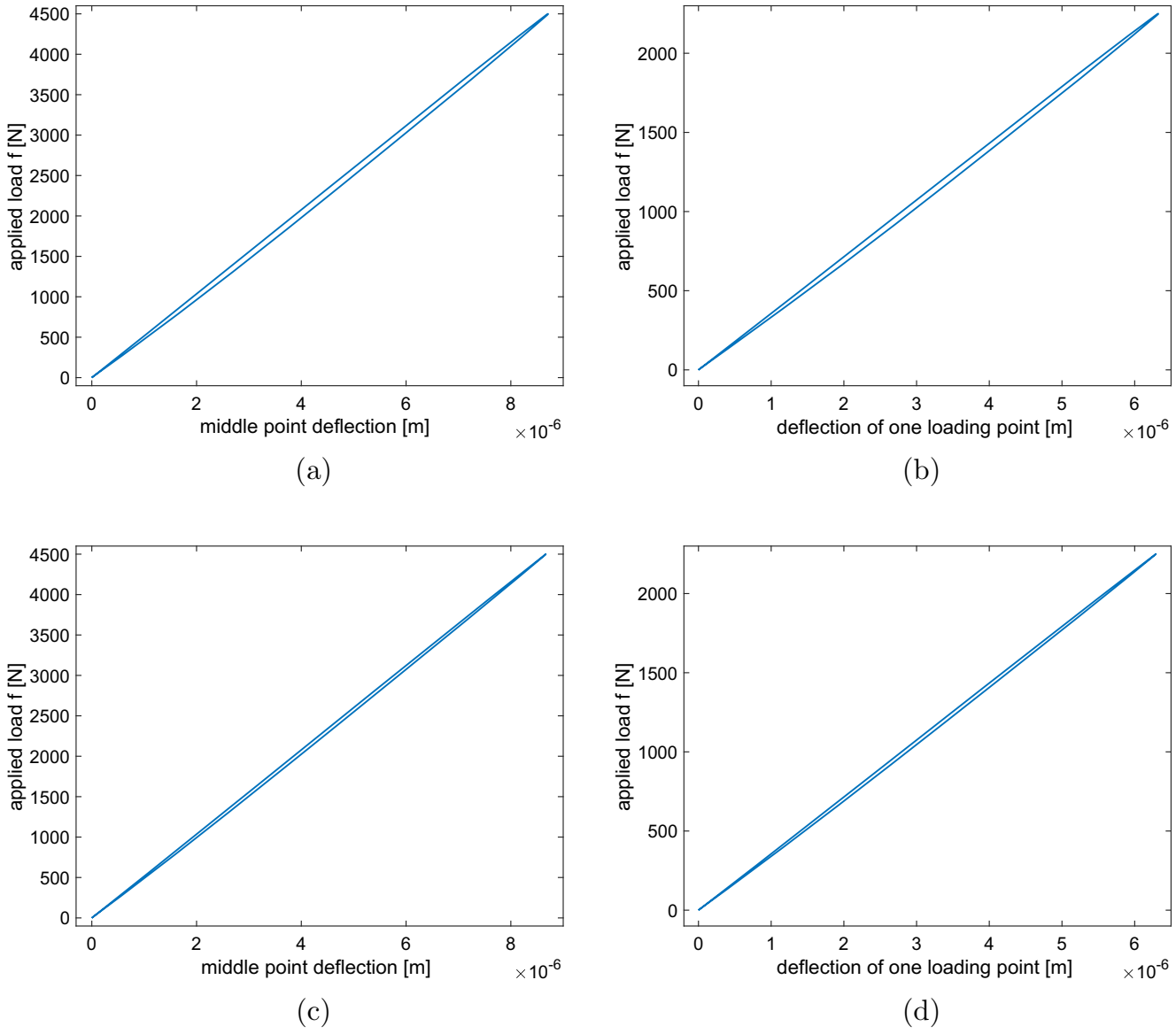


FIG. 13. Hysteresis cycles in the three-point bending test, for $k_{m2} = 0$ (N/m^4) and $k_{m2} = 1 \times 10^{20}$ (N/m^4), in (**a**) and (**c**) respectively, and in the four-point bending test, in (**b**) and (**d**) with the corresponding values of k_{m2} on the same row

deformation at one crack on the stress field in the neighborhood of another crack remains spatially uniform (Kachanov model). This model would allow to provide through a micro–macro-approach estimations of the coupling stiffnesses in Eq. (3), to be compared with those identified by inverse analyses on the basis of experimental data at the macroscale. Moreover, by properly describing the growth of the population of micro-cracks as well as the propagation and coalescence of cracks (see, e.g., [89]), also damage and fatigue phenomena can be modeled.

In this scenario, robust identification procedures are required, exploiting sensitivity analysis to realize non-trivial tests and selecting a suitable discrepancy function to minimize. For instance, the response in terms of displacements and rotations predicted by the proposed model can be validated experimentally by means of full-field measurements, see, e.g., [90,91]. As well known, kinematic data within a region of interest can be obtained through multiscale digital image correlation (DIC) techniques by processing digital images monitoring the sample deformation during the tests. Such images can be provided by a single optical camera, and in this case they provide information about plane displacements over the outer

flat surface of the sample (2D DIC); alternatively, three dimensional tomographic reconstructions can be acquired within a X-ray tomograp coupled with an "in situ" mechanical apparatus, and in this case they provide information about three dimensional displacements within the bulk of the sample (3D-Volume DIC). As measurable quantities in the identification procedures one could process also the temperature fields provided, for instance, by a thermal imaging camera, since the temperature distribution over the outer surface is expected to be correlated with the dissipated power density generated by the micro-slips. Moreover, recourse can be made to micro–macro computational strategies starting from simplified mechanical assumptions on the meso-structure, apt to compute the stiffnesses appearing in the expression of the energy Eq. (3).

Funding Open access funding provided by Politecnico di Milano within the CRUI-CARE Agreement.

Open Access. This article is licensed under a Creative Commons Attribution 4.0 International License, which permits use, sharing, adaptation, distribution and reproduction in any medium or format, as long as you give appropriate credit to the original author(s) and the source, provide a link to the Creative Commons licence, and indicate if changes were made. The images or other third party material in this article are included in the article's Creative Commons licence, unless indicated otherwise in a credit line to the material. If material is not included in the article's Creative Commons licence and your intended use is not permitted by statutory regulation or exceeds the permitted use, you will need to obtain permission directly from the copyright holder. To view a copy of this licence, visit http://creativecommons.org/licenses/by/4.0/.

Publisher's Note Springer Nature remains neutral with regard to jurisdictional claims in published maps and institutional affiliations.

References

[1] Misra, A., Biswas, D., Upadhyaya, S.: Physico-mechanical behavior of self-cementing class C fly ash-clay mixtures. Fuel **84**(11), 1410–1422 (2005). https://doi.org/10.1016/j.fuel.2004.10.018

[2] Contrafatto, L., Danzuso, C.L., Gazzo, S., Greco, L.: Physical, mechanical and thermal properties of lightweight insulating mortar with recycled Etna volcanic aggregates. Constr. Build. Mater. **240**, 117917 (2020). https://doi.org/10.1016/j.conbuildmat.2019.117917

[3] Sclofani, D.A.S., Contrafatto, L.: Experimental behaviour of polyvinyl-alcohol modified concrete. Adv. Mater. Res. **687**, 155–160 (2013). https://doi.org/10.4028/www.scientific.net/AMR.687.155

[4] Spagnuolo, M.: Symmetrization of mechanical response in fibrous metamaterials through micro-shear deformability. Symmetry **14**(12), 2660 (2022). https://doi.org/10.3390/sym14122660

[5] Javili, A., dell'Isola, F., Steinmann, P.: Geometrically nonlinear higher-gradient elasticity with energetic boundaries. J. Mech. Phys. Solids **61**(12), 2381–2401 (2013). https://doi.org/10.1016/j.jmps.2013.06.005

[6] Abhilash, P., Nayak, D.K., Sangoju, B., Kumar, R., Kumar, V.: Effect of nano-silica in concrete: a review. Constr. Build. Mater. **278**, 122347 (2021). https://doi.org/10.1016/j.conbuildmat.2021.122347

[7] Comi, C., Fedele, R., Perego, U.: A chemo-thermo-damage model for the analysis of concrete dams affected by alkali-silica reaction. Mech. Mater. **41**(3), 210–230 (2009). https://doi.org/10.1016/j.mechmat.2008.10.010

[8] Cefis, N., Tedeschi, C., Comi, C.: External sulfate attack in structural concrete made with Portland-limestone cement: an experimental study. Can. J. Civ. Eng. **48**(7), 731–739 (2021). https://doi.org/10.1139/cjce-2019-0354

[9] Scrofani, A., Barchiesi, E., Chiaia, B., Misra, A., Placidi, L.: Fluid diffusion related aging effect in a concrete dam modeled as a Timoshenko beam. Math. Mech. Complex Syst. **11**(2), 313–334 (2023). https://doi.org/10.2140/memocs.2023.11.313

[10] Barchiesi, E., Hamila, N.: Maximum mechano-damage power release-based phase-field modeling of mass diffusion in damaging deformable solids. Z. Angew. Math. Phys. **73**(1), 35 (2022). https://doi.org/10.1007/s00033-021-01668-7

[11] Sangadji, S., Schlangen, E.: Mimicking bone healing process to self repair concrete structure novel approach using porous network concrete. Procedia Engn. **54**, 315–326 (2013). https://doi.org/10.1016/j.proeng.2013.03.029

[12] Bednarczyk, E.I., Lekszycki, T., Glinkowski, W.: Effect of micro-cracks on the angiogenesis and osteophyte development during degenerative joint disease. Comput. Assist. Methods Eng. Sci. **24**(3), 149–156 (2018)

[13] Giorgio, I., Spagnuolo, M., Andreaus, U., Scerrato, D., Bersani, A.M.: In-depth gaze at the astonishing mechanical behavior of bone: a review for designing bio-inspired hierarchical metamaterials. Math. Mech. Solids **26**(7), 1074–1103 (2021). https://doi.org/10.1177/1081286520978516

[14] Xue, J., Briseghella, B., Huang, F., Nuti, C., Tabatabai, H., Chen, B.: Review of ultra-high performance concrete and its application in bridge engineering. Constr. Build. Mater. **260**, 119844 (2020). https://doi.org/10.1016/j.conbuildmat.2018.08.036
[15] Khristenko, U., Schuß, S., Krüger, M., Schmidt, F., Wohlmuth, B., Hesch, C.: Multidimensional coupling: a variationally consistent approach to fiber-reinforced materials. Comput. Methods Appl. Mech. Eng. **382**, 113869 (2021). https://doi.org/10.1016/j.cma.2021.113869
[16] Lamzin, D.A., Bragov, A., Lomunov, A., Konstantinov, A.Y., dell'Isola, F.: Analysis of the dynamic behavior of sand-lime and ceramic bricks. Mater. Phys. Mech. **42**(6), 691 (2019). https://doi.org/10.18720/MPM.4262019_1
[17] Kezmane, A., Chiaia, B., Kumpyak, O., Maksimov, V., Placidi, L.: 3D modelling of reinforced concrete slab with yielding supports subject to impact load. Eur. J. Environ. Civ. Eng. **21**(7–8), 988–1025 (2017). https://doi.org/10.1080/19648189.2016.1194330
[18] Funari, M.F., Spadea, S., Fabbrocino, F., Luciano, R.: A moving interface finite element formulation to predict dynamic edge debonding in FRP-strengthened concrete beams in service conditions. Fibers **8**(6), 42 (2020). https://doi.org/10.3390/fib8060042
[19] Augello, R., Carrera, E., Pagani, A., Arruda, M.R., Shen, J.: Node-dependent kinematic models applied to reinforced concrete structures. Math. Mech. Complex Syst. **11**(1), 19–43 (2023). https://doi.org/10.2140/memocs.2023.11.19
[20] Rezaei, N., Barchiesi, E., Timofeev, D., Tran, C.A., Misra, A., Placidi, L.: Solution of a paradox related to the rigid bar pull-out problem in standard elasticity. Mech. Res. Commun. **126**, 104015 (2022). https://doi.org/10.1016/j.mechrescom.2022.104015
[21] Rezaei, N., Yildizdag, M.E., Turco, E., Misra, A., Placidi, L.: Strain-gradient finite elasticity solutions to rigid bar pull-out test. Contin. Mech. Thermodyn. **36**, 607–617 (2024). https://doi.org/10.1007/s00161-024-01285-5
[22] Pietraszkiewicz, W., Eremeyev, V.A.: On vectorially parameterized natural strain measures of the non-linear Cosserat continuum. Int. J. Solids Struct. **46**(11–12), 2477–2480 (2009). https://doi.org/10.1016/j.ijsolstr.2009.01.030
[23] Giorgio, I., De Angelo, M., Turco, E., Misra, A.: A Biot–Cosserat two-dimensional elastic nonlinear model for a micromorphic medium. Contin. Mech. Thermodyn. **32**(5), 1357–1369 (2020). https://doi.org/10.1007/s00161-019-00848-1
[24] Turco, E., dell'Isola, F., Misra, A.: A nonlinear Lagrangian particle model for grains assemblies including grain relative rotations. Int. J. Numer. Anal. Methods Geomech. **43**(5), 1051–1079 (2019). https://doi.org/10.1002/nag.2915
[25] Spagnuolo, M., Franciosi, P., Dell'Isola, F.: A Green operator-based elastic modeling for two-phase pantographic-inspired bi-continuous materials. Int. J. Solids Struct. **188**, 282–308 (2020). https://doi.org/10.1016/j.ijsolstr.2019.10.018
[26] Ciallella, A., Giorgio, I., Eugster, S.R., Rizzi, N.L., dell'Isola, F.: Generalized beam model for the analysis of wave propagation with a symmetric pattern of deformation in planar pantographic sheets. Wave Motion **113**, 102986 (2022). https://doi.org/10.1016/j.wavemoti.2022.102986
[27] Vaiana, N., Sessa, S., Rosati, L.: A generalized class of uniaxial rate-independent models for simulating asymmetric mechanical hysteresis phenomena. Mech. Syst. Signal Process. **146**, 106984 (2021). https://doi.org/10.1016/j.ymssp.2020.106984
[28] Vaiana, N., Sessa, S., Marmo, F., Rosati, L.: A class of uniaxial phenomenological models for simulating hysteretic phenomena in rate-independent mechanical systems and materials. Nonlinear Dyn. **93**, 1647–1669 (2018). https://doi.org/10.1016/j.cemconres.2016.03.002
[29] Scerrato, D., Giorgio, I., Della Corte, A., Madeo, A., Dowling, N.E., Darve, F.: Towards the design of an enriched concrete with enhanced dissipation performances. Cem. Concr. Res. **84**, 48–61 (2016). https://doi.org/10.1016/j.cemconres.2016.03.002
[30] Cuomo, M.: Forms of the dissipation function for a class of viscoplastic models. Math. Mech. Complex Syst. **5**(3), 217–237 (2017). https://doi.org/10.2140/memocs.2017.5.217
[31] Ciallella, A., Pasquali, D., Gołaszewski, M., D'Annibale, F., Giorgio, I.: A rate-independent internal friction to describe the hysteretic behavior of pantographic structures under cyclic loads. Mech. Res. Commun. **116**, 103761 (2021). https://doi.org/10.1016/j.mechrescom.2021.103761
[32] Giorgio, I., Scerrato, D.: Multi-scale concrete model with rate-dependent internal friction. Eur. J. Environ. Civ. Eng. **21**(7–8), 821–839 (2017). https://doi.org/10.1080/19648189.2016.1144539
[33] dell'Erba, R.: Swarm robotics and complex behaviour of continuum material. Contin. Mech. Thermodyn. **31**(4), 989–1014 (2019). https://doi.org/10.1007/s00161-018-0675-1
[34] Della Corte, A., Battista, A., Dell'Isola, F., Giorgio, I.: Modeling deformable bodies using discrete systems with centroid-based propagating interaction: fracture and crack evolution. In: Dell'Isola, F., Sofonea, M., Steigmann, D. (eds.) Mathematical Modelling in Solid Mechanics. Advanced Structured Materials, vol. 69, pp. 59–88. Springer, Singapore (2017). https://doi.org/10.1007/978-981-10-3764-1_5
[35] Auffray, N., dell'Isola, F., Eremeyev, V.A., Madeo, A., Rosi, G.: Analytical continuum mechanics à la Hamilton–Piola least action principle for second gradient continua and capillary fluids. Math. Mech. Solids **20**(4), 375–417 (2015). https://doi.org/10.1177/1081286513497616
[36] dell'Isola, F., Eugster, S.R., Fedele, R., Seppecher, P.: Second-gradient continua: from Lagrangian to Eulerian and back. Math. Mech. Solids **17**(12), 2715–2750 (2022). https://doi.org/10.1177/10812865221078

[37] Fedele, R.: Third gradient continua: nonstandard equilibrium equations and selection of work conjugate variables. Math. Mech. Solids **27**(10), 2046–2072 (2022). https://doi.org/10.1177/10812865221098966
[38] dell'Isola, F., Andreaus, U., Placidi, L.: At the origins and in the vanguard of peridynamics, non-local and higher-gradient continuum mechanics: an underestimated and still topical contribution of Gabrio Piola. Math. Mech. Solids **20**(8), 887–928 (2015). https://doi.org/10.1177/1081286513509811
[39] Alibert, J.J., Seppecher, P., dell'Isola, F.: Truss modular beams with deformation energy depending on higher displacement gradients. Math. Mech. Solids **8**(1), 51–73 (2003). https://doi.org/10.1177/1081286503008001658
[40] Andreaus, U., dell'Isola, F., Giorgio, I., Placidi, L., Lekszycki, T., Rizzi, N.L.: Numerical simulations of classical problems in two-dimensional (non) linear second gradient elasticity. Int. J. Eng. Sci. **108**, 34–50 (2016). https://doi.org/10.1016/j.ijengsci.2016.08.003
[41] Fedele, R., Placidi, L., Fabbrocino, F.: A review of inverse problems for generalized elastic media: formulations, experiments, synthesis. Contin. Mech. Thermodyn. (2024). https://doi.org/10.1007/s00419-017-1266-5
[42] Giorgio, I., Hild, F., Gerami, E., dell'Isola, F., Misra, A.: Experimental verification of 2D Cosserat chirality with stretch-micro-rotation coupling in orthotropic metamaterials with granular motif. Mech. Res. Commun. **126**, 104020 (2022). https://doi.org/10.1016/j.mechrescom.2022.104020
[43] Fedele, R.: Piola's approach to the equilibrium problem for bodies with second gradient energies. Part I: first gradient theory and differential geometry. Contin. Mech. Thermodyn. **34**, 445–474 (2022). https://doi.org/10.1007/s00161-021-01064-6
[44] Fedele, R.: Approach à la Piola for the equilibrium problem of bodies with second gradient energies. Part II: variational derivation of second gradient equations and their transport. Contin. Mech. Thermodyn. **34**, 1087–1111 (2022). https://doi.org/10.1007/s00161-022-01100-z
[45] La Valle, G., Abali, B.E., Falsone, G., Soize, C.: Sensitivity of a homogeneous and isotropic second-gradient continuum model for particle-based materials with respect to uncertainties. J. Appl. Math. Mech. **103**(10), e202300068 (2023). https://doi.org/10.1002/zamm.202300068
[46] Chróścielewski, J., dell'Isola, F., Eremeyev, V.A., Sabik, A.: On rotational instability within the nonlinear six-parameter shell theory. Int. J. Solids Struct. **196**, 179–189 (2020). https://doi.org/10.1016/j.ijsolstr.2020.04.030
[47] Giorgio, I., Misra, A., Placidi, L.: Geometrically nonlinear Cosserat elasticity with chiral effects based upon granular micromechanics. In: Altenbach, H., Berezovski, A., Dell'Isola, F., Porubov, A. (eds.) Sixty Shades of Generalized Continua. Advanced Structured Materials, vol. 170, pp. 273–292. Springer, Cham (2023). https://doi.org/10.1007/978-3-031-26186-2_17
[48] dell'Isola, F., Madeo, A., Seppecher, P.: Boundary conditions at fluid-permeable interfaces in porous media: a variational approach. Int. J. Solids Struct. **46**(17), 3150–3164 (2009). https://doi.org/10.1016/j.ijsolstr.2009.04.008
[49] Madeo, A., dell'Isola, F., Darve, F.: A continuum model for deformable, second gradient porous media partially saturated with compressible fluids. J. Mech. Phys. Solids **61**(11), 2196–2211 (2013). https://doi.org/10.1016/j.jmps.2013.06.009
[50] Giorgio, I., dell'Isola, F., Andreaus, U., Misra, A.: An orthotropic continuum model with substructure evolution for describing bone remodeling: an interpretation of the primary mechanism behind Wolff's law. Biomech. Model. Mechanobiol. **22**(6), 2135–2152 (2023). https://doi.org/10.1007/s10237-023-01755-w
[51] Fabbrocino, F., Funari, M., Greco, F., Lonetti, P., Luciano, R., Penna, R.: Dynamic crack growth based on moving mesh method. Compos. Part B Eng. **174**, 107053 (2019). https://doi.org/10.1016/j.compositesb.2019.107053
[52] Placidi, L., Misra, A., Barchiesi, E.: Simulation results for damage with evolving microstructure and growing strain gradient moduli. Contin. Mech. Thermodyn. **31**, 1143–1163 (2019). https://doi.org/10.1007/s00161-018-0693-z
[53] Placidi, L., Barchiesi, E., Misra, A.: A strain gradient variational approach to damage: a comparison with damage gradient models and numerical results. Math. Mech. Complex Syst. **6**(2), 77–100 (2018). https://doi.org/10.2140/memocs.2018.6.77
[54] Placidi, L.: A variational approach for a nonlinear one-dimensional damage-elasto-plastic second-gradient continuum model. Contin. Mech. Thermodyn. **28**, 119–137 (2016). https://doi.org/10.1007/s00161-014-0405-2
[55] Luciano, R., Caporale, A., Darban, H., Bartolomeo, C.: Variational approaches for bending and buckling of non-local stress-driven Timoshenko nano-beams for smart materials. Mech. Res. Commun. **103**, 103470 (2020). https://doi.org/10.1016/j.mechrescom.2019.103470
[56] Giorgio, I.: A variational formulation for one-dimensional linear thermoviscoelasticity. Math. Mech. Complex Syst. **9**(4), 397–412 (2022). https://doi.org/10.2140/memocs.2021.9.397
[57] dell'Isola, F., Misra, A.: Principle of virtual work as foundational framework for metamaterial discovery and rational design. C. R Méc. **351**(S3), 1–25 (2023). https://doi.org/10.1016/10.5802/crmeca.151
[58] Bui, N.N., Ngo, M., Nikolic, M., Brancherie, D., Ibrahimbegovic, A.: Enriched Timoshenko beam finite element for modeling bending and shear failure of reinforced concrete frames. Comput. Struct. **143**, 9–18 (2014). https://doi.org/10.1016/j.compstruc.2014.06.004
[59] Endo, M.: Study on an alternative deformation concept for the Timoshenko beam and Mindlin plate models. Int. J. Eng. Sci. **87**, 32–46 (2015). https://doi.org/10.1016/j.ijengsci.2014.11.001

[60] Scerrato, D., Giorgio, I., Madeo, A., Limam, A., Darve, F.: A simple non-linear model for internal friction in modified concrete. Int. J. Eng. Sci. **80**, 136–152 (2014). https://doi.org/10.1016/j.ijengsci.2014.02.02
[61] Aretusi, G., Ciallella, A.: An application of Coulomb-friction model to predict internal dissipation in concrete. In: Marmo, F., Sessa, S., Barchiesi, E., Spagnuolo, M. (eds.) Mathematical Applications in Continuum and Structural Mechanics. Advanced Structured Materials, pp. 73–86. Springer, Cham (2021). https://doi.org/10.1007/978-3-030-42707-8_5
[62] Pensée, V., Kondo, D., Dormieux, L.: Micromechanical analysis of anisotropic damage in brittle materials. J. Eng. Mech. **128**(8), 889–897 (2002). https://doi.org/10.1061/(ASCE)0733-9399(2002)128:8(889)
[63] Fedele, R., Filippini, M., Maier, G.: Constitutive model calibration for railway wheel steel through tension-torsion tests. Comput. Struct. **83**(12), 1005–1020 (2005). https://doi.org/10.1016/j.compstruc.2004.10.006
[64] Fedele, R., Galantucci, L., Ciani, A., Casalegno, V., Ventrella, A., Ferraris, M.: Characterization of innovative CFC/Cu joints by full-field measurements and finite elements. Mat. Sci. Eng. A **595C**, 306–317 (2014). https://doi.org/10.1016/j.msea.2013.12.015
[65] Cefis, N., Fedele, R., Beghi, M.: An integrated methodology to estimate the effective elastic parameters of amorphous TiO_2 nanostructured films, combining SEM images, finite element simulations and homogenization techniques. Mech. Res. Commun. **131**, 104153 (2023). https://doi.org/10.1016/j.mechrescom.2023.104153
[66] Yang, H., Ganzosch, G., Giorgio, I., Abali, B.E.: Material characterization and computations of a polymeric metamaterial with a pantographic substructure. Z. Angew. Math. Phys. **69**, 1–16 (2018). https://doi.org/10.1007/s00033-018-1000-3
[67] Giorgio, I., Harrison, P., dell'Isola, F., Alsayednoor, J., Turco, E.: Wrinkling in engineering fabrics: a comparison between two different comprehensive modelling approaches. Proc. R. Soc. A Math. Phys. Eng. Sci. **474**(2216), 20180063 (2018). https://doi.org/10.1098/rspa.2018.0063
[68] Raveendra, B.R., Benipal, G.S., Singh, A.K.: Constitutive modelling of concrete: an overview. Asian J. Civ. Eng. **6**(4), 211–214 (2005)
[69] Bersani, A.M., Caressa, P.: Lagrangian descriptions of dissipative systems: a review. Math. Mech. Solids **26**(6), 785–803 (2021). https://doi.org/10.1177/1081286520971834
[70] Amir, M., Papakonstantinou, K., Warn, G.: A consistent Timoshenko hysteretic beam finite element model. Int. J. Nonlinear Mech. **119**, 103218 (2020). https://doi.org/10.1016/j.ijnonlinmec.2019.07.003
[71] Ismail, M., Ikhouane, F., Rodellar, J.: The hysteresis Bouc–Wen model, a survey. Arch. Comput. Methods Eng. **16**, 161–188 (2009). https://doi.org/10.1007/s11831-009-9031-8
[72] Ciallella, A., Scerrato, D., Spagnuolo, M., Giorgio, I.: A continuum model based on Rayleigh dissipation functions to describe a Coulomb-type constitutive law for internal friction in woven fabrics. Z. Angew. Math. Phys. **73**(5), 209 (2022). https://doi.org/10.1007/s00033-022-01845-2
[73] User's Guide: COMSOL Multiphysics® v. 6.2. COMSOL AB, Stockholm (2023)
[74] Greco, L., Cuomo, M., Contrafatto, L.: Two new triangular G1-conforming finite elements with cubic edge rotation for the analysis of Kirchhoff plates. Comput. Methods Appl. Mech. Eng. **356**, 354–386 (2019). https://doi.org/10.1016/j.cma.2019.07.026
[75] Greco, L., Castello, D., Cuomo, M.: An objective and accurate G1-conforming mixed Bézier FE-formulation for Kirchhoff–Love rods. Math. Mech. Solids **29**(4), 645–685 (2023). https://doi.org/10.1177/10812865231204972
[76] Eugster, S.R., Harsch, J.: A variational formulation of classical nonlinear beam theories. In: Abali, B., Giorgio, I. (eds.) Developments and Novel Approaches in Nonlinear Solid Body Mechanics. Advanced Structured Materials, vol. 130, pp. 95–121. Springer, Cham (2020). https://doi.org/10.1007/978-3-030-50460-1_9
[77] Balobanov, V., Niiranen, J.: Locking-free variational formulations and isogeometric analysis for the Timoshenko beam models of strain gradient and classical elasticity. Comput. Methods Appl. Mech. Eng. **339**, 137–159 (2018). https://doi.org/10.1016/j.cma.2018.04.028
[78] Giorgio, I.: A discrete formulation of Kirchhoff rods in large-motion dynamics. Math. Mech. Solids **25**(5), 1081–1100 (2020). https://doi.org/10.1177/1081286519900902
[79] Barchiesi, E., dell'Isola, F., Bersani, A.M., Turco, E.: Equilibria determination of elastic articulated duoskelion beams in 2D via a Riks-type algorithm. Int. J. Nonlinear Mech. **128**, 103628 (2021). https://doi.org/10.1016/j.ijnonlinmec.2020.103628
[80] Fedele, R., Maier, G., Miller, B.: Identification of elastic stiffness and local stresses in concrete dams by in situ tests and neural networks. Struct. Infrastruct. Eng. **1**(3), 165–180 (2005). https://doi.org/10.1080/15732470500030513
[81] Abali, B.E., Wu, C.C., Müller, W.H.: An energy-based method to determine material constants in nonlinear rheology with applications. Contin. Mech. Thermodyn. **28**, 1221–1246 (2016). https://doi.org/10.1007/s00161-015-0472-z
[82] De Angelo, M., Placidi, L., Nejadsadeghi, N., Misra, A.: Non-standard Timoshenko beam model for chiral metamaterial: identification of stiffness parameters. Mech. Res. Commun. **103**, 103462 (2020). https://doi.org/10.1016/j.mechrescom.2019.103462
[83] Ciallella, A., La Valle, G., Vintache, A., Smaniotto, B., Hild, F.: Deformation mode in 3-point flexure on pantographic block. Int. J. Solids Struct. **265**, 112129 (2023). https://doi.org/10.1016/j.ijsolstr.2023.112129

[84] Shekarchizadeh, N., Abali, B.E., Barchiesi, E., Bersani, A.M.: Inverse analysis of metamaterials and parameter determination by means of an automatized optimization problem. Z. Angew. Math. Mech. **101**(8), e202000277 (2021). https://doi.org/10.1002/zamm.202000277
[85] Tinoco, M.P., de Andrade Silva, F.: On the mechanical behavior of hybrid fiber reinforced strain hardening cementitious composites subjected to monotonic and cyclic loading. J. Mater. Res. Technol. **11**, 754–768 (2021). https://doi.org/10.1016/j.jmrt.2021.01.053
[86] Crambuer, R., Richard, B., Ile, N., Ragueneau, F.: Experimental characterization and modeling of energy dissipation in reinforced concrete beams subjected to cyclic loading. Eng. Struct. **56**, 919–934 (2013). https://doi.org/10.1016/j.engstruct.2013.06.024
[87] Jang, Y.H., Barber, J.: Frictional energy dissipation in materials containing cracks. J. Mech. Phys. Solids **59**(3), 583–594 (2011). https://doi.org/10.1016/j.jmps.2010.12.010
[88] Li, Y., Tham, L., Wang, Y., Tsui, Y.: A modified Kachanov method for analysis of solids with multiple cracks. Eng. Fract. Mech. **70**(9), 1115–1129 (2003). https://doi.org/10.1016/S0013-7944(02)00096-6
[89] Ray, S., Chandra Kishen, J.: Fatigue crack propagation model for plain concrete: an analogy with population growth. Eng. Fract. Mech. **77**(17), 3418–3433 (2010). https://doi.org/10.1016/j.engfracmech.2010.09.008
[90] Auger, P., Lavigne, T., Smaniotto, B., Spagnuolo, M., dell'Isola, F., Hild, F.: Poynting effects in pantographic metamaterial captured via multiscale DVC. J. Strain Anal. Eng. **56**(7), 462–477 (2021). https://doi.org/10.1177/0309324720976625
[91] Hild, F., Misra, A., dell'Isola, F.: Multiscale DIC applied to pantographic structures. Exp. Mech. **61**, 431–443 (2021). https://doi.org/10.1007/s11340-020-00636-y

Giuliano Aretusi and Antonello Salvatori
Department of Civil, Construction-Architectural and Environmental Engineering
Università dell'Aquila
P.zza Ernesto Pontieri 1, Monteluco di Roio
67100 L'Aquila
Italy

Christian Cardillo
Department of Civil Engineering and Architecture
Università di Catania
Via Santa Sofia, 64
95123 Catania
Italy

Ewa Bednarczyk
Faculty of Mechanical and Industrial Engineering
Warsaw University of Technology
Ludwika Narbutta 85
02-524 Warsaw
Poland

Roberto Fedele
Department of Civil and Environmental Engineering
Politecnico di Milano
Piazza Leonardo da Vinci 32
20133 Milan
Italy
e-mail: roberto.fedele@polimi.it

(Received: April 3, 2024; revised: July 21, 2024; accepted: July 23, 2024)

A dissipation model for concrete based on an enhanced Timoshenko beam

---

Chapter abstract

This chapter presents an enriched Timoshenko beam model to describe dissipation in cement-based materials, incorporating both flexural and axial behavior to study compression and combined compression-flexion effects. The model introduces a variable for relative sliding within microcracks, assuming constant microcrack density under small deformations. Using an extended virtual work principle, it accounts for external forces, internal elasticity, and dissipation from microcrack interactions, incorporating nonlinear effects.

Finite element simulations assess mechanical properties under three-point bending and compression, revealing energy dissipation during cyclic loading. A parametric study on friction force amplitude highlights a non-monotonic relationship with dissipation, identifying an optimal value. The model offers insights into cement-based material behavior, particularly in dissipation, crucial for structural applications.
Published in *Networks and Heterogeneous Media*, 2024.

Networks and Heterogeneous Media

https://www.aimspress.com/journal/nhm

NHM, 19(2): 700–723.
DOI: 10.3934/nhm.2024031
Received: 11 May 2024
Revised: 27 June 2024
Accepted: 01 July 2024
Published: 11 July 2024

Research article

A dissipation model for concrete based on an enhanced Timoshenko beam

Giuliano Aretusi[1], Christian Cardillo[2,*], Larry Murcia Terranova[3] and Ewa Bednarczyk[4]

[1] Department of Civil, Construction-Architectural and Environmental Engineering, Università dell'Aquila, L'Aquila 67100, Italy

[2] Department of Civil Engineering and Architecture, Università di Catania, Catania 95100, Italy

[3] Department of Information Engineering, Computer Science and Mathematics, Università dell'Aquila, L'Aquila 67100, Italy

[4] Faculty of Mechanical and Industrial Engineering, Warsaw University of Technology, Warsaw 00-661, Poland

* **Correspondence:** Email: christian.cardillo@phd.unict.it.

Abstract: A novel Timoshenko beam model enriched to account for dissipation in cement-based materials was presented in this paper. The model introduced a new variable representing the relative sliding inside microcracks within the material. In the paper, the microcrack density was not supposed to increase, assuming a small deformation regime that implied no damage growth. The model utilized an expanded version of the principle of virtual work whose contributions came from external forces, internal elastic forces, and dissipation due to the microcrack's microstructure. The elastic energy included terms related to microcrack sliding and micro-macro interactions, accounting for nonlinearity in the material behavior. Numerical simulations, conducted using the finite element method, evaluated the mechanical properties of cement-based materials under three-point flexural tests and compression tests. These tests enabled the assessment of the material dissipative behavior under cyclic loading. Results showed dissipated energy cycles and mechanical responses influenced by the microcrack mechanics. Additionally, a parametric study, varying the friction force amplitude, revealed its impact on dissipated energy. The study highlighted a non-monotonic relationship between friction force amplitude and dissipated energy, with an optimal value maximizing dissipation. Overall, the model provided insights into the mechanics of cement-based materials, particularly regarding dissipation, which was essential for understanding their behavior in structural applications.

Keywords: enhanced Timoshenko beam model; 1D continua with microstructure; microcrack sliding; cement-based materials; dissipated energy

1. Introduction

It is remarkable that despite its widespread use in civil engineering, concrete remains relatively unknown. Indeed, in technical practice, oversimplified models that ignore some essential aspects are used. From ancient times to the present day, human structures have been crafted from concrete, initially comprising rudimentary cement made by crushing and burning gypsum or limestone. Over the course of civil engineering history, concrete has evolved into a sophisticated composite material. Nowadays, concrete is a fundamental construction material that plays a pivotal role in shaping our built environment, providing stability, durability, and versatility in a wide range of construction projects. Ongoing research in concrete technology is crucial for advancing the construction industry, promoting sustainability, enhancing safety, and meeting the evolving demands of our built environment.

Among some of the most significant current research areas concerning concrete, we can summarize the following categories: i) supplementary cementitious materials (SCMs); ii) nanotechnology; iii) self-healing concrete; iv) ultra-high-performance concrete (UHPC); v) digital tools in concrete design.

SCMs are materials like fly ash, slag, and silica fume that can be added to concrete in addition to Portland cement to improve its properties and reduce its carbon footprint [1–3]. By incorporating these SCMs into concrete mixtures, construction professionals can decrease the amount of Portland cement needed, a significant source of carbon emissions in concrete production. This substitution not only improves the technical properties of concrete but also contributes to more sustainable and environmentally friendly construction practices, making it an essential aspect of modern concrete research and construction [4].

Incorporating nanomaterials into concrete formulations represents a promising possibility for enhancing the mechanical properties and longevity of the material. This research area is continually evolving and has the potential to revolutionize the construction industry by producing stronger, more durable, and sustainable concrete structures. Potentially, the inclusions could be nanoparticles [5], fibers [6–8], and suitable complex microstructures enancing the performaces [9–11]. Nanotechnology applied to concrete can improve particle packing and reduce permeability. Nanoparticles are much smaller in size than traditional concrete materials. When incorporated into the concrete mix, they fill in the gaps between larger particles, improving particle packing. This denser packing enhances the concrete's overall strength and reduces porosity, increasing surface area. Nanomaterials, such as nano-silica or nanotubes, have a high surface area-to-volume ratio [12]. This increased surface area allows for better bonding with cement particles and enhances chemical reactions. Moreover, they can be employed to form additional cementitious compounds that contribute to increased strength and durability, increased flexural and compressive strength, and shifting of the mitigation of early-age cracking. Nanomaterials can help mitigate early-age cracking by reducing the heat of hydration, controlling the formation of microcracks, and improving the overall curing process.

Research on self-healing concrete focuses on developing innovative materials and techniques that allow it to repair its cracks autonomously [13]. This area of study is essential for improving the durability and longevity of concrete structures. The idea of self-healing originates from the aim to enhance the performance of building materials like concrete with extra features mimicking the behavior of biological tissues, such as bone (see, e.g., [14, 15] to exploite mechanical properties, and [16–19] for biologocal processes that allow the healing of the tissue). Key aspects of research on self-healing concrete are self-healing mechanisms, healing agents, and microstructural changes. Self-healing concrete typically

relies on several mechanisms, including autogenous and encapsulated healing. Autogenous healing occurs when unhydrated cement particles in the presence of water fill small cracks through continued hydration, sealing the crack [20]. Encapsulated healing involves the use of microcapsules containing healing agents embedded in the concrete. When a crack forms, these capsules rupture, releasing healing agents that react and seal the crack [21]. Various healing agents can be embedded in self-healing concrete, such as bacteria, polymers, or organic and inorganic materials. Bacteria-based systems use specially designed bacteria that produce calcium carbonate ($CaCO_3$) when exposed to moisture and oxygen. This $CaCO_3$ seals cracks by precipitating in them. Polymer-based systems rely on the expansion of polymers to seal cracks. These polymers can be embedded within the concrete mix or applied as an external layer. This field of research aims to understand how self-healing affects the microstructure of concrete, ensuring that the healing process does not compromise the overall strength and durability of the material. Techniques like scanning electron microscopy (SEM) and X-ray micro-computed tomography (μ-CT) are used to analyze the effectiveness of self-healing mechanisms.

UHPC is a relatively recent development in the field of concrete technology [22]. It is characterized by its exceptional strength, durability, and unique properties that distinguish it from traditional concrete. UHPC typically comprises a precise blend of materials, including Portland cement, fine quartz or silica fume, very fine sand, high-range water-reducing admixtures, and sometimes steel fibers. The exact mix design can vary but is characterized by the use of outstanding materials and minimal water content.

Moreover, ultra high performance fiber-teinforced concrete (UHP FRC) is an advanced concrete variant that incorporates high-strength fibers to significantly enhance its mechanical and durability properties [23]. Characterized by a compressive strength greater than 150 MPa, UHP FRC surpasses conventional concrete, which typically ranges from 20 to 50 MPa. The inclusion of fibers like steel, glass, or synthetic materials boosts its tensile strength and ductility, enabling it to withstand greater tensile forces and deform more without cracking. UHP FRC features a dense matrix with very low porosity, making it highly resistant to water penetration and chemical attacks. This density is achieved through optimized particle packing and the use of fine powders such as silica fume, fly ash, and superplasticizers. The combination of a dense matrix and high fiber content results in exceptional durability, providing resistance to freeze-thaw cycles, abrasion, and aggressive environments. Typically self-consolidating, UHP FRC flows and fills complex molds without the need for mechanical vibration, facilitating the creation of intricate architectural elements. The components of UHP FRC include high-quality Portland cement as the primary binder, fine aggregates to ensure dense particle packing, silica fume to fill voids and increase strength, superplasticizers to enhance workability and fluidity without increasing water content, and high-strength fibers like steel, glass, polypropylene, or carbon to improve tensile strength and ductility. UHP FRC finds applications in bridges and infrastructure, architectural elements, repair and rehabilitation, and security and defense structures due to its high strength, durability, and impact resistance. Its advantages lie in its superior mechanical properties, exceptional durability, design flexibility, and potential contributions to sustainable construction through reduced material usage and longer lifespan. However, the production of UHP FRC is more costly than conventional concrete, requiring precise mix design, quality control, and specialized knowledge for design and construction. Despite these challenges, UHP FRC stands out as a cutting-edge material suitable for demanding applications in modern construction.

Computer simulations and modeling play a crucial role in designing and optimizing concrete structures. These tools provide technicians and engineers with valuable insights, enabling them to

make informed decisions, improve designs, and enhance the overall performance of concrete structures. Computer simulations and modeling provide a comprehensive and detailed understanding of how concrete structures perform in real-world conditions. This knowledge allows for more efficient and sustainable designs, reduced construction costs, improved safety, and enhanced durability, ultimately leading to better-engineered concrete structures. For instance, potential applications of this method include 3D modeling of concrete [24, 25], research focused on optimizing key aspects of concrete performance or its internal structure [26–28], and aided design techniques [29–31].

Fundamentally, it is the internal microstructure of concrete that defines its unique properties. Comprising components like Portland cement, sand, and gravel of various sizes and shapes, concrete is a highly heterogeneous material. Its strength is significantly influenced by factors such as the water-to-cement ratio and the incorporation of additives that chemically or mechanically alter its properties.

Describing the behavior of concrete poses numerous challenges from a modeling perspective. Among these challenges, the key is its nonlinear behavior both at the macro level of observation, in a standard context [32–34], as well as in porous materials [35], and at the microscopic level [36, 37], even under small deformations. The dissipative effects stemming from its microstructure in both elastic and plastic regimes [38] and the evolution of cracks within it [39] are also crucial.

At its core, the microstructure of concrete consists of a matrix formed by the solid phase of the cement paste, interspersed with pieces of inert material of varying sizes. Additionally, the microstructure is further complicated by factors such as chemical species and thermal cycles during curing, which naturally give rise to microcracks within the material. While these microcracks impact the macroscopic behavior of concrete, their effects remain subdued unless subjected to significant external loads [40].

Various models have been explored in the literature to predict concrete behavior. In addition to traditional models like the Cauchy model, alternative approaches within the framework of generalized continua have been investigated. Among them, we recall the second-gradient continua [41–44] or even of higher order [45], micromorphic continua [46–48], and functionally graded materials [49]. These include also Cosserat-type models to account for the presence of stiff aggregates and higher gradient continua to address the material strong heterogeneity (see, e.g., [50–54]).

Furthermore, concrete can be treated as a porous material due to voids formed during the curing process and microcracks [55, 56]. These microcracks, in particular, affect concrete behavior by introducing asymmetry in its mechanical response due to compressive or tensile loads, and generating internal friction under cyclic compressive loads.

Modeling the dissipation in concrete presents a significant challenge. While viscous models are commonly used, they often offer a simplistic linearization of dissipative actions. Alternatively, Coulomb-type friction between microcrack surfaces is proposed as a more appropriate mechanism for dissipative behavior, which remains nearly independent of frequency. Rheological models and thermodynamic frameworks with diffusive internal variables are also employed to address dissipation in solid materials [57–59].

Finally, while this paper primarily focuses on dissipative effects in concrete under small deformations, it is important to acknowledge ongoing research efforts related to plasticity and damage evolution (see, e.g., [60–63]). Variational formulations are favored for their logical consistency and ability to minimize unnecessary assumptions (see, e.g., applications to damage formulation [64–66], buckling [67], internal friction in solid materials [68, 69], and thermoelastic theory [70]). Recent studies explored the use of material particles akin to swarms of robots, offering promising computational efficiency [71].

In summary, this work aims to explore the Coulomb nature of dissipative effects in concrete due to the

mechanics of microcracks through numerical simulations obtained for a 1D generalized model, which is an enhanced version of the Timoshenko beam, built upon a previously introduced 3D model [72]. The proposed Timoshenko-like beam is a very efficient and powerful tool for quickly assessing material behavior. This novel beam model shows an improved capability to analyze the behavior of materials under certain circumstances, subsequently providing significant advantages over traditional beam models. In comparison with traditional beam models, this Timoshenko-like beam is more effective in predicting the dissipation in materials that are subjected to cyclic loads, and, as in the standard case, it is capable of more accurately predicting the effects of shear deformation. As a result of these improvements, the Timoshenko-like beam model can provide engineers and researchers with greater insight into the behavior of materials and allow them to make more informed decisions when designing structures and mechanical components.

2. The micromorphic beam model

The present section concerns a planar 1D model of a cement-based beam that can be described primarily by a reference curve $\mathscr{C}^*$ in the plane xy, which lies on the x-axis in its undeformed configuration and whose length is L. The current configuration of the beam, $\mathscr{C}$, is represented by the map $\boldsymbol{\chi}$, which depends on a generic S-abscissa, as illustrated in Figure 1. To this end, we propose to enlarge the standard kinematical description used in the Timoshenko model with a further descriptor that is able to take into account, to some extent, the sliding effect of the opposite faces of microcracks within the cement matrix [38, 72, 73]. Since we consider the small displacement and small deformation regime, we assume that the density of microcracks remains the same throughout the tests; thus, no damage evolution occurs. The fundamental kinematic assumption in the Timoshenko model is that, although the conservation of plane cross-sections and their rigidity apply, the orthogonality between the axial beam line and the cross-section is not retained. This refers to the hypothesis in which the influence of shear distortion on the beam deformation is not neglected [74]. The complete kinematical description of the system configuration is specified by means of the kinematic variables: u, v, φ, and γ. Expressly, these kinematical descriptors represent the longitudinal and transverse displacement of the beam axis, the cross-section rotation, and an average inner relative sliding between the opposite faces of microcracks, respectively. The first three variables are characteristic of the classical Timoshenko model accounting for extension, while the novel-introduced variable is assumed to be a scalar field since, as a first approximation, we can postulate that no preferential direction characterizes the microcracks and a random distribution of their orientation is in place [72, 75]. Thus, we define the map $\boldsymbol{\chi}$ as:

$$\boldsymbol{\chi} := \begin{cases} \boldsymbol{r} = \begin{cases} x = S + u(S) \\ y = v(S) \end{cases} \\ \hat{\varphi} = \varphi(S) \\ \hat{\gamma} = \gamma(S), \end{cases} \tag{2.1}$$

where the vector $\boldsymbol{r}$ specifies the position of the material particles lying on the axial line of the beam, and $\hat{\varphi}$ and $\hat{\gamma}$ are the characteristic features that describe the essential properties of the microstructure, i.e., the orientation of the cross-section and the sliding in the microcracks.

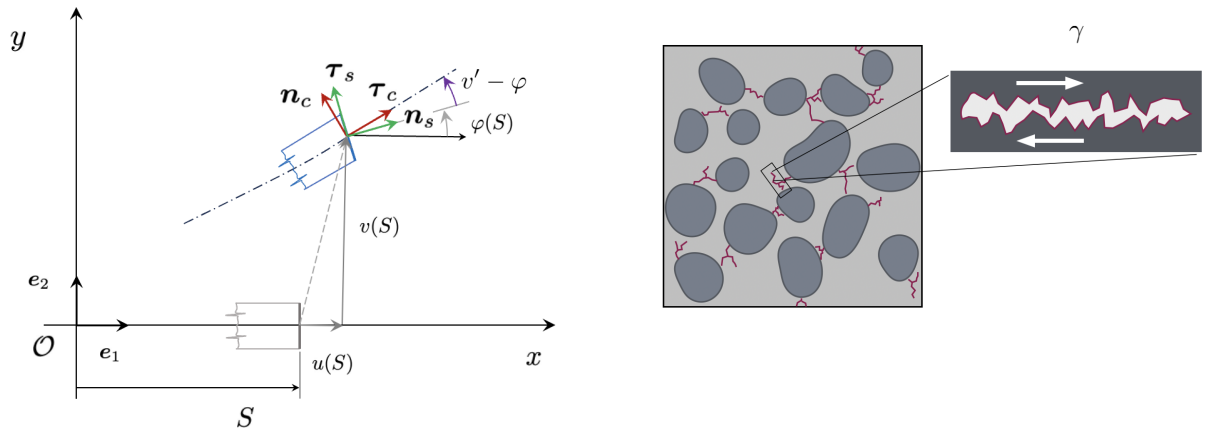


Figure 1. Kinematic descriptors of the beam (on the left); scheme of the microcrack microstructure of the beam material (on the right). $\boldsymbol{\tau}_c$ and $\boldsymbol{n}_c$ are the tangent and normal unit vectors to the axial curve of the beam, while $\boldsymbol{\tau}_s$ and $\boldsymbol{n}_s$ are the tangent and normal unit vectors to the beam cross-section. The red lines on the concrete section represent the microcracks; thus, γ can be interpreted as a descriptor of micro-slip accumulation within the material.

In order to characterize the behavior of the considered system, we employ an expanded version of the principle of virtual work (PVW). This principle states that, at equilibrium, the virtual work exerted by the external forces applied to the system, denoted by $\delta\mathcal{W}^{ext}$, must balance the virtual work performed by the internal contact forces, namely, $\delta\mathcal{W}^{el}$ for the conservative part associated with the elastic deformation, as well as any virtual work dissipated within the system, $\tilde{\delta}\mathcal{D}$, for the same virtual displacements; therefore, we consider the extended principle of virtual work as follows:

$$\delta\mathcal{W}^{el} + \tilde{\delta}\mathcal{D} = \delta\mathcal{W}^{ext}, \tag{2.2}$$

neglecting the inertial effects since we consider low-frequency applications of the materials. In this extended version of the variational principle, it is important to note that the dissipative contribution is not calculated as the first variation of $\mathcal{D}$. As a result, we use a different symbol, $\tilde{\delta}$, to account for the Rayleigh extension of Lagrangian formalism for dissipation.

The inner virtual work related to the elastic deformation is evaluated starting from a plausible expression of an elastic deformation energy based on the abovementioned kinematic variables:

$$\begin{aligned}\mathcal{W}^{el} = &\int_0^L \frac{1}{2}\mathrm{k}_b\,(\varphi')^2\,\mathrm{d}S + \int_0^L \frac{1}{2}\mathrm{k}_s\,(v'-\varphi)^2\,\mathrm{d}S + \int_0^L \frac{1}{2}\mathrm{k}_e\,(u')^2\,\mathrm{d}S + \\ &+ \int_0^L \frac{1}{2}\mathrm{k}_{m2}\,\gamma^2\mathrm{d}S + \int_0^L \frac{1}{4}\mathrm{k}_{m4}\,\gamma^4\mathrm{d}S + \\ &- \int_0^L \alpha_b\,\gamma\,\varphi'\mathrm{d}S - \int_0^L \alpha_s\,\gamma\,(v'-\varphi)\,\mathrm{d}S - \int_0^L \alpha_e\,\gamma u'\mathrm{d}S,\end{aligned} \tag{2.3}$$

where the material parameters k_b, k_s, k_e, k_{m2}, and k_{m4} are stiffnesses, while α_b, α_s, and α_e are coupling coefficients; all these parameters have to be determined by a micro-macro identification and validated

with experimental tests. This elastic energy represents the energy stored in a material due to deformation, therefore, it must be inherently positive because it represents the ability of the material to do work when it returns to its original shape. To ensure that the postulated energy $\mathcal{W}^{el}$ is positive definite, then, we can assume that the coefficients satisfy the following inequalities:

$$\mathrm{k}_b > 0, \quad \mathrm{k}_s > 0, \quad \mathrm{k}_e > 0, \quad \mathrm{k}_b\mathrm{k}_e\mathrm{k}_s\mathrm{k}_{m2} - \alpha_s^2\mathrm{k}_b\mathrm{k}_e - \alpha_e^2\mathrm{k}_b\mathrm{k}_s - \alpha_b^2\mathrm{k}_e\mathrm{k}_s > 0, \quad \mathrm{k}_{m4} > 0. \tag{2.4}$$

The first three contributions of the energy (2.3) represent the classical constitutive behavior of the extensible Timoshenko model. They are representative of the bending, the shear, and the elongation energy that can be stored in the beam. The other contributions newly introduced in (2.3), are linked to the energy associated with the microcracks. In particular, the terms quadratic and quartic in γ are the amount of elastic energy that can be stored in the microcracks. The idea behind that is related to the specific morphology of the microcracks. From a geometric perspective, ideally, a microcrack can be visualized as a coin-shaped empty space. The microcrack consists of two faces or lips on opposite sides, which delimit the crack. Each lip of the microcrack exhibits asperities that may interact when the two lips on the opposite side of a crack come into contact (see Figure 1). When this occurs, these asperities can bend and, therefore, store a certain amount of elastic energy. We postulate a material nonlinearity with the quartic term on the ground that many experimental observations show a macroscopic nonlinear behavior in cement-based materials even at the small displacement and deformation regime [76]. The last three contributions of Eq (2.3) stand for the coupling energy exchanged between the macroscopic bending deformation and the microscopic asperity deformation within the microcracks, between the macroscopic shear distortion of the beam and the asperity deformation, as well as between the macroscopic elongation of the beam and the asperity deformation. Naturally, we can assume that a bending, a shear, or a change-of-length deformation of the beam could be responsible for the sliding of the microcrack lips. We have to remark, though, that the effect of such a sliding is noticeable only if the opposite faces of the microcracks are pushed against each other. This means that this effect becomes significant only in the case of compression. When bending and shear deformation are activated, only the part of the cross-section interested in compression is affected by such a phenomenon. On the contrary, the tensile part is free from this type of energy exchange. However, since the model is mono-dimensional, we cannot distinguish between the compressed and stretched parts of the cross-section, and thus, we have only to consider whether or not a compressed region exists. Consequently, whenever the beam bends, it produces a compressed region, and, hence, we can imagine that this phenomenon can be activated in this simple 1D context. The virtual work exerted by the inner forces is straightforwardly computed by the first variation of the elastic energy (2.3) as:

$$\begin{aligned}\delta\mathcal{W}^{el} = &\int_0^L \mathrm{k}_b\,\varphi'\,\delta\varphi'\,\mathrm{d}S + \int_0^L \mathrm{k}_s\,(v'-\varphi)\,\delta\,(v'-\varphi)\,\mathrm{d}S + \int_0^L \mathrm{k}_e\,u'\,\delta u'\,\mathrm{d}S + \\ &+ \int_0^L \mathrm{k}_{m2}\gamma\,\delta\gamma\,\mathrm{d}S + \int_0^L \mathrm{k}_{m4}\gamma^3\,\delta\gamma\,\mathrm{d}S - \int_0^L \alpha_b\,(\varphi'\,\delta\gamma + \gamma\,\delta\varphi')\,\mathrm{d}S + \\ &- \int_0^L \alpha_s\,[(v'-\varphi)\,\delta\gamma + \gamma\,\delta\,(v'-\varphi)]\,\mathrm{d}S - \int_0^L \alpha_e\,(u'\,\delta\gamma + \gamma\,\delta u')\,\mathrm{d}S,\end{aligned} \tag{2.5}$$

and, by performing an integration by parts, we can rearrange the contributions of the internal elastic energy as follows:

$$\delta\mathcal{W}^{el} = -\int_0^L \left[(\mathrm{k}_b\varphi')' + \mathrm{k}_s\,(v'-\varphi) - (\alpha_b\gamma)' - \alpha_s\gamma\right]\,\delta\varphi\,\mathrm{d}S \;+\; (\mathrm{k}_b\varphi' - \alpha_b\gamma)\;\delta\varphi\Big|_0^L + \\ - \int_0^L \left[(\mathrm{k}_e u')' - (\alpha_e\gamma)'\right]\,\delta u\,\mathrm{d}S \;+\; (\mathrm{k}_e u' - \alpha_e\gamma)\;\delta u\Big|_0^L + \\ + \int_0^L \left[\mathrm{k}_{m2}\gamma + \mathrm{k}_{m4}\gamma^3 - \alpha_b\,\varphi' - \alpha_s\,(v'-\varphi) - \alpha_e\,u'\right]\,\delta\gamma\,\mathrm{d}S + \\ - \int_0^L \left\{[\mathrm{k}_s\,(v'-\varphi)]' - (\alpha_s\,\gamma)'\right\}\delta v\,\mathrm{d}S \;+\; [\mathrm{k}_s\,(v'-\varphi) - \alpha_s\gamma]\,\delta v\Big|_0^L. \quad (2.6)$$

In order to model the process of dissipation, we take into account the virtual work carried out by the friction force applied at the microcrack face level, as follows:

$$\tilde{\delta}\mathcal{D} = \int_0^L \zeta_b\,|\varphi'|\tanh(\eta\dot{\gamma})\,\delta\gamma\,\mathrm{d}S \;+\; \int_0^L \zeta_c\,\varsigma_C|u'|\tanh(\eta\dot{\gamma})\,\delta\gamma\,\mathrm{d}S. \quad (2.7)$$

The parameters ζ_b and ζ_c are related to the friction coefficient for the bending deformation and the compression, respectively. The appearance of the absolute value of the derivative of the angle of rotation $|\varphi'|$ in the first contribution of Eq (2.7) is due to the fact that when a cross-section undergoes a change in rotation, this can lead to a compression that closes the microcracks, at least in some parts of the cross-section. On the other hand, in the second integral, we consider the term $|u'|$, which represents a uniform compression within the cross-section that allows the microcracks to be closed. We have to remark that if the term $|u'|$ is originated by a tensile case, the dissipated energy associated with the second contribution must be erased from the model because there is no interaction between the microcrack asperities. For this reason, we introduce the boolean variable ς_C that assumes the value 1 for compression and 0 for traction. The concept of friction force could be accurately modeled with a Coulomb behavior. However, due to the non-Lipschitz continuity of the forcing term (a sign function), we lose the uniqueness of the solution. To overcome this challenge, a smoother version of the sign function, namely, the 'tanh'-term has been developed to mimic the Coulomb behavior while avoiding the issue mentioned above. This approach has proven to be effective in ensuring the accuracy of simulations and models in a variety of contexts. Moreover, it introduces a viscous behavior for small velocity $\dot{\gamma}$ which could be beneficial in some context, without mentioning that with the slope η, we can control the feature tuning of the mechanical response on the basis of experimental observations. Here, for the sake of simplicity, we consider the same value of η for both contributions in Eq (2.7). For a comprehensive understanding of the formulation of the dissipative term, refer to [77–79].

The virtual work of external forces and torques can be expressed as:

$$\delta\mathcal{W}^{ext} = \int_0^L b_x(S)\,\delta u\,\mathrm{d}S \;+\; F_x\delta u\Big|_0^L + \int_0^L b_y(S)\,\delta v\,\mathrm{d}S \;+\; F_y\delta v\Big|_0^L + \int_0^L \mu(S)\,\delta\varphi\,\mathrm{d}S \;+\; W\delta\varphi\Big|_0^L, \quad (2.8)$$

where we admit distributed forces b_x and b_y in the x-direction and y-direction as well as torques μ per unit length, point forces F_x and F_y in the x-direction and y-direction, as well as torques W applied at both ends, compatible with the energy (2.3).

By substituting the expressions (2.6)–(2.8) in the principle (2.2), the bulk equations are deduced

as below:

$$\begin{cases} -[\mathrm{k}_e u']' + (\alpha_e \gamma)' = b_x \\ -[\mathrm{k}_s (v' - \varphi)]' + (\alpha_s \gamma)' = b_y \\ -[(\mathrm{k}_b \varphi')' + \mathrm{k}_s (v' - \varphi) - (\alpha_b \gamma)' - \alpha_s \gamma] = \mu \\ \mathrm{k}_{m2}\gamma + \mathrm{k}_{m4}\gamma^3 - \alpha_b \varphi' - \alpha_s (v' - \varphi) - \alpha_e u' = -\zeta_b |\varphi'| \tanh(\eta\dot{\gamma}) - \zeta_c \varsigma_C |u'| \tanh(\eta\dot{\gamma}), \end{cases} \tag{2.9}$$

alongside the essential boundary conditions related to the values of u, v, and φ and the natural boundary conditions associated with the axial force, the shear force, and the bending moment:

$$N = \mathrm{k}_e u' - \alpha_e \gamma, \qquad T = \mathrm{k}_s (v' - \varphi) - \alpha_s \gamma, \qquad M = \mathrm{k}_b \varphi' - \alpha_b \gamma, \tag{2.10}$$

respectively. We remark that from the deduction of the PVW, no boundary condition is provided for the variable γ since, in the energy, this quantity does not appear with the spatial derivative. Naturally, in the actual concrete sample, we do not have access to the microcracks, so we cannot give any boundary conditions on that level.

3. Numerical simulations

To evaluate the mechanical properties of cement-based materials, three-point flexural tests and compression tests are performed through numerical simulations to assess the predictive properties of the proposed model. The main advantage of these tests is the ease of specimen preparation and testing as well as widely available testing equipment. In the bending tests, a sample (in the shape of a parallelepiped of side $d \times d \times L$, namely, $25 \times 25 \times 87.5$ cm) is placed on two supports positioned at a distance of $\ell = 75$ cm from each other, and a force is applied at the center on the top. These setups create a scenario where the material is subjected to both tension and compression, allowing for the measurement of various mechanical properties. The compression tests are instead performed on a cylindrical sample with a diameter ϕ of 11.28 cm and a height L of 22 cm. In particular, hereby, we are interested in evaluating the dissipative behavior of the specimen.

Table 1. Values of the coefficients used as a reference in the three-point flexural tests for the prism specimen.

k_b	k_s	k_e	k_{m2}	k_{m4}
1.023×10^7 N m^2	7.121×10^8 N	1.544×10^9 N	7.5×10^8 N/m^2	1.0×10^8 N/m^4
α_b	α_s	α_e	ζ_b	ζ_c
2.764×10^7 N	2.5×10^6 N/m	1.25×10^8 N/m	3.68×10^8 N	2.212×10^8 N/m

Table 2. Values of the coefficients used as a reference in the compression tests for the cylindrical specimen.

k_b	k_s	k_e	k_{m2}	k_{m4}
2.499×10^5 N m^2	1.366×10^8 N	3.143×10^8 N	7.5×10^8 N/m^2	1.0×10^8 N/m^4
α_b	α_s	α_e	ζ_b	ζ_c
9.48×10^6 N	2.5×10^6 N/m	1.25×10^8 N/m	3.68×10^6 N	2.212×10^8 N/m

The numerical computations are carried out using the commercial software COMSOL Multiphysics®, which enabled the direct use of Eq (2.2) with the weak form partial differential equation (PDE) package. Since a generalized continuum model of the first gradient in the kinematical descriptors is employed, we opted for the standard Lagrangian quadratic polynomials as the shape functions for the finite element interpolation. It is worth noting that said shape functions are particularly suited for such a formulation involving, at most, only the first derivative of the kinematical descriptors. For further details regarding the numerical implementation of similar problems, we refer the interested reader to [80, 81] for the isogeometric analysis and [82–85] for lumped models.

Specifically, we assumed for the considered material a Young modulus, $Y_c = 31.45$ GPa, and a Poisson ratio $\nu = 0.15$. Using the isotropic material symmetry the shear modulus is, thus, $G_c = Y_c/[2\,(1+\nu)]$. This information can be used to evaluate the classical stiffnesses for the bending $\mathrm{k}_b = Y_c\,J$, being J the second moment of area of the beam cross-section and for the shear stiffness $\mathrm{k}_s = 5/6\,G_c\,d^2$ for the three-point bending test, while $\mathrm{k}_s = G_c\,\pi\,(\phi/2)^2$ is the expression considered in the cylinder specimen. The stiffness due to the stretching/compression deformation $\mathrm{k}_e = Y_c\,A_c$, where A_c is the area of the cross-section. The slope characterizing the dissipative behavior in Eq (2.7) is set to be $\eta = 225$ s/m. To summarize, all values needed for the simulations are reported in Tables 1 and 2 for the bending and compression tests, respectively. The process of identifying all the necessary parameters that characterize the model can pose a significant challenge due to the complex mechanical responses that must be considered. However, it is pertinent to note that specific techniques commonly used for complex generalized materials, such as digital image correlation (DIC), energy methods, and neural networks, can also be applied in this context. These methods have proven to be effective tools in similar situations, as evidenced by their successful application in previous studies (see, for instance, references [86–95]). To analyze the dissipation, an external cyclic force with a sinusoidal trend is applied to the sample, as follows:

$$f(t) = \begin{cases} \frac{F_p}{2}\left[1 - \cos\left(\pi f_q\, t\right)\right] & \forall t < t_s = 1/f_q \\ F_p + \frac{F_0}{2}\left[1 - \cos\left(2\pi f_q\, t\right)\right] & \forall t \geq t_s, \end{cases} \tag{3.1}$$

where the amplitude of oscillation is F_0, and F_p is a small force set to ensure the adhesion and the closure of the microcracks with a pre-compression originated by the specific test (in the compression test, it is uniform, while in the bending test, it is related only to half part of the cross-section, where actually the dissipation occurs); in the numerical simulations, we set its value to $F_p = 0.1\,F_0$. The time $t_s = 0.1$ s defines the interval of application of the initial ramp of amplitude F_p (see Figure 2). The value of F_0 has been meticulously selected to mitigate any potential growth of microcracks. The force magnitude applied during the two tests was appropriately small to ensure reliable and accurate results. Specifically, $F_0 = 100$ kN for the compression tests and $F_0 = 15$ kN for the three point bending tests. The frequency f_q of the sinusoidally varying contribution is set to 10 Hz.

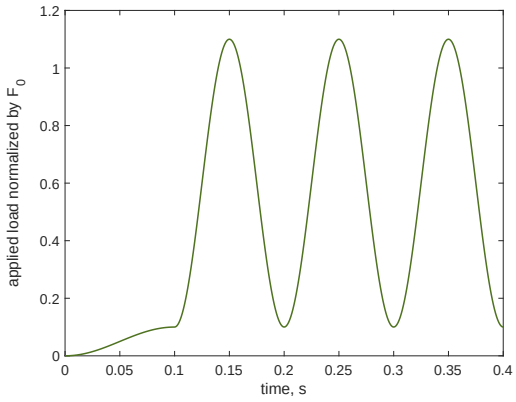
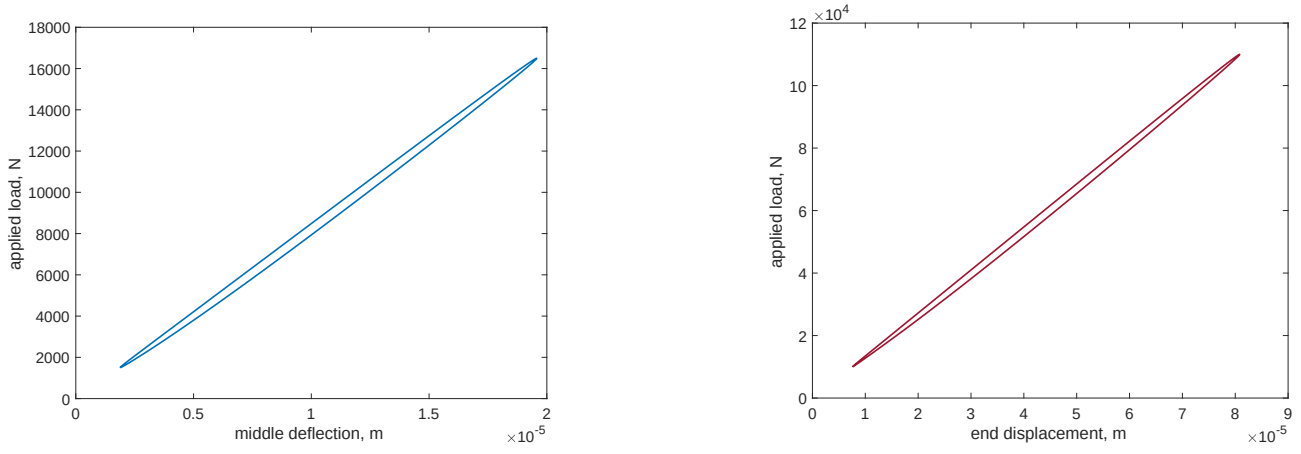


Figure 2. Normalized force applied to the samples for the cyclic tests.

4. Results and Discussion

The mechanical responses obtained performing finite-element-method-based numerical simulations are collected and discussed in this section. To begin, we consider two tests, the three-point and the compression one, with assumed reference parameters (see Tables 1 and 2) that allow us to mimic with reasonable accuracy the known experimental behavior of a building beam made of plain concrete. In addition to these reference cases, here we explore the influence of some crucial parameters, especially concerning the dissipative behavior of the material.

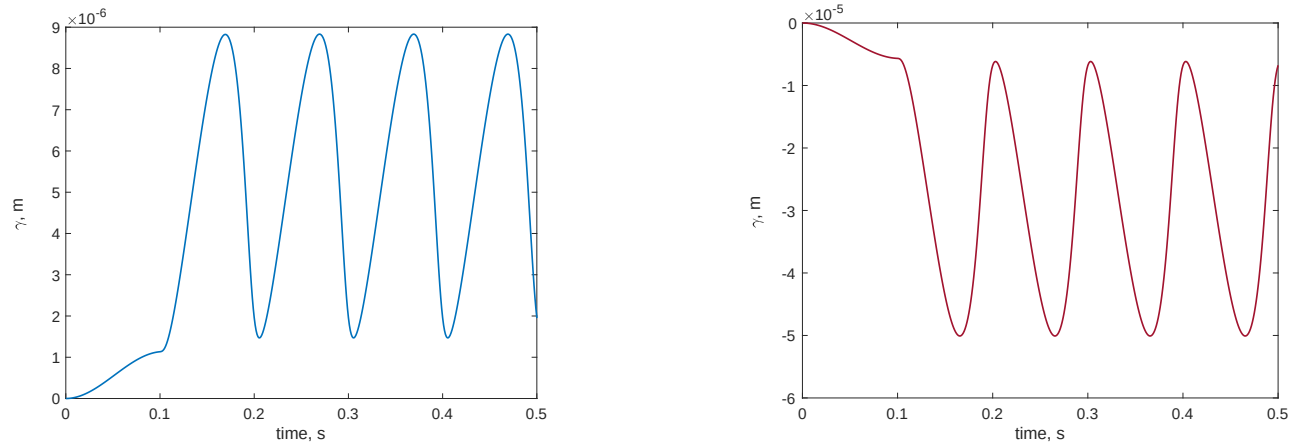
Figure 3 shows a cycle of loading and unloading for the two tests, namely, the three-point bending test and the compression test. Therefore, we can compare the two cases. The pictures display the external load versus the displacement of the loading point. The cycle area has been computed using a numerical approximated integral exploiting the trapezoidal rule. For the three-point bending test, we get a dissipated energy of 0.0074 J, and for the compression test, we evaluate a dissipated energy of 0.1699 J.



(a) **(b)**

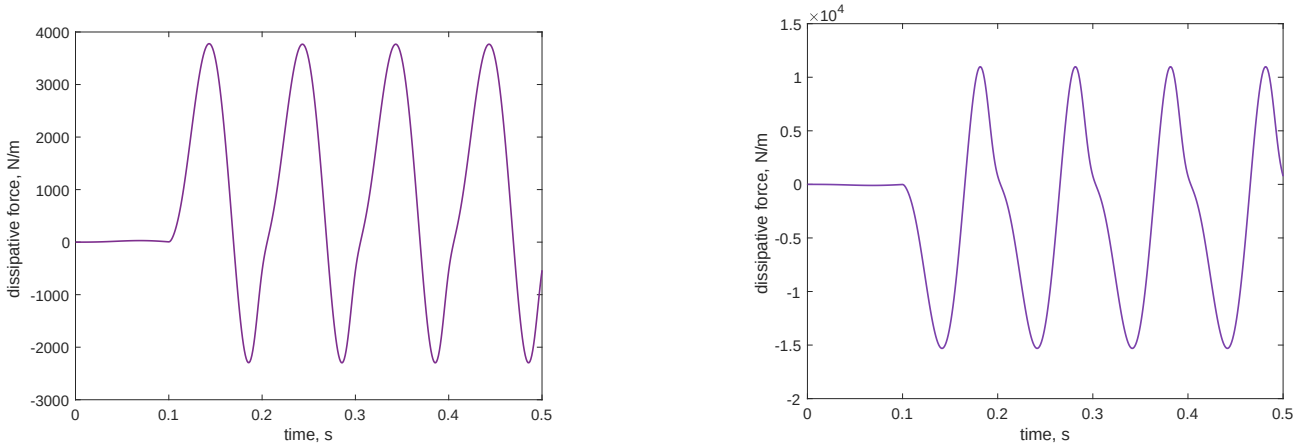
Figure 3. Dissipative cycles for the three-point flexural test (a), and the compression test (b).

In order to provide a comprehensive understanding of the analyzed phenomenon, Figures 4 and 5 depict the time histories of the relative slip variable γ and the friction forces, $\zeta_b|\varphi'|\tanh(\eta\dot{\gamma})$ and $\zeta_c\,\varsigma_C|u'|\tanh(\eta\dot{\gamma})$, at the points of maximum load, respectively. These observations were made in the center of the beam during the three-point bending test and at the point where the load was applied in the compression test. It is worth noting that the behavior of these variables related to the mechanics of the microcracks is nonlinear; thus, we might expect nonlinear behavior even at the microscopic level.



(a) **(b)**

Figure 4. Time history of the relative sliding, γ for the three-point flexural test at the middle point (a), and for the compression test at the loading point (b).

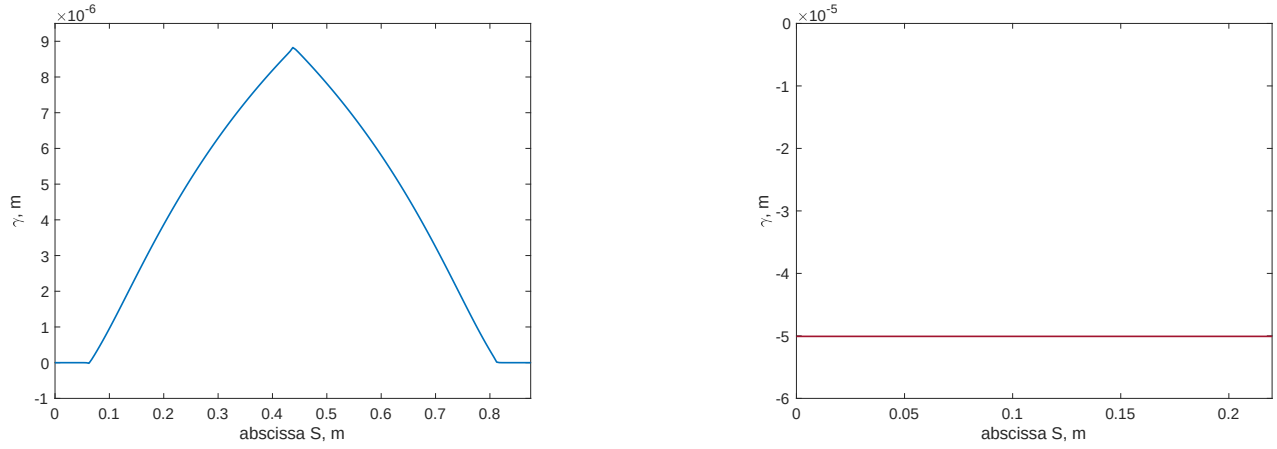


(a) **(b)**

Figure 5. Time history of the friction force, $\zeta_b|\varphi'|\tanh(\eta\dot{\gamma})$, for the three-point flexural test at the middle point (a), and $\zeta_c\,\varsigma_C|u'|\tanh(\eta\dot{\gamma})$ for the compression test at the loading point (b).

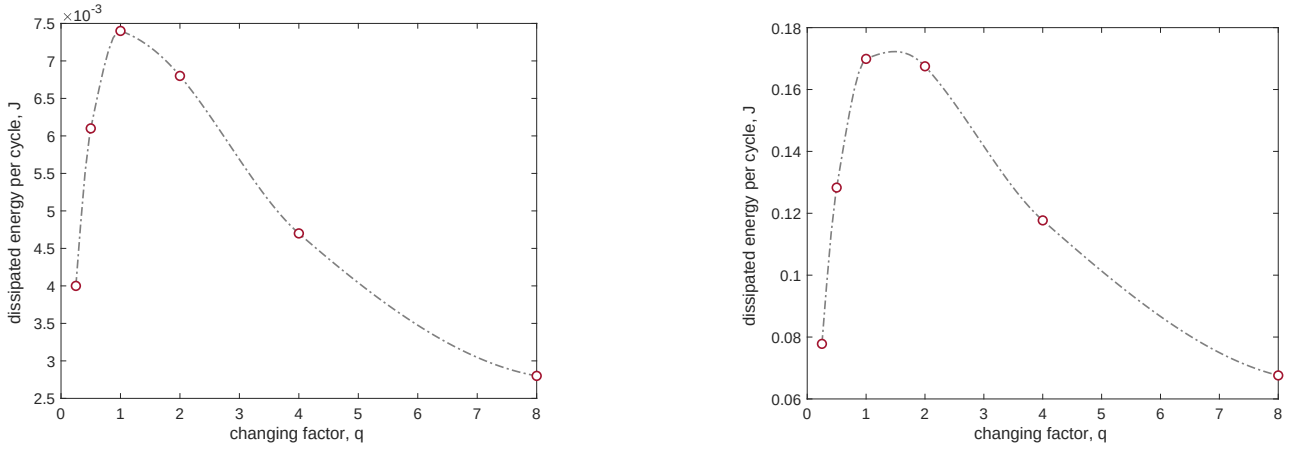
The relative sliding at the level of microcracks, γ are depicted in Figure 6 at the time instant of about 0.15 s corresponding to a maximum in the load amplitude. For the three-point flexural test, the new variable γ has significant values only in the portion of the beam where there is a flexural deformation, which, in turn, is directly related to compression in half of the cross-section, where the microcracks

close and, due to some distortions in the shape of the beam, we can experience some sliding at that level of observation. For the compression test, instead, we observe that γ is constant since the compression is as such.



(a)

Figure 6. The relative sliding at the level of microcracks γ at one maximum value of the force at about 0.15 s, for the three-point flexural test (a) and for the compression test (b).



(a) **(b)**

Figure 7. Influence of the parameters ζ_b and ζ_c on the dissipative cycles for the three-point flexural test (a), and the compression test (b), respectively.

In order to obtain a more comprehensive understanding of the model outcomes, a parametric study is conducted. Specifically, we vary the amplitude of the friction force, denoted by ζ_b and ζ_c, by employing a scale factor, q. This approach allows us to investigate the effects of altering the frictional force on the model performance and overall behavior. Through this study, we are able to draw meaningful conclusions that can inform future research and improve our understanding of the mechanisms underlying the model. Figure 7 shows the results of such a parametric study. In fact, for different multiplying factors q, specifically $\{0.25, 0.5, 2, 4, 8\}$, we compute the loading-unloading cycles

for the two categories of tests and evaluate the area of the cycles, i.e., the lost energy of the system. We get the dissipated energy $\{0.0040, 0.0061, 0.0074, 0.0068, 0.0047, 0.0028\}$ J for the three-point bending tests and larger values $\{0.0778, 0.1283, 0.1699, 0.1675, 0.1177, 0.0676\}$ J for the compression tests. These results are summarized in a plot in Figure 7. The dotted lines are regressed curves made from each series of six simulations made for the considered tests. The simulations of both tests show the same trend, highlighting the presence of a maximum of dissipated energy. This behavior is typical of phenomena with two competitive aspects. In this case, we have that with low friction forces, the energy dissipated is little; in this range, if the friction coefficient is increased, more energy is dissipated. On the other hand, when the friction force is too large, the relative motion of the microcrack faces becomes increasingly smaller as the friction force increases, and, therefore, the dissipated energy inevitably decreases. Consequently, it is possible to determine a friction coefficient such as to have the maximum dissipated energy in this framework. From the perspective of engineering the cementitious material, this aspect is crucial since acting only on increasing the friction coefficient within the microcracks can even be counterproductive if the friction effect is exaggerated.

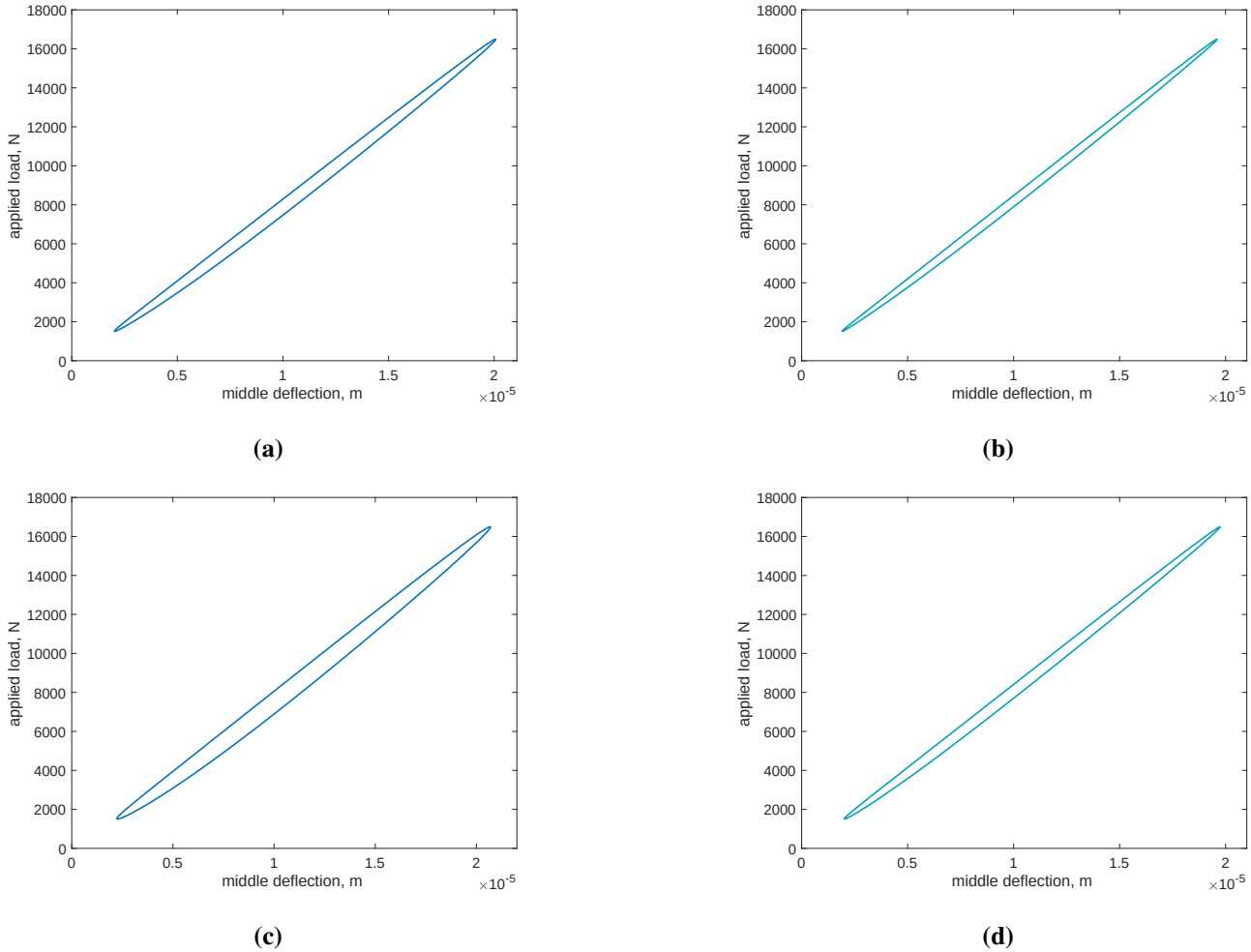
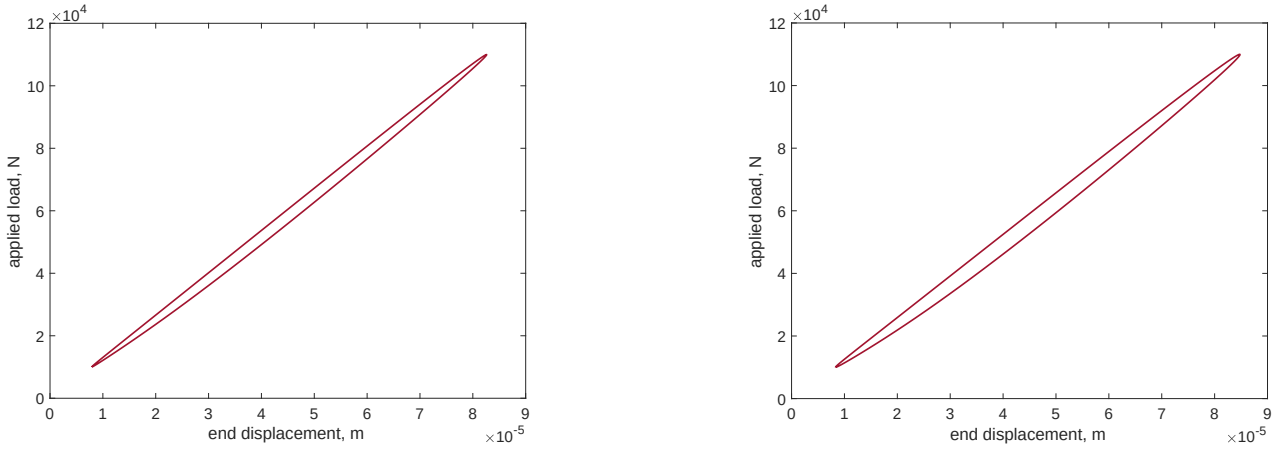


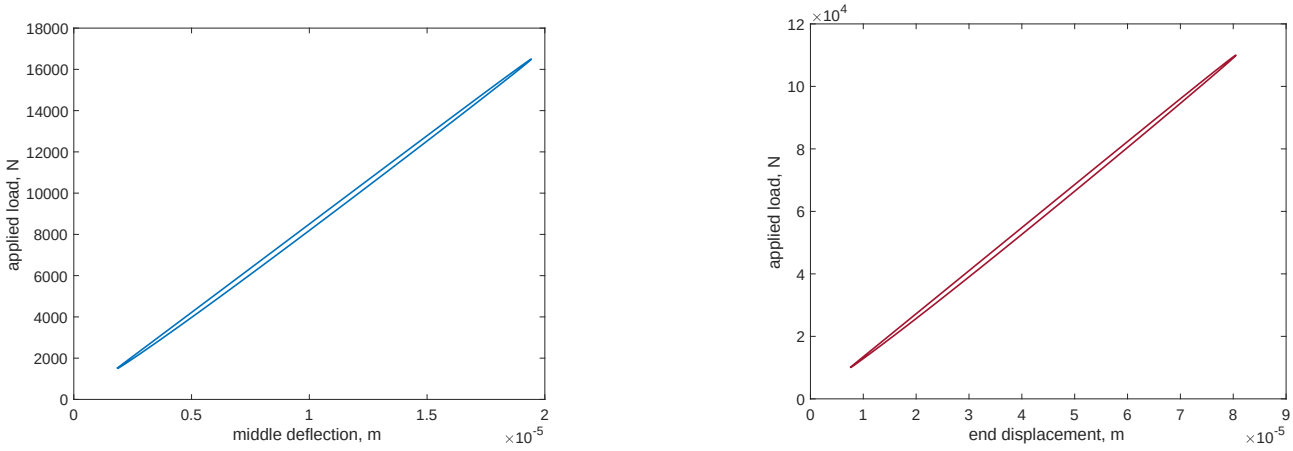
Figure 8. Influence of the parameter α_b on the dissipative cycles for the three-point flexural test with an amplifier factor of 1.2 (a) and 1.4 (c), and of α_s with 2 amplification (b), and 4 amplification (d).

Turning our focus to the coupling parameters, we analyze the effect of the coefficient α_b increasing its value by 20 and 40% with respect to the reference value. Figure 8 presents the dissipative cycles obtained via simulations conducted for the previously considered tests. The plots depicted in the figure show that increasing the coupling α_b results in a more considerable dissipation. For the three-point flexural test, we evaluate a dissipated energy of 0.0114 and 0.0167 J, respectively, when the coupling increases by 20 and 40%. The same analysis has been conducted for the coupling coefficient α_s. However, since this coefficient is less significant in the overall behavior, it is observed that with the same changes with respect to the reference case, the dissipation is almost the same. Therefore, the shear coupling has been increased by 100 and 200%, in the case of the three-point flexural test, resulting in a dissipation of energy of 0.0078 and 0.0097 J, respectively (see Figure 8). Overall, the general trend is the same but less effective.



(a) **(b)**

Figure 9. Influence of the parameter α_e on the dissipative cycles for the compressive test with an amplifier factor of 1.2 (a) and 1.4 (b).



(a) **(b)**

Figure 10. Influence of the parameter k_{m4} on the dissipative cycles for the three-point flexural test (a), and the compression test (b).

Similarly, in the compression test, we obtain 0.2554 J and 0.36589 J of dissipated energy for a 20 and 40% increase in the the coupling α_e, respectively (see Figure 9).

Therefore, in designing a building material to be earthquake-proof, i.e., capable of dissipating as much energy as possible, it seems very promising to concentrate our attention on those additives that increase these coupling coefficients without jeopardizing the mechanical strength and pursuing the optimal friction coefficient that provides the maximum level of dissipation simultaneously.

Finally, regarding the nonlinear stiffness k_{m4}, we carry out simulations to explore the influence of such a parameter. Figure 10 shows the dissipative cycles obtained by setting high values of k_{m4}. The dissipated energy obtained is 0.0043 J for the three-point flexural test with $k_{m4} = 1 \times 10^{19}$ N/m^4. Meanwhile, for the compression test, 0.1210 J of energy is dissipated in the loading-unloading cycle with $k_{m4} = 1 \times 10^{17}$ N/m^4. Thus, a greater stiffening of the asperities leads to a decrease in the energy dissipated.

5. Conclusions

In this paper, we propose a Timoshenko beam model augmented with a microcrack sliding descriptor that provides a promising framework for describing the mechanical behavior of cement-based materials. It is a very effective and efficient modeling tool that provides a beneficial computational advantage in evaluating both the strength of the material and also its dissipative behavior. Indeed, by introducing the variable γ to represent the relative sliding of microcracks within the material, the model captures additional dissipative mechanisms that contribute to energy loss during loading-unloading cycles.

Finite element method-based numerical simulations conducted using COMSOL Multiphysics demonstrated the effectiveness of the model in replicating experimental tests. The simulations revealed the influence of various parameters on the mechanical response of the material, including the dissipated energy and the behavior of kinematic descriptors such as longitudinal and transverse displacement, cross-section orientation, and relative sliding at microcracks.

A parametric study investigating the effects of altering the frictional force parameters provided insights into the relationship between frictional forces and energy dissipation. The study revealed a nonlinear relationship between these parameters and dissipated energy, with an optimal frictional force value maximizing energy dissipation.

The model predictions align well with known experimental behavior observed in flexural and compression tests of cement-based materials. This validation underscores the model ability to capture the complex mechanical response of such materials under loading and unloading conditions.

The insights gained from this study can inform the design and optimization of cement-based structures, particularly in applications where energy dissipation and mechanical resistance are critical factors, for example, in the case of earthquakes. By accurately modeling the dissipation mechanisms within the material, engineers can develop more resilient and durable structures.

Further research could focus on refining the model by incorporating additional complexities, such as heterogeneities in material properties and multi-axial loading conditions. Additionally, experimental validation of the model predictions using a wider range of test configurations and material compositions would enhance its applicability and robustness.

Overall, the study underscores the importance of considering microstructural phenomena, such as microcrack sliding, in developing accurate models for predicting the mechanical behavior of cement-

based materials. By integrating such phenomena into computational models, researchers can advance our understanding of material behavior and contribute to the development of more resilient and sustainable infrastructure solutions.

Author contributions

G.A., C.C., L.M.T. and E.B.: Conceptualization, Idealization, Methodology, Formal Analysis, Numerical Simulation, Writing. E.B.: Supervision, Revising.

Use of AI tools declaration

The authors declare they have not used Artificial Intelligence (AI) tools in the creation of this article.

Conflict of interest

The authors declare that they have no conflict of interest.

References

1. A. Misra, Stabilization characteristics of clays using class C fly ash, *Transp. Res. Rec.*, **1611** (1998), 46–54. https://doi.org/10.3141/1611-06
2. D. A. S. Sclofani, L. Contrafatto, Experimental behaviour of polyvinyl-alcohol modified concrete, *Adv. Mater. Res.*, **687** (2013), 155–160. https://doi.org/10.4028/www.scientific.net/AMR.687.155
3. L. Contrafatto, 8-Volcanic ash, in *Sustainable Concrete Made with Ashes and Dust from Different Sources*, (eds. R. Siddique and R. Belarbi), Elsevier, (2022), 331–418. https://doi.org/10.1016/B978-0-12-824050-2.00011-5
4. L. Contrafatto, R. Cosenza, R. Barbagallo, S. Ognibene, Use of recycled aggregates in road sub-base construction and concrete manufacturing, *Ann. Geophys.*, **61** (2018), SE223. https://doi.org/10.4401/ag-7785
5. G. Goel, P. Sachdeva, A. K. Chaudhary, Y. Singh, The use of nanomaterials in concrete: A review, *Mater. Today Proc.*, **69** (2022), 365–371. https://doi.org/10.1016/j.matpr.2022.09.051
6. P. Franciosi, M. Spagnuolo, O. U. Salman, Mean Green operators of deformable fiber networks embedded in a compliant matrix and property estimates, *Continuum Mech. Thermodyn.*, **31** (2019), 101–132. https://doi.org/10.1007/s00161-018-0668-0
7. M. Spagnuolo, Symmetrization of mechanical response in fibrous metamaterials through micro-shear deformability, *Symmetry*, **14** (2022), 2660. https://doi.org/10.3390/sym14122660
8. M. Spagnuolo, P. Franciosi, F. Dell'Isola, A Green operator-based elastic modeling for two-phase pantographic-inspired bi-continuous materials, *Int. J. Solids Struct.*, **188** (2020), 282–308. https://doi.org/10.1016/j.ijsolstr.2019.10.018
9. I. Giorgio, N. L. Rizzi, E. Turco, Continuum modelling of pantographic sheets for out-of-plane bifurcation and vibrational analysis, *Proc. R. Soc. A*, **473** (2017), 1–21. https://doi.org/10.1098/rspa.2017.0636

10. E. Turco, M. Golaszewski, I. Giorgio, F. D'Annibale, Pantographic lattices with non-orthogonal fibres: Experiments and their numerical simulations, *Composites, Part B*, **118** (2017), 1–14. https://doi.org/10.1016/j.compositesb.2017.02.039

11. E. Turco, I. Giorgio, A. Misra, F. Dell'Isola, King post truss as a motif for internal structure of (meta) material with controlled elastic properties, *R. Soc. Open Sci.*, **4** (2017), 171153. https://doi.org/10.1098/rsos.171153

12. P. P. Abhilash, D. K. Nayak, B. Sangoju, R. Kumar, V. Kumar, Effect of nano-silica in concrete; a review, *Constr. Build. Mater.*, **278** (2021), 122347. https://doi.org/10.1016/j.conbuildmat.2021.122347

13. N. De Belie, E. Gruyaert, A. Al-Tabbaa, P. Antonaci, C. Baera, D. Bajare, et al., A review of self-healing concrete for damage management of structures, *Adv. Mater. Interfaces*, **5** (2018), 1800074. https://doi.org/10.1002/admi.201800074

14. S. Sangadji, E. Schlangen, Mimicking bone healing process to self repair concrete structure novel approach using porous network concrete, *Procedia Eng.*, **54** (2013), 315–326. https://doi.org/10.1016/j.proeng.2013.03.029

15. A. Casalotti, F. D'annibale, G. Rosi, Multi-scale design of an architected composite structure with optimized graded properties, *Composite Structures*, **252** (2020), 112608. https://doi.org/10.1016/j.compstruct.2020.112608

16. T. Lekszycki, F. Dell'Isola, A mixture model with evolving mass densities for describing synthesis and resorption phenomena in bones reconstructed with bio-resorbable materials, *ZAMM Z. Angew. Math. Mech.*, **92** (2012), 426–444. https://doi.org/10.1002/zamm.201100082

17. E. I. Bednarczyk, T. Lekszycki, W. Glinkowski, Effect of micro-cracks on the angiogenesis and osteophyte development during degenerative joint disease, *Comput. Assisted Methods Eng. Sci.*, **24** (2018), 149–156. http://doi.org/10.24423/cames.191

18. I. Giorgio, F. Dell'Isola, U. Andreaus, F. Alzahrani, T. Hayat, T. Lekszycki, On mechanically driven biological stimulus for bone remodeling as a diffusive phenomenon, *Biomech. Model. Mechanobiol.*, **18** (2019), 1639–1663. https://doi.org/10.1007/s10237-019-01166-w

19. I. Giorgio, F. Dell'Isola, U. Andreaus, A. Misra, An orthotropic continuum model with substructure evolution for describing bone remodeling: an interpretation of the primary mechanism behind Wolff's law, *Biomech. Model. Mechanobiol.*, **22** (2023), 2135–2152. https://doi.org/10.1007/s10237-023-01755-w

20. M. Rajczakowska, K. Habermehl-Cwirzen, H. Hedlund, A. Cwirzen, Autogenous self-healing: A better solution for concrete, *J. Mater. Civ. Eng.*, **31** (2019), 03119001. https://doi.org/10.1061/(ASCE)MT.1943-5533.0002764

21. M. E. Espitia-Nery, D. E. Corredor-Pulido, P. A. Castaño-Oliveros, J. A. Rodríguez-Medina, Q. Y. Ordoñez-Bello, M. S. Pérez-Fuentes, Mechanisms of encapsulation of bacteria in self-healing concrete, *Dyna*, **86** (2019), 17–22. https://doi.org/10.15446/dyna.v86n210.75343

22. J. Xue, B. Briseghella, F. Huang, C. Nuti, H. Tabatabai, B. Chen, Review of ultra-high performance concrete and its application in bridge engineering, *Constr. Build. Mater.*, **260** (2020), 119844. https://doi.org/10.1016/j.conbuildmat.2020.119844

23. L. Placidi, F. Dell'Isola, A. Kandalaft, R. Luciano, C. Majorana, A. Misra, A granular micromechanic-based model for Ultra High Performance Fiber-Reinforced Concrete (UHP FRC), *Int. J. Solids Struct.*, **297** (2024), 112844. https://doi.org/10.1016/j.ijsolstr.2024.112844

24. V. Nguyen-Van, B. Panda, G. Zhang, H. Nguyen-Xuan, P. Tran, Digital design computing and modelling for 3-D concrete printing, *Autom. Constr.*, **123** (2021), 103529. https://doi.org/10.1016/j.autcon.2020.103529

25. A. Kezmane, B. Chiaia, O. Kumpyak, V. Maksimov, L. Placidi, 3D modelling of reinforced concrete slab with yielding supports subject to impact load, *Eur. J. Environ. Civ. Eng.*, **21** (2017), 988–1025. https://doi.org/10.1080/19648189.2016.1194330

26. A. Casalotti, F. D'Annibale, G. Rosi, Optimization of an architected composite with tailored graded properties, *Z. Angew. Math. Phys.*, **75** (2014), 126. https://doi.org/10.1007/s00033-024-02255-2

27. I. Giorgio, A. Ciallella, D. Scerrato, A study about the impact of the topological arrangement of fibers on fiber-reinforced composites: Some guidelines aiming at the development of new ultra-stiff and ultra-soft metamaterials, *Int. J. Solids Struct.*, **203** (2020), 73–83. https://doi.org/10.1016/j.ijsolstr.2020.07.016

28. A. Ciallella, F. D'Annibale, D. Del Vescovo, I. Giorgio, Deformation patterns in a second-gradient lattice annular plate composed of "spira mirabilis" fibers, *Continuum Mech. Thermodyn.*, **35** (2023), 1561–1580. https://doi.org/10.1007/s00161-022-01169-6

29. T. Wangler, N. Roussel, F. P. Bos, T. A. M. Salet, R. J. Flatt, Digital concrete: A review, *Cem. Concr. Res.*, **123** (2019), 105780. https://doi.org/10.1016/j.cemconres.2019.105780

30. N. Rezaei, E. Barchiesi, D. Timofeev, C. A. Tran, A. Misra, L. Placidi, Solution of a paradox related to the rigid bar pull-out problem in standard elasticity, *Mech. Res. Commun.*, **126** (2022), 104015. https://doi.org/10.1016/j.mechrescom.2022.104015

31. M. F. Funari, S. Spadea, F. Fabbrocino, R. Luciano, A moving interface finite element formulation to predict dynamic edge debonding in FRP-strengthened concrete beams in service conditions, *Fibers*, **8** (2020), 42. https://doi.org/10.3390/fib8060042

32. W. Pietraszkiewicz, V. A. Eremeyev, On vectorially parameterized natural strain measures of the non-linear Cosserat continuum, *Int. J. Solids Struct.*, **46** (2009), 2477–2480. https://doi.org/10.1016/j.ijsolstr.2009.01.030

33. G. La Valle, A new deformation measure for the nonlinear micropolar continuum, *Z. Angew. Math. Phys.*, **73** (2022), 78. https://doi.org/10.1007/s00033-022-01715-x

34. I. Giorgio, A. Misra, L. Placidi, Geometrically nonlinear Cosserat elasticity with chiral effects based upon granular micromechanics, in *Sixty Shades of Generalized Continua*, (eds. H. Altenbach, A. Berezovski, F. Dell'Isola and A. Porubov), Springer, **170** (2023), 273–292. https://doi.org/10.1007/978-3-031-26186-2_17

35. I. Giorgio, M. De Angelo, E. Turco, A. Misra, A Biot–Cosserat two-dimensional elastic nonlinear model for a micromorphic medium, *Continuum Mech. Thermodyn.*, **32** (2020), 1357–1369. https://doi.org/10.1007/s00161-019-00848-1

36. E. Turco, F. Dell'Isola, A. Misra, A nonlinear Lagrangian particle model for grains assemblies including grain relative rotations, *Int. J. Numer. Anal. Methods Geomech.*, **43** (2019), 1051–1079. https://doi.org/10.1002/nag.2915

37. E. Turco, Forecasting nonlinear vibrations of patches of granular materials by elastic interactions between spheres, *Mech. Res. Commun.*, **122** (2022), 103879. https://doi.org/10.1016/j.mechrescom.2022.103879

38. D. Scerrato, I. Giorgio, A. Della Corte, A. Madeo, N. E. Dowling, F. Darve, Towards the design of an enriched concrete with enhanced dissipation performances, *Cem. Concr. Res.*, **84** (2016), 48–61. https://doi.org/10.1016/j.cemconres.2016.03.002

39. A. Scrofani, E. Barchiesi, B. Chiaia, A. Misra, L. Placidi, Fluid diffusion related aging effect in a concrete dam modeled as a Timoshenko beam, *Math. Mech. Complex Syst.*, **11** (2023), 313–334. https://doi.org/10.2140/memocs.2023.11.313

40. I. Giorgio, D. Scerrato, Multi-scale concrete model with rate-dependent internal friction, *Eur. J. Environ. Civ. Eng.*, **21** (2017), 821–839. https://doi.org/10.1080/19648189.2016.1144539

41. G. Jouan, P. Kotronis, F. Collin, Using a second gradient model to simulate the behaviour of concrete structural elements, *Finite Elem. Anal. Des.*, **90** (2014), 50–60. https://doi.org/10.1016/j.finel.2014.06.002

42. P. Germain, The method of virtual power in the mechanics of continuous media, I: Second-gradient theory, *Math. Mech. Complex Syst.*, **8** (2020), 153–190. https://doi.org/10.2140/memocs.2020.8.153

43. G. La Valle, B. E. Abali, G. Falsone, C. Soize, Sensitivity of a homogeneous and isotropic second-gradient continuum model for particle-based materials with respect to uncertainties, *ZAMM Z. Angew. Math. Mech.*, **103** (2023), e202300068. https://doi.org/10.1002/zamm.202300068

44. F. Dell'Isola, S. R. Eugster, R. Fedele, P. Seppecher, Second-gradient continua: From Lagrangian to Eulerian and back, *Math. Mech. Solids*, **27** (2022), 2715–2750. https://doi.org/10.1177/10812865221078822

45. F. Dell'Isola, U. Andreaus, L. Placidi, At the origins and in the vanguard of peridynamics, non-local and higher-gradient continuum mechanics: an underestimated and still topical contribution of Gabrio Piola, *Math. Mech. Solids*, **20** (2015), 887–928. https://doi.org/10.1177/1081286513509811

46. A. Berezovski, I. Giorgio, A. D. Corte, Interfaces in micromorphic materials: Wave transmission and reflection with numerical simulations, *Math. Mech. Solids*, **21** (2016), 37–51. https://doi.org/10.1177/1081286515572244

47. M. Golaszewski, R. Grygoruk, I. Giorgio, M. Laudato, F. D. Cosmo, Metamaterials with relative displacements in their microstructure: Technological challenges in 3D printing, experiments and numerical predictions, *Continuum Mech. Thermodyn.*, **31** (2019), 1015–1034. https://doi.org/10.1007/s00161-018-0692-0

48. A. Ciallella, I. Giorgio, S. R. Eugster, N. L. Rizzi, F. Dell'Isola, Generalized beam model for the analysis of wave propagation with a symmetric pattern of deformation in planar pantographic sheets, *Wave Motion*, **113** (2022), 102986. https://doi.org/10.1016/j.wavemoti.2022.102986

49. O. Szlachetka, I. Giorgio, Heat conduction in multi-component step-wise FGMs, *Continuum Mech. Thermodyn.*, (2024), 1–19. https://doi.org/10.1007/s00161-024-01296-2

50. V. A. Eremeyev, W. Pietraszkiewicz, Material symmetry group and constitutive equations of micropolar anisotropic elastic solids, *Math. Mech. Solids*, **21** (2016), 210–221. https://doi.org/10.1177/1081286515582862

51. G. La Valle, S. Massoumi, A new deformation measure for micropolar plates subjected to in-plane loads, *Continuum Mech. Thermodyn.*, **34** (2022), 243–257. https://doi.org/10.1007/s00161-021-01055-7

52. I. Giorgio, F. Dell'Isola, A. Misrav, Chirality in 2D Cosserat media related to stretch-micro-rotation coupling with links to granular micromechanics, *Int. J. Solids Struct.*, **202** (2020), 28–38. https://doi.org/10.1016/j.ijsolstr.2020.06.005

53. I. Giorgio, F. Hild, E. Gerami, F. Dell'Isola, A. Misra, Experimental verification of 2D Cosserat chirality with stretch-micro-rotation coupling in orthotropic metamaterials with granular motif, *Mech. Res. Commun.*, **126** (2022), 104020. https://doi.org/10.1016/j.mechrescom.2022.104020

54. G. La Valle, C. Soize, A higher-order nonlocal elasticity continuum model for deterministic and stochastic particle-based materials, *Z. Angew. Math. Phys.*, **75** (2024). https://doi.org/10.1007/s00033-024-02196-w

55. A. Madeo, F. Dell'Isola, F. Darve, A continuum model for deformable, second gradient porous media partially saturated with compressible fluids, *J. Mech. Phys. Solids*, **61** (2013), 2196–2211. https://doi.org/10.1016/j.jmps.2013.06.009

56. F. Dell'Isola, A. Madeo, P. Seppecher, Boundary conditions at fluid-permeable interfaces in porous media: A variational approach, *Int. J. Solids Struct.*, **46** (2009), 3150–3164. https://doi.org/10.1016/j.ijsolstr.2009.04.008

57. I. Giorgio, A variational formulation for one-dimensional linear thermoviscoelasticity, *Math. Mech. Complex Syst.*, **9** (2022), 397–412. https://doi.org/10.2140/memocs.2021.9.397

58. E. Barchiesi, N. Hamila, Maximum mechano-damage power release-based phase-field modeling of mass diffusion in damaging deformable solids, *Z. Angew. Math. Phys.*, **73** (2022). https://doi.org/10.1007/s00033-021-01668-7

59. A. Ramírez-Torres, R. Penta, A. Grillo, Effective properties of fractional viscoelastic composites via two-scale asymptotic homogenization, *Math. Methods Appl. Sci.*, **46** (2023), 16500–16520. https://doi.org/10.1002/mma.9457

60. L. Placidi, E. Barchiesi, Energy approach to brittle fracture in strain-gradient modelling, *Proc. R. Soc. A*, **474** (2018), 20170878. https://doi.org/10.1098/rspa.2017.0878

61. F. Fabbrocino, M. F. Funari, F. Greco, P. Lonetti, R. Luciano, R. Penna, Dynamic crack growth based on moving mesh method, *Composites, Part B*, **174** (2019), 107053. https://doi.org/10.1016/j.compositesb.2019.107053

62. C. Comi, R. Fedele, U. Perego, A chemo-thermo-damage model for the analysis of concrete dams affected by alkali-silica reaction, *Mech. Mater.*, **41** (2009), 210–230. https://doi.org/10.1016/j.mechmat.2008.10.010

63. A. Bilotta, A. Morassi, E. Turco, Simple convolutional neural networks for the damage identification in composite steel-concrete beams, in *International Conference on Experimental Vibration Analysis for Civil Engineering Structures*, Springer, **433** (2023), 422–431. https://doi.org/10.1007/978-3-031-39117-0_43

64. L. Placidi, A variational approach for a nonlinear one-dimensional damage-elasto-plastic second-gradient continuum model, *Continuum Mech. Thermodyn.*, **28** (2016), 119–137. https://doi.org/10.1007/s00161-014-0405-2

65. L. Placidi, E. Barchiesi, A. Misra, A strain gradient variational approach to damage: A comparison with damage gradient models and numerical results, *Math. Mech. Complex Syst.*, **6** (2018), 77–100. https://doi.org/10.2140/memocs.2018.6.77

66. L. Placidi, A. Misra, E. Barchiesi, Simulation results for damage with evolving microstructure and growing strain gradient moduli, *Continuum Mech. Thermodyn.*, **31** (2019), 1143–1163. https://doi.org/10.1007/s00161-018-0693-z

67. R. Luciano, A. Caporale, H. Darban, C. Bartolomeo, Variational approaches for bending and buckling of non-local stress-driven Timoshenko nano-beams for smart materials, *Mech. Res. Commun.*, **103** (2020), 103470. https://doi.org/10.1016/j.mechrescom.2019.103470

68. Ciallella, A and Pasquali, D and Gołaszewski, M and D'Annibale, F and Giorgio, I, A rate-independent internal friction to describe the hysteretic behavior of pantographic structures under cyclic loads, *Mech. Res. Commun.*, **116** (2021), 103761.

69. A. Ciallella, D. Pasquali, M. Gołaszewski, F. D'Annibale, I. Giorgio, Shear rupture mechanism and dissipation phenomena in bias-extension test of pantographic sheets: Numerical modeling and experiments, *Math. Mech. Solids*, **27** (2022), 2170–2188. https://doi.org/10.1016/j.mechrescom.2021.103761

70. I. Giorgio, L. Placidi, A variational formulation for three-dimensional linear thermoelasticity with 'thermal inertia', *Meccanica*, (2024). https://doi.org/10.1007/s11012-024-01796-0

71. A. Battista, L. Rosa, R. Dell'Erba, L. Greco, Numerical investigation of a particle system compared with first and second gradient continua: Deformation and fracture phenomena, *Math. Mech. Solids*, **22** (2017), 2120–2134. https://doi.org/10.1177/1081286516657889

72. D. Scerrato, I. Giorgio, A. Madeo, A. Limam, F. Darve, A simple non-linear model for internal friction in modified concrete, *Int. J. Eng. Sci.*, **80** (2014), 136–152. https://doi.org/10.1016/j.ijengsci.2014.02.021

73. D. Scerrato, I. Giorgio, A. Della Corte, A. Madeo, A. Limam, A micro-structural model for dissipation phenomena in the concrete, *Int. J. Numer. Anal. Methods Geomech.*, **39** (2015), 2037–2052. https://doi.org/10.1002/nag.2394

74. I. Giorgio, M. Spagnuolo, L. Greco, F. D'Annibale, A. Cazzani, A variational approach to address the problem of planar nonlinear beams, in *Comprehensive Mechanics of Materials*, (eds. V. Silberschmidt), Elsevier, **1** (2024), 67–97. https://doi.org/10.1016/B978-0-323-90646-3.00027-7

75. V. Pensée, D. Kondo, L. Dormieux, Micromechanical analysis of anisotropic damage in brittle materials, *J. Eng. Mech.*, **128** (2002), 889–897. https://doi.org/10.1061/(ASCE)0733-9399(2002)128:8(889)

76. B. R. Raveendra, G. S. Benipal, A. K. Singh, Constitutive modelling of concrete: An overview, *Asian J. Civ. Eng.*, **6** (2005), 211–214.

77. A. M. Bersani, P. Caressa, F. Dell'Isola, Approximation of dissipative systems by elastic chains: Numerical evidence, *Math. Mech. Solids*, **28** (2023), 501–520. https://doi.org/10.1177/10812865221081851

78. A. M. Bersani, P. Caressa, A. Ciallella, Numerical evidence for the approximation of dissipative systems by gyroscopically coupled oscillator chains, *Math. Mech. Complex Syst.*, **10** (2022), 265–278. https://doi.org/10.2140/memocs.2022.10.265

79. A. Ciallella, D. Scerrato, M. Spagnuolo, I. Giorgio, A continuum model based on Rayleigh dissipation functions to describe a Coulomb-type constitutive law for internal friction in woven fabrics, *Z. Angew. Math. Phys.*, **73** (2022). https://doi.org/10.1007/s00033-022-01845-2

80. L. Greco, M. Cuomo, L. Contrafatto, Two new triangular G1-conforming finite elements with cubic edge rotation for the analysis of Kirchhoff plates, *Comput. Methods Appl. Mech. Eng.*, **356** (2019), 354–386. https://doi.org/10.1016/j.cma.2019.07.026

81. L. Greco, D. Castello, M. Cuomo, An objective and accurate G1-conforming mixed Bézier FE-formulation for Kirchhoff–Love rods, *Math. Mech. Solids*, **29** (2024), 645–685. https://doi.org/10.1177/10812865231204972

82. I. Giorgio, A discrete formulation of Kirchhoff rods in large-motion dynamics, *Math. Mech. Solids*, **25** (2020), 1081–1100. https://doi.org/10.1177/1081286519900902

83. I. Giorgio, D. Del Vescovo, Energy-based trajectory tracking and vibration control for multilink highly flexible manipulators, *Math. Mecha. Complex Syst.*, **7** (2019), 159–174. https://doi.org/10.2140/memocs.2019.7.159

84. D. Baroudi, I. Giorgio, A. Battista, E. Turco, L. A. Igumnov, Nonlinear dynamics of uniformly loaded elastica: Experimental and numerical evidence of motion around curled stable equilibrium configurations, *ZAMM Z. Angew. Math. Mech.*, **99** (2019), e201800121. https://doi.org/10.1002/zamm.201800121

85. E. Turco, Discrete is it enough? The revival of Piola–Hencky keynotes to analyze three-dimensional Elastica, *Continuum Mech. Thermodyn.*, **30** (2018), 1039–1057. https://doi.org/10.1007/s00161-018-0656-4

86. R. Fedele, G. Maier, B. Miller, Identification of elastic stiffness and local stresses in concrete dams by in situ tests and neural networks, *Struct. Infrastruct. Eng.*, **1** (2005), 165–180. https://doi.org/10.1080/15732470500030513

87. R. Fedele, G. Maier, B. Miller, Image correlation-based identification of fracture parameters for structural adhesives, *Tech. Mech. Eur. J. Eng. Mech.*, **32** (2012), 195–204.

88. B. E. Abali, C. C. Wu, W. H. Müller, An energy-based method to determine material constants in nonlinear rheology with applications, *Continuum Mech. Thermodyn.*, **28** (2016), 1221–1246. https://doi.org/10.1007/s00161-015-0472-z

89. M. De Angelo, L. Placidi, N. Nejadsadeghi, A. Misra, Non-standard Timoshenko beam model for chiral metamaterial: Identification of stiffness parameters, *Mech. Res. Commun.*, **103** (2020), 103462. https://doi.org/10.1016/j.mechrescom.2019.103462

90. A. Ciallella, G. La Valle, A. Vintache, B. Smaniotto, F. Hild, Deformation mode in 3-point flexure on pantographic block, *Int. J. Solids Struct.*, **265** (2023), 112129. https://doi.org/10.1016/j.ijsolstr.2023.112129

91. M. De Angelo, E. Barchiesi, I. Giorgio, B. E. Abali, Numerical identification of constitutive parameters in reduced-order bi-dimensional models for pantographic structures: Application to out-of-plane buckling, *Arch. Appl. Mech.*, **89** (2019), 1333–1358. https://doi.org/10.1007/s00419-018-01506-9

92. N. Shekarchizadeh, B. E. Abali, E. Barchiesi, A. M. Bersani, Inverse analysis of metamaterials and parameter determination by means of an automatized optimization problem, *ZAMM Z. Angew. Math. Mech.*, **101** (2021), e202000277. https://doi.org/10.1002/zamm.202000277

93. I. Giorgio, P. Harrison, F. Dell'Isola, J. Alsayednoor, E. Turco, Wrinkling in engineering fabrics: A comparison between two different comprehensive modelling approaches, *Proc. R. Soc. A*, **474** (2018), 20180063. https://doi.org/10.1098/rspa.2018.0063

94. R. Fedele, A. Ciani, L. Galantucci, V. Casalegno, A. Ventrella, M. Ferraris, Characterization of innovative CFC/Cu joints by full-field measurements and finite elements, *Mater. Sci. Eng. A*, **595** (2014), 306–317. https://doi.org/10.1016/j.msea.2013.12.015

95. N. Cefis, R. Fedele, M. G. Beghi, An integrated methodology to estimate the effective elastic parameters of amorphous TiO2 nanostructured films, combining SEM images, finite element simulations and homogenization techniques, *Mech. Res. Commun.*, **131** (2023), 104153. https://doi.org/10.1016/j.mechrescom.2023.104153



AIMS Press

© 2024 the Author(s), licensee AIMS Press. This is an open access article distributed under the terms of the Creative Commons Attribution License (https://creativecommons.org/licenses/by/4.0)

An enhanced beam model incorporating a hysteresis-based solid friction damping mechanism for cementitious materials

---

Chapter abstract

This chapter investigates cyclic internal dissipation in cement-based materials using a 1D-enhanced micromorphic beam model with a dynamic friction term. Microcracks are considered key to energy dissipation, driven by relative sliding under cyclic loading without macroscopic damage. The friction model, based on P. R. Dahl's dry friction law, evolves over time, exhibiting elastoplastic behavior.

The proposed model captures energy exchange between bending, shear distortion, and microcrack sliding, including energy storage in asperities and dissipation from their interaction. Finite element simulations in COMSOL Multiphysics analyze kinematic descriptors and dissipative cycles.
Published in *Continuum Mechanics and Thermodynamics*, 2025.

Continuum Mech. Thermodyn.
https://doi.org/10.1007/s00161-024-01335-y

ORIGINAL ARTICLE

Larry Murcia Terranova · Christian Cardillo · Giuliano Aretusi

An enhanced beam model incorporating a hysteresis-based solid friction damping mechanism for cementitious materials

Received: 14 July 2024 / Accepted: 24 September 2024
© The Author(s), under exclusive licence to Springer-Verlag GmbH Germany, part of Springer Nature 2024

Abstract In this work, we investigate a dynamic internal dissipation mechanism in the context of cement-based materials by introducing a 1D-enhanced micromorphic beam model with a dynamic internal friction term. Here, we consider an inherent feature in concrete-like materials arising from the multi-scale structure, namely, microcracks. Thus, we assume that the internal dissipation of the energy depends on the overall relative sliding displacement of the opposite faces in the microcracks under the effects of an applied cyclic load whenever no significant phenomena related to damage occur at the macroscopic level. The dynamic friction term is based on a well-known model for dry friction in solids due to P. R. Dahl, where the friction force depends only on the sliding displacement and evolves in time, reproducing an elastoplastic behavior. The model proposed in this paper takes into account a mechanical energy interchange between both bending and shear distortion in the beam with the sliding occurring at the microcracks, a storage of mechanical energy because of the asperities inside the faces of the microcracks, and the dissipation of the energy that follows from the interaction between the bending and the microcracks. Numerical simulations of the kinematic descriptors and the dissipative cycles are also provided by using the Finite Element Method and the commercial software COMSOL Multiphysics®.

Keywords Timoshenko beam model · Concrete · Dahl-type friction force model · Energy dissipation · 1D continuum micromorphic model · Microcracks · Hysteretic damping

1 Introduction

Concrete is ubiquitous in the development of building environments in human societies [1]. Notwithstanding this, a rigorous understanding of all features and potential applications of cement-based materials like concrete itself, has not been achieved yet. In fact, many features of concrete and novel procedures to improve its performance are topics under current investigation. Moreover, since resources required to produce this type of materials, for instance, water and heat energy, are considerable and its recycling is not a straightforward

Christian Cardillo and Giuliano Aretusi have contributed equally to this work.

L. Murcia Terranova ( )
Department of Information Engineering, Computer Science and Mathematics, Università dell'Aquila, 67100 Coppito, L'Aquila, Italy
e-mail: larry.murciaterranova@graduate.univaq.it

C. Cardillo
Department of Civil Engineering and Architecture, Università di Catania, Piazza Università, 95100 Catania, Italy
e-mail: christian.cardillo@phd.unict.it

G. Aretusi
Department of Civil, Construction-Architectural and Environmental Engineering, Università dell'Aquila, Monteluco di Roio, 67100 L'Aquila, Italy
e-mail: giuliano.aretusi@graduate.univaq.it

Published online: 14 November 2024

process [2], concrete-like materials pose an environmental, social and economic efficiency problem of major interest to the scientific community. For instance, current research topics in this regard are: *supplementary cementitious materials* aimed primarily to mitigate carbon emission in manufacturing but also to enhance concrete features [3,4], *nanotechnology improvements* to advance properties like durability, particle packing and reduce the porosity [5–7], *self-healing technology* in concrete allowing the material to repair its own cracks by autogenous or encapsulated healing [8–12], and the development of *ultrahigh performance concrete* with outstanding properties [13].

Cement-based materials like concrete are widely acknowledged as heterogeneous materials that consist of a distribution of different types and quantities of microcracks, pores and solid phases. Furthermore, important properties of concrete, like strength, depend on factors such as the water-to-cement ratio and the incorporation of aggregates into the cement paste that mechanically or chemically modify its natural behavior. In this way, concrete could be conceived as a multi-scale engineered material with a complex microstructure that can be tailored to improve its macroscopic responses [3,14–16]. Therefore, inspired by the richness of applications in multiple contexts of this type of materials, in this paper, we are interested in the dissipation of energy for earthquake-proof applications of cement-based materials arising from the incorporation of supplements and aggregates in the mixture. It is worth noting that supplementary materials and aggregates are actively being investigated [17–21]. In fact, this research framework opens the gates to possibilities such as an improved dissipation from mechanical to internal energy. However, the dissipation that we study in the current work is due to internal friction tightly linked to reversible changes, a behavior observed experimentally in dissipative cycles that could have a substantial effect in practice: enhanced concrete-like materials that can dissipate as much energy as possible (because of an increasing of the internal friction) while preserving their strength (for further information on the study of dissipative systems, the reader can refer to, e.g., [22–24]).

From this point of view, it is possible to consider concrete as a mechanical metamaterial by incorporating micro-fillers that aim at enhancing its performance, particularly in dynamic applications. Indeed, mechanical metamaterials are engineered materials designed to have properties not found in naturally occurring materials, often through the use of specific microstructures or micro-fillers that impart unique mechanical characteristics [25–28]. By introducing microfillers, the microstructure of concrete can be tailored to achieve improved mechanical properties, such as increased strength, toughness, and dynamic performance. Possible types of microfillers are: *i*) nanoparticles, namely, materials like carbon nanotubes, graphene, or nano-silica can significantly enhance the mechanical properties of concrete; *ii*) fibers, e.g., steel, glass, polypropylene that can improve tensile strength, ductility, and crack resistance; *iii*) phase change materials (PCMs) that can enhance thermal properties and provide additional energy dissipation under dynamic loading; *iv*) magnetic or electro-responsive particles that can be used to create smart concrete with adaptive properties. This approach leverages the principles of metamaterial design to create concrete composites with tailored properties that meet specific engineering requirements, opening up new possibilities for advanced structural applications with superior dynamic performance.

Recent works in the literature follow different approaches to model, from a mathematical perspective, concrete's behavior, e.g., by means of tools like the classical Cauchy model, generalized continua models where aggregates can be added to the mixture [29], higher order continua descriptions that account for the material heterogeneity [30–36], and multi-scale models that describe phenomena in the macro, meso and microscale. Additionally, in the last few years, multiple works have tackled the modeling of energy dissipation in concrete through approaches ranging from experimental to analytical formulations, and with the objective of introducing mathematical tools for the study of advanced concrete in the context of earthquake-proof designs [2,37–42]. More precisely, inspired by experimental evidence, recent works like [37–39] describe friction phenomena and dissipation in modified concrete obtained by adding selected micro-particles/fillers in concrete pores to increase the internal dissipation under the effect of uniaxial dynamic cyclic loading in 3D concrete. In fact, in works like [2,39–42] micromorphic multi-scale models are introduced to explain dissipative loops arising from cyclic uniaxial loads for small strains in 3D concrete, and enhanced Timoshenko-like beam models with static friction, i.e., a stationary constitutive equation relating the friction force considered to a micro/macro-descriptor, to study dissipation mechanisms in cement-based materials whenever cyclic loads are considered.

On the other hand, it is worth mentioning that one of the inherent phenomena occurring in concrete-like materials due to the multi-scale structure is microcracks. Microcracks can be modeled from a geometrical point of view as empty coin-shaped spaces that can open and close, and consist of two delimiting opposite faces with asperities that can interact whenever the microcracks are closed. This kind of microstructure could be of particular interest in comprehending a source of damage evolution in the material body as well as internal

energy dissipation. In fact, recent works like [43–48] consider damage-related phenomena in the presence of microstructures such as microcracks. Concretely, in [43], the authors aim to explain, in a general framework, the development of new microstructures due to damage with a monotonic evolution rule and employing a strain gradient regularization of continuum damage mechanics. Then, in [44] and [45], the damage and deformation within a concrete dam due to diffusion of an aging fluid is described through a Timoshenko beam model, and a novel model for cohesive interfaces based on thermodynamic principles and compatible with continuum damage mechanics is introduced. In the last case, the model employs friction that degrades with damage and allows for the description of the opening and reclosing at the interface level, even when permanent relative displacements occur. We remark that microcracks in cement-based materials can be generated by relative motions between cement paste and other aggregates added to the mixture and that these motions could be induced, for example, during the drying or cooling processes. Thus, microcracks can be found in concrete even when no load has been applied [1].

In this paper, we aim to investigate the internal dissipation mechanisms observed in the context of cement-based materials under the hypothesis that at the macroscopic level, no significant phenomena related to damage occur, and hence, the internal dissipation is assumed to rely upon the relative motion in the microcracks. Therefore, a first scalar term describing the average sliding displacement between opposite faces of the microcracks within the material is introduced. This path has been explored in works mentioned before with outstanding results that reveal an agreement between the model and experimental measurements. In particular, the authors in [37–40] introduced a friction force term arising from a mix between a Coulomb-type friction model and a viscous term, due to the different kinds of allowed deformations and associated with the internal dissipation because of the relative motion of opposite faces of microcracks. This approach has extended to other configurations like in [49], where the dissipation properties are analytically and experimentally investigated in the context of Pantographic fabrics (see [50,51] for a comprehensive discussion about Pantographic metamaterials) by means of a second-gradient continuum model enriched with a Dahl-type friction term [52] for the dissipative effects at the interconnecting pivots, and in [53] where the response and effects of friction phenomena between fibers in woven fabric are modeled by a Rayleigh dissipative potential based on a Coulomb-type friction.

Even though in multiple works regarding energy dissipation it can be observed a tendency for introducing a Coulomb-type friction term based on a constitutive relation describing the evolution of the sliding and its coupling [54–58], there exist some efforts to generalize this approach through a second step where an additional kinematical descriptor is introduced, more precisely, a term modeling the relative motion of the microstructure asperities. For instance, in [2], the authors employ an adapted version of the LuGre-type model built upon the Coulomb-type friction force and a description of the "Stribeck effect" for the relative motion of both the faces of the microcracks and the asperities inside them. Following this approach, in the current work where a dynamic point of view is considered, i.e., the friction force evolves in accordance with a differential equation relating different internal variables in the framework of the Timoshenko beam model. More precisely, we consider a solid friction model introduced by P. R. Dahl in [52,59] (Dahl-type friction force) that reproduces a nonlinear elastoplastic behavior where the response is almost linearly elastic for small deformations and plastic for large deformations. In Dahl's formulation, the friction force, henceforth denoted by F, is assumed to depend only on the sliding displacement γ in such a way that $\frac{dF}{d\gamma} > 0$ at all times, even if $\dot{\gamma}$ changes its sign. Additionally, if F_c denotes the magnitude of the Coulomb friction force, then $F \to F_c$ monotonically as long as $\dot{\gamma} > 0$, and $F \to -F_c$ monotonically as long as $\dot{\gamma} < 0$ (see Sect. 2 for more details).

Modeling microcracks' behavior is not an easy task, and from a mechanical point of view, it seems that simplified models are frequently employed to predict phenomena in specific regimes. Moreover, because of the microcracks considered here, in addition to the dissipation of the energy, a nonlinear elastic behavior is expected. This approach arises as an alternative path to describe the internal dissipation experimentally observed and lies in the field of micromorphic continuum models, which are highly suitable when describing complex phenomena similar to those explained by higher gradient models [60–64].

This work is organized as follows. In Sect. 2, we provide a more detailed discussion about our approach and introduce the enhanced micromorphic beam model. Later, in Sect. 3, numerical results and examples are given to corroborate that a proper adjustment to the parameters associated with the evolution of the friction term could allow for the model to explain mechanical responses with different ranges of energy dissipation. Finally, concluding remarks about the results are reported in Sect. 4.

2 Enhanced beam model

In this section, we introduce the framework of our study and the improved 1D micromorphic continuum beam model for cementitious metamaterials [65–73]. The exploited approach is built upon an extended version of the Principle of Virtual Work to take into account the internal elastic contributions in the material, the external contributions due to three-point flexural tests, which is carried out through cyclic loads, as well as a dissipative contribution due to the presence of microcracks. First, let us emphasize that here we are mainly interested in the effect of this last contribution, i.e., in studying dissipation of mechanical energy due to micro–macro interactions and under the assumption of a small deformation regime (no damage growth under fatigue tests).

Thus, in the light of the previous premise, let us consider a planar xy reference framework and a simple 1D characterization of the beam such that, in the reference configuration, it is described by a curve of length L lying on the x-axis, and in the current configuration it is described by a map $\mathcal{X}$ that depends on the abscissa X (x-axis coordinate). Here, we consider the effects of bending and shear distortions on the beam and neglect the effects of stretching. In addition to that, we improve the classical Timoshenko beam model by including an additional scalar kinematical descriptor which accounts for the relative micro-sliding accumulation within the material due to the sliding between opposite faces of the microcracks in the beam. For that purpose, we assume that the microcracks are randomly distributed along the beam, and hence, no further consideration about their orientation is required.

Following on from those considerations, the map $\mathcal{X}(X)$ describing the current configuration consists of the following kinematical descriptors: the transverse displacement of the beam axis material particles in the y direction, denoted by $v(X)$, the angle of the cross-section $\varphi(X)$, and the overall relative microsliding $\gamma(X)$. Here, the model aims to consider a mechanical energy interchange between both bending and shear distortion with the sliding occurring at the micro level (microcracks), a storage of mechanical energy because of the asperities inside the faces of the microcracks which are deformed when they are in contact, and a subsequent dissipation of the energy that follows from the interaction between the bending (change of orientation of the cross-sections) and the microcracks. This last interaction potentially induces compression in some parts of the cross-section that is assumed to activate the dissipation mechanism. More precisely, we assume that there is a compression-caused effect along cross-sections, which consists of a closing of the microcracks so that the opposite faces are forced to get in contact. It is worth mentioning at this point that because of our assumption about the stretching contribution, uniform compression in the x-axial direction is not considered here. Nevertheless, an analysis including this last contribution may be carry on by following the ideas in [42].

Next, we introduce an extension of the Principle of Virtual Work (PVW) that allows us to include any virtual work dissipated in a system (see, for example, the discussion in [2,41]). This extended PVW asserts that, at equilibrium, the virtual work exerted by the external forces applied to the beam, $\delta\mathcal{W}^{ext}$, must balance both the virtual work done by the elastic inner forces, $\delta\mathcal{W}^{el}$, and the virtual work dissipated $\delta\mathcal{D}$. Thus, at the equilibrium configuration of the beam model, we have that

$$\delta\mathcal{W}^{ext} + \delta\mathcal{W}^{el} + \delta\mathcal{D} = 0. \tag{1}$$

Henceforth, for the sake of simplicity, let us assume that our kinematical descriptors lie in the proper space of functions in such a way that the following expression is a viable internal elastic energy $\mathcal{E}^{el} = -\mathcal{W}^{el}$:

$$\begin{aligned}\mathcal{E}^{el} = &\int_0^L \frac{1}{2}K_b(\varphi')^2 dX + \int_0^L \frac{1}{2}K_s(v'-\varphi)^2 dX + \int_0^L \frac{1}{2}K_2\gamma^2 dX \\ &+ \int_0^L \frac{1}{4}K_4\gamma^4 dX - \int_0^L \alpha_b\varphi'\gamma dX - \int_0^L \alpha_s(v'-\varphi)\gamma dX,\end{aligned} \tag{2}$$

where K_b, K_s, K_2 an K_4 denote material parameters corresponding to stiffness coefficients for the bending, the shear distortion, and the nonlinear internal restoring force induced at the microcracks level, and α_b, α_s denote coupling coefficients between the macro-descriptors (macroscopic bending and macroscopic shear distortion) and the micro-descriptor (microcrack sliding).

We remark that tests carried out with cyclic loads in this context (see, for instance, [2]) reveal that even for small strains, the stress–strain constitutive equation seems to be nonlinear. Thus, it is possible to assume that this nonlinear behavior, whenever a cyclic load is applied, is induced by internal factors like microcracks and that it poses an elastic nature. Here, we consider an elastic contribution in γ given by a fourth order and even polynomial that vanishes at $\gamma \equiv 0$. This postulate follows from the geometry of the microcracks and the interaction of the faces due to bending (the asperities in the opposite faces of microcracks can bend and

store elastic energy), and it is motivated by experimental observations for cement-based materials [74]. It is worth emphasizing once again that we remain in the small deflection regime and that our assumptions in this regard are motivated by the fact that, during the micro–macro interactions, small contributions, likely arising due to higher order terms as the one associated with K_4, should be taken into account. We also observe that the proposed elastic energy is non-objective for large deformations. Therefore, the expression (2) should be appropriately modified for such a regime.

Moreover, due to the coupling terms in the internal elastic energy (2), sufficient conditions over the control parameters are required in order to have a valid expression for the energy. In fact, if $K_4 > 0$, then the expression obtained collecting the remaining terms in (2) arises from a quadratic form which is positive definite whenever the next conditions hold nontrivially: $i)$ $K_b > 0$; $ii)$ $K_s > 0$ and $iii)$ $K_b K_s K_2 > \alpha_s^2 K_b + \alpha_b^2 K_s$.

On the other hand, it is worth noting that in the study of the friction phenomena in solids, we can distinguish between static and dynamic friction models (see for instance [75,76]). In the first case, a constitutive equation describes the relation between the friction force and a micro/macro level variable, and in the second case, the friction force evolves in accordance with a differential equation relating different internal variables [75,77–79]. Here, we proposed a model based on the ideas in works like [41,42], nevertheless, contrary to the static analysis reported there, where a Coulomb-type friction force model was considered, in this work, a dissipation micromechanism given by a Dahl-type friction force is introduced throughout the faces of the microcracks in the material. This implies a new contribution is taken into account because of the coupling between the evolution of γ and the Dahl-type friction force.

Additionally, in the modeling of internal dissipation in solids, we can distinguish between dissipated energy associated with damage and plastic phenomena (which could increase the density of microcracks or enlarge those already existing), and the dissipated energy associated with the friction phenomena that induces a reversible internal motion (no damage occur at the macroscopic level). Some works in this line are [80,81], where the number of microcracks and their mechanical and geometrical properties are invariant when dynamic loads are applied.

Now, with a view to considering mechanical energy dissipation, we introduce a mechanism of solid friction [59], more precisely, a shear stress between the contact area of opposite faces of a microcrack that is induced by dry sliding friction. In general, solid friction has been considered a quasi-static phenomenon mainly caused by contact stress and a subsequent process of creation and rupture of bonds between the surface elements of the material bodies in contact (quasi-static properties of materials). This last process is entirely dynamic and can be described by the motion of the bodies due to external or inertial forces [59]. In this way, the friction function F, considered as a function of the relative displacement γ (in our case, the overall relative micro-sliding), can evolve in time. Thus, the time rate of change of the friction function introduces a constitutive equation for F such that

$$\dot{F}(\gamma) = \frac{dF}{d\gamma}(\gamma)\dot{\gamma}. \tag{3}$$

In fact, as in many problems in engineering, we can expect hysteretic behavior of the friction force for this case, i.e., a lagging effect from the change of the friction in response to a reversing in the direction of the motion. This behavior is resembled by the assumption that F depends only on γ [52], and it can be generated by a friction slope of the form

$$\frac{dF}{d\gamma}(\gamma) = \sigma_0 \left| 1 - \frac{F(\gamma)}{F_c}\,\mathrm{sgn}(\dot{\gamma}) \right|^{\beta} \mathrm{sgn}\left(1 - \frac{F(\gamma)}{F_c}\,\mathrm{sgn}(\dot{\gamma}) \right), \tag{4}$$

where β and σ_0 are parameters associated with the basic shape of the friction law at hand and the rest stiffness at $F = 0$ (slope of the stress/force–deflection curve), respectively. In fact, the parameter β induces a type of friction force for which the material is ductile whenever $\beta \geq 1$ and brittle whenever $0 \leq \beta < 1$. In practice, these parameters should be properly estimated by studying the stress/force–deflection test data.

Dahl's friction model is based on a Coulomb-type friction mechanism, where the last one can be thought of as a yield force for which the "unloading" path, in a friction force–deflection context (see [59]), exhibits plastic behavior. More precisely, the friction slope (4) shows that for small displacements, the friction force F, seems to be linear and elastic (in general, it resembles a nonlinear but soft spring), and after a certain threshold for the displacement, F is required to change its sign to reach small displacements again, this is the plastic nature for large deflections.

At this point, we remark that for this kind of dynamic friction model, the dissipative cycles do not depend on the frequency of the applied load [2]. Nevertheless, it is worth noting, as it was done in [59], that there

is a stochastic nature behind the friction curve caused by the random distribution of the contact area, matter that we have overcome by defining γ as the overall sliding of the opposite faces of a uniform distribution of penny-shaped microcracks.

Hence, we model the dissipated work in terms of the sliding γ by considering the Dahl-type friction model with a friction force per unit line of magnitude $\mathcal{F}(\gamma)$ that evolves in time in accordance with (3)-(4), and such that

$$\delta\mathcal{D} = -\int_0^L \mathcal{F}(\gamma)\delta\gamma dX, \tag{5}$$

We remark that in the overall friction term considered in (5), there exists an implicit coupling between the bending (a change in the cross-section orientation) and a subsequent compression that potentially closes microcracks along some part of the cross-section. In other words, the dissipative effect of the sliding is activated when compression pushes the microcrack faces together.

Now, because of the modeling approach followed in this work and the expression for the elastic energy (2), it is straightforward to conclude that the possible external forces, namely, vertical direction forces on the bulk, b_y, concentrated forces in the vertical direction, $\bar{b}$, torques per unit line, μ, and torques acting on edges, $\bar{\mu}$, induce the following virtual work contribution $\delta\mathcal{W}^{ext}$

$$\delta\mathcal{W}^{ext} = \int_0^L \mu(X)\delta\varphi dX + \int_0^L b_y(X)\delta v dX + \bar{\mu}(X)\delta\varphi|_0^L + \bar{b}(X)\delta v|_0^L. \tag{6}$$

Moreover, it is not difficult to check through a direct computation and integrating by parts that the first variation of the internal elastic contribution is given by

$$\begin{aligned}\delta\mathcal{E}^{el} = &-\int_0^L [(K_b\varphi')' + K_s(v'-\varphi) - (\alpha_b\gamma)' - \alpha_s\gamma]\delta\varphi dX\\ &-\int_0^L [K_s(v'-\varphi)' - (\alpha_s\gamma)']\delta v dX\\ &+\int_0^L [K_2\gamma + K_4\gamma^3 - \alpha_s\varphi' - \alpha_s(v'-\varphi)]\delta\gamma dX\\ &+(K_b\varphi - \alpha_b\gamma)\delta\varphi|_0^L + (K_s(v'-\varphi) - \alpha_s\gamma)\delta v|_0^L.\end{aligned} \tag{7}$$

In this sense, we can define the bending moment M, the shear force T and Γ as follows:

$$M{:=}K_b\varphi' - \alpha_b\gamma, \quad , T{:=}K_s(v'-\varphi) - \alpha_s\gamma, \quad \Gamma{:=}K_2\gamma + K_4\gamma^3 - \alpha_b\varphi' - \alpha_s(v'-\varphi),$$

so that the PVW implies that the bulk equations, along with the corresponding boundary conditions for the system considered here, are given by

$$\begin{cases} -(M'+T) - \mu = 0,\\ -T' - b_y = 0,\\ \Gamma + \mathcal{F}(\gamma) = 0,\\ (M-\bar{\mu})|_{0,L} = 0,\\ (T-\bar{b})|_{0,L} = 0. \end{cases} \tag{8}$$

It is worth noting that, as mentioned in [41,42], the PVW employed to deduce the boundary value problem describing the equilibrium of the beam does not provide nor impose any boundary condition over the bulk for γ.

Table 1 Values of the parameters for the numerical simulations

Parameters	Values
d	150.0 mm
L	600.0 mm
ℓ	450.0 mm
K_b	1.330×10^6 N m^2
K_s	2.560×10^8 N
K_2	7.500×10^8 N m^{-2}
K_4	1.000×10^8 N/m^4
α_b	8.050×10^6 N
α_s	0.5000×10^7 N m^{-1}

3 Numerical simulations and results

In this section, we provide numerical evidence about the dissipation mechanism and the mechanical properties of cement-based metamaterials described by the improved beam model introduced in the previous section. For that purpose, we consider a three-point bending test (3PB) and a concrete specimen as in [41]. Thus, the study consists of a sample with the geometry of a parallelepiped of dimensions $d \times d \times L$, which is placed over two fixed supports located at a distance ℓ from each other, and a cyclic load that is applied on the top center of the sample. It is worth recalling that here, we neglect uniform tension/compression of the beam in the x-axis direction, but we are interested in bending deformations of the specimen along with the subsequent shear distortions perceived when the concentrated cyclic load is applied.

Table 1 contains the values of geometry parameters, material parameters and coupling coefficients employed in the numerical simulations. We point out that sufficient conditions $i) - iii)$ given in page 7 for the positive definiteness of the postulated elastic energy are verified for these values of the parameters. More precisely, we assume a material with a Young modulus $Y_0 = 31.450 \times 10^9$Pa and a Poisson ration $\nu = 015$. Following on from this assumption, we can compute the stiffness coefficients for both the bending and shear distortion in a classical way by using the second moment of area of the beam cross-section J and the shear modulus $G_0 = {}^{Y_0}/_{2(1+\nu)}$, so that $K_b = Y_0 J$ and $K_s = {}^5/_6 G_0 d^2$. The remaining coefficients K_2 and K_4, associated with the internal restoring force due to the deformation of microcracks' asperities, and the coupling coefficients α_b and α_s, are estimated through a delicate adjustment to produce the desired response. Furthermore, the cyclic load leading to the external contribution in our system is assumed to be applied in the transverse direction to the beam axis, over the middle point of this last one, and with a time dependent magnitude given by

$$f_y(t) = \frac{A_0}{2}(1 - \cos(2\pi\omega t)), \tag{9}$$

where A_0=4.500 kN is the maximum load and $\omega = 10.00$ Hz is the frequency.

Henceforth, with a view to understanding the effects of a long-term cyclic load on our descriptors, we consider a 10-cycle test, which does not deviate from what it is reported to be in agreement with a seismic activity [39]. Additionally, as mentioned in [39], the maximum load has to be chosen in such a way that an unsafe level of stress in the material is avoided, whilst the minimum level of compressible stress is enough to guarantee that some interactions between opposite faces of microcracks occur.

The numerical results in this section are obtained by means of the commercial software COMSOL Multiphysics®, which allows us to employ the improved model proposed here in its extended PVW formulation (1) with the Weak Form PDE module. Since only first order derivatives of the kinematical descriptors are considered, our micromorphic model belongs to the class of first gradient continuum models, and thus, standard Lagrangian quadratic polynomials can be utilized as shape functions for the Finite Element interpolation (for more efficient numerical methods, the reader can refer to [82–87]). At this point, it is worth addressing that, in general, identifying the proper set of parameters that characterizes this kind of model is not an easy problem because of the complex mechanical responses that can eventually take place. Besides, when considering multi-scale phenomena such as those in the present work, a delicate micro–macro identification process is required to achieve a satisfactory correspondence between experimental data and numerical simulations. For instance, in [39], a parameter identification for a micromorphic model describing the effect of micro-particle addition on the internal dissipation in concrete is performed to show that the model is suitable to forecast dissipative behavior. This is a cornerstone matter because, in practice, the additives/fillers could either decrease or

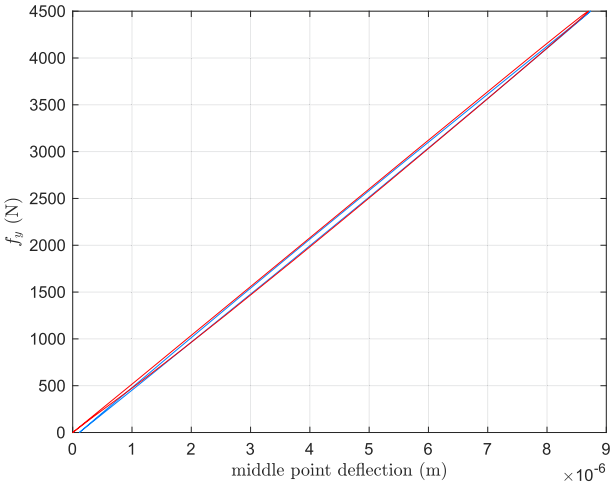


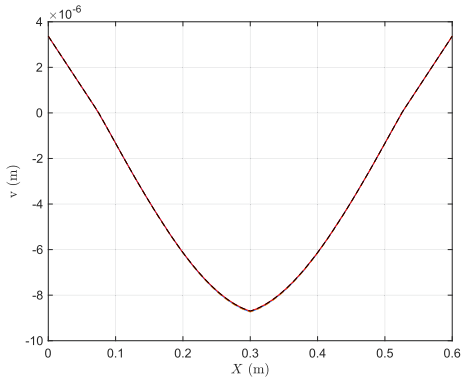
Fig. 1 Comparison between dissipative cycles obtained for two improved Timoshenko beam models, one with a Dahl-type friction force (blue) and the other with a Coulomb-type friction term (red), for the loading and unloading during the 10th-cycle for the 3PB test (color figure online)

increase the internal friction and even degrade the mechanical strength (see also discussions in [39,88]), and therefore, an optimal percentage of their amount is required. In this context, there exist different techniques, such as digital image correlation (DIC), energy methods, and neural networks that can be employed when studying complex generalized materials. To see different applications of these techniques in recent works, the reader is referred to [88–94].

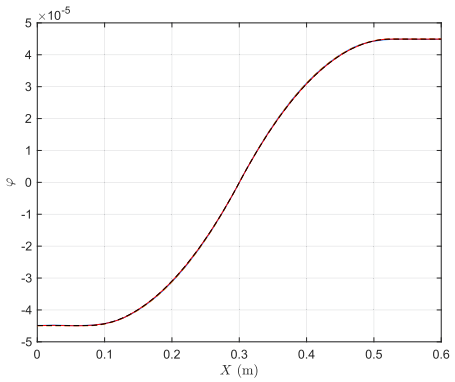
Figure 1 shows a comparison between dissipative cycles obtained under a 3PB test for the improved Timoshenko beam model with the Dahl-like friction term here considered (blue) and a static friction term based on a smoother version of the Coulomb model (red) [37]. More precisely, in the first case, a friction term per unit line of magnitude $\mathcal{F}$ based on a Dahl-type friction force F verifying the evolution law (3)-(4) is employed with $\beta = 6.689 \times 10^5$ and $\sigma_0 = 4.691 \times 10^{11}\,\mathrm{N\,m^{-1}}$. The exponent β is selected from the range of values for which the model describes solid friction in ductile materials since asperities in the microcracks can be deformed without damage, at least in the small deflection regime. In the second case, a friction force term per unit line of magnitude $\zeta|\varphi'|\tanh(\eta\dot{\gamma})$ is employed for $\zeta = 2.950 \times 10^8\mathrm{N}$ and $\eta = 225.0\mathrm{s\,m^{-1}}$. This last concept of friction force has been recently included in works like [41,42] to accurately describe the experimental observations of a beam made of concrete in the context of energy dissipation, and it represents a Coulomb-type viscous friction that depends on the sliding velocity, $\dot{\gamma}$, with a friction coefficient (dissipation) due to microscopic sliding displacements induced by bending deformations, ζ, and the characteristic slope of the sliding velocity, η (inverse of the reference velocity, employed to modulate the extension of the viscous range whenever tanh is introduced).

On the other hand, the dissipated energy associated with the numerical results can be measured, for instance, by computing the areas of the corresponding dissipative cycles that originate from each branch of loading and unloading. Here, the areas of dissipative cycles depicted in Fig. 1 are numerically estimated by using the trapezoidal rule so that for the improved Timoshenko beam model with a dynamic friction term, we obtain an approximate dissipated energy of 4.170×10^{-4} J whilst for the model with a static Coulomb-type friction term we obtain an approximate dissipated energy of 6.183×10^{-4} J. We emphasize that a proper adjustment to the exponent β and the coefficient σ_0 can be done to achieve higher dissipated energy, possibly greater than the one illustrated here (Fig. 8, presented at the end of this section, illustrates how the dissipated energy changes when β is small and big enough).

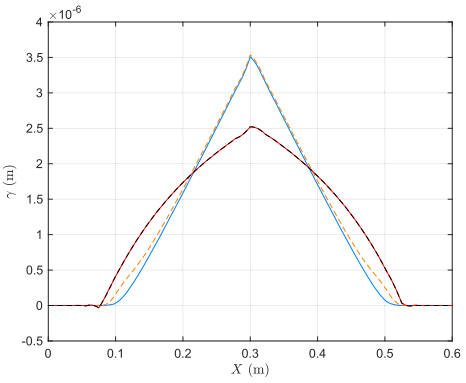
A careful inspection of Fig. 1 reveals that there is a slight displacement of the starting point (strain) of the cycle in blue with respect to the starting point of the cycle in red. This discrepancy is explained by the long-term cyclic load that was considered for the simulations. In fact, for the initial cycles, we observed a relatively small discrepancy between the starting point when loading and the ending point when unloading for the dynamic friction term, and as the test progressed, this gap was considerably mitigated. Moreover, as mentioned in [39], the behavior of the cycles is convergent towards a conservative limit cycle, and thus, we expect our numerical simulations to be reliable when compared with experimental measurements.



(a) Comparison between the vertical displacements.



(b) Comparison between the cross-section rotations.



(c) Comparison between inner relative sliding displacements.

Fig. 2 Comparison between the descriptors of the improved Timoshenko-like beam models employing an internal dynamic friction term (Dahl-type friction; solid blue and dashed orange) and the Coulomb-type friction (solid red and dashed black), for two instants of maximum applied load in the 3PB test of 10-cycles and load magnitude f_y, at the middle point of the sample (color figure online)

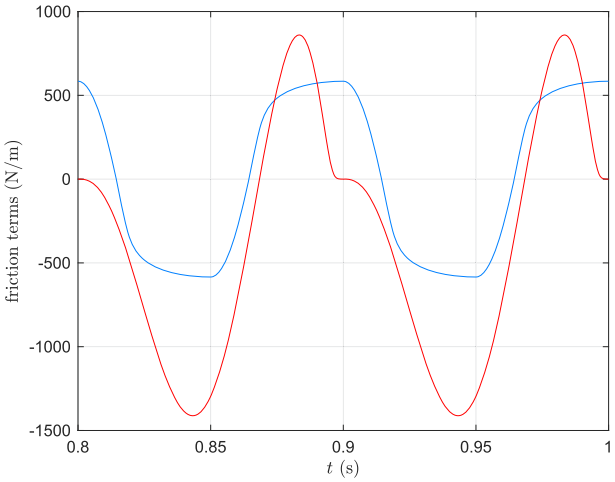


Fig. 3 Comparison between the friction forces per unit line at the middle point of the sample based on Dahl's model (blue) and Coulomb's model (red) during the last two cycles (color figure online)

Now, regarding the kinematical descriptors taken into account in our formulation, Fig. 2 shows a comparison between the vertical displacements 2a, the orientations of the cross-sections 2b, and the relative sliding displacement 2c, at the maximum applied load of magnitude f_y for the model proposed in the current work (solid blue line at $t = 0.05$s; dashed orange line at $t = 0.95$s), and for the model with a Coulomb-type friction force (solid red line at $t = 0.05$s; dashed black line at $t = 0.95$s). A thorough observation reveals that, for the values of the parameters considered in this case, no major deviation regarding the shape of both vertical displacements and orientations of the cross-sections is perceived. Hence, besides small quantitative differences, the mechanical responses at the macroscopic level provided by the dynamic and static approaches are in agreement. The response at the microscopic level is slightly different between the two models, where a greater relative sliding displacement γ at the middle point of the beam is perceived under the same conditions of loading for the model introduced in this work.

A comparison between the evolution in time of the friction forces per unit line is presented in Fig. 3. More precisely, the curve in blue portrays the Dahl-type friction force and the curve in red portrays the Coulomb-type friction force, in both cases for the last two cycles of the applied load. Figure 4 shows the expected hysteretic behavior of the magnitude $\mathcal{F}$ (hysteretic damping) that evolves in accordance with (3)-(4). It is worth mentioning at this point that, even though the dynamic friction in blue approaches the static one in red near the times for which the maximum load is applied (see Fig. 3), the overall behavior is rather different. This last remark is supported by the nature of the friction terms at hand, i.e., in addition to the explicit evolution in time of the dynamic term here introduced, we have a different measurement of similar phenomena since for the dynamic term it is assumed a dependence only on the relative displacement instead of the corresponding velocity.

Figure 5 shows the evolution in time for the complete 3PB test of the relative sliding γ at the middle point for both models, one with the dynamic friction term (blue) and the other one with the static friction term (red). The sliding responses are quite similar regarding their amplitude; nevertheless, it seems that the sliding corresponding to the dynamic term is shifted some tenths of micrometers over the common baseline from which both curves start.

Figure 6 shows a comparison between shear forces and between bending moments at the maximum applied load in the last cycle. More precisely, the shear stresses and bending moments are portrayed, respectively, in Fig. 6a and b, for the improved Timoshenko-beam model here considered (solid blue) and the model with a static friction term, both at time $t = 0.95$s. A careful inspection reveals that no significant changes in the behavior of the shear force T and the bending moment M occur when the dynamic friction term and the static friction term are considered. This observation is in agreement with the behavior described in [41] where it is stated that the stresses are not significantly influenced by the mechanics at the microcracks level.

Figure 7 shows the dissipated power given by the model considered in this work. Figure 7a illustrates the evolution of the dissipated power throughout the complete 3PB test, whilst Fig. 7b shows a close-up of the same quantity in an interval of time where it may reach positive values. In fact, a visual inspection of Fig. 7a

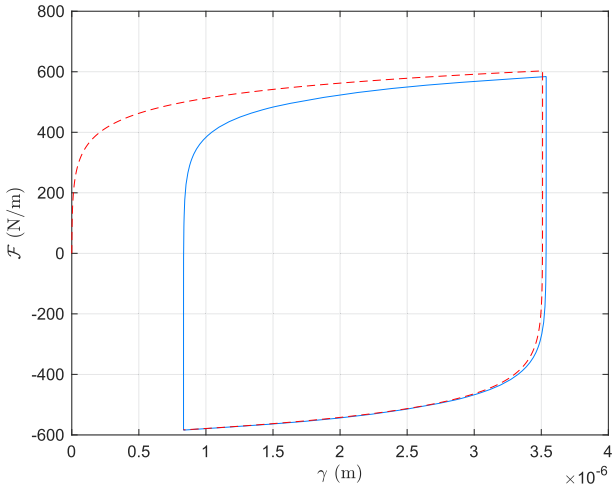


Fig. 4 Dahl-type friction term magnitude $\mathcal{F}$ at the middle point of the sample for the first (red) and last (blue) cycles in the 3PB test (color figure online)

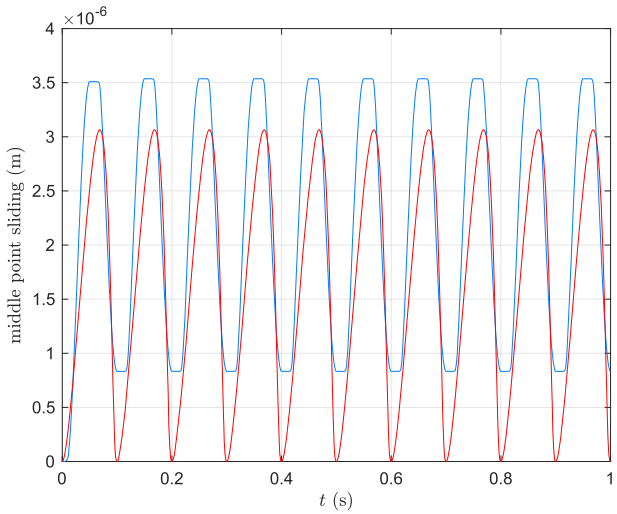


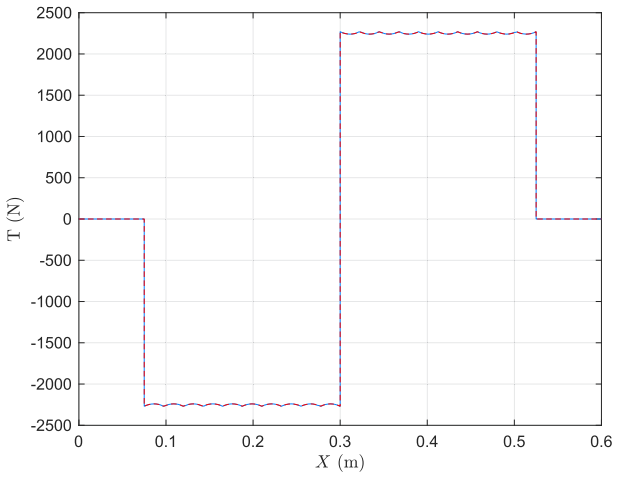
Fig. 5 Evolution in time of the relative sliding γ at the middle point of the sample for the 3PB test

reveals that the overall dissipated power leads to a passive operator ensuring dissipation of the energy for a system with a dynamic friction term (see [2] and the references therein for more details).

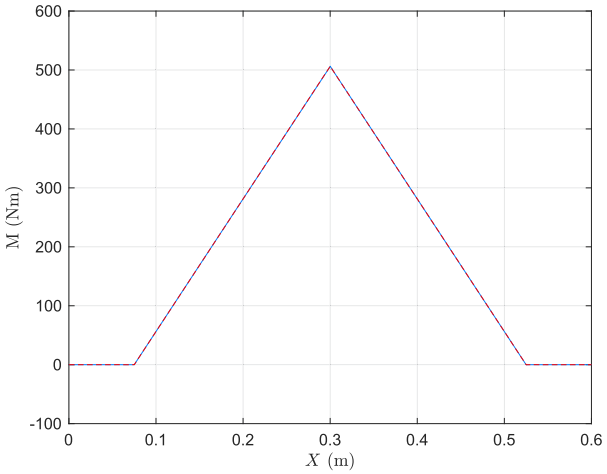
Some dissipative cycles obtained under a 3PB test using different values of the control parameters σ_0 and β are provided in Fig. 8. The cycle in Fig. 8a was obtained for $\sigma_0 = 1.425 \times 10^9\,\mathrm{N\,m^{-1}}$ and $\beta = 25$, and the corresponding dissipated energy in this case is 2.867×10^{-7}J: a rather small variation of the macro-descriptors υ (concentrated around the middle point) and φ (near the boundary of the sample) is perceived while the amplitude of the micro-descriptor γ decreases and remains always under the response provided by the model employing Coulomb-type friction. A higher value of the dissipated energy can be obtained if β is increased. Figure 8b shows the dissipative cycle for $\sigma_0 = 8.867 \times 10^{10}\,\mathrm{N\,m^{-1}}$ and $\beta = 5.500 \times 10^5$: in this case, the dissipated energy is 4.090×10^{-4}J.

4 Concluding remarks

In this work, we introduced a Timoshenko-like beam model employing a dynamic friction term with a view to improving the understanding of energy dissipation in the context of concrete-based materials and metamaterials. Our approach assumes that microcracks are inhere in the material's inner structure, leading to both an elastic mechanical contribution and a dissipation micromechanism under the effect of cyclic loads applied on the



(a) Shear forces T.

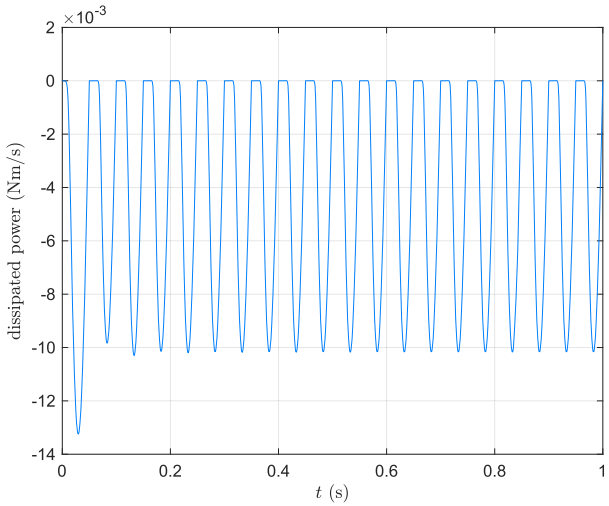


(b) Bending moments M.

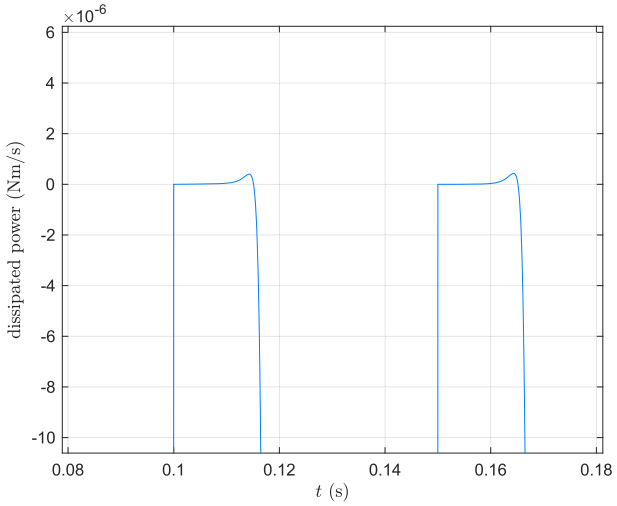
Fig. 6 Comparison between internal stresses at the maximum applied load for the last cycle employing Dahl's model (solid blue) and Coulomb's model (dashed red) (3PB) (color figure online)

middle point of the beam. The novel contribution of this paper consists in the fact that the dynamic friction term is built upon the quasi-static description proposed by P. R. Dahl for dry friction in solids [59], in our case, a friction force arising due to some (partial) compression in some part of the cross-section caused by a bending deformation as the flexural test is carried out. This compression leads to the closing of the microcracks so that the opposite faces are forced to get in contact from where a sliding displacement between opposite faces of a microcrack occurs. Thus, the friction term considered here evolves in time and describes an elastoplastic response enriching the scope of phenomena that can be perceived in the system through a 1D micromorphic continuum model. In fact, some characteristics of a plastic behavior are illustrated numerically in the simulations reported in this work, whilst those descriptors not directly affected by the inner friction contribution seem to concur with predictions previously reported in works like [41].

The model and the analysis provided in this paper could be of interest, for example, to researchers in the field of dissipation mechanisms for cementitious materials since a suitable adjustment to the control parameters, in particular those associated with the evolution law of the friction force (3)-(4), namely σ_0 and β, could provide a grasp in quantifying, after a careful identification process, the amount of aggregates/fillers required in the mixture to obtain a material with the desired mechanical features. Thus, the approach in this work could be



(a) Dissipated power.

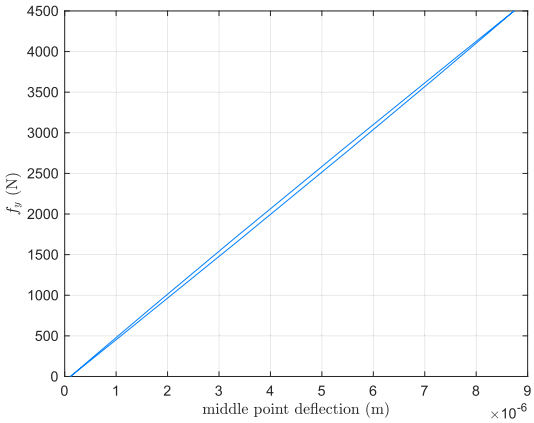


(b) Close-up of the dissipated power

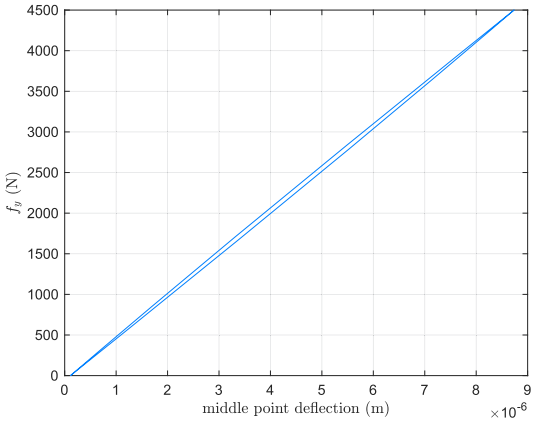
Fig. 7 Dissipated power for the complete 3PB test

potentially considered as a simplified tool in the first stage of assessing major aspects like energy dissipation and the mechanical response reliability for earthquake-proof concrete. Nevertheless, we note that, in order to provide insights leading to further levels of assessment, an experimental campaign to validate the scope of the proposed model is required. In fact, similar experimental campaigns were reported in works like [38,39]. Perhaps the approach in the aforementioned papers could lead to devising an experimental testing procedure, considering different additives, to assess the connection between friction and the mechanical properties of cementitious materials in our context.

We emphasize that some efforts to accomplish the modeling of advanced features and phenomena in concrete-like metamaterials can be made. For instance, in [41], the authors suggest a different approach where the first scalar descriptor γ could be instead considered as a microstructural parameter so that a dependence on γ' of the energy is introduced. Furthermore, in recent works like [95], [96] and [97], the authors consider the underlying connection between Mohr's circles and the definition of Cauchy stress, the strain problem associated with the inclusion of a particular incompressible liquid in an infinite anisotropic elastic matrix subjected to uniform loading at infinite, and the possibility of expressing a three-dimension state of stress by



(a) Dissipative cycle obtained for $\sigma_0 = 1.425 \times 10^9\,\mathrm{N\,m^{-1}}$ and $\beta = 25$.



(b) Dissipative cycle obtained for $\sigma_0 = 8.867 \times 10^{10}\,\mathrm{N\,m^{-1}}$ and $\beta = 5.500 \times 10^5$.

Fig. 8 Dissipative cycles for the improved Timoshenko beam model with a Dahl-type friction term for different values of the parameters σ_0 and β

means of a single scalar function, respectively. Perhaps a suitable adaptation of the treatments and notions in the aforementioned works could allow us to, for example, better characterize the stress in cement-based materials, leading to significant improvements in determining if microstructures, such as the microcracks, are open, to describe phenomena like water inclusion in concrete-like metamaterials, and to obtain particular solutions of the governing equations in this regard by considering a lower dimension approach. These results open the gates to further insights into concrete-like materials and may be considered to improve our model in future works.

Furthermore, dissipation is always connected with the transformation of mechanical energy into heat. In specific applications, an increase in temperature can significantly affect the mechanical response of the material. Therefore, introducing thermal effects will contribute to developing a comprehensive topic formulation (see for an efficient formulation of the thermoelastic problem [98,99]).

Funding None.

References

1. Monteiro, P., Mehta, P.: Concrete: Microstructure, Properties and Materials (2006)
2. Giorgio, I., Scerrato, D.: Multi-scale concrete model with rate-dependent internal friction. Eur. J. Environ. Civ. Eng. **21**(7–8), 821–839 (2016). https://doi.org/10.1080/19648189.2016.1144539
3. Misra, A.: Stabilization characteristics of clays using class C fly ash. Transp. Res. Rec. J. Transp. Res. Board **1611**(1), 46–54 (1998). https://doi.org/10.3141/1611-06
4. Contrafatto, L., Lazzaro Danzuso, C., Gazzo, S., Greco, L.: Physical, mechanical and thermal properties of lightweight insulating mortar with recycled Etna volcanic aggregates. Constr. Build. Mater. **240**, 117917 (2020). https://doi.org/10.1016/j.conbuildmat.2019.117917
5. Goel, G., Sachdeva, P., Chaudhary, A.K., Singh, Y.: The use of nanomaterials in concrete: a review. Mater. Today Proc. **69**, 365–371 (2022). https://doi.org/10.1016/j.matpr.2022.09.051
6. P. P., A., Nayak, D.K., Sangoju, B., Kumar, R., Kumar, V.: Effect of nano-silica in concrete; a review. Constr. Build. Mater. **278**, 122347 (2021). https://doi.org/10.1016/j.conbuildmat.2021.122347
7. Alasfar, R.H., Ahzi, S., Barth, N., Kochkodan, V., Koç, M.: Modeling and experimental validation of the elastic modulus of polysulfone membranes reinforced with cellulose nanofibers. Math. Mech. Complex Syst. **10**(4), 413–429 (2023). https://doi.org/10.2140/memocs.2022.10.413
8. De Belie, N., Gruyaert, E., Al-Tabbaa, A., Antonaci, P., Baera, C., Bajare, D., Darquennes, A., Davies, R., Ferrara, L., Jefferson, T., Litina, C., Miljevic, B., Otlewska, A., Ranogajec, J., Roig-Flores, M., Paine, K., Lukowski, P., Serna, P., Tulliani, J., Vucetic, S., Wang, J., Jonkers, H.M.: A review of self-healing concrete for damage management of structures. Adv. Mater. Interfaces (2018). https://doi.org/10.1002/admi.201800074
9. Rajczakowska, M., Habermehl-Cwirzen, K., Hedlund, H., Cwirzen, A.: Autogenous self-healing: a better solution for concrete. J. Mater. Civ. Eng. (2019). https://doi.org/10.1061/(asce)mt.1943-5533.0002764
10. Espitia Nery, M.E., Corredor Pulido, D.E., Castaño Oliveros, P.A., Rodriguez Medina, J.A., Ordoñez Bello, Q.Y., Perez Fuentes, M.S.: Mechanisms of encapsulation of bacteria in self-healing concrete: review. DYNA **86**(210), 17–22 (2019). https://doi.org/10.15446/dyna.v86n210.75343
11. Giorgio, I., Spagnuolo, M., Andreaus, U., Scerrato, D., Bersani, A.M.: In-depth gaze at the astonishing mechanical behavior of bone: a review for designing bio-inspired hierarchical metamaterials. Math. Mech. Solids **26**(7), 1074–1103 (2021). https://doi.org/10.1177/10812865209785
12. Scerrato, D., Bersani, A.M., Giorgio, I.: Bio-inspired design of a porous resorbable scaffold for bone reconstruction: a preliminary study. Biomimetics **6**(1), 18 (2021). https://doi.org/10.3390/biomimetics6010018
13. Xue, J., Briseghella, B., Huang, F., Nuti, C., Tabatabai, H., Chen, B.: Review of ultra-high performance concrete and its application in bridge engineering. Constr. Build. Mater. **260**, 119844 (2020). https://doi.org/10.1016/j.conbuildmat.2020.119844
14. Turco, E., Golaszewski, M., Giorgio, I., D'Annibale, F.: Pantographic lattices with non-orthogonal fibres: experiments and their numerical simulations. Compos. Part B Eng. **118**, 1–14 (2017). https://doi.org/10.1016/j.compositesb.2017.02.039
15. Ciallella, A., D'Annibale, F., Del Vescovo, D., Giorgio, I.: Deformation patterns in a second-gradient lattice annular plate composed of "spira mirabilis" fibers. Contin. Mech. Thermodyn. **35**(4), 1561–1580 (2023). https://doi.org/10.1007/s00161-022-01169-6
16. Eremeyev, V.A., Turco, E.: Enriched buckling for beam-lattice metamaterials. Mech. Res. Commun. **103**, 103458 (2020). https://doi.org/10.1016/j.mechrescom.2019.103458
17. Dobiszewska, M., Beycioğlu, A.: Physical properties and microstructure of concrete with waste basalt powder addition. Materials **13**(16), 3503 (2020). https://doi.org/10.3390/ma13163503
18. Sucharda, O., Marcalikova, Z., Gandel, R.: Microstructure, shrinkage, and mechanical properties of concrete with fibers and experiments of reinforced concrete beams without shear reinforcement. Materials **15**(16), 5707 (2022). https://doi.org/10.3390/ma15165707
19. Xu, F., Li, Z., Li, T., Wang, S.: The mechanical properties and microstructure of tailing recycled aggregate concrete. Materials **17**(5), 1058 (2024). https://doi.org/10.3390/ma17051058
20. Ahmad Wani, T., Ganesh, S.: Study on fresh properties, mechanical properties and microstructure behavior of fiber reinforced self compacting concrete: A review. Mater. Today Proc. **62**, 6663–6670 (2022). https://doi.org/10.1016/j.matpr.2022.04.666
21. Guo, N., Guo, J.: Mechanical properties and crack detection method of nano concrete. Int. J. Microstruct. Mater. Prop. **16**(1), 90 (2022). https://doi.org/10.1504/ijmmp.2022.123331
22. Bersani, A.M., Caressa, P.: Lagrangian descriptions of dissipative systems: a review. Math. Mech. Solids **26**(6), 785–803 (2021). https://doi.org/10.1177/1081286520971
23. Bersani, A.M., Caressa, P., dell'Isola, F.: Approximation of dissipative systems by elastic chains: numerical evidence. Math. Mech. Solids **28**(2), 501–520 (2023). https://doi.org/10.1177/10812865221081851
24. Bersani, A.M., Caressa, P., Ciallella, A.: Numerical evidence for the approximation of dissipative systems by gyroscopically coupled oscillator chains. Math. Mech. Complex Syst. **10**(3), 265–278 (2022). https://doi.org/10.2140/memocs.2022.10.265
25. Dell'Isola, F., Lekszycki, T., Pawlikowski, M., Grygoruk, R., Greco, L.: Designing a light fabric metamaterial being highly macroscopically tough under directional extension: first experimental evidence. Zeitschrift für angewandte Mathematik und Physik **66**, 3473–3498 (2015). https://doi.org/10.1007/s00033-015-0556-4
26. Barchiesi, E., dell'Isola, F., Hild, F.: On the validation of homogenized modeling for bi-pantographic metamaterials via digital image correlation. Int. J. Solids Struct. **208**, 49–62 (2021). https://doi.org/10.1016/j.ijsolstr.2020.09.036
27. Yildizdag, M.E., Tran, C.A., Barchiesi, E., Spagnuolo, M., Dell'Isola, F., Hild, F.: A multi-disciplinary approach for mechanical metamaterial synthesis: a hierarchical modular multiscale cellular structure paradigm. State of the art and future trends in material modeling, 485–505 (2019) https://doi.org/10.1007/978-3-030-30355-6_20
28. Misra, A., Lekszycki, T., Giorgio, I., Ganzosch, G., Müller, W.H., Dell'Isola, F.: Pantographic metamaterials show atypical Poynting effect reversal. Mech. Res. Commun. **89**, 6–10 (2018). https://doi.org/10.1016/j.mechrescom.2018.02.003

29. Bongué Boma, M., Brocato, M.: A continuum model of micro-cracks in concrete. Contin. Mech. Thermodyn. **22**(2), 137–161 (2009). https://doi.org/10.1007/s00161-009-0130-4
30. Carcaterra, A., dell'Isola, F., Esposito, R., Pulvirenti, M.: Macroscopic description of microscopically strongly inhomogenous systems: a mathematical basis for the synthesis of higher gradients metamaterials. Arch. Ration. Mech. Anal. **218**(3), 1239–1262 (2015). https://doi.org/10.1007/s00205-015-0879-5
31. Jouan, G., Kotronis, P., Collin, F.: Using a second gradient model to simulate the behaviour of concrete structural elements. Finite Elem. Anal. Des. **90**, 50–60 (2014). https://doi.org/10.1016/j.finel.2014.06.002
32. Germain, P.: The method of virtual power in the mechanics of continuous media, I: second-gradient theory. Math. Mech. Complex Syst. **8**(2), 153–190 (2020). https://doi.org/10.2140/memocs.2020.8.153
33. dell'Isola, F., Andreaus, U., Placidi, L.: At the origins and in the vanguard of peridynamics, non-local and higher-gradient continuum mechanics: an underestimated and still topical contribution of Gabrio Piola. Math. Mech. Solids **20**(8), 887–928 (2015). https://doi.org/10.1177/10812865135098
34. Placidi, L., dell'Isola, F., Kandalaft, A., Luciano, R., Majorana, C., Misra, A.: A granular micromechanic-based model for Ultra High Performance Fiber-Reinforced Concrete (UHP FRC). Int. J. Solids Struct. **297**, 112844 (2024). https://doi.org/10.1016/j.ijsolstr.2024.112844
35. Eremeyev, V.A., Reccia, E.: Nonlinear strain gradient and micromorphic one-dimensional elastic continua: comparison through strong ellipticity conditions. Mech. Res. Commun. **124**, 103909 (2022). https://doi.org/10.1016/j.mechrescom.2022.103909
36. dell'Isola, F., Eugster, S.R., Fedele, R., Seppecher, P.: Second-gradient continua: from lagrangian to eulerian and back. Math. Mech. Solids **27**(12), 2715–2750 (2022). https://doi.org/10.1177/1081286522107882
37. Scerrato, D., Giorgio, I., Madeo, A., Limam, A., Darve, F.: A simple non-linear model for internal friction in modified concrete. Int. J. Eng. Sci. **80**, 136–152 (2014). https://doi.org/10.1016/j.ijengsci.2014.02.021
38. Scerrato, D., Giorgio, I., Della Corte, A., Madeo, A., Limam, A.: A micro-structural model for dissipation phenomena in the concrete. Int. J. Numer. Anal. Methods Geomech. **39**(18), 2037–2052 (2015). https://doi.org/10.1002/nag.2394
39. Scerrato, D., Giorgio, I., Della Corte, A., Madeo, A., Dowling, N.E., Darve, F.: Towards the design of an enriched concrete with enhanced dissipation performances. Cem. Concr. Res. **84**, 48–61 (2016). https://doi.org/10.1016/j.cemconres.2016.03.002
40. Aretusi, G., Ciallella, A.: An Application of Coulomb-Friction Model to Predict Internal Dissipation in Concrete, pp. 73–86. Springer (2021). https://doi.org/10.1007/978-3-030-42707-8_5
41. Aretusi, G., Cardillo, C., Salvatori, A., Bednarczyk, E., Fedele, R.: A simple extension of Timoshenko beam model to describe dissipation in cementitious elements. Zeitschrift für angewandte Mathematik und Physik (2024). https://doi.org/10.1007/s00033-024-02304-w
42. Aretusi, G., Cardillo, C., Murcia Terranova, L., Bednarczyk, E.: A dissipation model for concrete based on an enhanced Timoshenko beam. Netw. Heterog. Media **19**, 700–723 (2024). https://doi.org/10.3934/nhm.2024031
43. Placidi, L., Misra, A., Barchiesi, E.: Simulation results for damage with evolving microstructure and growing strain gradient moduli. Contin. Mech. Thermodyn. **31**(4), 1143–1163 (2018). https://doi.org/10.1007/s00161-018-0693-z
44. Scrofani, A., Barchiesi, E., Chiaia, B., Misra, A., Placidi, L.: Fluid diffusion related aging effect in a concrete dam modeled as a Timoshenko beam. Math. Mech. Complex Syst. **11**(2), 313–334 (2023). https://doi.org/10.2140/memocs.2023.11.313
45. Cuomo, M., Contrafatto, L., Greco, L.: A cohesive interface model with degrading friction coefficient. Math. Mech. Complex Syst. **12**(2), 113–133 (2024). https://doi.org/10.2140/memocs.2024.12.113
46. Yilmaz, N., Yildizdag, M.E., Fabbrocino, F., Placidi, L., Misra, A.: Emergence of critical state in granular materials using a variationally-based damage-elasto-plastic micromechanical continuum model. Int. J. Numer. Anal. Methods Geomech. (2024). https://doi.org/10.1002/nag.3795
47. Funari, M.F., Spadea, S., Fabbrocino, F., Luciano, R.: A moving interface finite element formulation to predict dynamic edge debonding in FRP-strengthened concrete beams in service conditions. Fibers **8**(6), 42 (2020). https://doi.org/10.3390/fib8060042
48. Comi, C., Fedele, R., Perego, U.: A chemo-thermo-damage model for the analysis of concrete dams affected by alkali-silica reaction. Mech. Mater. **41**(3), 210–230 (2009). https://doi.org/10.1016/j.mechmat.2008.10.010
49. Ciallella, A., Pasquali, D., Gołaszewski, M., D'Annibale, F., Giorgio, I.: A rate-independent internal friction to describe the hysteretic behavior of pantographic structures under cyclic loads. Mech. Res. Commun. **116**, 103761 (2021). https://doi.org/10.1016/j.mechrescom.2021.103761
50. dell'Isola, F., Seppecher, P., Alibert, J.J., Lekszycki, T., Grygoruk, R., Pawlikowski, M., Steigmann, D., Giorgio, I., Andreaus, U., Turco, E., Gołaszewski, M., Rizzi, N., Boutin, C., Eremeyev, V.A., Misra, A., Placidi, L., Barchiesi, E., Greco, L., Cuomo, M., Cazzani, A., Corte, A.D., Battista, A., Scerrato, D., Eremeeva, I.Z., Rahali, Y., Ganghoffer, J.-F., Müller, W., Ganzosch, G., Spagnuolo, M., Pfaff, A., Barcz, K., Hoschke, K., Neggers, J., Hild, F.: Pantographic metamaterials: an example of mathematically driven design and of its technological challenges. Contin. Mech. Thermodyn. **31**(4), 851–884 (2019). https://doi.org/10.1007/s00161-018-0689-8
51. dell'Isola, F., Seppecher, P., Spagnuolo, M., Barchiesi, E., Hild, F., Lekszycki, T., Giorgio, I., Placidi, L., Andreaus, U., Cuomo, M., Eugster, S.R., Pfaff, A., Hoschke, K., Langkemper, R., Turco, E., Sarikaya, R., Misra, A., De Angelo, M., D'Annibale, F., Bouterf, A., Pinelli, X., Misra, A., Desmorat, B., Pawlikowski, M., Dupuy, C., Scerrato, D., Peyre, P., Laudato, M., Manzari, L., Göransson, P., Hesch, C., Hesch, S., Franciosi, P., Dirrenberger, J., Maurin, F., Vangelatos, Z., Grigoropoulos, C., Melissinaki, V., Farsari, M., Muller, W., Abali, B.E., Liebold, C., Ganzosch, G., Harrison, P., Drobnicki, R., Igumnov, L., Alzahrani, F., Hayat, T.: Advances in pantographic structures: design, manufacturing, models, experiments and image analyses. Contin. Mech. Thermodyn. **31**(4), 1231–1282 (2019). https://doi.org/10.1007/s00161-019-00806-x
52. Dahl, P.R.: Solid friction damping of mechanical vibrations. AIAA J. **14**(12), 1675–1682 (1976). https://doi.org/10.2514/3.61511
53. Ciallella, A., Scerrato, D., Spagnuolo, M., Giorgio, I.: A continuum model based on Rayleigh dissipation functions to describe a Coulomb-type constitutive law for internal friction in woven fabrics. Zeitschrift für angewandte Mathematik und Physik (2022). https://doi.org/10.1007/s00033-022-01845-2

54. Kachanov, M.L.: A microcrack model of rock inelasticity part I: frictional sliding on microcracks. Mech. Mater. **1**(1), 19–27 (1982). https://doi.org/10.1016/0167-6636(82)90021-7
55. Hernández-Olivares, F., Barluenga, G., Bollati, M., Witoszek, B.: Static and dynamic behaviour of recycled tyre rubber-filled concrete. Cem. Concr. Res. **32**(10), 1587–1596 (2002). https://doi.org/10.1016/s0008-8846(02)00833-5
56. Pensée, V., Kondo, D., Dormieux, L.: Micromechanical analysis of anisotropic damage in brittle materials. J. Eng. Mech. **128**(8), 889–897 (2002). https://doi.org/10.1061/(asce)0733-9399(2002)128:8(889)
57. El Shamy, U., Denissen, C.: Microscale energy dissipation mechanisms in cyclically-loaded granular soils. Geotech. Geol. Eng. **30**(2), 343–361 (2011). https://doi.org/10.1007/s10706-011-9472-3
58. Zhu, Q., Kondo, D., Shao, J., Pensee, V.: Micromechanical modelling of anisotropic damage in brittle rocks and application. Int. J. Rock Mech. Min. Sci. **45**(4), 467–477 (2008). https://doi.org/10.1016/j.ijrmms.2007.07.014
59. Dahl, P.R.: A Solid Friction Model (1968). https://doi.org/10.21236/ada041920
60. dell'Isola, F., Seppecher, P., Della Corte, A.: The postulations á la D'Alembert and á la Cauchy for higher gradient continuum theories are equivalent: a review of existing results. Proc. R. Soc. A Math. Phys. Eng. Sci. **471**(2183), 20150415 (2015). https://doi.org/10.1098/rspa.2015.0415
61. Abali, B.E., Müller, W.H., dell'Isola, F.: Theory and computation of higher gradient elasticity theories based on action principles. Arch. Appl. Mech. **87**(9), 1495–1510 (2017). https://doi.org/10.1007/s00419-017-1266-5
62. Alibert, J.-J., Seppecher, P., dell'Isola, F.: Truss modular beams with deformation energy depending on higher displacement gradients. Math. Mech. Solids **8**(1), 51–73 (2003). https://doi.org/10.1177/1081286503008001
63. La Valle, G., Soize, C.: Identifying second-gradient continuum models in particle-based materials with pairwise interactions using acoustic tensor methodology. J. Elast. (2024). https://doi.org/10.1007/s10659-024-10067-8
64. Eremeyev, V.A., Elishakoff, I.: On rotary inertia of microstuctured beams and variations thereof. Mech. Res. Commun. **135**, 104239 (2024). https://doi.org/10.1016/j.mechrescom.2023.104239
65. Del Vescovo, D., Giorgio, I.: Dynamic problems for metamaterials: review of existing models and ideas for further research. Int. J. Eng. Sci. **80**, 153–172 (2014). https://doi.org/10.1016/j.ijengsci.2014.02.022
66. dell'Isola, F., Bucci, S., Battista, A.: Against the Fragmentation of Knowledge: The Power of Multidisciplinary Research for the Design of Metamaterials, pp. 523–545. Springer (2016). https://doi.org/10.1007/978-981-10-0959-4_28
67. Eugster, S., dell'Isola, F., Steigmann, D.: Continuum theory for mechanical metamaterials with a cubic lattice substructure. Math. Mech. Complex Syst. **7**(1), 75–98 (2019). https://doi.org/10.2140/memocs.2019.7.75
68. Turco, E., Barchiesi, E., Giorgio, I., dell'Isola, F.: A Lagrangian Hencky-type non-linear model suitable for metamaterials design of shearable and extensible slender deformable bodies alternative to timoshenko theory. Int. J. Non-Linear Mech. **123**, 103481 (2020). https://doi.org/10.1016/j.ijnonlinmec.2020.103481
69. Turco, E., Barchiesi, E., dell'Isola, F.: Nonlinear dynamics of origami metamaterials: energetic discrete approach accounting for bending and in-plane deformation of facets. Zeitschrift für angewandte Mathematik und Physik (2022). https://doi.org/10.1007/s00033-022-01917-3
70. Turco, E., Barchiesi, E., Causin, A., dell'Isola, F., Solci, M.: Kresling tube metamaterial exhibits extreme large-displacement buckling behavior. Mech. Res. Commun. **134**, 104202 (2023). https://doi.org/10.1016/j.mechrescom.2023.104202
71. Barchiesi, E., dell'Isola, F., Seppecher, P., Turco, E.: A beam model for duoskelion structures derived by asymptotic homogenization and its application to axial loading problems. Eur. J. Mech. A/Solids **98**, 104848 (2023). https://doi.org/10.1016/j.euromechsol.2022.104848
72. Ciallella, A., Giorgio, I., Barchiesi, E., Alaimo, G., Cattenone, A., Smaniotto, B., Vintache, A., D'Annibale, F., dell'Isola, F., Hild, F., Auricchio, F.: A 3D pantographic metamaterial behaving as a mechanical shield: experimental and numerical evidence. Mater. Des. **237**, 112554 (2024). https://doi.org/10.1016/j.matdes.2023.112554
73. Turco, E., Barchiesi, E., Causin, A., dell'Isola, F., Solci, M.: Harnessing unconventional buckling of tube origami metamaterials based on Kresling pattern. Int. J. Solids Struct. **300**, 112925 (2024). https://doi.org/10.1016/j.ijsolstr.2024.112925
74. Babu, R., Benipal, G., Singh, A.: Constitutive modeling of concrete: an overview. Asian J. Civ. Eng. (Build. Hous.) **6**, 211–246 (2005)
75. Olsson, H., Åström, K.J., Wit, C., Gäfvert, M., Lischinsky, P.: Friction models and friction compensation. Eur. J. Control **4**(3), 176–195 (1998). https://doi.org/10.1016/s0947-3580(98)70113-x
76. Savkoor, A.R.: Section 8.3 - models of friction. In: Lemaitre, J. (ed.) Handbook of Materials Behavior Models, pp. 700–759. Academic Press, Burlington (2001). https://doi.org/10.1016/B978-012443341-0/50075-2 . https://www.sciencedirect.com/science/article/pii/B9780124433410500752
77. Wit, C., Olsson, H., Astrom, K.J., Lischinsky, P.: A new model for control of systems with friction. IEEE Trans. Autom. Control **40**(3), 419–425 (1995). https://doi.org/10.1109/9.376053
78. Dankowicz, H.: On the modeling of dynamic friction phenomena. ZAMM **79**(6), 399–409 (1999). DOI: https://doi.org/10.1002/(sici)1521-4001(199906)79:6<399::aid-zamm399>3.0.co;2-k
79. Swevers, J., Al-Bender, F., Ganseman, C.G., Projogo, T.: An integrated friction model structure with improved presliding behavior for accurate friction compensation. IEEE Trans. Autom. Control **45**(4), 675–686 (2000). https://doi.org/10.1109/9.847103
80. Bhattacharjee, S.S., Léger, P.: Seismic cracking and energy dissipation in concrete gravity dams. Earthq. Eng. Struct. Dyn. **22**(11), 991–1007 (1993). https://doi.org/10.1002/eqe.4290221106
81. Adelaide, L., Richard, B., Ragueneau, F., Cremona, C.: Thermodynamical admissibility of a set of constitutive equations coupling elasticity, isotropic damage and internal sliding. C. R. Méc. **338**(3), 158–163 (2010). https://doi.org/10.1016/j.crme.2010.03.005
82. Niiranen, J., Khakalo, S., Balobanov, V., Niemi, A.H.: Variational formulation and isogeometric analysis for fourth-order boundary value problems of gradient-elastic bar and plane strain/stress problems. Comput. Methods Appl. Mech. Eng. **308**, 182–211 (2016). https://doi.org/10.1016/j.cma.2016.05.008
83. Baroudi, D., Giorgio, I., Battista, A., Turco, E., Igumnov, L.A.: Nonlinear dynamics of uniformly loaded elastica: experimental and numerical evidence of motion around curled stable equilibrium configurations. ZAMM-Zeitschrift für Angewandte Mathematik und Mechanik **99**(7), 201800121 (2019). https://doi.org/10.1002/zamm.201800121

84. Giorgio, I., Del Vescovo, D.: Energy-based trajectory tracking and vibration control for multilink highly flexible manipulators. Math. Mech. Complex Syst. **7**(2), 159–174 (2019)
85. Giorgio, I.: A discrete formulation of Kirchhoff rods in large-motion dynamics. Math. Mech. Solids **25**(5), 1081–1100 (2020). https://doi.org/10.1177/1081286519900902
86. Greco, L.: An iso-parametric G^1-conforming finite element for the nonlinear analysis of Kirchhoff rod. Part I: the 2D case. Contin. Mech. Thermodyn. **32**(5), 1473–1496 (2020). https://doi.org/10.1007/s00161-020-00861-9
87. Greco, L., Cammarata, A., Castello, D., Cuomo, M.: An objective FE-formulation for Cosserat rods based on the spherical Bézier interpolation. Comput. Methods Appl. Mech. Eng. **425**, 116947 (2024). https://doi.org/10.1016/j.cma.2024.116947
88. Angelo, M.D., Placidi, L., Nejadsadeghi, N., Misra, A.: Non-standard Timoshenko beam model for chiral metamaterial: identification of stiffness parameters. Mech. Res. Commun. **103**, 103462 (2020). https://doi.org/10.1016/j.mechrescom.2019.103462
89. Fedele, R., Maier, G., Miller, B.: Identification of elastic stiffness and local stresses in concrete dams by in situ tests and neural networks. Struct. Infrastruct. Eng. **1**(3), 165–180 (2005). https://doi.org/10.1080/15732470500030513
90. Fedele, R.: Simultaneous assessment of mechanical properties and boundary conditions based on Digital Image Correlation. Exp. Mech. **55**, 139–153 (2015). https://doi.org/10.1007/s11340-014-9931-x
91. Abali, B.E., Wu, C.-C., Müller, W.H.: An energy-based method to determine material constants in nonlinear rheology with applications. Contin. Mech. Thermodyn. **28**(5), 1221–1246 (2015). https://doi.org/10.1007/s00161-015-0472-z
92. De Angelo, M., Barchiesi, E., Giorgio, I., Abali, B.E.: Numerical identification of constitutive parameters in reduced-order bi-dimensional models for pantographic structures: application to out-of-plane buckling. Arch. Appl. Mech. **89**(7), 1333–1358 (2019). https://doi.org/10.1007/s00419-018-01506-9
93. Shekarchizadeh, N., Abali, B.E., Barchiesi, E., Bersani, A.M.: Inverse analysis of metamaterials and parameter determination by means of an automatized optimization problem. ZAMM - Journal of Applied Mathematics and Mechanics / Zeitschrift für Angewandte Mathematik und Mechanik **101**(8) (2021) https://doi.org/10.1002/zamm.202000277
94. Ciallella, A., La Valle, G., Vintache, A., Smaniotto, B., Hild, F.: Deformation mode in 3-point flexure on pantographic block. Int. J. Solids Struct. **265–266**, 112129 (2023). https://doi.org/10.1016/j.ijsolstr.2023.112129
95. Heiduschke, K.: On tensor projections, stress or stretch vectors and their relations to Mohr's three circles. Math. Mech. Complex Syst. **12**(2), 173–216 (2024). https://doi.org/10.2140/memocs.2024.12.173
96. Wang, X., Schiavone, P.: An elliptical incompressible liquid inclusion in an infinite anisotropic elastic space. Math. Mech. Complex Syst. **12**(2), 217–232 (2024). https://doi.org/10.2140/memocs.2024.12.217
97. Federico, S., Alhasadi, M.F., Imatani, S., Epstein, M.: A three-dimensional Airy stress function. Math. Mech. Complex Syst. **11**(3), 429–449 (2023). https://doi.org/10.2140/memocs.2023.11.429
98. Giorgio, I.: A variational formulation for one-dimensional linear thermoviscoelasticity. Math. Mech. Complex Syst. **9**(4), 397–412 (2022). https://doi.org/10.2140/memocs.2021.9.397
99. Giorgio, I., Placidi, L.: A variational formulation for three-dimensional linear thermoelasticity with 'thermal inertia'. Meccanica (2024). https://doi.org/10.1007/s11012-024-01796-0

Publisher's Note Springer Nature remains neutral with regard to jurisdictional claims in published maps and institutional affiliations.

Springer Nature or its licensor (e.g. a society or other partner) holds exclusive rights to this article under a publishing agreement with the author(s) or other rightsholder(s); author self-archiving of the accepted manuscript version of this article is solely governed by the terms of such publishing agreement and applicable law.

Non-linear effects in seismic waves in high energy earthquakes

---

Chapter abstract

Linear models are commonly used in geophysics and civil engineering to describe earthquakes and seismic wave propagation. However, large soil deformations challenge this assumption, particularly near discontinuities where strain concentrations invalidate the small deformation hypothesis.

This chapter examines the limitations of the linear approach in a simplified yet relevant case inspired by the 2009 L'Aquila earthquake. A 2D piecewise homogeneous domain, resembling the Aterno River Valley, is modeled with a viscoelastic, isotropic, and geometrically nonlinear material. Applying seismic excitation, we compare linear and nonlinear responses, showing that differences originate near discontinuities and propagate throughout the domain. Numerical results demonstrate that nonlinear models better predict frequency ratios, ground acceleration, and amplitude, aligning more closely with experimental data.
Published in *Mathematics and Mechanics of Solids*, 2025

Check for updates

Article

MMS

Mathematics and Mechanics of Solids
1–32
© The Author(s) 2025
Article reuse guidelines:
sagepub.com/journals-permissions
DOI: 10.1177/10812865251320071
journals.sagepub.com/home/mms
Sage

Non-linear effects in seismic waves in high-energy earthquakes: A two-dimensional analysis for non-homogeneous isotropic media with a view towards the study of the 2009 L'Aquila earthquake

Angelo Scrofani
Università degli studi di Sassari, Alghero, Italy

Giuliano Aretusi
Università degli Studi dell'Aquila, L'Aquila, Italy

Antonello Salvatori
Università degli Studi dell'Aquila, L'Aquila, Italy

Marco Tallini
Università degli Studi dell'Aquila, L'Aquila, Italy

Ivan Giorgio
Università degli Studi dell'Aquila, L'Aquila, Italy

Francesco D'Annibale
Università degli Studi dell'Aquila, L'Aquila, Italy

Francesco Fabbrocino
Pegaso-Università Telematica, Napoli, Italy

Luca Placidi
Università Telematica Internazionale UNINETTUNO, Roma, Italy

Corresponding author:
Luca Placidi, Università Telematica Internazionale UNINETTUNO, Corso Vittorio Emanuele II, 39, 00186, Roma, Italy.
Email: lplacidi@gmail.com

Gaetano De Luca
Istituto Nazionale di Geofisica e Vulcanologia, L'Aquila, Italy

Francesco dell'Isola
Università degli Studi dell'Aquila, L'Aquila, Italy; Warsaw University of Technology, Warsaw, Poland; ENS Paris-Saclay, Cachan, France

Received 16 July 2024; accepted 27 January 2025

Abstract
It is usually accepted in geophysics (and in civil engineering) that linear models can be used for describing an earthquake and the consequent seismic waves' propagation. However, the large deformation experienced by the soil in these situations suggests that this paradigm requires more critical consideration. In fact, we claim that, in the vicinity of some discontinuities (that are common in all the geophysical applications of continuum models), the corresponding strain concentrations make the hypothesis of small deformation to be inadequate. In this paper, we verify the inappropriateness of the linear paradigm in a simple but reasonable case, with a view to a future application of this study to the effects of the 2009 L'Aquila earthquake. To this aim, we start with an analysis which is restricted to a two-dimensional body (i) with an inhomogeneity that resembles the Aterno River Valley, central Italy and (ii) with a non-linearity that is the most simple one, choosing the strain energy to be quadratic in the non-linear measures of deformation. More precisely, we consider a 2D piecewise homogeneous domain and a material that is viscoelastic isotropic and geometrically non-linear. We apply, to the bottom of such a domain, a seismic excitation and calculate the differences in the response between the linear and the geometrically non-linear cases. Using a suitably designed numerical model, we prove that, as conjectured, these differences not only originate near the pre-defined geometrical discontinuities but also propagate throughout the rest of the domain. Moreover, we find numerical predictions of the frequency ratios and ground acceleration time dependence and amplitude that produce, in the case of non-linear models, predictions which are closer to experimental evidence than those obtained using the corresponding linear model.

Keywords
Earthquake, waves, dynamics of soils, non-linear effects

1. Introduction

The current paradigm, usually accepted in geophysics, assumes that linear models can be used for describing the wave propagation consequent to tectonic or volcanics energy release, in what is called an earthquake. This paradigm is persistent, albeit more sophisticated non-linear studies in two- and three-dimensional domains, are widely present in the literature and deal with a wide class of mechanical phenomena [1–9] also related to the waves propagation [10–12]. For these types of applications of non-linear continuum mechanics , parameter identification represents a delicate point in the modelling process [13–17]. In the present paper, we will not try to get such an identification in the context of earthquakes modelling: instead we will explore the model's potentialities by means of a qualitative and semi-quantitative analysis, establishing the conceptual bases for further investigations.

While the linearised approach to earthquake dynamics and wave propagation, often linked to the forcing and free vibration of the structures [18–23], has produced very interesting and useful results, we claim that non-linear continuum mechanics gives a logical evidence that, in some specific instances, this approach cannot be accepted and must be modified. In particular, we state that when the medium in which the waves are propagating is strongly inhomogeneous, so that the fields of stiffnesses are suffering

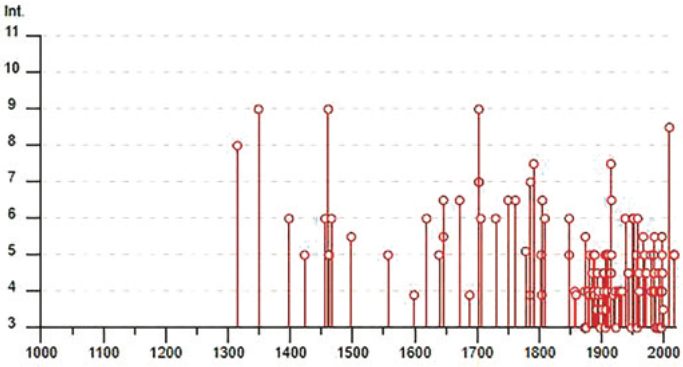


Figure 1. Macroseismic intensities relating to the city of L'Aquila plotted as time(years) vs intensity.

high gradients, and when the earthquake energy release is sufficiently high, then non-linear behaviour may become not negligible [24–27], also in the simplest case of purely geometrical non-linearities: to be more precise we remark here that, in the case examined in the numerical simulations of this paper, the released energy is estimated to be equivalent to the energy of an earthquake with a moment magnitude of 6, as described by Luca et al. [28]. As a consequence of our results, we urge for the introduction of more sophisticated non-linear models and numerical techniques, in order to get the required precise predictions of the earthquakes effects, especially when their energy is large. In this paper, the analysis is restricted to a two-dimensional case in order to get qualitative and preliminary quantitative information about the properties of considered mechanical systems and in order to prepare the more realistic three-dimensional analysis, which is needed to face the modelling problem arising when dealing with seismic propagation in the Aterno River Valley, where the city of L'Aquila is located. To make clearer the modelling challenges to be confronted we shortly recall, in what follow, the basic phenomenology whose modelling we intend to develop here and in our future planned investigations. The city of L'Aquila is located in the central part of the Apennine chain (central Italy), in a seismic area characterized by normal fault earthquakes [28,29]. This area (called "aquilano") has been struck in the past by numerous earthquakes such as those of 1315, 1349, 1461, 1703 and the recent one on 6 April 2009 (M_W6.3, [30] which macroseismic intensities up to XI on the Mercalli–Cancani–Sieberg scale (MCS), corresponding to an Ms close to 7 and causing deaths and damage; the Figure 1 shows the macroseismic intensities relating to the city of L'Aquila [31,32].

Before the 2009 event, the presence of seismic amplification in the city of L'Aquila was already known (within its historic walls) [33], and since then, numerous work were published on seismic microzonation [34–41], on strong motion data [42–47], on earthquake engineering [48–54], on damage distribution [53,55–57], on geological works [58–63], on geotechnical works ([43,64,65], and on numerical modeling ([46,66–72]. We remark that in Luca et al.'s study, [33] one can find a first attempt aimed to explain the observed seismic wave amplification effect (up to 10) in the 0.4–0.8 Hz frequency range. Of course, the 2009 L'Aquila earthquake has been largely discussed in the literature [30,33,44,69,71–73], and it is well-established that this geographic area shows different geological layers, as it was exposed already by Luca et al. [33], some years before of the seismic event that occurred in the city of L'Aquila in 2009. Always in Luca et al.'s study [33]: (1) some preliminary 1-D and 2-D linear continuum models for the superficial crust under the city of L'Aquila were introduced, and it was proven that, also by using such linear models, it can be forecast that the discontinuity of stiffnesses must greatly affect the ground accelerations, the frequency ratios and the seismic wave propagation velocities; (2)) some interesting experimental investigations in the urban area of the city were presented: in particular weak-motion data from earthquakes and ambient noise data were collected and analyzed. This experimental evidence given by weak-motion data share the same characteristics as the strong-motion records and shows clearly the presence of the amplification effect in the city. The geophysical model on which Luca et al. [33] is based proves that *the ground-motion amplification in the city of L'Aquila is related to the presence of a sedimentary basin, filled by lacustrine sediments, with a maximum depth of about* 250 *m*. Such area, situated in central Italy, is formed by NW-SE-dipping normal faults which produced rift valleys features typical to the intermontane basins

[74–77]. Several of these faults are still active and they may be responsible for further future earthquakes [78–81].

In this paper, we investigate the wave propagation in a two-dimensional continuous Cauchy medium caused by a forcing excitation, modelling the effects of high-energy earthquakes (moment magnitude higher than 6) originated at hypocenters far from the modelled region, where the seismic wave propagation is studied. In fact, the source of the seismic excitation in 2009 L'Aquila Earthquake was located 10km below the modelled region, whose thickness is about 1km: we explicitly remark that cannot use here the expression "deeper hypocenter", as the usual geological meaning of the term "deeper" in this context indicates that the hypocenter is located in the mantel under the crust. We consider, at first, linear models, that are models in which the deformation energy is assumed to be isotropic and quadratic in the linear deformation measure (i.e. the so-called infinitesimal strain tensor). Our aim, in this paper, is to prove that linear models are not fully capable to describe the phenomena occurring when it is necessary to consider continuous models featuring stiffness fields with high spatial gradients: this being the case when strongly non-homogeneous seismic wave propagation regions are to be considered [82–84]. In order to consider the simplest non-linear model, we introduce what is usually called a geometric non-linearity, by assuming that the isotropic deformation energy depends quadratically but on the finite strain tensor instead of depending on the linearised deformation measure [85]. We prove, with numerical simulations, that, the predictions of non-linear models dramatically differ from those obtained with linear models. These results seem to indicate, in particular in the case of the earthquakes propagating in the Aterno River Valley, that more sophisticated analyses are needed, if one wants to predict in a reliable way the effects of seismic waves on buildings and infrastructures. In fact, in the Aterno Valley, it is well-established that (see Luca et al. [33] and the references there cited) the ratio between the average stiffnesses observed in the soft alluvial sand or silt deposits layers and in the hard bedrock or calcareous breccia layer is, at least, one to four, so that high gradients of the stiffness fields are concentrated at the interface regions between these different layers or between the bedrock and the soft materials. It has to be remarked that in the literature also different modelling approaches have been attempted when considering linear or non-linear waves propagation. In fact, some discrete models based on lattice dynamics methods could be applied: see, for example Sharma and Eremeyev [86], Placidi et al. [87, 88] where transmission, refraction, and leakage of wave in the vicinity of surface defect were considered. Moreover, some surface-related phenomena in layered structures have been studied recently by Mikhasev et al. [89], where other references could be found. We believe, however, that the numerical implementation of continuum models, also in the presence of non-linearities, is so well-established and reliable that, at the moment, the approach which we used must be preferred. Because of the numerical simulations which we have performed, we have observed that the field of deformation (and kinetic) energy density difference between the linear and non-linear predictions, normalised with respect to the average deformation (and kinetic) energy in the non-linear case, starts being concentrated in the hard/soft interfaces at the beginning of the dynamic load (modelling the earthquake) and then propagates in both the soft and hard region: the amplitude of this propagating field may reach the values higher than 100% in a large region of the domain. Because of their applicative importance, the linear and non-linear acceleration field in several points close to the boundaries and their differences are calculated and discussed. The accelerations are normalised with respect to the gravity acceleration g and the difference between these two quantities can reach values around $0.77g$. We can conclude that the numerical evidence, which we have obtained, demands the development of more refined non-linear models for describing, in particular, the phenomenology observed in the city of L'Aquila during high-energy earthquakes. Albeit for the numerical simulations we have used the standard package included in COMSOL, some non-trivial encoding solutions have been used: (1)) the same finite-elements procedure has been used for solving simultaneously the linear and non-linear problem, (2)) a purely variational approach has been implemented, using suitable Hamilton conservative and Rayleigh dissipation functionals in the coding procedure, (3)) in order to avoid the reflection back inside the region of interest of the passing wave at its boundaries, we have chosen suitable optimal boundary conditions implementing viscoelastic displacement-force relationships at the lateral boundaries of the considered wave propagating region, while at its bottom a spherical displacement wave, originated in the hypocenter is imposed: the fact that the forcing action is originated by a far hypocenter is modelled by imposing at the basis of the bedrock a displacement calculated with a spherical wave transporting the required earthquake energy [90,91]. The very preliminary results, which we announce here, require the

development of a more sophisticated analysis in which: (1) isotropy hypothesis is relaxed; (2) the material elastic non-linearities are included in the modelling scheme; (3) the creep, damage, and plasticity effects are suitably accounted for; (4) the second-gradient deformation energy is postulated, for giving a better description of the boundary layers formed at the interfaces [92–100], also accounting for the change of the microstructure [101–104] and of the granular (and porous) nature of the soils [105–110] due to which strong local and macro-to-micro scale differences can be highlighted; (5)) the complete three-dimensional problem for the Aterno Valley is considered, in order to fully account for the peculiar behaviour experimentally observed by Luca et al. [33].

2. Geological setting of L'Aquila basin

In this section, we motivate our modeling assumptions based on the geological structure of the crust beneath the city of L'Aquila. It is located in a tectonic basin (Aterno river valley) bounded by a northwest-southeast-active normal fault ($https://diss.ingv.it/new-in-diss-3-3-0$), and it was founded in 1245, so that we have somehow detailed records about the seismic activity in its basic since then. The current tectonic setting of central Italy is due to the superposition of a previous a compressive phase (middle Oligocene - lower Pliocene, 28-3.6 Myr) during which the Apennine chain was created and the subsequent the post-orogenic extensional phase characterized by the origin of intermontane basins scattered in the central Apennine chain (such as L'Aquila basin - henceforth LAB in which is placed L'Aquila city) in the Messinian–Quaternary (7 Myr till now) [58,75–77]. LAB is placed in a NW-SE trending Plio-Quaternary intermontane tectonic basin bounded by SW dipping active normal fault accountable for the current and historical seismicity [31,81]. LAB is filled up by lacustrine, slope and alluvial deposits dated back from the upper Pliocene to the present (3.6 Myr till now) and laying via an unconformity surface onto the Messinian (7.2–5.3 Myr) terrigenous units and Meso-Cenozoic (100–70 and 20–12 Myr) carbonate units. LAB oldest post-orogenic deposits, made up by slope breccias and alluvial conglomerates, belong to the Colle Cantaro-Cave Formation (CCF) (upper Piacenzian-Gelasian 3.0–1.8 Myr) [61,77,111]. The Madonna della Strada Synthem (MDS), (in this study the soft layer) which is separated from the underlying CCF by an unconformity boundary, is made up by clayey–sandy silts and sands of Calabrian age (1.8–0.8 Myr) and referred to an alluvial meandering system within a wide and swampy flood plain [77]. Above MDS, separated by an unconformity boundary, the Middle Pleistocene (0.8–0.12 Myr) Fosso Genzano Synthem (FGS) is placed. It consists of gravels and sands referred to alluvial fans and plains [63]. The hill, where the L'Aquila historic downtown stands, is mainly made up by late Middle Pleistocene (0.3–0.12 Myr) calcareous breccias (in this study, the hard layer) which, via an erosive boundary, are superimposed on the underlying MDS and FGS deposits and the Meso-Cenozoic bedrock [112]. In fact, the historical part of the city (within the ancient walls) is placed on a fluvial terrace in the left bank of the Aterno River. The elevation of the terrace reaches 900 m a.s.l. (above mean sea level) in the NE part of the city and slopes down to 675 m in the SW direction. The terrace ends at the Aterno River which flows 50 m below yet. The terrace is made up of alluvial deposits created in the lower Quaternary age and is composed of breccias with limestone boulders and clasts in a marly matrix. The dimensions of these clasts can range from centimeters to some meters. This deposit is common in the Abruzzo region and may be related to catastrophic alluvial events associated with landslides [113]. These terrace were studied by Demageout [114], who named them "megabrecce". The "megabrecce" (called "mega breaches" in English) represents a well-defined geological unit with a thickness of some tens of meters. These deposits (megabrecce) are placed on the lacustrine sediments composed mainly of silty and sandy layers and minor gravel beds that can generate earthquakes with maximum expected magnitudes up to 6.5–7 [81]. The lacustrine sediments have their maximum thickness (around 300 m) in the center of the city of L'Aquila. In contrast, in the Aterno River valley, at north of L'Aquila, the thickness of the sediments is never greater than 100 m.

Further information about geological setting of L'Aquila basin will be exploited in future modelling efforts: in particular when 3D models will be used for getting the required predictions.

3. Modelling and coding assumption

In this section, we define univocally both the linear and non-linear models on the basis of which the analyses will be performed. The soil is modelled as a 2-dimensional domain and each of its material particles

will be characterised with the coordinate $\mathbf{X} = X_i\hat{\mathbf{e}}_i$ (where $\|\hat{\mathbf{e}}_i\| = 1$ and $i = 1, 2$) in a given reference configuration. The set of the kinematical descriptors, which depend upon the coordinates $\mathbf{X}$ and the time t, is composed of (1) the horizontal displacement $u_1\,(X_1, X_2, t)$ and (2) the vertical displacement $u_2\,(X_1, X_2, t)$. Let $\mathbf{u}(\mathbf{X}, t) = u_i\hat{\mathbf{e}}_i$ be the displacement vector of the generic point with X_i coordinates, $(\mathbf{X}, t)$ be the placement function, $\mathbb{F}$ be the deformation gradient tensor and $\mathbb{G}$ be the finite strain tensor. We will indicate with $\mathbf{x} = x_i\hat{\mathbf{e}}_i$ the coordinates in the current configuration, of the material point having coordinates $\mathbf{X}$ in the reference configuration. In formulae,

$$\mathbf{x} = (\mathbf{X}, t) = \mathbf{X} + \mathbf{u}, \qquad \mathbb{F} = \nabla\,, \qquad \mathbb{G} = \frac{1}{2}(\mathbb{F}^T\mathbb{F} - \mathbb{I}) \tag{1}$$

or, in index notation:

$$\Phi_i = X_i + u_i, \qquad F_{ij} = \frac{\partial \Phi_i}{\partial X_j} = u_{i,j} + \delta_{ij}, \qquad G_{ij} = \frac{1}{2}(F_{ki}F_{kj} - \delta_{ij}) \tag{2}$$

where

$$u_{i,j} = \frac{\partial u_i}{\partial X_j} \qquad \text{and} \qquad \delta_{ij} = \begin{cases} 1 & i = j \\ 0 & i \neq j \end{cases} \tag{3}$$

3.1. Deformation and kinetic energies and Rayleigh functional

Let $\mathcal{W}^{el}$ and $\mathcal{K}$ be the elastic internal deformation and the kinetic energies, respectively, and let $\partial_f\mathcal{B}$ be a subdomain of the boundary $\partial\mathcal{B}$ of the body $\mathcal{B}$ (see the Figure 2)

$$\mathcal{W}^{el} = \int_{\mathcal{B}} \left[\frac{1}{2}\lambda(tr\,\mathbb{G})^2 + \mu tr(\mathbb{G}^2)\right] dA + \int_{\partial_f\mathcal{B}} \frac{1}{2} K\mathbf{u}\cdot\mathbf{u} ds \tag{4}$$

$$\mathcal{K} = \int_{\mathcal{B}} \frac{1}{2}\rho\dot{\mathbf{u}}\cdot\dot{\mathbf{u}} dA \tag{5}$$

where λ and μ are the 2D Lamè coefficients and ρ is the mass density (per unit area) of the 2D domain, listed in Table 1, and K is the elastic stiffness per unit line of the bed of springs applied at the vertical boundaries $\partial_f B$, also listed in Table 1 (and shown in Figure 2). The dot between two vectors $\mathbf{a}$ and $\mathbf{b}$, denoted by $\mathbf{a}\cdot\mathbf{b}$, is their scalar product. Let the dissipation energy be:

$$\mathcal{W}^{dis} = \int_{\mathcal{B}} \mathcal{R}_{\mathcal{B}} dA + \int_{\partial_f\mathcal{B}} \mathcal{R}_f ds \tag{6}$$

and the two integrands have the following expression,

$$\mathcal{R}_{\mathcal{B}} = \frac{1}{2}\lambda_v(tr\,\dot{\mathbb{G}})^2 + \mu_v tr(\dot{\mathbb{G}}^2) \tag{7}$$

$$\mathcal{R}_f = \frac{1}{2} c\dot{\mathbf{u}}\cdot\dot{\mathbf{u}} \tag{8}$$

here, λ_v is a coefficient of viscosity and μ_v is the shear viscosity of the 2D domain, listed in Table 1 and c is the damping coefficient per unit line of the bed of dashpots applied at the vertical boundaries $\partial_f B$, also listed in Table 1. The Rayleigh dissipative term $\mathcal{R}_{\mathcal{B}}$, introduced in equation (7), acts within the domain, while the boundary dissipative term $\mathcal{R}_f$, defined in equation (8), mitigates non-physical wave reflections at the domain boundaries, as illustrated in Figure 2. Given that the domain represents a portion of soil, it

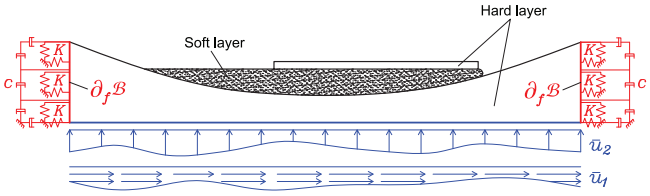


Figure 2. Boundary conditions: three boundary conditions were taken into account. On the two red lateral boundaries, indicating as $\partial_f\mathcal{B}$, are imposed a damping condition, derived from equation (19), and an elastic one, derived from equation (20). On the blue bottom boundary one has a boundary condition in terms of the displacements, see equations (32) and (33).

is reasonable to assume that seismic waves would naturally propagate beyond the model boundaries, dissipating into the surrounding soil mass. The linear approximation of the non-linear deformation defined at the third equation of (1) is given by

$$\mathbb{G} = \frac{1}{2}\left(\nabla\mathbf{u} + \nabla\mathbf{u}^T + \nabla\mathbf{u}^T\nabla\mathbf{u}\right) \quad \longrightarrow \quad \mathbb{E} = \frac{1}{2}\left(\nabla\mathbf{u} + \nabla\mathbf{u}^T\right). \tag{9}$$

So that in index notation we have

$$E_{ij} = \frac{1}{2}(u_{i,j} + u_{j,i}) \tag{10}$$

From the virtual work principle [115], indicating with t_1 and t_2 two different instants of time where the displacements $\mathbf{u}(\mathbf{X}, t_1)$ and $\mathbf{u}(\mathbf{X}, t_2)$ are known, the action is defined as a functional of the displacement function $\mathbf{u}(\mathbf{X}, t)$ as follows:

$$\mathcal{A}(u_1, u_2) = \int_{t_1}^{t_2} [\mathcal{W}^{el} - \mathcal{K}]dt \tag{11}$$

its first variation is:

$$\delta\mathcal{A} = \mathcal{A}(u_1 + \delta u_1, u_2 + \delta u_2) - \mathcal{A}(u_1, u_2) \tag{12}$$

By separately examining the two terms of equation (11), the variation (12) can be decomposed into the sum of the following quantities:

$$\int_{t_1}^{t_2} \delta\mathcal{W}^{el} = \int_{t_1}^{t_2} \frac{\partial\mathcal{W}^{el}}{\partial G_{ij}}\delta G_{ij}dt = \int_{t_1}^{t_2}\int_{\mathcal{B}} [\lambda G_{ii}\delta G_{jj} + 2\mu G_{ij}\delta G_{ij}]dAdt + \int_{t_1}^{t_2}\int_{\partial_f\mathcal{B}} Ku_i\delta u_i dsdt \tag{13}$$

and

$$\int_{t_1}^{t_2} \delta\mathcal{K}dt = \int_{t_1}^{t_2}\int_{\mathcal{B}} \rho\dot{\mathbf{u}}\cdot\delta\dot{\mathbf{u}}dAdt \tag{14}$$

Upon integration of equation (13) by parts, certain spatial boundary terms arise naturally. It is important to note that, following integration by parts, only on the boundary denoted by $\partial_f\mathcal{B}$ (see Figure 2) natural boundary conditions need to be added. This is because on the bottom blue boundary (see Figure 2), displacements (i.e. essential boundary conditions) are imposed, and therefore their variation is zero. Instead, integrating (14) by parts in time, we obtain

$$\begin{aligned}\int_{t_1}^{t_2} \delta\mathcal{K}dt &= \int_{t_1}^{t_2}\int_{\mathcal{B}} \frac{\partial}{\partial t}\left[\rho\dot{\mathbf{u}}\cdot\delta\mathbf{u}\right]dAdt - \int_{t_1}^{t_2}\int_{\mathcal{B}} \rho\ddot{\mathbf{u}}\cdot\delta\mathbf{u}dAdt \\ &= \int_{\mathcal{B}} \left[\rho\dot{\mathbf{u}}\cdot\delta\mathbf{u}\right]_{t_1}^{t_2} dA - \int_{t_1}^{t_2}\int_{\mathcal{B}} \rho\ddot{\mathbf{u}}\cdot\delta\mathbf{u}dAdt\end{aligned} \tag{15}$$

If the displacement at the times t_1 and t_2 are known and their variation $\delta\mathbf{u}$, for those instants of time, are equal to 0, then from equation (15) we have,

$$\int_{t_1}^{t_2} \delta\mathcal{K} dt = -\int_{t_1}^{t_2} \int_{\mathcal{B}} [\rho\ddot{\mathbf{u}} \cdot \delta\mathbf{u}]\, dA dt \tag{16}$$

The variation of the dissipative term $\mathcal{W}^{dis}$ in the equation (6) is defined as $\tilde{\delta}\mathcal{W}^{dis}$. The symbol of the variation operator we used for this quantity is different with respect total one present in equation (12) because such term is not a classic variation. The variation of the dissipative term is defined by the following expression:

$$\tilde{\delta}\mathcal{W}^{dis} = \int_{t_1}^{t_2} \left[\int_{\mathcal{B}} \frac{\partial \mathcal{R}_{\mathcal{B}}}{\partial \dot{G}_{ij}} \delta G_{ij} dA + \int_{\partial_f \mathcal{B}} \frac{\partial \mathcal{R}_f}{\partial \dot{u}_i} \delta u_i ds \right] dt \tag{17}$$

Also for equation (17) the integration by parts provides naturally the boundaries terms on $\partial_f\mathcal{B}$, where no kinematical restrictions are imposed. Finally, the variational principle is formulated as follows:

$$\delta\mathcal{A} + \tilde{\delta}\mathcal{W}^{dis} = 0 \tag{18}$$

for any admissible variation of the kinematic descriptors. On the red lateral boundaries (Figure 2) two different conditions are imposed: (1) a boundary damping constrain (as it is prescribed in the equation (8)) modeled as a bed of dashpots to avoid non-realistic reflections of the wave at the boundaries of the model. Some dissipation phenomena [116] may essentially change the wave propagation, see e.g. Eremeyev [117]. Insertion of equation (8) into equation (17) yields from equation (18) a standard dissipative force at the vertical boundary,

$$\int_{\partial\mathcal{B}} c\dot{\mathbf{u}} \cdot \delta\mathbf{u} ds. \tag{19}$$

and (2) a distributed force, modeled by means a bed of springs with stiffness equal to K and prescribed in the last boundary term of equation (4), to simulate the reaction of the lateral ground. Insertion of the last term of equation (4) into equation (11) yields from equation (18) a standard elastic force at the vertical boundary,

$$\int_{\partial\mathcal{B}} K\mathbf{u} \cdot \delta\mathbf{u} ds \tag{20}$$

3.2. The stiffness fields in the soft and hard region and kinematic boundary conditions

Based on the evidence made available, e.g., by Luca et al. [33], the region where seismic waves propagate is supposed to be constituted by two different materials, characterised by two different stiffnesses (the Young's moduli of the softest and the stiffest layers exhibit a 1/4 ratio as shown in the Table 1) and the 2D Lamè parameters were determined (the justification of the whole modelling procedure is similar to what done in Barchiesi et al. [118], to which we refer) using the following relationships for the plane stress case:

$$\lambda = \frac{Y\nu}{(1+\nu)(1-2\nu)},\ \mu = \frac{Y}{2(1+\nu)} \tag{21}$$

where Y represents the 2D Young's modulus and ν is the 2D Poisson coefficient. In the Table 1, we use the index s and h to denote that the parameter is linked either to the softer or to harder layers. The softer layer is located between the two harder layers as it is shown in Figure 2.

Clearly the distance $r(X_1, 0)$ of the generic point of the bottom boundary (blue part of the boundary in Figure 2), with coordinates $(X_1, 0)$ (with $X_1 \in [0, 7]$ km), from the hypocenter is:

$$r = \sqrt{(X_1 - X_{H1})^2 + (X_2 - X_{H2})^2} = \sqrt{(X_1 - X_{H1})^2 + X_{H2}^2} \tag{22}$$

Table 1. Material parameters that are used on the simulations. The indices *s* and *h* are linked with the layer in which the parameter is defined, respectively *softer* and *harder* one in Figure 2. Boundary parameters are also defined.

Soft domain	Hard domains	Boundary
$Y_s = 10\text{GPa}$	$Y_h = 40\text{GPa}$	$c = 10^8 \frac{\text{Ns}^2}{\text{m}^2}$
$\nu_s = 0.1$	$\nu_h = 0.25$	$K = 4.5 \frac{\text{N}}{\text{m}^2}$
$\lambda_{vs} = 5.2 \cdot 10^7 \text{Nms}^2$	$\lambda_{vh} = 2 \cdot 10^5 \text{Nms}^2$	
$\mu_{vs} = 1.44 \cdot 10^8 \text{Nms}^2$	$\mu_{vh} = 4 \cdot 10^5 \text{Nms}^2$	
$\rho_s = 1500 \frac{\text{kg}}{\text{m}^3}$	$\rho_h = 2700 \frac{\text{kg}}{\text{m}^3}$	

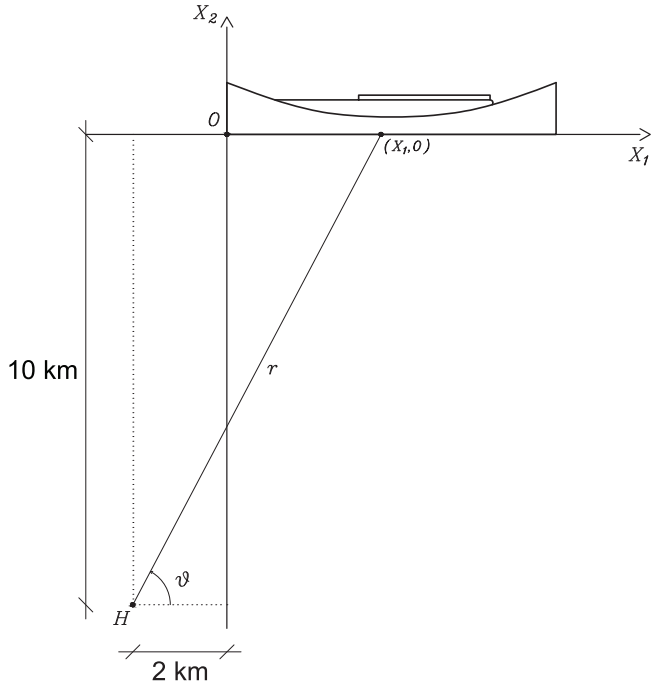


Figure 3. 2-D model: the body is modeled as a domain that consists of three main parts, in which two of these are harder then the other one. The seismic excitation starts at the hypocenter having coordinates $H \equiv (X_{H1}, X_{H2}) = (-2\text{km}, -10\text{km})$.

In the Figure 2, one can see how on the blu boundary at the bottom, the displacement $\bar{\mathbf{u}}$ is imposed for modelling the seismic action. The excitation originates from the hypocenter (point H in Figure 3), spreads into the ground until it reaches the "inhomogeneous superficial region" where wave propagation is analysed. The seismic excitation is assumed to last 3 seconds. Roughly speaking the imposed displacement is the result of the compositions of several waves (three longitudinal and three shear ones). To be more precise, the seismic excitation is modelled by means of the following simplifying assumptions: (1) it propagates as a spheric wave that diffuses, under the studied region of propagation, from an hypocenter H (see Figure 3), with coordinates $(X_{H1}, X_{H2}) = (-2\text{km}, -10\text{km})$, that resides beneath the domain of our investigation; (2)) it interacts with the inhomogeneous superficial region through the blu boundary by "imposing" its displacement; (3)) it does not affect the lateral boundary of the inhomogeneous superficial region, where only linear elastic conservative and dissipative interactions occur between the neighbouring parts of crust. This last modelling choice, of course, limits the quantitative predictability of the introduced model, but we believe that it does not affect the qualitative features of the

calculated solutions and makes reasonable the computing burden: it will be improved in future investigations, where more powerful computing tools will be used. Starting from the meaning of the symbol used in Figure 3 the unit vector $\hat{\mathbf{r}}$ indicates the direction of the vector r and its orthogonal unit vector $\hat{\mathbf{t}}$ (they are needed to determine, respectively, the longitudinal and the shear waves oscillation direction) can be written as:

$$\hat{\mathbf{r}} = \cos\vartheta\hat{\mathbf{e}}_1 + \sin\vartheta\hat{\mathbf{e}}_2 \tag{23}$$

$$\hat{\mathbf{t}} = -\sin\vartheta\hat{\mathbf{e}}_1 + \cos\vartheta\hat{\mathbf{e}}_2 \tag{24}$$

The vector displacement (see e.g. Mancusi et al. [21] for a similar analysis), assuming that the discrete spectrum includes three different frequencies, is the real part of:

$$\bar{\mathbf{u}} = \Sigma_{j=1}^{3}\left[\frac{A_{jl}}{r}\hat{\mathbf{r}}e^{i(\omega_{jl}t-k_{jl}r)} + \frac{A_{js}}{r}\hat{\mathbf{t}}e^{i(\omega_{js}t-k_{js}r)}\right] \tag{25}$$

where

$$\omega_j = \omega_{jl} = \omega_{js} \qquad \text{for } j = 1,2,3 \tag{26}$$

$$A_j = A_{jl} = A_{js} \qquad \text{for } j = 1,2,3 \tag{27}$$

where (1) ω_{jl} and ω_{js} are the frequencies of the longitudinal (index l) and shear (index s) waves which are equal to each other in the analysed example (26), (2) A_{jl} and A_{js} represented the source of the longitudinal and the shear waves respectively, (3) k_{jl} and k_{js} are the wavenumber of the longitudinal and the shear waves respectively and the ratios between those terms and the frequency ω_j is related to the velocities of the waves (principal and shear waves), as follows

$$k_{jl} = \frac{\omega_j}{v_{wl}} \qquad \text{for } j = 1,2,3 \qquad \text{(for the longitudinal waves)} \tag{28}$$

$$k_{js} = \frac{\omega_j}{v_{ws}} \qquad \text{for } j = 1,2,3 \qquad \text{(for the shear waves)} \tag{29}$$

It is possible to prove that the velocities are also related to the Lamè constants as follows,

$$v_{wl} = \sqrt{\frac{\lambda+2\mu}{\rho}} \tag{30}$$

$$v_{ws} = \sqrt{\frac{\mu}{\rho}} \tag{31}$$

Manipulating equations (23) and (24) by means the equation (22), the displacements imposed at the bottom boundary, by the equation (25), are:

$$\bar{u}_1(X_1) = a_{n1}(t)\Sigma_{h=1}^{3}\left[\frac{X_1 - X_{H1}}{r^2}A_h\sin(\omega_h t - k_{hl}r) - \frac{X_{H2}}{r^2}A_h\sin(\omega_h t - k_{hs}r)\right] \tag{32}$$

$$\bar{u}_2(X_1) = a_{n1}(t)\Sigma_{h=1}^{3}\left[\frac{-X_{H2}}{r^2}A_h\sin(\omega_h t - k_{hl}r) - \frac{X_1 - X_{H1}}{r^2}A_h\sin(\omega_h t - k_{hs}r)\right] \tag{33}$$

where we have pre-multiplied the equation (32) and the equation (33) with a_{n1} that is a window function that allow to consider only the signals into a specific time interval. Note that the amplitude of the imposed waves near the lower blue boundary (which is farther from the hypocenter where the waves originate and propagate through the ground) is on the order of millimeters.

Table 2. Waves paramters we used on the simulations. The indices *l* and *s* refer to the longitudinal and shear waves, respectively.

Wave 1	Wave 2	Wave 3
$\omega_1 = 1.571\,\frac{\text{rad}}{\text{s}}$	$\omega_2 = 3.142\,\frac{\text{rad}}{\text{s}}$	$\omega_3 = 15.708\,\frac{\text{rad}}{\text{s}}$
$v_{wl} = 4216.4\,\frac{\text{m}}{\text{s}}$	$v_{wl} = 4216.4\,\frac{\text{m}}{\text{s}}$	$v_{wl} = 4216.4\,\frac{\text{m}}{\text{s}}$
$v_{ws} = 2434.3\,\frac{\text{m}}{\text{s}}$	$v_{ws} = 2434.3\,\frac{\text{m}}{\text{s}}$	$v_{ws} = 2434.3\,\frac{\text{m}}{\text{s}}$
$k_{1l} = 3.726 \cdot 10^{-4}\,\frac{\text{l}}{\text{m}}$	$k_{2l} = 7.451 \cdot 10^{-4}\,\frac{\text{l}}{\text{m}}$	$k_{3l} = 3.726 \cdot 10^{-3}\,\frac{\text{l}}{\text{m}}$
$k_{1s} = 6.453 \cdot 10^{-4}\,\frac{\text{l}}{\text{m}}$	$k_{2s} = 7.451 \cdot 10^{-4}\,\frac{\text{l}}{\text{m}}$	$k_{3s} = 6.453 \cdot 10^{-3}\,\frac{\text{l}}{\text{m}}$
$A_1 = 320\text{m}^2$	$A_2 = 240\text{m}^2$	$A_3 = 160\text{m}^2$

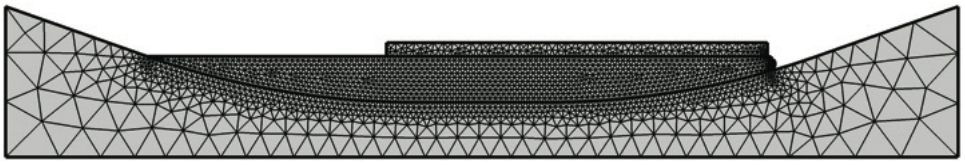


Figure 4. Triangular finite elements.

In Figure 4 the mesh employed is shown. It consists of triangular elements with dimensions not exceeding 469 m in the lower layer (bedrock). Element dimensions. Element dimensions decrease in proximity to the boundary layers, reaching (for the soft layer) maximum dimensions of 40 m.

The three-dimensional Young's moduli Y_s, Y_h, presented in Table 1, are multiplied by an assumed out of plane depth of $d = 1$m to derive the analogous quantities for the bi-dimensional domain, $Y_s^{2D} = Y_s d$ and $Y_h^{2D} = Y_h d$. Then, the Lamè coefficients employed in equation (4) for both the softer and harder layers are determined by equation (21), under the following assumptions:

$$Y = Y_s^{2D}, \quad \nu = \nu_s \qquad \text{for the softer layer} \tag{34}$$

$$Y = Y_h^{2D}, \quad \nu = \nu_h \qquad \text{for the harder layers} \tag{35}$$

Also the mass densities ρ_s and ρ_h are multiplied for the same assumed out of plane depth $d = 1$m to yield the density for the two-dimensional domain under investigation to insert into the equation (5) under the following assumption:

$$\rho = \rho_s^{2D} \qquad \text{for the softer layer} \tag{36}$$

$$\rho = \rho_h^{2D} \qquad \text{for the harder layers} \tag{37}$$

The waves' parameters are shown in Table 2

3.3. Description of the COMSOL code

The analysis described in this work was conducted using COMSOL, a multiphysics finite element software; using this software we were able to carry out a more refined analysis with respect that one by Luca et al. [33]. The model has 30456 degrees of freedom and 3690 triangular elements, into which it has been divided. The size of the elements varies depending on the area of the model: it is reduced near the boundary sharing two subregion with different stiffnesses. The used shape functions are Lagrangian of quadratic order. The implicit methods are more complicated than the explicit ones, in which it is possible to find the solution at the next step by means the only that at the current step, because it is necessary to

solve an equation for each time step that depend for both the states of the system (the current one and the next one). So, mathematically, if $s(t)$ is the state of the system at the current time t and $s(t+\Delta t)$ is the state of the system at the later instant $t+\Delta t$, one has:

$$\begin{aligned} s(t+\Delta t) &= F(s(t)) \qquad \text{for the explicit methods} \\ H(s(t), s(t+\Delta t)) &= 0 \qquad \text{for the implicit methods} \end{aligned} \tag{38}$$

The solver we used for calculate the results is based on the implicit method called *generalized-α* method. Those methods are similar to the second-order BDF (backward differentiation formulas) solver, also based on an implicit method. Unlike this latter method, the generalized-α is a method that allows to control better the degree of damping of high frequencies in the solution and it is more accurate. So that if a solution with sharp gradients is expected, one does not get a very smooth solution due to the damping in the backward method. It is worth to note that, for those same reasons it is also less stable. We used an dynamic load characterised by a discrete spectrum and a time step $t = (800Hz)^{-1}$.

4. Analysis of results

In this section, the comparison between the deformation and the kinetic energy fields and the horizontal and vertical components of the acceleration vector, for the linear and non-linear cases, is shown to emphasize how the non-linear contribution should be taken into consideration when a seismic analysis is carried out. As it is shown in the following subsections the differences, in suitable relative terms, are very large. In the following the superscript *nl* indicates that the corresponding quantity is calculated with the non-linear finite strain tensor $\mathbb{G}$, the third quantity in equation (1) and with the general non-linear evolution equations. Moreover, the superscript *l* indicates that the corresponding quantity is calculated with the linearised version of the strain tensor: i.e. equation (10) and with the linearised evolution equations. Hence, the deformation energies for non-linear and linear cases are denoted as follows,

$$\mathcal{W}^{nl} \qquad \text{for the non-linear case} \tag{39}$$

$$\mathcal{W}^{l} \qquad \text{for the linear case} \tag{40}$$

In the same way, the kinetic energies for non-linear and linear cases are denoted as follows,

$$\mathcal{K}^{nl} \qquad \text{for the non-linear case} \tag{41}$$

$$\mathcal{K}^{l} \qquad \text{for the linear case} \tag{42}$$

Hence, the relative non-linear/linear energies are calculated in the following way:

$$\tilde{\mathcal{W}} = \frac{\mathcal{W}^{nl} - \mathcal{W}^{l}}{\bar{\mathcal{W}}^{l}} \tag{43}$$

$$\tilde{\mathcal{K}} = \frac{\mathcal{K}^{nl} - \mathcal{K}^{l}}{\bar{\mathcal{K}}^{l}} \tag{44}$$

where the symbols $\bar{\mathcal{W}}^{l}$ and $\bar{\mathcal{K}}^{l}$ represent the average, on the domain, of the linear deformation and kinetic energy respectively. The accelerations (and their difference between the non-linear and linear case) are normalized by the gravity acceleration g. Taking into account that the displacements are denoted as u_i for the linear case and as v_i for the non-linear case, the horizontal and vertical accelerations for each point for the linear and for the non-linear cases are denoted, respectively, as follows,

$$\tilde{\ddot{u}}_i = \frac{\ddot{u}_i}{g} \qquad \text{for the linear case} \tag{45}$$

$$\tilde{\ddot{v}}_i = \frac{\ddot{v}_i}{g} \qquad \text{for the non-linear case} \tag{46}$$

and the comparison has been obtained by the difference:

$$\tilde{a}_i = \tilde{\ddot{v}}_i - \tilde{\ddot{u}}_i \tag{47}$$

Clearly the index i takes on values equal to 1 (horizontal acceleration) or 2 (vertical acceleration).

4.1. Comparison of the deformation energy fields in linear and non-linear cases and formation of energy difference boundary layers

The deformation energy represents an important measure of the deformations during the seismic action that it is worth to be investigated. In the Figure 5, it is shown the highest (or lowest) amount of the percentage difference $\tilde{\mathcal{W}}$, in the equation (43), reached on the domain for each time instant.

Note that some extreme values are due clearly to numerical errors that are concentrated only in isolated elements. In Figure 5, the lines corresponding to $y = \pm 1$ are highlighted to show how large are the relative errors between the two methods (clearly the value 1 means differences equal to 100%). Future numerical simulations, with more powerful computing tools, will eliminate these spurious values by using finer finite elements and regularization techniques, such as higher gradient models, which are better suited for discontinuous stiffness fields. To mitigate the impact of the aforementioned numerical errors [119], the color legend in the following contour plots is restricted to the range [–1, 1]. However, for some plots (e.g., Figure 6(b)), a different range might seem more appropriate. These choices were made to improve the readability of the plots when the actual range of values is too small to be effectively represented within the wider range [–1, 1]. The contour plots of the deformation energy in the non-linear case $\mathcal{W}^{nl}$ and its comparison $\tilde{\mathcal{W}}$ with respect the linear one are shown for some time instants in Figure 6–9. In the Figure 5(a) (and clearer in Figure 5(b)) notice that, already during the first seconds when the seismic action excites the ground, the relative difference $\tilde{\mathcal{W}}$ is not negligible (having value much higher then 100%).

Note that from the very beginning, the (albeit small) differences are concentrated at the material transition, from the bedrock to the softer intermediate layer. In addiction, the deformation energy (at the Figure 6(a) and (b) appears almost uniform, and it is the result of the composition of several spherical waves with different velocities and wave lengths. Despite that some differences are present close to the boundary layer as it is shown in Figure 6(c).

It has to be observed that from the beginning of the simulation, the relative difference is substantial (Figure 7(c)) with an extensive region where the difference $\tilde{\mathcal{W}}$ exceeds 20% warrants attention.

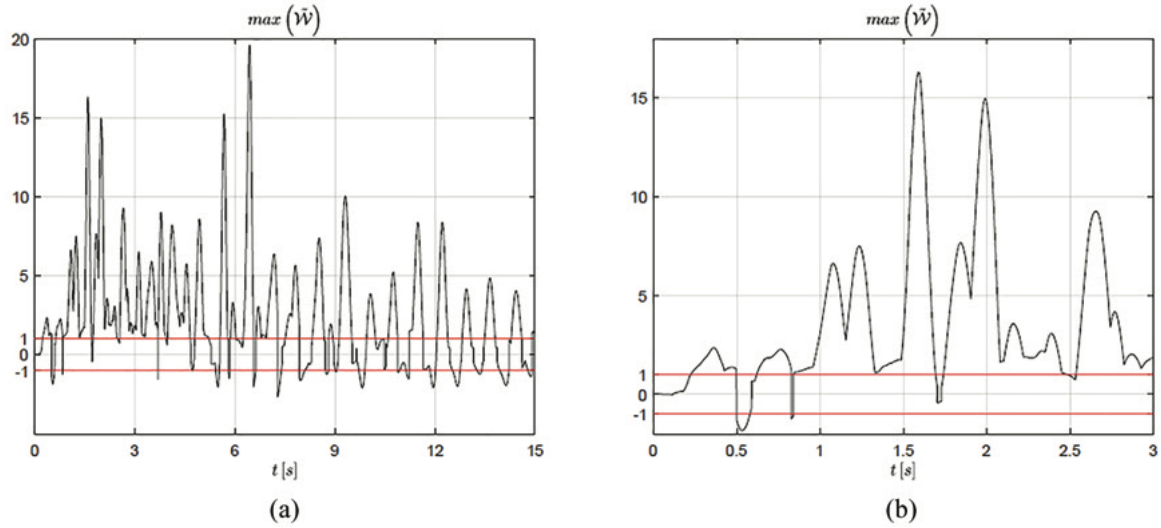


Figure 5. Maximum value of $\tilde{\mathcal{W}}$, defined in equation (43), for (a) the whole analyses and (b) a zooming of the first 3 seconds.

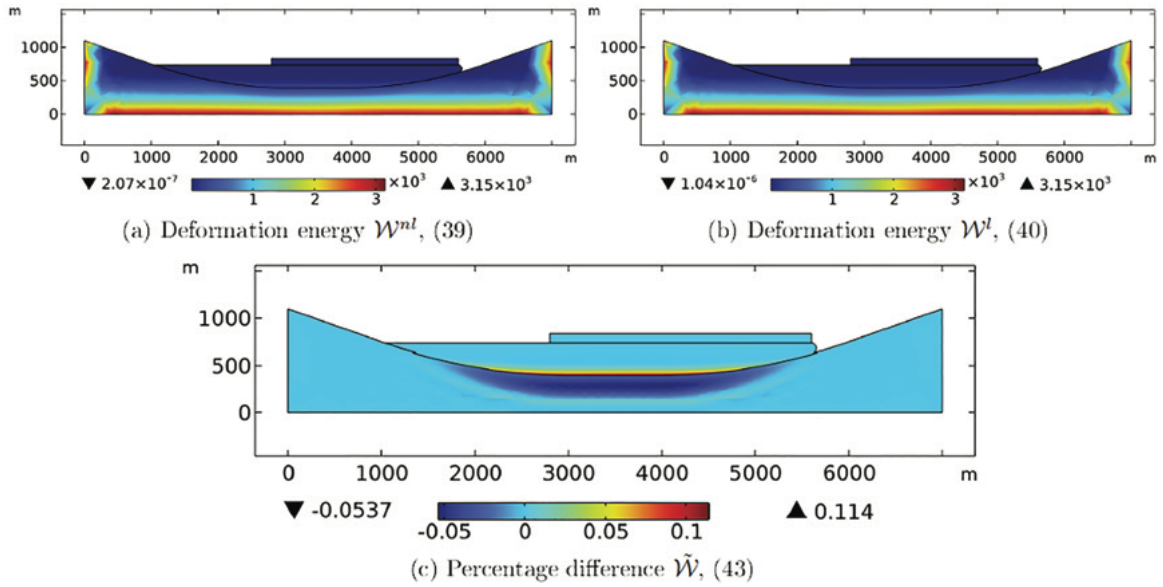


Figure 6. Deformation energy calculated using (a) a non-linear approach, $\mathcal{W}^{nl}$ (Pa), (b) a linear approach, $\mathcal{W}^{l}$ (Pa), and (c) the percentage difference, $\tilde{\mathcal{W}}$, between the non-linear and linear cases at $t = 0.15$s.

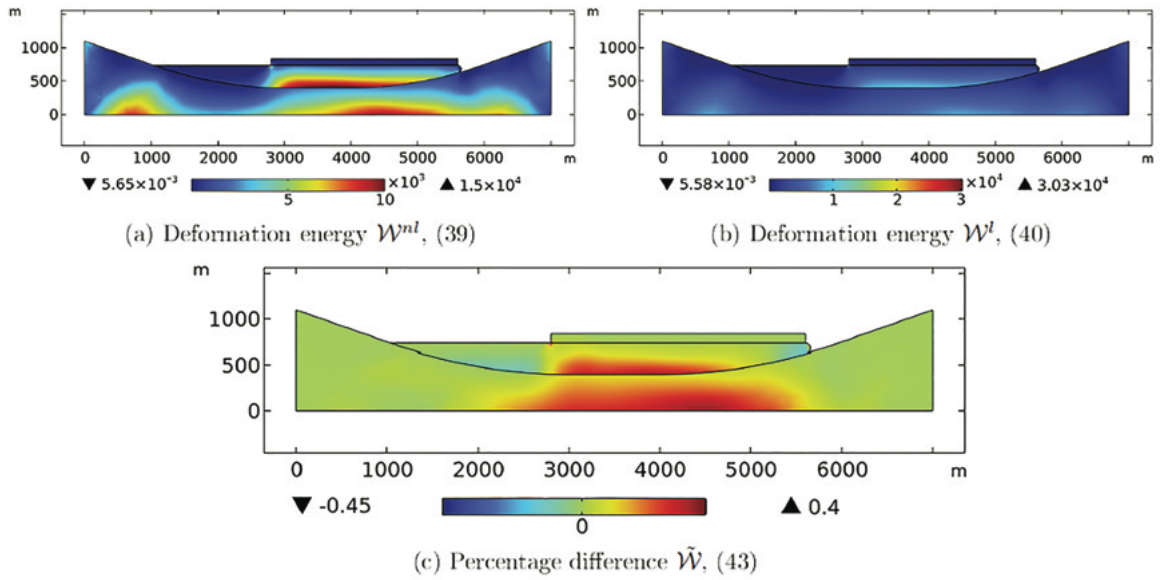


Figure 7. Deformation energy calculated using (a) a non-linear approach, $\mathcal{W}^{nl}$ (Pa), (b) a linear approach, $\mathcal{W}^{l}$ (Pa), and (c) the percentage difference, $\tilde{\mathcal{W}}$, between the non-linear and linear cases at $t = 0.5$s.

Figure 8(c) reveals significantly larger differences. Notably, even after excluding the extreme values, the energy relative difference exceeds 100% close to the boundary layer.

The whole evolution in time of the difference $\tilde{\mathcal{W}}$ with respect the linear case (43), is shown in a video, which is included in the form of supplementary materials.

4.2. Comparison of the kinetic energy fields in linear and non-linear cases and the formation of energy difference boundary layers

Kinetic energy fields serve as key indicators of velocities within a system under consideration and deserve thorough investigation. Following Section 4.1, the highest (or lowest) value of the difference of the kinetic energy, denoted by $\tilde{\mathcal{K}}$ and defined in equation (44), reached in the domain for each instant of time is shown

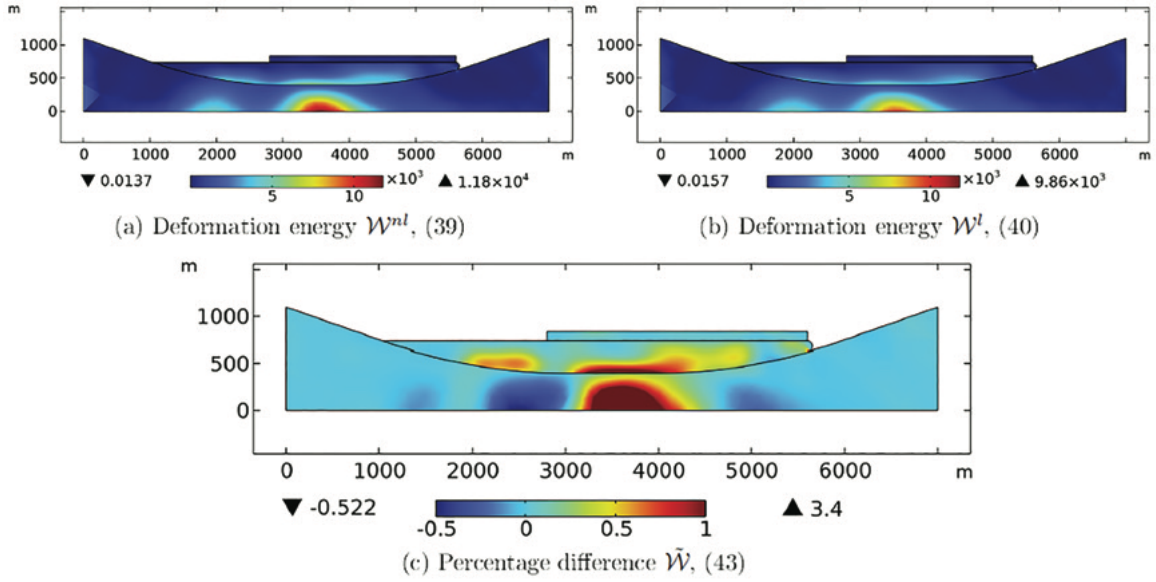


Figure 8. Deformation energy calculated using (a) a non-linear approach, $\mathcal{W}^{nl}$ (Pa), (b) a linear approach, $\mathcal{W}^{l}$ (Pa), and (c) the percentage difference, $\tilde{\mathcal{W}}$, between the non-linear and linear cases at $t = 1.5$s.

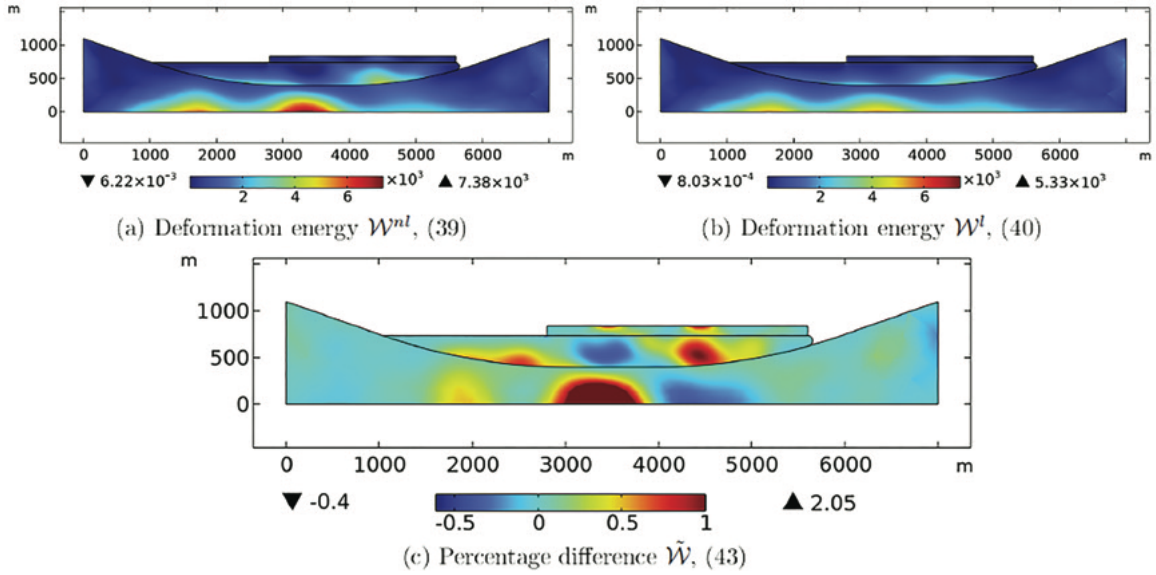


Figure 9. Deformation energy calculated using (a) a non-linear approach, $\mathcal{W}^{nl}$ (Pa), (b) a linear approach, $\mathcal{W}^{l}$ (Pa), and (c) the percentage difference, $\tilde{\mathcal{W}}$, between the non-linear and linear cases at $t = 3$s.

in Figure 10. Then, the contour plots of both the kinetic energy $\mathcal{K}^{nl}$ calculated with our non-linear model and the difference $\tilde{\mathcal{K}}$ are presented in Figures 11–14, 15, and 16.

As seen in Figure 11, the two considered models, linear and non-linear, show a remarkable difference near the boundary where the transition from an harder to a softer layer occurs, i.e., where strong material inhomogeneity occurs. It is worth noting that, just as in the Section 4.1, also for the kinetic energy we focus on the first 3 seconds, i.e., in the time interval when the seismic waves acts on the domain. As one can see, the difference continues to be not negligible also after the third second.

Figures 11(c) and 12(c) reveal that the largest differences in kinetic energy are initially concentrated near the boundary between the bedrock and the softer layer. Subsequently, these differences propagate

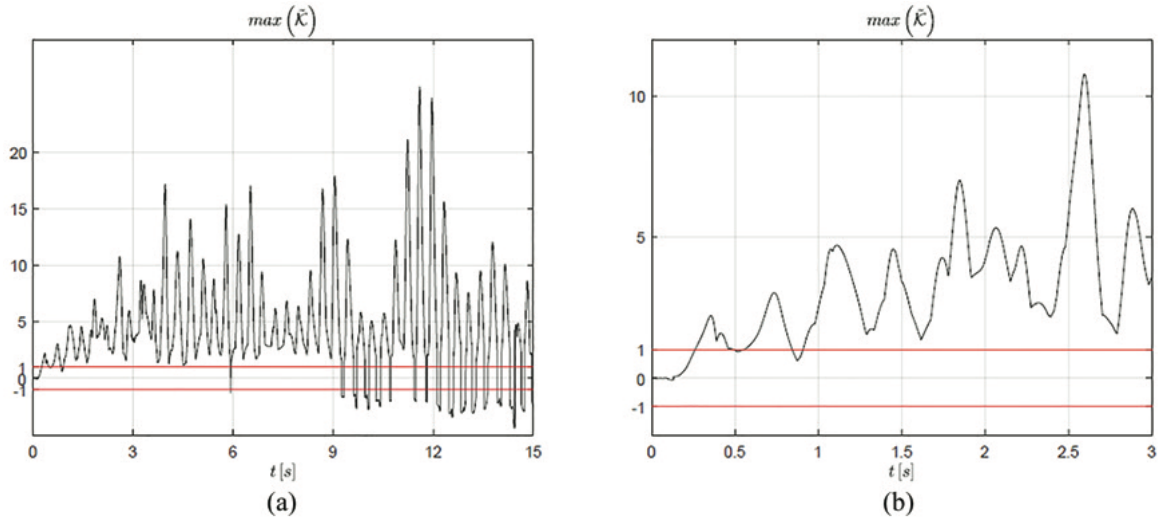


Figure 10. Maximum value of differences $\tilde{\mathcal{K}}$ with respect the time between the two cases (linear and non-linear) for (a) the whole time interval of the performed analyses and (b) a zooming of the first 3 seconds.

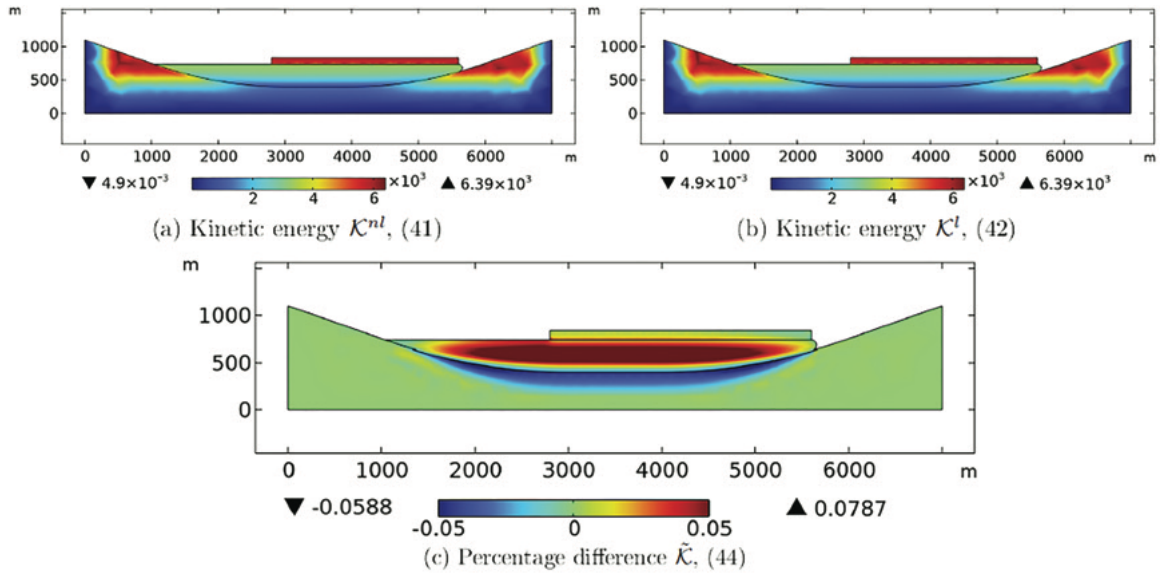


Figure 11. Kinetic energy calculated using (a) a non-linear approach, $\mathcal{K}^{nl}$ (Pa), (b) a linear approach, $\mathcal{K}^{l}$ (Pa), and (c) the percentage difference, $\tilde{\mathcal{K}}$, between the non-linear and linear cases at $t = 0.15$s.

through the softer material towards the rigid top layer. Notably, even during the initial stages of ground excitation by the seismic action, the relative difference is substantial. For example, Figure 12(c) shows that the difference between the non-linear and linear analyses can exceed 100%.

During the first fractions of second, period in which the seismic wave acts on the considered propagation region (remember that the seismic action goes on for 3 s) the higher differences are concentrated at the top of the propagation region, and exactly where the stiffness changes and a material non-linearity is activated. The difference propagates from the harder layer, at the top, to the softer one and vice versa because the reflection of the seismic wave (Figures 12(c) and 13(c)).

During the seismic excitation significant differences between linear and non-linear models are calculated. For example at $t = 2$ s (in Figure 14), it can observe that the main differences are mostly concentrated in the top harder layer, and its value increases noticeably reaching very relevant values as it is shown, for example, in Figure 14(c).

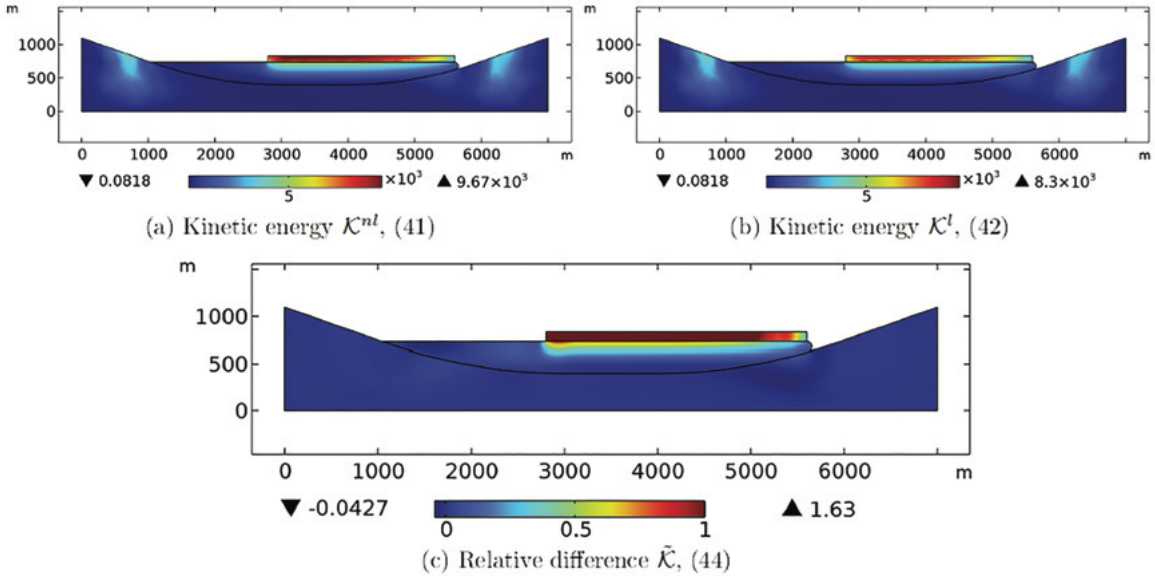


Figure 12. Kinetic energy calculated using (a) a non-linear approach, $\mathcal{K}^{nl}$ (Pa), (b) a linear approach, $\mathcal{K}^{l}$ (Pa), and (c) the percentage difference, $\tilde{\mathcal{K}}$, between the non-linear and linear cases at $t = 0.3$s.

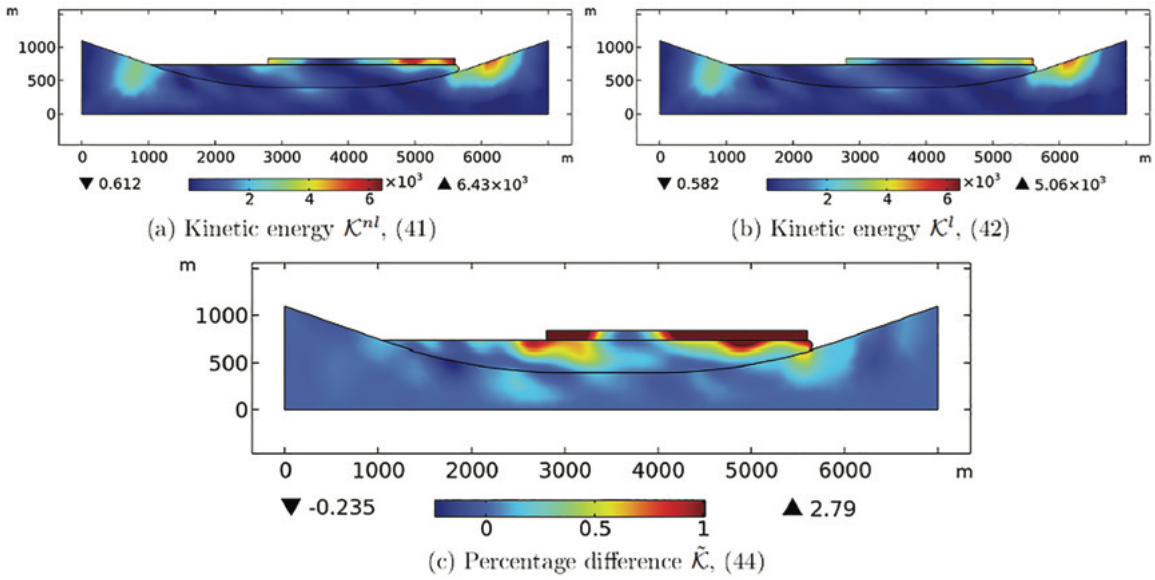


Figure 13. Kinetic energy calculated using (a) a non-linear approach, $\mathcal{K}^{nl}$ (Pa), (b) a linear approach, $\mathcal{K}^{l}$ (Pa), and (c) the percentage difference, $\tilde{\mathcal{K}}$, between the non-linear and linear cases at $t = 1$s.

In Figure 10(b), a big peak of relative difference is clearly evident. To avoid commenting on values that may be due to numerical errors, the contour plot in the neighboring of that instant of time (specifically at $t = 2.6$ s), is shown in Figure 15. At this instant, the value of the difference is very high. Moreover, on the harder top layer a region is clearly visible where the kinetic energy reaches a high value. This makes the difference $\tilde{\mathcal{K}}$ (see the Figure 15(c)) absolutely non-negligible.

At the instant $t = 3$ s (Figure 16), when the seismic excitation ends, its effects continue to be relevant in the region where the wave propagation is studied.

Also after the instant $t = 3$, the differences between the predictions of non-linear and linear models increase significantly as shown in Figure 10(a). This implies that the kinetic energy (and therefore

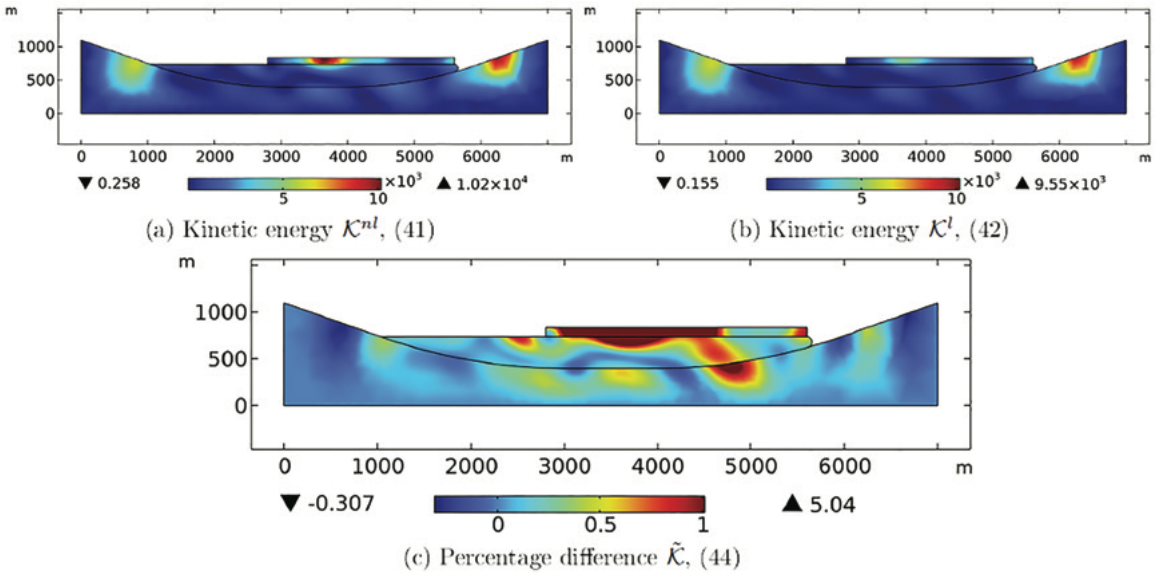


Figure 14. Kinetic energy calculated using (a) a non-linear approach, $\mathcal{K}^{nl}$ (Pa), (b) a linear approach, $\mathcal{K}^{l}$ (Pa), and (c) the percentage difference, $\tilde{\mathcal{K}}$, between the non-linear and linear cases at $t = 2$s.

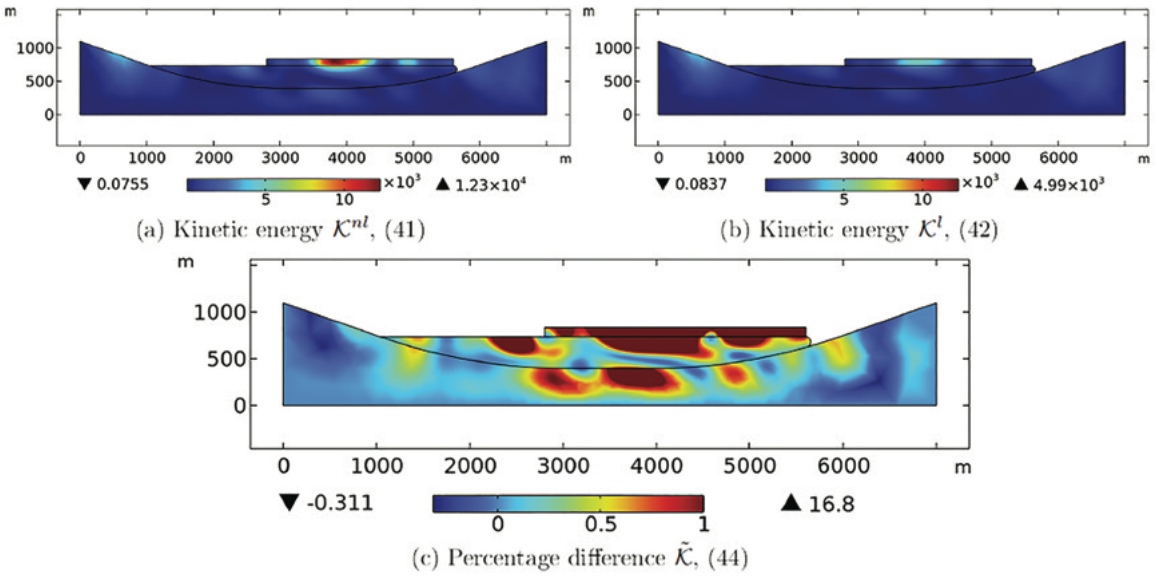


Figure 15. Kinetic energy calculated using (a) a non-linear approach, $\mathcal{K}^{nl}$ (Pa), (b) a linear approach, $\mathcal{K}^{l}$ (Pa), and (c) the percentage difference, $\tilde{\mathcal{K}}$, between the non-linear and linear cases at $t = 2.6$s.

the velocities of each material point) calculated by means of a linear model does not seem to give reliable predictions. It is clear that such differences cannot be overlooked and that more careful modelling assumptions are required. The whole evolution in time of the relative difference $\tilde{\mathcal{K}}$ with respect to the kinetic energy calculated using the non-linear and the linear model (44), is shown with a video included in the form of supplementary materials.

4.3. Comparison of acceleration fields

The accelerations (45) and (46) (either horizontal and vertical) in certain points have been calculated and their differences (47) (between the non-linear and linear models) are seen to be substantial. These results indicate a need to reconsider the current approaches used to predict seismic phenomena. The Figure 17

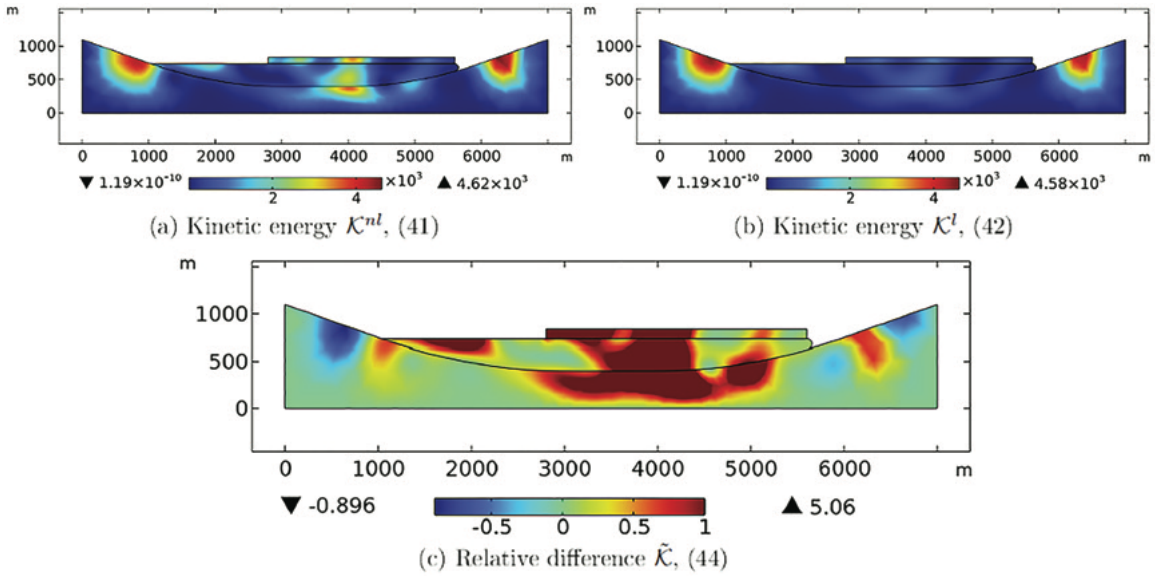


Figure 16. Kinetic energy calculated using (a) a non-linear approach, $\mathcal{K}^{nl}$ (Pa), (b) a linear approach, $\mathcal{K}^{l}$ (Pa), and (c) the percentage difference, $\tilde{\mathcal{K}}$, between the non-linear and linear cases at $t = 3$s.

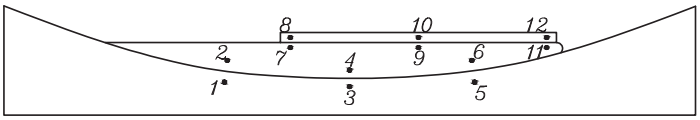


Figure 17. Analyzed points.

shows the points which we have chosen, on the basis of the evidence gathered by Luca et al. [33], in order to compare the predictions of linear and non-linear models: recall that the accelerations difference used for getting the presented comparisons is defined in equation (47).

The first 6 point are chosen near the boundary between the bedrock layer and the softer one, while the next 6 ones are taken close to the boundary between the softer and the top rigid layer. Either the horizontal and vertical accelerations ($\tilde{\ddot{u}}_i$ and $\tilde{\ddot{v}}_i$ respectively for the linear and non-linear cases) and the difference $\tilde{a}_i$ (calculated as in equations (45)–(47)) are plotted in Figures 18–29 for all the points defined in Figure 17. The figures below (namely 18–29) are structured with the following scheme:

- On the left hand side the evolution in time of the accelerations, defined as in equations (45) and (46) and scaled by the gravity acceleration g, of the considered point (for the linear $\tilde{\ddot{u}}_i$ and non-linear $\tilde{\ddot{v}}_i$ case) are shown for each direction (i.e. for $i = 1, 2$).
- On the right hand side the differences $\tilde{a}_i$, denoted as in equation (47), are shown. Notably, these differences are plotted as a fraction of the gravitational acceleration g.

In Figures 18–23, the accelerations of the points close to the boundary between the bedrock and the softer layer are shown.

In Figures 18 and 19, the first couple of points are considered (Point 1 and Point 2). Although, for this couple of points, the differences $\tilde{a}_i$ in equation (47) do not reach their highest values, they are also higher than $0.2g$ which corresponds to an approximate difference of $2\frac{\mathrm{m}}{\mathrm{s}^2}$.

Analyzing the couple of point that follows (i.e. Point 3 (Figure 20) and 4 (Figure 21)), the difference increases by a substantial amount (see the differences of the vertical accelerations), reaching the important value of about $0.7g$. Those clearly are quantities that must warn the modellers and all those whose decisions depend on their predictions.

At the upper boundary, between the softer layer and the harder block, on which the downtown of L'Aquila is located, the values of the differences continue to be very high, having values higher than

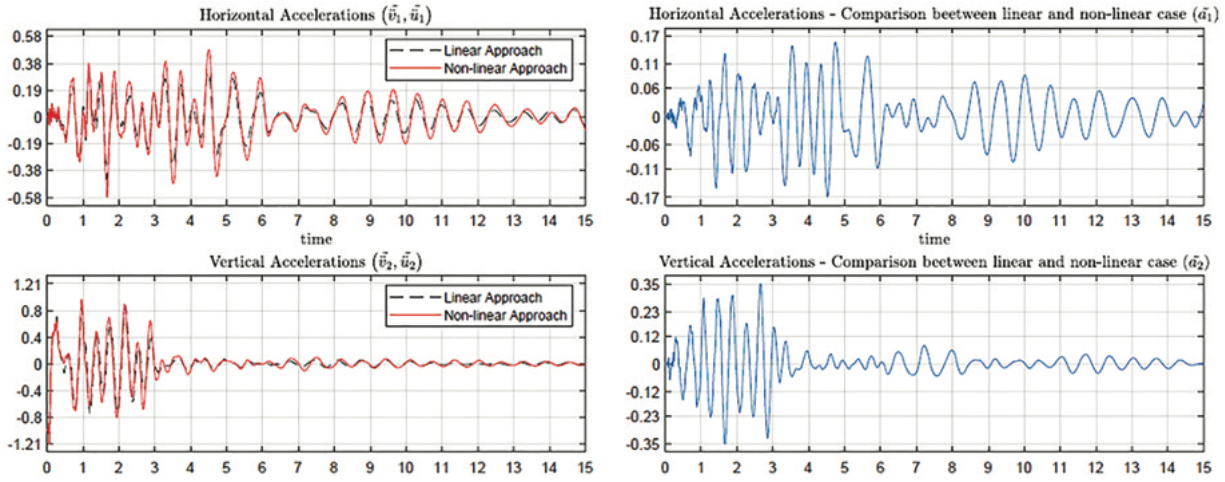


Figure 18. Comparison of the horizontal and vertical accelerations, between the non-linear $\tilde{v}_i$ and linear $\tilde{u}_i$ cases (pictures on the left) and their differences $\tilde{a}_i$ (pictures on the right), gotten by the equations (45)–(47) for the Point 1.

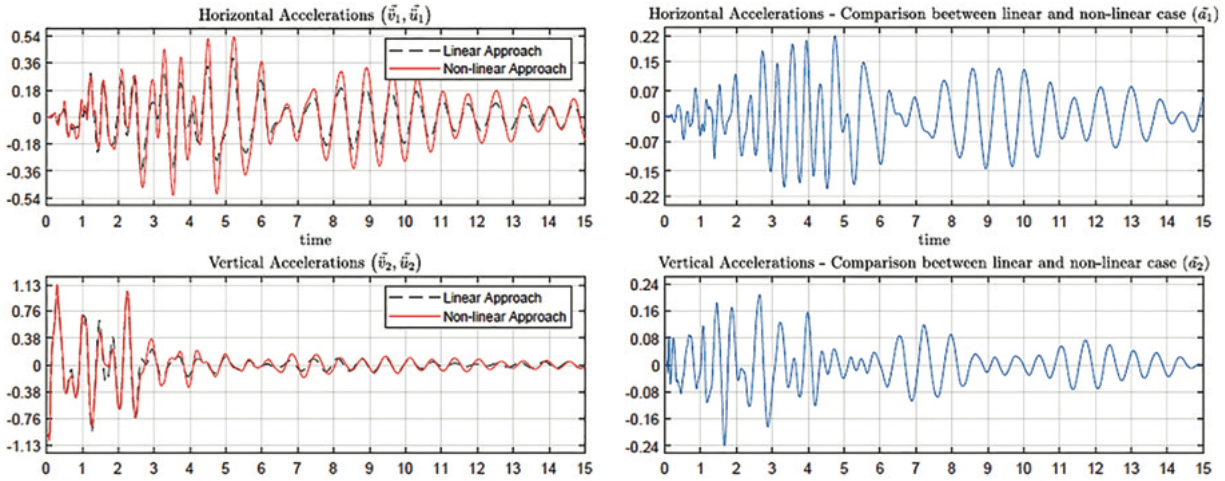


Figure 19. Comparison of the horizontal and vertical accelerations, between the non-linear $\tilde{v}_i$ and linear $\tilde{u}_i$ case, (pictures on the left) and their differences $\tilde{a}_i$ (picture on the right) gotten by the equations (45)–(47) for the Point 2.

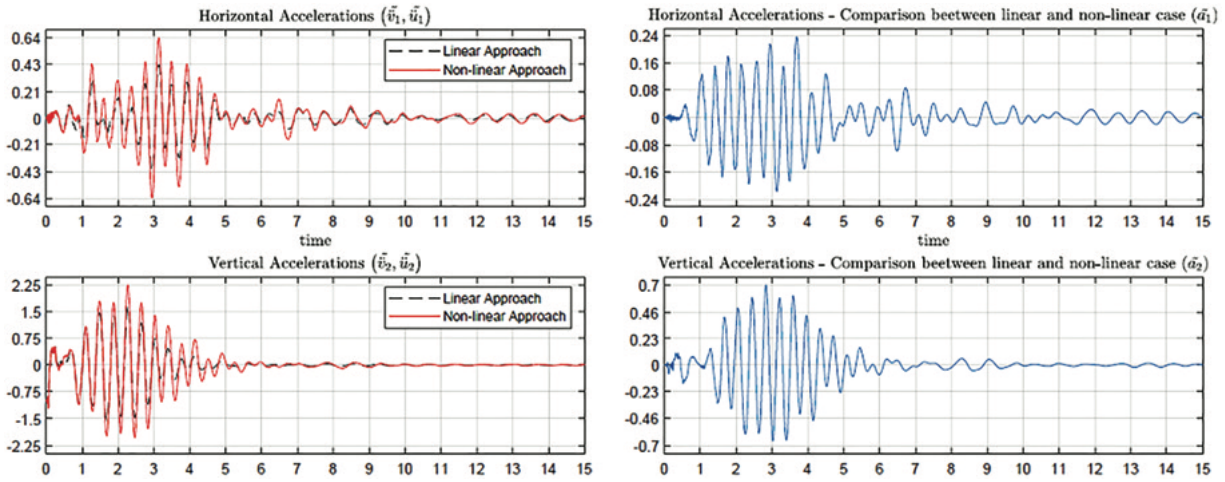


Figure 20. Comparison of the horizontal and vertical accelerations, between the non-linear $\tilde{v}_i$ and linear $\tilde{u}_i$ case, (pictures on the left) and their differences $\tilde{a}_i$ (picture on the right) gotten by the equations (45)–(47) for the Point 3.

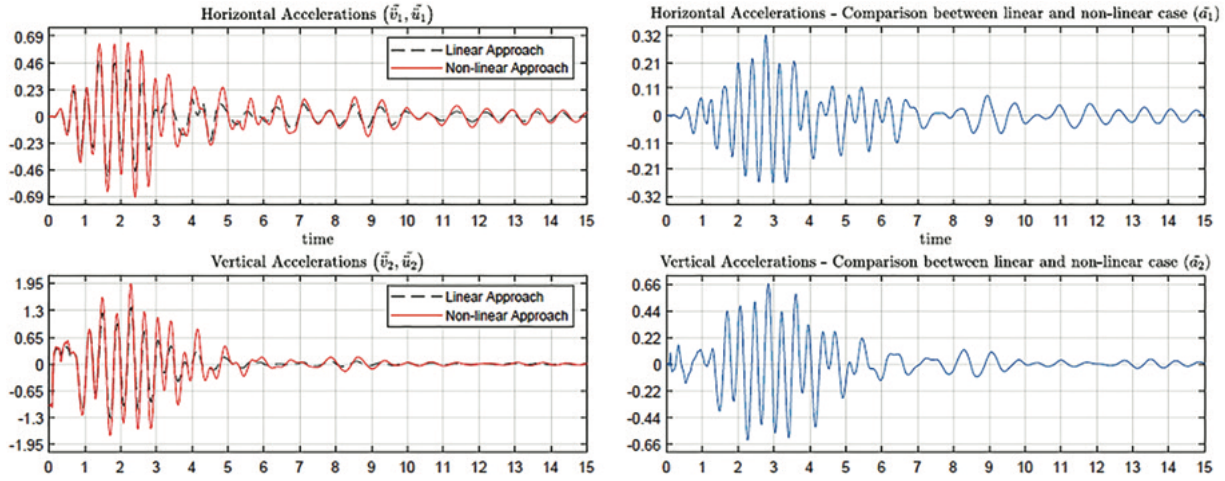


Figure 21. Comparison of the horizontal and vertical accelerations, between the non-linear $\tilde{\vec{v}}_i$ and linear $\tilde{\vec{u}}_i$ case, (pictures on the left) and their differences $\tilde{a}_i$ (picture on the right) gotten by the equations (45)–(47) for the Point 4.

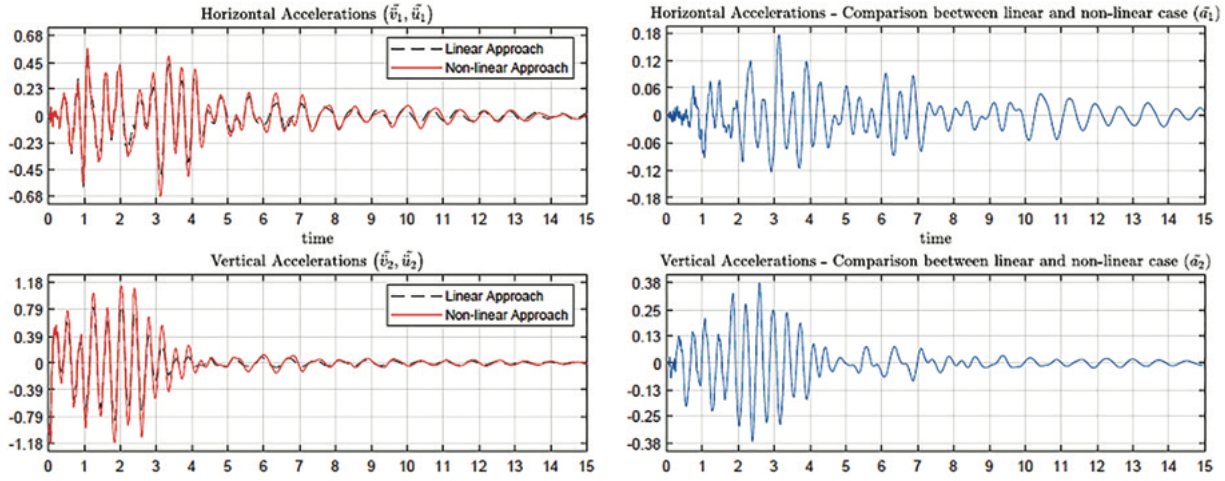


Figure 22. Comparison of the horizontal and vertical accelerations, between the non-linear $\tilde{\vec{v}}_i$ and linear $\tilde{\vec{u}}_i$ case, (pictures on the left) and their differences $\tilde{a}_i$ (picture on the right) gotten by the equations (45)–(47) for the Point 5.

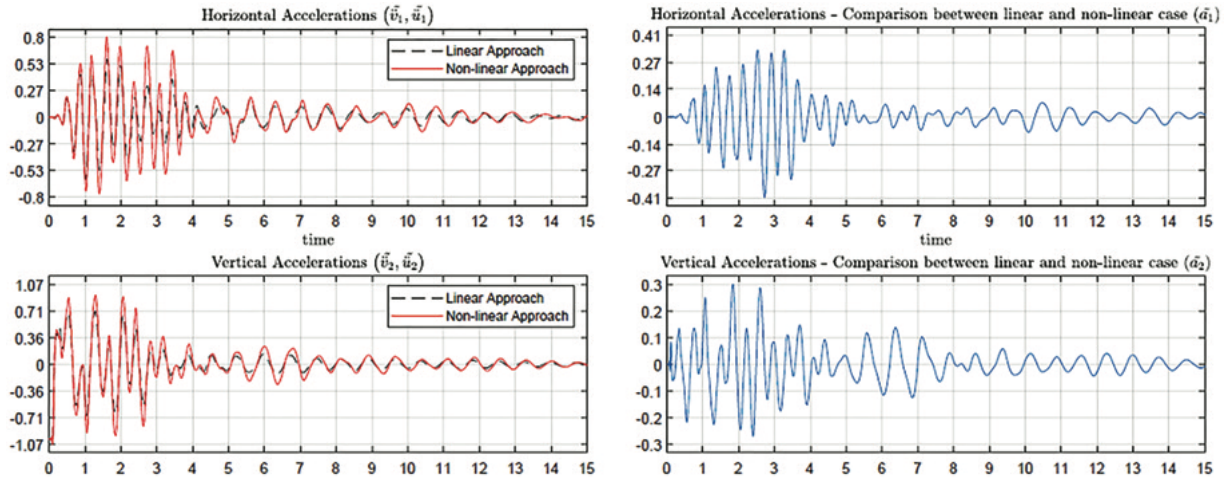


Figure 23. Comparison of the horizontal and vertical accelerations, between the non-linear $\tilde{\vec{v}}_i$ and linear $\tilde{\vec{u}}_i$ case, (pictures on the left) and their differences $\tilde{a}_i$ (picture on the right) gotten by the equations (45)–(47) for the Point 6.

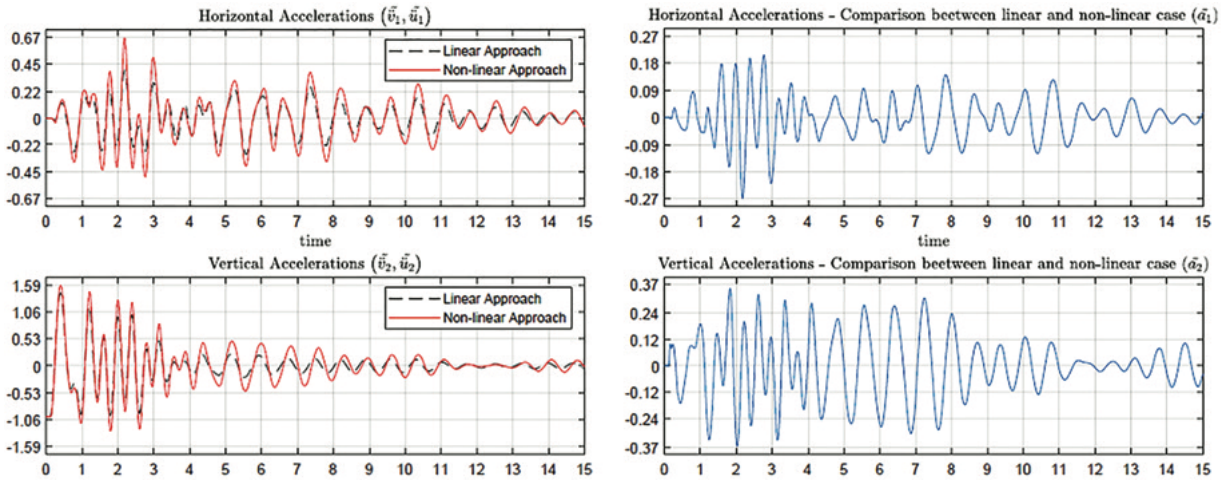


Figure 24. Comparison of the horizontal and vertical accelerations, between the non-linear $\tilde{v}_i$ and linear $\tilde{u}_i$ case, (pictures on the left) and their differences $\tilde{a}_i$ (picture on the right) gotten by the equations (45)–(47) for the Point 7.

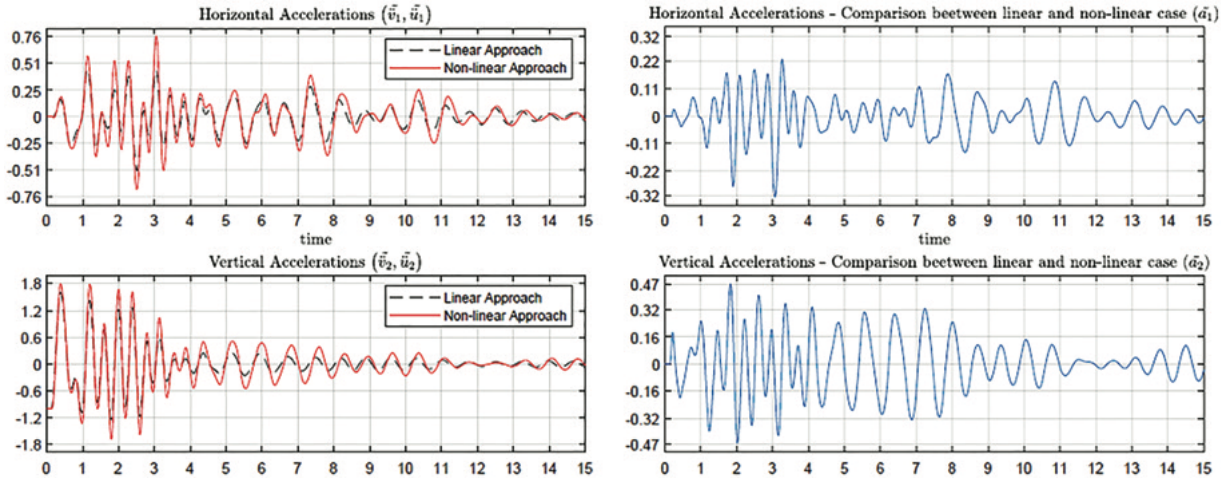


Figure 25. Comparison of the horizontal and vertical accelerations, ween the non-linear $\tilde{v}_i$ and linear $\tilde{u}_i$ case, (pictures on the left) and their differences $\tilde{a}_i$ (picture on the right) gotten by the equations (45)–(47) for the Point 8.

20% of g and, in same case, reaching error around 70% of g (as in the Figures 27 and 29). In the following figures, these strongly high values of the errors are shown.

The observed substantial discrepancies in the acceleration field impose a paradigm change in the choices to be accepted when modelling seismic wave propagation. The non-linear phenomena require a careful consideration due to their proven potential for significant impact. This emphasis is particularly relevant in the light of the findings presented in this work: moreover, by now, modern theoretical and numerical tools allow for the development of predictive analyses based on sophisticated non-linear models.

5. Conclusion

The results of the numerical simulations presented in this work demonstrate that the thesis on which we have based our investigation is correct: linear continuous models are not suitable to describe the effects at ground of large energy earthquakes (Magnitude larger than 6 Mw), in particular when the superficial

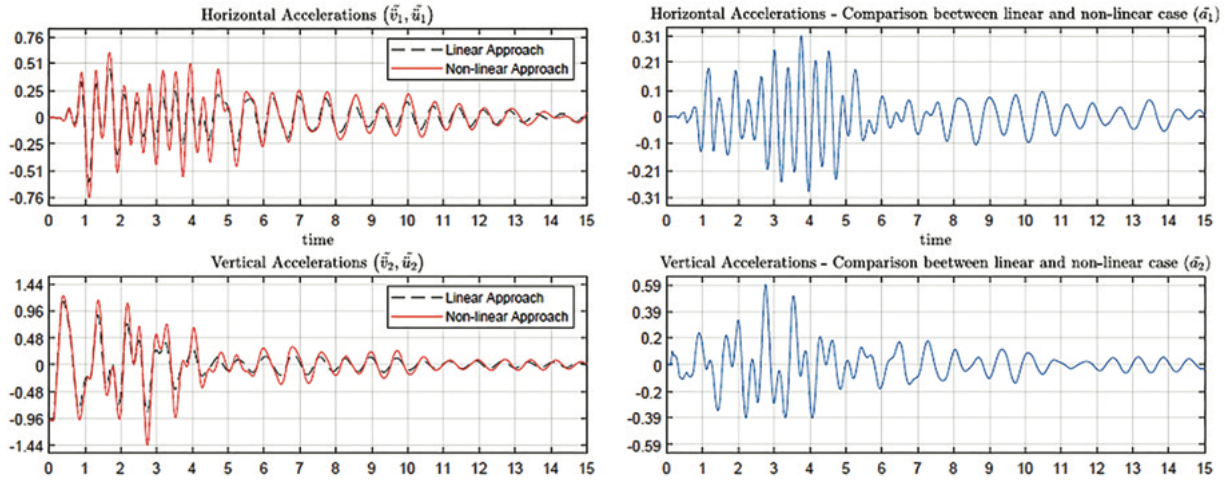


Figure 26. Comparison of the horizontal and vertical accelerations, between the non-linear $\ddot{\vec{v}}_i$ and linear $\ddot{\vec{u}}_i$ case, (pictures on the left) and their differences $\tilde{a}_i$ (picture on the right) gotten by the equationsss (45)–(47) for the Point 9.

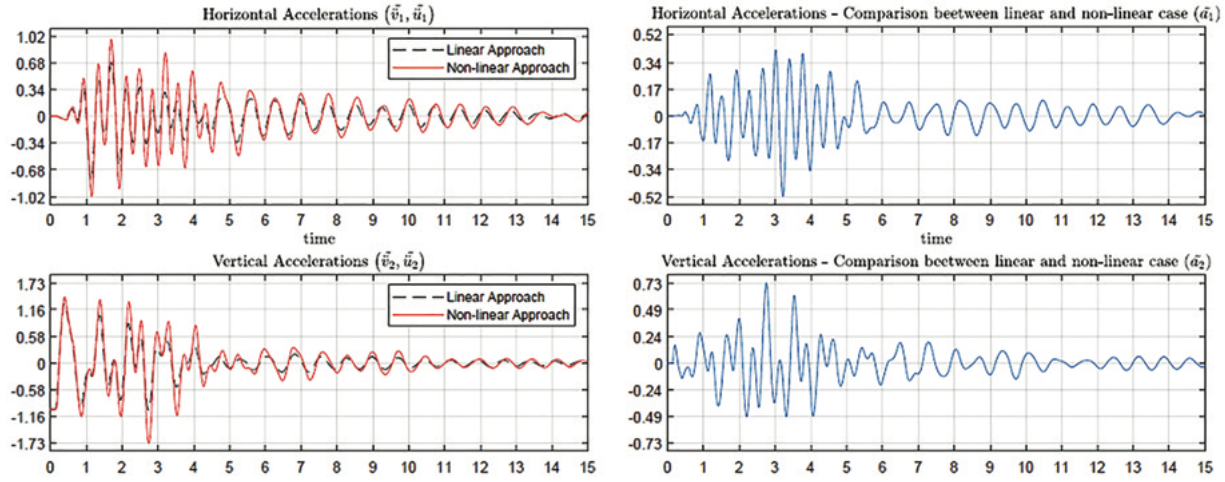


Figure 27. Comparison of the horizontal and vertical accelerations, between the non-linear $\ddot{\vec{v}}_i$ and linear $\ddot{\vec{u}}_i$ case, (pictures on the left) and their differences $\tilde{a}_i$ (picture on the right) gotten by the (45)–(47) for the Point 10.

crust is constituted by inhomogeneous materials. We therefore claim that it is worth considering non-linearities when conducting the analysis of seismic effects on structures and infrastructures. As it shown at the section 4 large differences in the predicted values of deformations, velocities, and accelerations are found when using linear or non-linear models. Moreover, using the non-linear inhomogeneous model presented here we can predict where the highest values of accelerations must be expected, and therefore we believe to have supplied an important guide to future experimental and surveying activities. Moreover the supplied predictions could change the seismic hazard evaluation, to be incorporated in the design prescriptions. Aforementioned differences can make the linear seismic study useless, as not only the predicted values of most relevant quantities are quantitatively different, but also the qualitative features of predicted phenomena may differ drastically. While the preliminary non-linear model presented here requires significant refinement to accurately capture the complexities of the 2009 L'Aquila Earthquake, it demonstrates a superior fit to available experimental data compared to linear models. To further assess the model's capabilities and limitations and to generalize its applicability beyond the specific case of the Aterno River Valley and the 2009 L'Aquila earthquake, a systematic comparison with a wider range of well-documented earthquake events will be the focus of future research. This will allow us to evaluate the model's robustness and identify any limitations in its predictive capabilities under various seismic

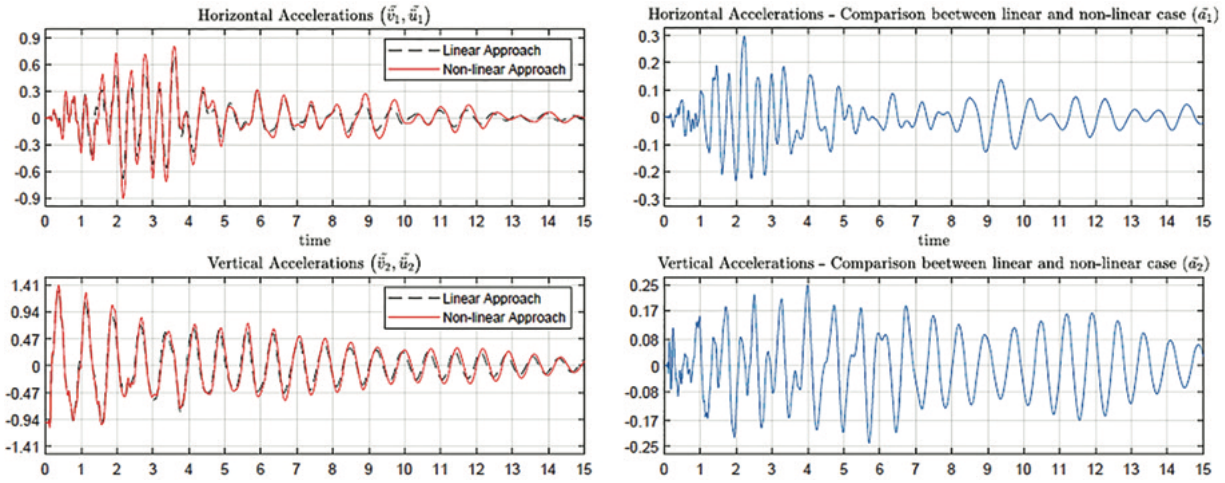


Figure 28. Comparison of the horizontal and vertical accelerations, between the non-linear $\tilde{\tilde{v}}_i$ and linear $\tilde{\tilde{u}}_i$ case, (pictures on the left) and their differences $\tilde{a}_i$ (picture on the right) gotten by the (45)–(47) for the Point 11.

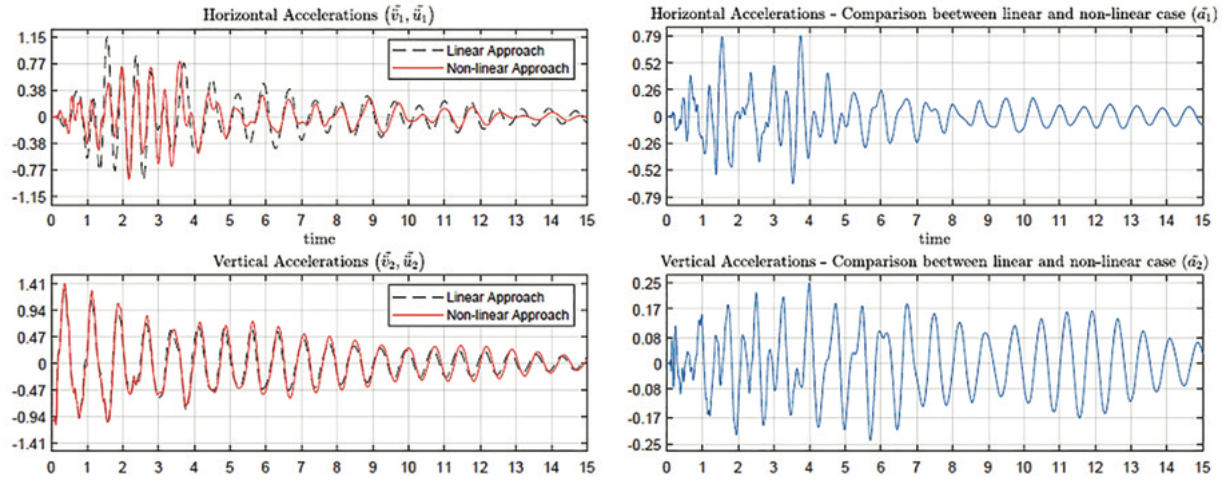


Figure 29. Comparison of the horizontal and vertical accelerations, between the non-linear $\tilde{\tilde{v}}_i$ and linear $\tilde{\tilde{u}}_i$ case, (pictures on the left) and their differences $\tilde{a}_i$ (picture on the right) gotten by the (45)–(47) for the Point 12.

conditions. In particular, we remark that with our 2D geometrically non-linear isotropic model, in which stiffnesses are piecewise constant, we can predict more carefully, both quantitatively and qualitatively, some experimental evidence concerning the measured spectral ratios: while this subject will be carefully described in a future paper, in the present conclusion we will start reporting about preliminary, but very suggestive, results concerning these ratios. This study highlights the significant role of assumptions, such as boundary conditions and material properties, in influencing the accuracy of non-linear models. While acknowledging the potential impact of simplified boundary conditions on the model's ability to replicate experimental data, it is crucial to recognize the complex interplay of various factors governing the behavior of such systems. Geometric non-linearities represent one aspect of this complex interaction, alongside other factors such as material non-linearities (e.g., plasticity, damage, cracking) and more sophisticated boundary conditions. Future investigations will delve deeper into the influence of these additional factors to provide a more comprehensive understanding of the system's behavior. We expect that a predictive modelling for the seismic wave propagation in the Aterno River Valley must include novel and relevant material non-linearity assumptions, considered the proven expected high concentration of deformation energy at the discontinuity interfaces and the present knowledge about the mechanical properties of geomaterials. In fact, only by assuming the simplest geometric non-linearity behaviour, exposed in this work

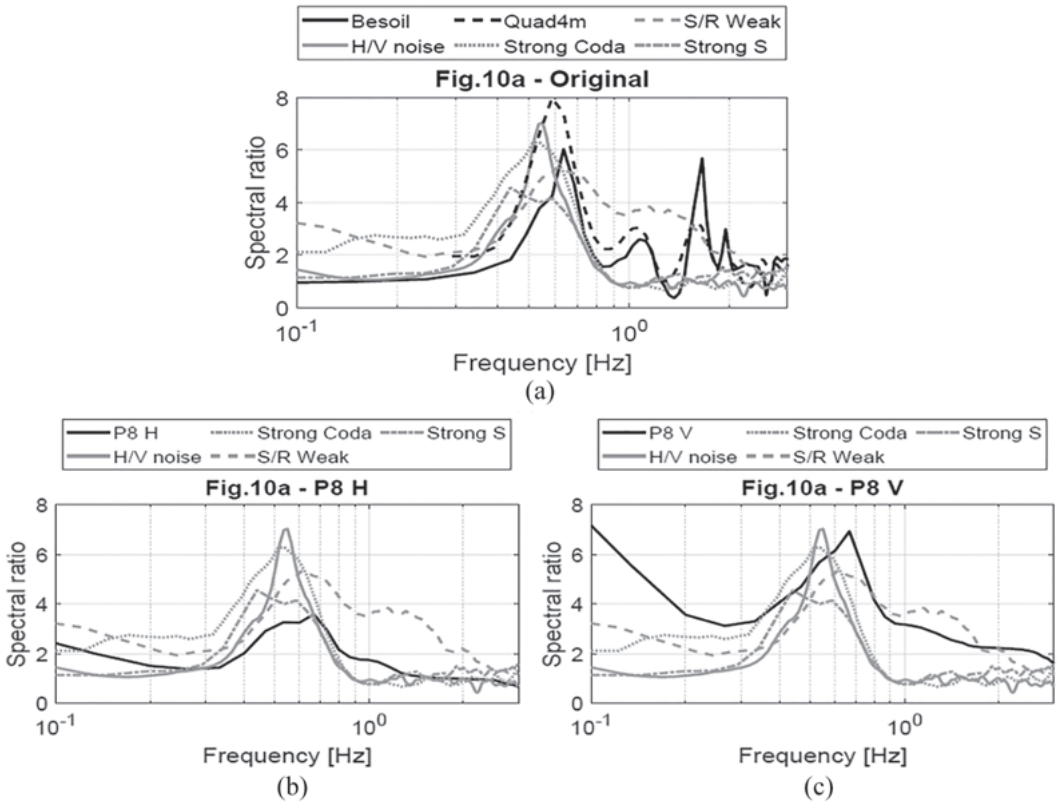


Figure 30. The spectral ratio between the horizontal (b) and vertical (c) non-linear accelerations of the Point 8 and the Point 1 (that is situated into the bedrock, see Figure 17) compared with the Figure 11(a) from Luca et al. [33], shown at the top of the figure (a). The spectral are smoothed with a 50 points moving window.

at the Section 3 (particularly at the Section 3.1), one has shown the highlighted remarkable differences in the obtained predictions, when comparing them with those given by linear models. The results in Section 4.1, relating to the deformation energy, give us important informations about the evolution of the deformative state of the domain $\mathcal{B}$ for each case (either linear and non-linear) showing as the analysis by a non-linear approach implies the possibility to describe relevant and expected phenomena. Also the results show in the Section 4.2 provides an idea of how much more realistic it is to approach the seismic problem with a non-linear modelling. Clearly, the most significative and impactful results for applications are those relating to the accelerations (Section 4.3). These results deserve close attention because high differences are visible and, even more importantly, it clearly shows that the linear approach, almost always, underestimates this quantity. A quantity is the acceleration that represent the most important parameter to consider not only during the study of seismic events but also in anti-seismic structural design. It has to be remarked that a relevant underestimation of experimentally observed accelerations, in the framework of linear theories, seems to have been already underlined in the literature (see EarthQuake Spectra by Luca et al. [33]) Having obtained the prediction for seismic accelerations one can calculate, by means of the fast Fourier transform (using a strong smoothing in order to avoid the peaks generated by numerical errors), the spectrum ratios between the horizontal and vertical accelerations of some specifically chosen points in the considered region (Point 8 and Point 12 in Figure 17) and the horizontal and vertical accelerations spectrum of a reference point (Point 1 in Figure 17); The chosen reference point for spectral ratios is the Point 1 because it stays into the bedrock. These plots are shown at the Figures 30 and 31. Then these ratios have been compared with the Figure 32 that shows the Figure 11 (reproduced here without any change) from Luca et al. [33]. In particular the comparison is carried out with the Figure 11a (for the Point 8 in Figure 30) and the Figure 11b (for the Point 12 in Figure 31). The station named *AQPK*

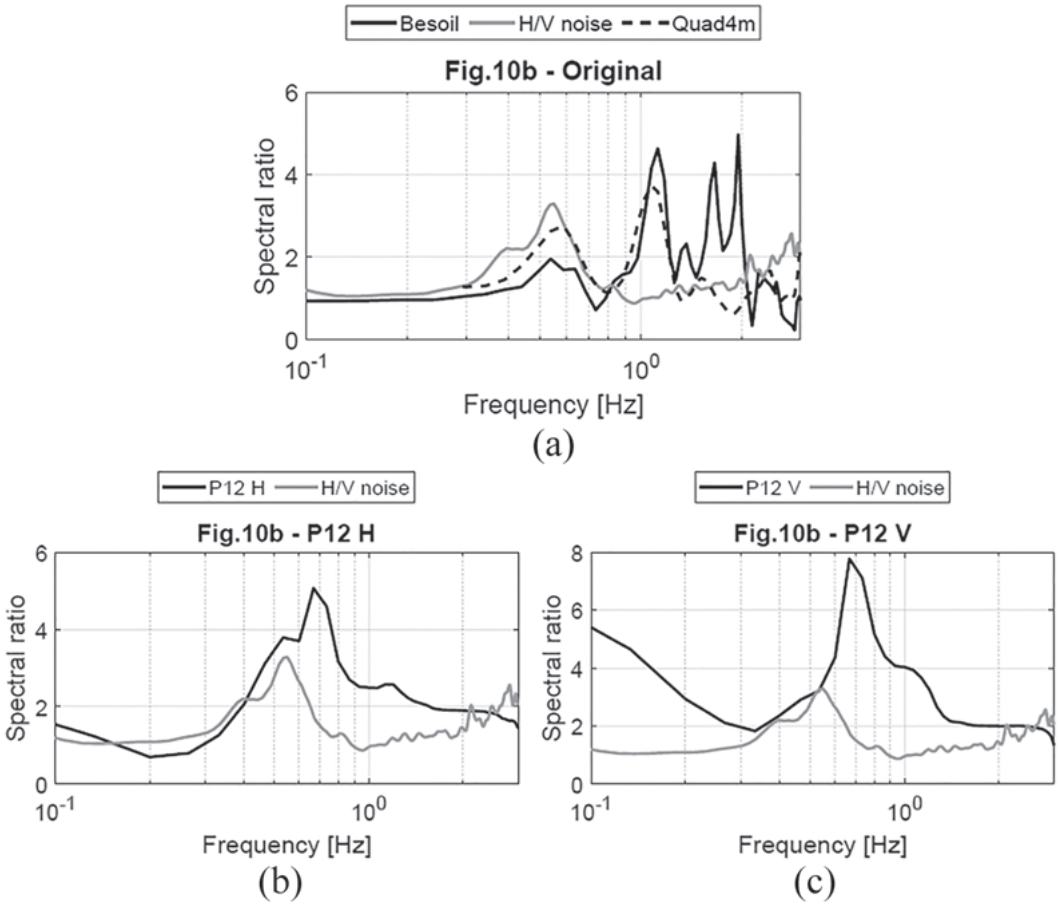


Figure 31. The spectral ratio between the horizontal (b) and vertical (c) non-linear accelerations of the Point 12 and the Point 1 (that is situated into the bedrock, see Figure 17) compared with the Figure 11(b) from Luca et al. [33], shown at the top of the figure (a). The spectral are smoothed with a 50 points moving window.

in Figure 32 is located not far from the Point 8 whereas the station named *GDIF*in Figure 32 is located not far from the Point 12.

Comparing the Figure 30 with the Figure 11(a) by Luca et al. [33], it is clear that the non-linear analysis fits better with the experimental data than the linear analysis. Figure 10(a) and (b) of Luca et al. [33] (both shown in Figure 32) compare QUAD4M and BESOIL results, and confirm that both codes are able to predict the low-frequency amplification peak in the deepest part of the basin. BESOIL solutions are more complex because the code allows higher frequencies. The high-frequency behavior found using BESOIL code cannot be considered physically significant because the model used is not realistic at a small scale. Also the QUAD4M results seem to be less sensitive to frequencies higher than 1.5 Hz because of the grid spacing used. Furthermore, non-linear analysis removes the non-experimentally observed peaks in the frequency range higher than 1Hz that were found by Luca et al. [33], which used the linear codes (*Besoil* and *Quad4m*). The non-linear approach naturally cuts off these peaks. Future analysis will detail the reasons for which this qualitative property of non-linear models holds and will give stronger motivations for the use of spectral ratios to validate continuum models for the "seismic wave propagation" zone studied in the present paper.

A 2D model, while insufficient to fully capture the complex 3D geological structure of the Aterno River Valley, offers a computationally efficient approach to investigate the influence of non-linearity on system behaviour under large excitations. While acknowledging the inherent limitations of such a simplification, we argue that this 2D model effectively demonstrates the significant role of non-linearity. Future investigations will need to refine the just mentioned analysis, by introducing a careful and more realistic

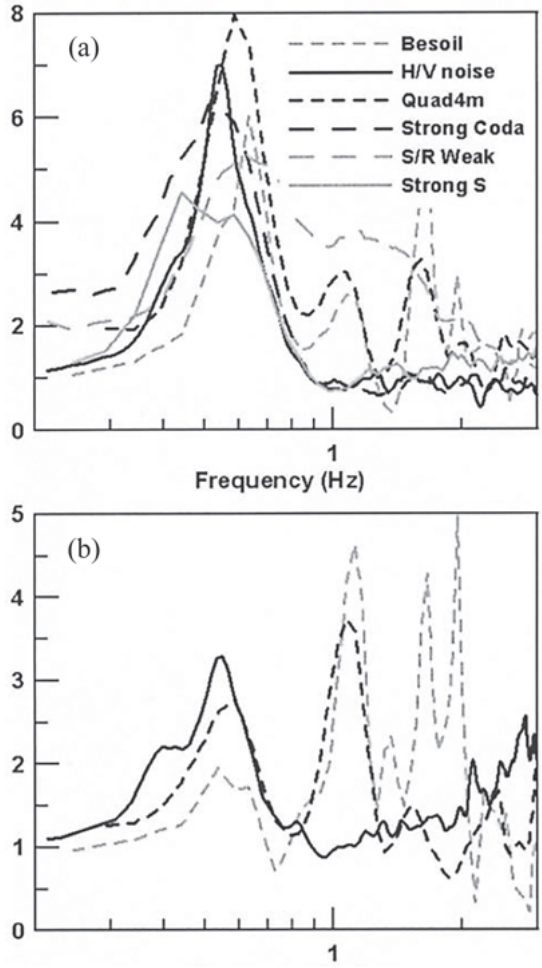


Figure 32. Figure 11 from Luca et al. [33] (figure and caption are not modified): *"(a) QUAD4M and BESOIL solutions compared with H/V applied to strong-motion and microtremor data and S/R applied to weak-motion data at the AQPK site. (b) QUAD4M and BESOIL solutions compared with H/V applied to microtremor data at the GDIF site. The line symbol are the same in both (a) and (b)"*

3D modelling, developing appropriate numerical method for non-linear system [120,121], enlarging the region where wave propagation is studied, in order to include the sites where other accelerometer stations of National Survey Network of Civil Protection were localised. These stations have been active since the middle of 1990s and have recorded a large number of earthquakes having different magnitude and hypocenters. Moreover in order to get a careful prediction of origins and onset of the seismic actions, from a geological and mechanical point of view, models of tectonic dynamic crack propagation must be considered, generalising and adapting the methods presented by Barchiesi et al. [122], Fabbrocino et al. [123], Placidi and Barchiesi [124], Placidi et al. [125], Turco et al. [126]. In this way, it will be possible to extend the regions where wave propagation is predicted, to include also hypocenters. We also expect that the presented results will allow for a more effective design for the new structures (and for the restoration of the damaged one) by exploiting the also knowledge and the conceptual tools which are already available and were used, e.g., by Masi et al. [127], Saitta et al. [128], Salvatori [129]. In conclusion, it is clearly well-established that the computational cost associated with non-linear analysis is significantly higher than that of linear one. Consequently, it is reasonable to question the extent to which such computational demands are justified in the study of seismic phenomena. However, the results obtained from our non-linear analysis provide compelling evidence to support this approach. These findings cannot be disregarded and warrant careful consideration, as they offer a more accurate means of predicting the effects of high-energy seismic events given the current state of technology. As long as our non-linear

models continue to yield results that deviate significantly from those obtained through linear analysis, while simultaneously demonstrating a high degree of agreement with experimental data, we believe that further refinement of these models is warranted. Such refinements are essential for enhancing the safety of human life and improving the design of structures.

Funding

The author(s) received no financial support for the research, authorship, and/or publication of this article.

ORCID iDs

Ivan Giorgio https://orcid.org/0000-0002-0044-9188
Luca Placidi https://orcid.org/0000-0002-1461-3997

References

[1] Eremeyev, VA, Alzahrani, FS, Cazzani, A, et al. On existence and uniqueness of weak solutions for linear pantographic beam lattices models. *Continuum Mech Therm* 2019; 31(6): 1843–1861.
[2] Ciallella, A, Pasquali, D, D'Annibale, F, et al. Shear rupture mechanism and dissipation phenomena in bias-extension test of pantographic sheets: numerical modeling and experiments. *Math Mech Solids* 2022; 27(10): 2170–2188.
[3] Laudato, M, and Barchiesi, E. Non-linear dynamics of pantographic fabrics: modelling and numerical study. In: Sumbatyan, MA (ed.) *Wave dynamics, mechanics and physics of microstructured metamaterials: Theoretical and experimental methods*. Cham: Springer, 2019, pp. 241–254.
[4] dell'isola, F, Corte, AD, Battista, A, et al. Extensible beam models in large deformation under distributed loading: a numerical study on multiplicity of solutions. In: Altenbach, H, Müller, WH, and Abali, BE (eds) *Higher gradient materials and related generalized continua*. Cham: Springer, 2019, pp. 19–41.
[5] Eremeyev, V, and Zubov, L. On constitutive inequalities in nonlinear theory of elastic shells. *J Appl Math Mech* 2007; 87(2): 94–101.
[6] Abali, BE, Müller, WH, and Eremeyev, VA. Strain gradient elasticity with geometric nonlinearities and its computational evaluation. *Mech Adv Mater Modern Process* 2015; 1(1): 1–11.
[7] Eremeyev, VA, Cazzani, A, and Dell'isola, F. On nonlinear dilatational strain gradient elasticity. *Continuum Mech Therm* 2021; 33(4): 1429–1463.
[8] Eremeyev, VA, and Pietraszkiewicz, W. The nonlinear theory of elastic shells with phase transitions. *J Elasticity* 2004; 74(1): 67–86.
[9] Eugster, SR. Numerical analysis of nonlinear wave propagation in a pantographic sheet. *Math Mech Complex Syst* 2022; 9(3): 293–310.
[10] Turco, E, Barchiesi, E, Ciallella, A, et al. Nonlinear waves in pantographic beams induced by transverse impulses. *Wave Motion* 2022; 115: 103064.
[11] Eremeyev, VA, Lebedev, LP, and Cloud, MJ. Acceleration waves in the nonlinear micromorphic continuum. *Mech Res Commun* 2018; 93: 70–74.
[12] Abd-alla, A, Alshaikh, F, Giorgio, I, et al. A mathematical model for longitudinal wave propagation in a magnetoelastic hollow circular cylinder of anisotropic material under the influence of initial hydrostatic stress. *Math Mech Solids* 2016; 21(1): 104–118.
[13] Abali, BE, and Barchiesi, E. Additive manufacturing introduced substructure and computational determination of metamaterials parameters by means of the asymptotic homogenization. *Continuum Mech Therm* 2021; 33(4): 993–1009.
[14] Cefis, N, Fedele, R, and Beghi, MG. An integrated methodology to estimate the effective elastic parameters of amorphous tio2 nanostructured films, combining sem images, finite element simulations and homogenization techniques. *Mech Res Commun* 2023; 131: 104153.
[15] Fedele, R, and Maier, G. Flat-jack tests and inverse analysis for the identification of stress states and elastic properties in concrete dams. *Meccanica* 2007; 42(4): 387–402.
[16] Fedele, R, Sessa, S, and Valoroso, N. Image correlation-based identification of fracture parameters for structural adhesives. *Tech Mech-Eur J Eng Mech* 2019; 32(2–5): 195–204.
[17] Darban, H, Luciano, R, Caporale, A, et al. Higher modes of buckling in shear deformable nanobeams. *Int J Eng Sci* 2020; 154: 103338.
[18] Bormann, P, Baumbach, M, Bock, G, et al. Seismic sources and source parameters. In: Bormann P (ed.) *New manual of seismological observatory practice (NMSOP-1)*. Potsdam: Deutsches GeoForschungsZentrum GFZ, 2009, pp. 1–94.
[19] Turco, E, and Barchiesi, E. Kinematically-triggered nonlinear vibrations of Hencky-type pantographic sheets. *Math Mech Complex Syst* 2021; 9: 311–335.

[20] Luciano, R, Darban, H, Bartolomeo, C, et al. Free flexural vibrations of nanobeams with non-classical boundary conditions using stress-driven nonlocal model. *Mech Res Commun* 2020; 107: 103536.
[21] Mancusi, G, Fabbrocino, F, Feo, L, et al. Size effect and dynamic properties of 2D lattice materials. *Compos B Eng* 2017; 112: 235–242.
[22] Funari, MF, Spadea, S, Fabbrocino, F, et al. A moving interface finite element formulation to predict dynamic edge debonding in FRP-strengthened concrete beams in service conditions. *Fibers* 2020; 8(6): 42.
[23] Turco, E, and Barchiesi, E. Kinematically triggered nonlinear vibrations of Hencky-type pantographic sheets. *Math Mech Complex Syst* 2022; 9(3): 311–335.
[24] Javili, A, Dell'isola, F, and Steinmann, P. Geometrically nonlinear higher-gradient elasticity with energetic boundaries. *J Mech Phys Solids* 2013; 61(12): 2381–2401.
[25] Placidi, L, Barchiesi, E, Dell'isola, F, et al. On a hemi-variational formulation for a 2D elasto-plastic-damage strain gradient solid with granular microstructure. *Math Eng* 2022; 5: 1–24.
[26] Scrofani, A, Barchiesi, E, Chiaia, B, et al. Fluid diffusion related aging effect in a concrete dam modeled as a Timoshenko beam. *Math Mech Complex Syst* 2023; 11(2): 313–334.
[27] Chiaia, B, Biagi, VD, and Placidi, L. A damaged non-homogeneous Timoshenko beam model for a dam subjected to aging effects. *Math Mech Solids* 2021; 26(5): 694–707.
[28] Luca, GD, Scarpa, R, Filippi, L, et al. A detailed analysis of two seismic sequences in Abruzzo, Central Apennines, Italy. *J Seismol* 2000; 4(1): 1–21.
[29] Scognamiglio, L, Tinti, E, and Quintiliani, M. Time Domain Moment Tensor (TDMT) [Data set]. Istituto Nazionale di Geofisica e Vulcanologia (INGV), 2006. DOI: 10.13127/TDMT.
[30] Chiarabba, C, Amato, A, Anselmi, M, et al. The 2009 L'Aquila (Central Italy) mw6.3 earthquake: main shock and aftershocks. *Geophys Res Lett* 2009; 36(18): 1–6.
[31] Rovida, A, Locati, M, Camassi, R, et al. Catalogo Parametrico dei Terremoti Italiani (CPTI15), versione 4.0 [Data set]. Istituto Nazionale di Geofisica e Vulcanologia (INGV), 2022. DOI: 10.13127/cpti/cpti15.4.
[32] Rovida, A, Locati, M, Camassi, R, et al. The Italian earthquake catalogue CPTI15. *B Earthq Eng* 2020; 18(7): 2953–2984.
[33] Luca, GD, Marcucci, S, Milana, G, et al. Evidence of low-frequency amplification in the city of L'Aquila, Central Italy, through a multidisciplinary approach including strong- and weak-motion data, ambient noise, and numerical modelling. *Bull Seismol Soc Am* 2005; 95(4): 1469–1481.
[34] Milana, G, Azzara, RM, Bertrand, E, et al. The contribution of seismic data in microzonation studies for downtown L'Aquila. *B Earthq Eng* 2011; 9(3): 741–759.
[35] Puglia, R, Ditommaso, R, Pacor, F, et al. Frequency variation in site response as observed from strong motion data of the L'Aquila (2009) seismic sequence. *B Earthq Eng* 2011; 9(3): 869–892.
[36] Ragozzino, E. Nonlinear seismic response in the western L'Aquila basin (Italy): numerical FEM simulations vs. ground motion records. *Eng Geol* 2014; 174: 46–60.
[37] Ferraro, A, Grasso, S, Maugeri, M, et al. Seismic response analysis in the southern part of the historic centre of the city of L'Aquila (Italy). *Soil Dyn Earthq Eng* 2016; 88: 256–264.
[38] Giulio, GD, Gaudiosi, I, Cara, F, et al. Shear-wave velocity profile and seismic input derived from ambient vibration array measurements: the case study of downtown L'Aquila. *Geophys J Int* 2014; 198: 848–866.
[39] Tallini, M, Sardo, LL, and Spadi, M. Seismic site characterisation of red soil and soil-building resonance effects in L'Aquila downtown (Central Italy). *Bull Eng Geol Environ* 2020; 79(8): 4021–4034.
[40] Bergamaschi, F, Cultrera, G, Azzara, R, et al. Evaluation of site effects in the Aterno river valley (Central Italy) from aftershocks of the 2009 L'Aquila earthquake. *B Earthq Eng* 2011; 9: 697–715.
[41] Calderoni, G, Rovelli, A, and Giovambattista, RD. Large amplitude variations recorded by an on-fault seismological station during the L'Aquila earthquakes: evidence for a complex fault-induced site effect. *Geophys Res Lett* 2010; 37: L24305.
[42] Akinci, A, Malagnini, L, and Sabetta, F. Characteristics of the strong ground motions from the 6 April 2009 L'Aquila earthquake, Italy. *Soil Dyn Earthq Eng* 2010; 30(5): 320–335.
[43] Lanzo, G, and Pagliaroli, A. Seismic site effects at near-fault strong-motion stations along the Aterno River Valley during the Mw=6.3 2009 L'Aquila earthquake. *Soil Dyn Earthq Eng* 2012; 40: 1–14.
[44] Bindi, D, Pacor, F, Luzi, L, et al. The Mw 6.3, 2009 L'Aquila earthquake: source, path and site effects from spectral analysis of strong motion data. *Geophys J Int* 2009; 179(3): 1573–1579.
[45] Ameri, G, Bindi, D, Pacor, F, et al. The 2009 April 6, Mw 6.3, L'Aquila (Central Italy) earthquake: finite-fault effects on intensity data. *Geophys J Int* 2011; 186(2): 837–851.
[46] Ugurhan, B, Askan, A, Akinci, A, et al. Strong-ground-motion simulation of the 6 April 2009 L'Aquila, Italy, earthquake. *Bull Seismol Soc Am* 2012; 102(4): 1429–1445.
[47] Felicetta, C, Russo, E, D'Amico, M, et al. Italian Accelerometric Archive v4.0. Istituto Nazionale di Geofisica e Vulcanologia, Dipartimento della Protezione Civile Nazionale, 2023. DOI: 10.13127/itaca.4.0.
[48] Celebi, M, Bazzurro, P, Chiaraluce, L, et al. Recorded motions of the 6 April 2009 Mw 6.3 L'Aquila, Italy, earthquake and implications for building structural damage: overview. *Earthq Spectra* 2010; 26(3): 651–684.

[49] Stewart, JP, Lanzo, G, Pagliaroli, A, et al. Ground motion recordings from the Mw 6.3 2009 L'Aquila earthquake in Italy and their engineering implications. *Earthq Spectra* 2012; 28(1): 317–345.
[50] Rupakhety, R, and Sigbjörnsson, R. A note on the L'Aquila earthquake of 6 April 2009: permanent ground displacements obtained from strong-motion accelerograms. *Soil Dyn Earthq Eng* 2010; 30(4): 215–220.
[51] Augenti, N, and Parisi, F. Learning from construction failures due to the 2009 L'Aquila, Italy, earthquake. *J Perform Constr Fac* 2010; 24: 536–555.
[52] Cucci, L, and Tertulliani, A. Clues for a relation between rotational effects induced by the 2009 Mw 6.3 L'Aquila (Central Italy) earthquake and site and source effects. *B Seismol Soc Am* 2011; 101: 1109–1120.
[53] Tertulliani, A, Leschiutta, I, Bordoni, P, et al. Damage distribution in L'Aquila city (Central Italy) during the 6 April 2009 earthquake. *Bull Seismol Soc Am* 2012; 102(4): 1543–1553.
[54] Mannella, A, Macerola, L, Martinelli, A, et al. The local seismic response and the effects of the 2016 Central Italy earthquake on the buildings of L'Aquila downtown. *Boll Geofis Teor Appl* 2019; 60(2): 263–276.
[55] Douglas, J, Monfort, D, Negulescu, C, et al. Limits on the potential accuracy of earthquake risk evaluations using the L'Aquila (Italy) earthquake as an example. *Ann Geophys* 2015; 58: S0214.
[56] Vannoli, P, Burrato, P, and Valensise, G. The seismotectonics of the Po Plain (Northern Italy): tectonic diversity in a blind faulting domain. *Pure Appl Geophys* 2015; 172: 1105–1142.
[57] Tertulliani, A, Arcoraci, L, Berardi, M, et al. An application of EMS98 in a medium-sized city: the case of L'Aquila (Central Italy) after the April 6, 2009 Mw 6.3 earthquake. *B Earthq Eng* 2011; 9: 67–80.
[58] Blumetti, AM, Manna, PD, Comerci, V, et al. Paleoseismicity of the San Demetrio ne' Vestini fault (L'Aquila Basin, Central Italy): implications for seismic hazard. *Quatern Int* 2017; 451: 129–142.
[59] Bruno, PPG, Villani, F, and Improta, L. High-resolution seismic imaging of fault-controlled basins: a case study from the 2009 Mw 6.1 Central Italy earthquake. *Tectonics* 2022; 41(4): e2022TC007207.
[60] Civico, R, Sapia, V, Giulio, GD, et al. Geometry and evolution of a fault-controlled quaternary basin by means of TDEM and single-station ambient vibration surveys: the example of the 2009 L'Aquila earthquake area, Central Italy. *J Geophys Res Solid Earth* 2017; 122(3): 2236–2259.
[61] Nocentini, M, Cosentino, D, Spadi, M, et al. Plio-Quaternary geology of the Paganica-San Demetrio-Castelnuovo Basin (Central Italy). *J Maps* 2018; 14: 411–420.
[62] Spadi, M, Tallini, M, Albano, M, et al. New insights on bedrock morphology and local seismic amplification of the castelnuovo village (L'Aquila Basin, Central Italy). *Eng Geol* 2022; 297: 106506.
[63] Tallini, M, Spadi, M, Cosentino, D, et al. High-resolution seismic reflection exploration for evaluating the seismic hazard in a Plio-Quaternary intermontane basin (L'Aquila downtown, Central Italy). *Quatern Int* 2019; 532: 34–47.
[64] Cultrera, G, Mucciarelli, M, and Parolai, S. The L'Aquila earthquake—a view of site effects and building behavior from temporary networks. *B Earthq Eng* 2011; 9(3): 691–695.
[65] Monaco, P, and Amoroso, S. Site effects from the building scale to the seismic microzonation scale: examples from the experience of L'Aquila. *Procedia Engineer* 2016; 158: 517–522.
[66] Nunziata, C, and Costanzo, M. Ground motion modeling for site effects at L'Aquila and middle Aterno river valley (Central Italy) for the Mw 6.3, 2009 earthquake. *Soil Dyn Earthq Eng* 2014; 61–62: 107–123.
[67] Nunziata, C, Vaccari, F, and Panza, GF. The Mw 6.3, 2009 LAquila earthquake: Linear and nonlinear site effects. In: Mazzolani FM (ed.) *Urban Habitat Constructions Under Catastrophic Events: Proceedings of the Cost C26 Action Final Conference*. London: Taylor & Francis Group, 2010.
[68] Nunziata, C, Costanzo, M, Vaccari, F, et al. Evaluation of linear and nonlinear site effects for the MW 6.3, 2009 L'Aquila earthquake. *Earthquake Research and AnalysiseNew Frontiers in Seismology* 2012; 5: 155e176.
[69] Magnoni, F, Casarotti, E, Michelini, A, et al. Spectral-element simulations of seismic waves generated by the 2009 L'Aquila earthquake. *Bull Seismol Soc Am* 2014; 104(1): 73–94.
[70] Smerzini, C, and Villani, M. Broadband numerical simulations in complex near-field geological configurations: the case of the 2009 Mw 6.3 L'Aquila earthquake. *Bull Seismol Soc Am* 2012; 102(6): 2436–2451.
[71] Michele, FD, May, J, Pera, D, et al. Spectral element numerical simulation of the 2009 L'Aquila earthquake on a detailed reconstructed domain. *Geophys J Int* 2022; 230(1): 29–49.
[72] Gaudiosi, I, Monaco, FD, Milana, G, et al. Site effects in the Aterno river valley (L'Aquila, Italy): comparison between empirical and 2D numerical modelling starting from April 6th 2009 Mw 6.3 earthquake. *B Earthq Eng* 2014; 12(2): 697–716.
[73] Margheriti, L, Chiaraluce, L, Voisin, C, et al. Rapid response seismic networks in Europe: lessons learnt from the L'Aquila earthquake emergency. *Ann Geophys* 2011; 54: 392–399.
[74] Barchi, M, Lavecchia, G, Galadini, F, et al. Sintesi delle conoscenze sulle faglie attive in italia centrale: Parametrizzazione ai fini della caratterizzazione della pericolosità sismica, 2000.
[75] Carminati, E, Lustrino, M, Cuffaro, M, et al. Tectonics, magmatism and geodynamics of Italy: what we know and what we imagine, in: Beltrando, M., Peccerillo, A., Mattei, M., Conticelli, S., Doglioni, C. (Eds.), The Geology of Italy: tectonics and life along plate margins. *J Virtual Expl, Electronic Edition* 2010; 36: 1441–8142.

[76] Cavinato, GP, P, G, and Celles, PGD. Extensional basins in the tectonically bimodal central apennines fold-thrust belt, Italy: response to corner flow above a subducting slab in retrograde motion. *Geology* 1999; 27(10): 955–958.
[77] Cosentino, D, Asti, R, Nocentini, M, et al. New insights into the onset and evolution of the central apennine extensional intermontane basins based on the tectonically active L'Aquila basin (Central Italy). *Bull Cl Sci Math Nat Sci Math* 2017; 129(9–10): 1314–1336.
[78] Boncio, P, Lavecchia, G, and Pace, B. Defining a model of 3D seismogenic sources for seismic hazard assessment applications: the case of central apennines (Italy). *J Seismol* 2004; 8(9–10): 407–425.
[79] Devoti, R, Pietrantonio, G, Pisani, AR, et al. Present day kinematics of Italy. *J Virtual Expl* 2010; 36(2): 1–14.
[80] Pondrelli, S, Salimbeni, S, Ekström, G, et al. The Italian CMT dataset from 1977 to the present. *Phys Earth Planet Inter* 2006; 159(3): 286–303.
[81] Galadini, F, and Galli, P. Active tectonics in the central Apennines (Italy) – input data for seismic hazard assessment. *Nat Hazards* 2000; 22(3): 225–268.
[82] Malikan, M, and Eremeyev, VA. On time-dependent nonlinear dynamic response of micro-elastic solids. *Int J Eng Sci* 2023; 182: 103793.
[83] Apuzzo, A, Barretta, R, Fabbrocino, F, et al. Axial and torsional free vibrations of elastic nano-beams by stress-driven two-phase elasticity. *J Appl Comput Mech* 2019; 5(2): 402–413.
[84] Barretta, R, Faghidian, SA, and Luciano, R. Longitudinal vibrations of nano-rods by stress-driven integral elasticity. *Mech Adv Mater Struc* 2019; 26(15): 1307–1315.
[85] Heiduschke, K. On tensor projections, stress or stretch vectors and their relations to Mohr's three circles. *Math Mech Complex Syst* 2024; 12(2): 173–216.
[86] Sharma, BL, and Eremeyev, VA. Wave transmission across surface interfaces in lattice structures. *Int J Eng Sci* 2019; 145: 103173.
[87] Placidi, L, Girolamo, FD, and Fedele, R. Variational study of a Maxwell–Rayleigh-type finite length model for the preliminary design of a tensegrity chain with a tunable band gap. *Mech Res Commun* 2024; 136: 104255.
[88] Placidi, L, Sherbiny, MGE, and Baragatti, P. Experimental investigation for the existence of frequency band gap in a microstructure model. *Math Mech Complex Syst* 2022; 9(4): 413–421.
[89] Mikhasev, G, Erbaş, B, and Eremeyev, VA. Anti-plane shear waves in an elastic strip rigidly attached to an elastic half-space. *Int J Eng Sci* 2023; 184: 103809.
[90] Askes, H, and Wallace, AR. Dynamic Bergan–Wang theory for thick plates. *Math Mech Complex Syst* 2022; 10(2): 191–204.
[91] Ko, KY, and Solyaev, Y. Explicit benchmark solution for topology optimization of variable-thickness plates. *Math Mech Complex Syst* 2023; 11(3): 381–392.
[92] Andreaus, U, dell'isola, F, Giorgio, I, et al. Numerical simulations of classical problems in two-dimensional (non) linear second gradient elasticity. *Int J Eng Sci* 2016; 108: 34–50.
[93] dell'isola, F, Eugster, SR, Fedele, R, et al. Second-gradient continua: from Lagrangian to Eulerian and back. *Math Mech Solids* 2022; 27(12): 2715–2750.
[94] Solyaev, Y, Lurie, S, Barchiesi, E, et al. On the dependence of standard and gradient elastic material constants on a field of defects. *Math Mech Solids* 2020; 25(1): 35–45.
[95] Placidi, L, Rosi, G, Giorgio, I, et al. Reflection and transmission of plane waves at surfaces carrying material properties and embedded in second-gradient materials. *Math Mech Solids* 2014; 19(5): 555–578.
[96] Rosi, G, Giorgio, I, and Eremeyev, VA. Propagation of linear compression waves through plane interfacial layers and mass adsorption in second gradient fluids. *J Appl Math Mech* 2013; 93(12): 914–927.
[97] Yang, B, Bacciocchi, M, Fantuzzi, N, et al. Wave propagation in periodic nano structures through second strain gradient elasticity. *Int J Mech Sci* 2023; 260: 108639.
[98] Cornacchia, F, Fabbrocino, F, Fantuzzi, N, et al. Analytical solution of cross- and angle-ply nano plates with strain gradient theory for linear vibrations and buckling. *Mech Adv Mater Struc* 2021; 28(12): 1201–1215.
[99] Cuomo, M, Contrafatto, L, and Greco, L. A cohesive interface model with degrading friction coefficient. *Math Mech Complex Syst* 2024; 12(2): 113–133.
[100] Ponomarev, D. A generalised time-evolution model for contact problems with wear and its analysis. *Math Mech Complex Syst* 2022; 10(3): 279–319.
[101] Grillo, A, and Stefano, SD. An a posteriori approach to the mechanics of volumetric growth. *Math Mech Complex Syst* 2023; 11(1): 57–86.
[102] Grillo, A, and Stefano, SD. Comparison between different viewpoints on bulk growth mechanics. *Math Mech Complex Syst* 2023; 11(2): 287–311.
[103] Tepedino, M. The mechanical role of the periodontal ligament for developing mathematical models in orthodontics. *Math Mech Complex Syst* 2023; 11(4): 525–539.
[104] Olive, M, and Auffray, N. Symmetry classes in piezoelectricity from second-order symmetries. *Math Mech Complex Syst* 2021; 9: 77–105.
[105] Misra, A, Placidi, L, Dell'isola, F, et al. Identification of a geometrically nonlinear micromorphic continuum via granular micromechanics. *Z fur Angew Math Physik* 2021; 72(4): 157.

[106] Sciarra, G, dell'Isola, F, and Coussy, O. Second gradient poromechanics. *Int J Solids Struct* 2007; 44(20): 6607–6629.
[107] Timofeev, D, Barchiesi, E, Misra, A, et al. Hemivariational continuum approach for granular solids with damage-induced anisotropy evolution. *Math Mech Solids* 2021; 26(5): 738–770.
[108] Turco, E, dell'Isola, F, and Misra, A. A nonlinear Lagrangian particle model for grains assemblies including grain relative rotations. *Int J Numer Anal Met* 2019; 43(5): 1051–1079.
[109] Placidi, L, Barchiesi, E, Dell'isola, F, et al. A granular-based elasto-plastic–damage energy formulation for strain gradient solids. In: *Book of Abstracts*, 2021.
[110] Barchiesi, E, Misra, A, Placidi, L, et al. Identification, based on granular micromechanics, of elastic isotropic strain gradient stiffness matrices for geometrically nonlinear deformations, 2021. Available at: https://iris.uninettunouniversity.net/handle/20.500.14086/2320
[111] Nocentini, M, Asti, R, Cosentino, D, et al. Plio-quaternary geology of L'Aquila–Scoppito Basin (Central Italy). *J Maps* 2017; 13.2: 563–574.
[112] Antonielli, B, Seta, MD, Esposito, C, et al. Quaternary rock avalanches in the Apennines: new data and interpretation of the huge clastic deposit of the L'Aquila basin (Central Italy). *Geomorphology* 2020; 361: 107194.
[113] Blumetti, AM. Neotectonic investigations and evidence of paleoseismicity in the epicentral area of the January–February 1703, Central Italy, earthquakes. *Perspect Paleoseismol* 1995; 6: 83–100.
[114] Bruyelle, P. Jean Demangeot—Géomorphologie des Abruzzes adriatiques. Thèse pour le doctorat ès-lettres. Centre de Recherches et documentation cartographique et géographiques, n° hors-série-1965. *Hommes terres nord* 1966; 1(1): 120–121.
[115] Giorgio, I. A variational formulation for one-dimensional linear thermoviscoelasticity. *Math Mech Complex Syst* 2022; 4(9): 397–412.
[116] Bersani, AM, Caressa, P, and Ciallella, A. Numerical evidence for the approximation of dissipative systems by gyroscopically coupled oscillator chains. *Math Mech Complex Syst* 2022; 10(3): 265–278.
[117] Eremeyev, VA. Surface finite viscoelasticity and surface anti-plane waves. *Int J Eng Sci* 2024; 196: 104029.
[118] Barchiesi, E, Misra, A, Placidi, L, et al. Granular micromechanics-based identification of isotropic strain gradient parameters for elastic geometrically nonlinear deformations. *Z Angew Math Mech* 2021; 101(11): 1–21.
[119] Soize, C. An overview on uncertainty quantification and probabilistic learning on manifolds in multiscale mechanics of materials. *Math Mech Complex Syst* 2023; 11(1): 87–174.
[120] Salnikov, V. On numerical approaches to the analysis of topology of the phase space for dynamical integrability. *Chaos Solitons Fractals* 2013; 57: 155–161.
[121] Salnikov, V, and Hamdouni, A. From modelling of systems with constraints to generalized geometry and back to numerics. *J Appl Math Mech* 2019; 99(6): e201800218.
[122] Barchiesi, E, Yang, H, Tran, C, et al. Computation of brittle fracture propagation in strain gradient materials by the fenics library. *Math Mech Solids* 2021; : 325–340.
[123] Fabbrocino, F, Funari, MF, Greco, F, et al. Dynamic crack growth based on moving mesh method. *Compos B Eng* 2019; 174: 107053.
[124] Placidi, L, and Barchiesi, E. Energy approach to brittle fracture in strain-gradient modelling. *Proc R Soc A Math Phys Eng Sci* 2018; 474: 20170878.
[125] Placidi, L, Misra, A, and Barchiesi, E. Simulation results for damage with evolving microstructure and growing strain gradient moduli. *Continuum Mech Therm* 2019; 31(4): 1143–1163.
[126] Turco, E, Barchiesi, E, Ciallella, A, et al. A new block-based approach for the analysis of damage in masonries undergoing large deformations. *Continuum Mech Therm* 2023; 35: 1625–1654.
[127] Masi, A, Manfredi, V, Vona, M, et al. Prestazioni delle tamponature e tramezzature negli edifici in c.a.: implicazioni progettuali e costruttive alla luce dell'esperienza del terremoto dell'abruzzo 2009. *Progettazione Sismica* 2009; 3: 51–66.
[128] Saitta, F, Clemente, P, Buffarini, G, et al. Base isolation of buildings with curved surface sliders: basic design criteria and critical issues. *Adv Civil Eng* 2018; 2018: 1569683.
[129] Salvatori, A. Seismic base isolation: retrofitting application in structures damaged by earthquake. In: *Proceedings of 16th European conference on earthquake engineering ECEE*, Thessaloniki, Greece, 18-21 June, 2018.

An analytical model for debonding of composite cantilever beams under point loads

---

Chapter abstract

The chapter presents an analytical model to study shear-driven debonding of a composite cantilever beam under a point load. The model uses cohesive zone models to simulate joint degradation with non-continuous and linear softening. Results are expressed in non-dimensional parameters, yielding quasi-static equilibrium paths with snap-back responses. The research significance lies in its application to structural engineering, where composites are widely used. The study emphasizes the role of the interface layer strength in maintaining composite integrity. The proposed model introduces a constitutive relation for the interface accounting for step-wise mechanical property changes. The governing equations derive from equilibrium of forces and moments, considering the relative tangential displacement at the interface. The model delineates three stages of interface degradation: no slip, plastic deformation, and progressive debonding. Analytical solutions provide insights into beam deflection, shear stress, and axial force distribution. This research offers a refined analytical approach to study debonding in composite beams, improving design and analysis of composite structures.
Published in *Continuum Mechanics and Thermodynamics*, 2025.

Continuum Mech. Thermodyn.
https://doi.org/10.1007/s00161-024-01332-1

ORIGINAL ARTICLE

Marcin Białas · Giuliano Aretusi

An analytical model for debonding of composite cantilever beams under point loads

Received: 16 August 2024 / Accepted: 25 October 2024
© The Author(s), under exclusive licence to Springer-Verlag GmbH Germany, part of Springer Nature 2024

Abstract The paper presents an analytical model to study the shear driven debonding of a composite cantilever beam subjected to a point load. The composite structure consists of two elastic beams connected by an interface layer, and the model uses cohesive zone models to simulate the degradation process at the joint. These cohesive zone models are characterized by non-continuous and linear softening in the relationship between shear stress and relative tangential displacement. The results are expressed using non-dimensional parameters, and the model yields quasi-static equilibrium paths that demonstrate snap-back responses in both force and displacement values. The significance of the research lies in its application to structural engineering, where composite materials are extensively used. The study emphasizes the critical role of the interface layer strength in maintaining the structural integrity of composites. The proposed model advances the understanding of debonding by introducing a constitutive relation for the interface that accounts for the step-wise change in mechanical properties. The governing equations for the cantilever beam are derived, considering the equilibrium of forces and moments, and the relative tangential displacement at the interface. The model delineates three stages of interface degradation: no relative slip, plastic deformation, and progressive debonding. The analytical solutions for each stage provide insights into the beam deflection, shear stress, and axial force distribution. This research contributes to the field by offering a more refined analytical approach to study debonding in composite beams, which is essential for improving the design and analysis of composite structures.

Keywords Cantilever · Debonding · Cohesive zone · Analytical model · Snap-back

1 Introduction

Composite beams are an essential component in structural engineering, combining two or more different materials to achieve better performance than each material could provide on its own. The combination of different materials into composites plays an enormous role in many structural elements in civil engineering. Steel beams supporting concrete plates make bridge spans. Wood beams or pillars made of several components can be tied together by bolts, nails, or designated glues to face particular loading conditions. The different materials in a composite beam complement each other strengths. For example, in a steel beam with a concrete slab, steel provides high tensile strength, while concrete offers excellent compressive strength. The clear advantage of using composites is the possibility of creating structural parts made of different materials, where each component can work in conditions best suited for its microstructure [1–5]. Composite beams can be designed and tailored to suit various architectural and engineering requirements, making them suitable for

M. Białas
Faculty of Mechanical and Industrial Engineering, Warsaw University of Technology, Warsaw, Poland

G. Aretusi ( )
Department of Civil, Construction-Architectural and Environmental Engineering, University of L'Aquila, L'Aquila, Italy
e-mail: giuliano.aretusi@graduate.univaq.it

Published online: 20 November 2024

a wide range of applications, from bridges to high-rise buildings. The key aspect when designing such a composite is the strength of the interface, i.e., the layer binding materials together. Composite beams often use materials more efficiently, reducing the overall weight of the structure and potentially leading to cost savings in material and labor. Besides, they can also exploit electromagnetic properties to achieve specific performances, such as vibration damping. Examples of these composite structures include piezo-electro-mechanical or piezo-magnetic structures [6–10]. Topological optimization may be used to enhance the design and performance of composite structures. It is a computational technique that determines the optimal material layout within a given design space for specified loading and boundary conditions. For composite materials, this helps distribute different materials effectively to achieve desired mechanical properties while minimizing weight [11–14]. Other technique of optimization can be integrated with manufacturing constraints and processes specific to composite materials, such as additive manufacturing, filament winding, or lamination. This ensures that the optimized design is not only theoretically optimal but also feasible to produce [15,16]. Mechanical modeling of composite beams involves a detailed analysis of how these beams behave under various loads and conditions. This modeling is crucial to ensure that the beams can safely and effectively support the structures they are part of. From this point of view, some critical aspects which need to be considered are: 1) the difference in shrinkage and creep between the different components that can lead to additional stresses and deformations [17]; 2) thermal expansion or contraction can induce additional stresses in composite beams, especially in environments with significant temperature variations (see, e.g., [18–21] for some recent development in this regards); 3) in addition to strength, the mechanical modeling of composite beams must ensure that deflections, vibrations, and other serviceability criteria are within acceptable limits [22–27]. Moreover, the models to describe composite structures can be developed with the use of micromorphic, higher gradient, or non-local continua to ensure the description of a panoply of different responses stemming from the microstructure underlying their constitution (see, e.g., [28–34]).

To obtain a good bonding, the ideal solution would be to realize a rigid joint with mechanical strength much higher than those of composite components. Due to stress concentration at the interface area, we are faced with components separation or debonding phenomena. Debonding of composite beams or pillars is a subject treated by many researchers. We could mention here the pioneering works of Newmark et al. [35], Granholm [36] or Pleshkov [37]. Starting from the Bernoulli-Euler beam theory, the authors analyzed a composite in which its components and the interfaces are loaded in an elastic range only. Goodman and Popkov [38] used a nonlinear constitutive relation for the bounding material. Murakami [39] introduced laminated beam theory, allowing for general physical relation between stresses and strains of the interface area. A slightly different approach was to use equations of the theory of elasticity as the starting point. We could mention here the works of Rao and Ghosh [40] or Fazio and Hussein [41]. Focusing on sandwich structures, the authors used only linear relations for interface zones. That was mainly due to complicated algebraic formulas that were developed. Obtained analytical solutions could be used only for a limited number of boundary problems. Giorgio and Scerrato [42] proposed a non-linear model to describe internal friction in composite concrete structures. They aimed at measuring dissipation induced by the motion of the faces of micro-cracks by adopting Coulomb-like interaction between contacting interfaces. This Coulomb-type dissipative mechanism was also addressed in Ciallella et al. [43] and in augmented form with internal kinematical variables in Ciallella et al. [44] and [45]. Friction effects are often combined with wear since they relate to contact problems (see, e.g., [46]). This erosion caused by friction can also be significantly influenced by fluid infiltration, especially at a potential interface (see [47,48] for some recent results).

Some studies examine the debonding of a perfectly adherent FRP (fiber-reinforced polymer) reinforcement from a masonry pillar or between FRP strips and concrete [49–52]. The findings indicate that the width of the FRP significantly affects damage propagation, peak strength, ductility, and fracture energy. Observations include the formation of a concrete bulb at the strip end, influencing the maximum load. These studies generalizes the prediction of ultimate interfacial load and bond length for nonlinear reinforcements, proposing expressions for both.

Damage in composite structures can arise due to a variety of factors. Composite materials are often used for their high strength-to-weight ratio and excellent mechanical properties, but they are also susceptible to different types of damage mechanisms. The matrix, or the binding material in a composite, can develop cracks due to excessive stress. These cracks can reduce the composite stiffness and strength and may lead to debonding. The reinforcing fibers in a composite provide the majority of the material strength. Fibers can break due to excessive loads, fatigue [53], or impact [54]. Fiber breakage can lead to a significant reduction in load-carrying capacity. Repeated cyclic loading can lead to fatigue damage in composites. This can manifest as matrix cracking, fiber breakage, or debonding over time. Under sustained loading, composites can exhibit creep and stress relaxation

(reduction in stress over time), which can lead to damage or failure over long periods. Understanding these damage mechanisms is crucial for designing, maintaining, and repairing composite structures to ensure their long-term reliability and performance. A powerful tool to model this phenomenon consists of the variational formulation. It can be easily integrated with computational tools and software, making it suitable for a wide range of applications [55–59].

Numerical methods are the obvious choice to treat real engineering problems related to composite materials. Thompson et al. [60] analyzed multi-layered structures using the finite element method. Cheung et al. [61], Hu and Hartley [62], Kukreti and Cheraghi [63] simplified the considerations by focusing on two dimensional structures consisting of concrete plates resting on steel beams. By artificially separating the plates from the beams, they neglected the effect of shear loads at the interfaces, which, in turn, resulted in the inaccurate description of structural response. The model suggested by Sapountzakis and Katsikadelis [64] introduced the shear loading at the interface and added concrete creep and shrinkage. Handling complex media may require special attention when it comes to numerical simulations. Standard procedures can sometimes fail and need to be improved, especially when a high level of smoothness is needed for the interpolating functions or to optimize the number of degrees of freedom for proper convergence. The isogeometric finite element method can be used in such cases, as shown in [65–67]. On the other hand, *ad hoc* discrete formulations can also be developed to efficiently perform numerical simulations using Hencky-type discretization [68–70], particularly for tackling dynamic problems [71–73].

Interfaces within granular media were addressed by Turco et al. [74]. The authors introduced defects into the material patterns to effectively analyze mechanisms leading to failure development. In general, modeling interfaces is very challenging, and significant effects can be detected or not, depending on the accuracy of the adopted model (see, e.g., [75–77]).

The works of Oehlers and Sved [78] and Nguyen et al. [79] introduce interaction factors for concrete-steel beams and suggest design guidelines by focusing on limit load capacity and the relative slippage on a concrete-steel interface. The authors state that the main factor in structural loss of stability is the degradation of the joint between concrete and steel. Plastic strains developing in the particular materials are of less importance for an overall structural response.

There are several test setups used to experimentally examine propagation of debonding zone in beam structures. For mode II fracture they are end-notched flexure (ENF), end-loaded split (ELS) and four-point and notched flexure. The geometry of ELS specimen has a big advantage over others, since it results in stable initiation of crack propagation. De Moura and de Morais [80] used equivalent crack methods to estimate fracture toughness of ENF and ELS debonding tests. They performed finite element modeling to estimate values of critical energy release rates in mode II. Bui et al. [81] applied applied cohesive models combined with R-curves to describe the delamination in end-loaded split specimen. The authors were able to show development of strain energy release rate as a function of crack length. Dourado et al. [82] used genetic algorithm to determine parameters of bilinear cohesive law in conjunction with inverse analysis for end-notched flexure test. Bilinear cohesive law was also addressed by Giuliese at al. [83] in application for double cantilever beam and end notched flexure of carbon fiber epoxy resin specimens. This type of law came out to be necessary to fit into the experiential behavior of interface within nanofiber interleaved laminate material as presented by Moroni et al. [84].

Blackman et al. [85,86] presented results from tests performed on bonded composite beams loaded by end-loaded split setup. The authors used the crack length parameter to determine values of the critical energy rate. They also observed a micro-cracked region ahead of the crack tip and addressed difficulties in measuring crack length. The work of Wang et al. [87] also focuses on the problem of the location of the crack tip. They introduced a cohesive zone model incorporating fiber bridging and micro-cracking phenomena. The approach was validated for one and two dimensional mode II fracture. Solis et al. [88] analyzed a cracked beam using an end notch flexure test and simulated debonding using a continuum damage model. The work identifies the need for a more accurate representation of fiber orientation when modeling debonding in composite beams.

Pereira and de Morais [89], de Morais and Pereira [90] and de Morais [91] dealt with experimental and theoretical description of debonding within end-notched flexure and double cantilever beams. The authors confirmed dependence of initiation toughness on test geometry. Cao et al. [92] developed a semi-analytical model to capture the bridging effect at the crack tip based on experimental load–displacement relation. They integrated the bridging traction into a linear cohesive law and were able to depict the debonding process of the composite structure. Various shapes and parameters of cohesive zone models were analyzed by Heidari-Rarani and Ghasemi [93]. The authors applied four different traction-separation laws and tried to match with experimental data the load–displacement response for composite beam specimens by performing finite element

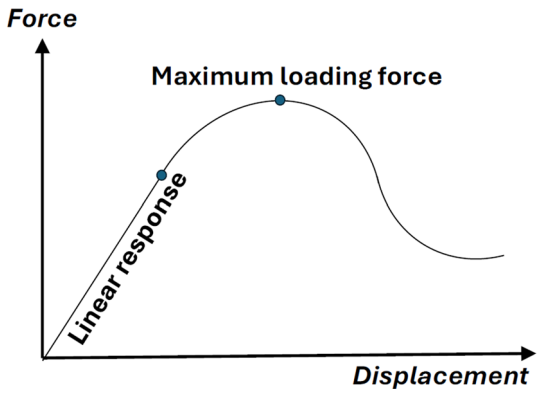


Fig. 1 Load–displacement curve for ELS and ENF specimens

simulations. Similar simulations were performed by Shahverdi et al. [94] with the use of an exponential cohesive zone model combined with a virtual crack closure technique.

The common feature related to the experimental results obtained for ELS or ENF specimens is a relation between loading force and measured displacement. Initially it is a straight line. We can see a nonliner response next. It is related to crack propagation at the interface. Eventually maximum loading force is reached and, depending on specimens geometry and interface mechanical features, we can observe even abrupt decrease of loading force as schematically presented in Fig. 1. Debonding process can also result in dynamic response of specimen, making it difficult to properly interpret the results. The way to theoretically track the system is to create a mathematical model with a suitable choice of governing parameter in a way that specimen's response depends on it. This parameter can be a crack length, because it allows to obtain quasi static response related to snap-back character of load–displacement curve, see Mróz and Białas [95] and Białas and Mróz [96].

When studying composite materials, it is essential to consider a variety of uncertainties. These uncertainties can impact boundary conditions, geometric variations from the intended design to the actual properties, and the material current properties. They also involve hidden degrees of freedom that are not considered in simplified models, such as using some specific beam theory instead of the full three-dimensional model (see, e.g., [97,98]).

Cohesive zone models follow the idea originally proposed by Barenblatt [99], where a zone of microcrack formation was introduced ahead of crack tip. The softening relation between interfacial traction and relative displacement at the debonding area could be presented by different functions: constant with step-wise change in mechanical toughness, linear, bilinear or exponential softening [100–102]. Some authors focused on introduction of frictional traction to shear driven crack development [95,96]. Cohesive zone modeling can be easily combined with extended finite elements approach providing powerful tool in numerical modeling of failure [103].

The subject of the paper is the analytical analysis of shear driven debonding of a composite beam loaded by a bending force. The composite beam consists of two elastic materials bound together by an interface layer. For the description of the mechanical behavior of the interface layer, two constitutive relations are used. The model interface develops a cohesive zone ahead of the crack tip. This is done in line with the approach suggested by Williams and Hadavin [104], presenting an analysis of a beam detached from a rigid substrate. The main difference between reported results and those presented by Newmark et al. [35], Goodman and Popkov [38], Murakami [39], Oehlers and Sved [78], Nguyen et al. [79] is the constitutive relation for the interface with step-wise change of its mechanical properties. This behavior was reported in the experimental works of Oehlers and Coughlan [105].

2 Governing equations

Let us consider a cantilever beam loaded by a point force, as presented in Fig. 2. It consists of two beams made of two different materials joined together at the interface. We assume that the interface width b is constant and does not depend on location x. Area of cross section of upper beam is A_1, moment of inertia is designated by J_1. Area of cross section of lower beam and its moment of inertia are A_2 and J_2, respectively. Values of A_1, J_1, A_2 and J_2 are constant and do not depend on location x.

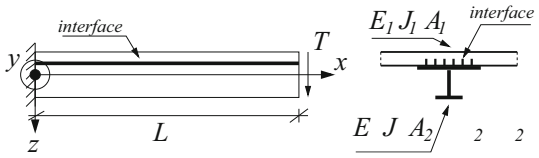


Fig. 2 Composite cantilever beam loaded by a point force

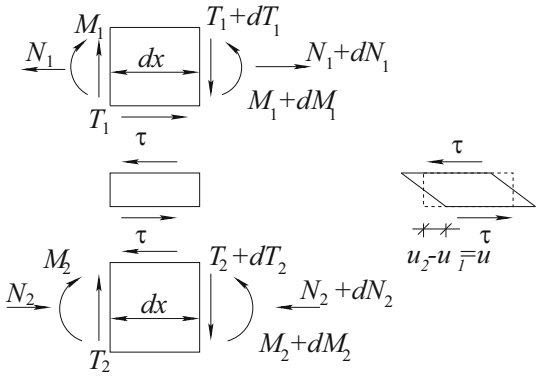


Fig. 3 Forces acting on an infinitesimal beam element. Relative displacement at the interface

Forces acting on infinitesimal beam element are presented in Fig. 3. By formulating equilibrium equations we obtain following differential relations:

- Upper beam

$$\frac{\mathrm{d}N_1}{\mathrm{d}x} = -b\,\tau, \tag{1}$$

where: N_1—is an axial force acting on the upper beam;
τ—is a shear force at the interface.

- Lower beam

$$\frac{\mathrm{d}N_2}{\mathrm{d}x} = b\,\tau, \tag{2}$$

where: N_2—is an axial force acting on the lower beam;
τ—is a shear force at the interface.

Equilibrium of axial forces acting on the cantilever beam results in following equality:

$$N_1 = N_2 \equiv N. \tag{3}$$

It says that the value of axial force acting on the upper beam is the same as the force acting on the lower beam. The only difference is that they have opposite signs.

Equilibrium of all moments acting on a beam cross section provides us with equation

$$M_1 + M_2 - \frac{j_1 + j_2}{2}\,N = -T\,(L - x) \equiv M \tag{4}$$

where: j_1—is the distance from the interface to the center of gravity of the upper beam cross section;
j_2—is the distance from the interface to the center of gravity of the lower beam cross section;
M_1—bending moment for the upper beam;
M_2—bending moment for the lower beam;
M—total bending moment acting on the cantilever at location x.

Let us formulate equation for the relative tangential displacement of the at the interface. It is equal to the difference between tangential displacement of uppermost fibers of the lower beam, denoted by u_2, and u_1

being the displacement of lowermost fiber of upper beam. By assuming linear, elastic beams response and using Bernoulli beam theory, we can write:

$$\frac{\mathrm{d}u_1}{\mathrm{d}x} = \frac{N}{A_1\,E_1} + \frac{M_1}{E_1\,J_1}\cdot\frac{j_1}{2}, \tag{5}$$

$$\frac{\mathrm{d}u_2}{\mathrm{d}x} = -\frac{N}{A_2\,E_2} - \frac{M_2}{E_2\,J_2}\cdot\frac{j_2}{2}. \tag{6}$$

Relative displacement of the fibers, being the slippage at the interface will be denoted by u and we have $u = u_2 - u_1$. From formulas (5) and (6) we immediately have:

$$\frac{\mathrm{d}u}{\mathrm{d}x} = \frac{\mathrm{d}u_2}{\mathrm{d}x} - \frac{\mathrm{d}u_1}{\mathrm{d}x} = -\lambda_1\,N - \lambda_2\,M, \tag{7}$$

where:

$$\lambda_1 = \frac{1}{A_1\,E_1} + \frac{1}{A_2\,E_2} + \frac{(j_1+j_2)^2}{4(E_1\,J_1 + E_2\,J_2)},$$

$$\lambda_2 = \frac{j_1+j_2}{2(E_1\,J_1 + E_2\,J_2)}.$$

We shall deliver now equations for cantilever beam displacement. We assume that deflection of upper beam w_1 is equal to the deflection of lower beam w_2, $w_1 = w_2$. It means that the second derivatives are also equal $w_1'' = w_2''$. Bernoulli beam theory allows us to write:

$$w'' \equiv w_1'' = w_2'' = -\frac{M_1}{E_1\,J_1} = -\frac{M_2}{E_2\,J_2} = -\frac{M_1+M_2}{E_1\,J_1 + E_2\,J_2}.$$

By using Eq. (4) we finally obtain

$$w'' = -\lambda_2\left(N + \frac{2\,M}{j_1+j_2}\right). \tag{8}$$

Relations (1)÷(8) allow us to analytically analyze debonding of composite beam by introduction of simple constitutive relations for the interface.

3 Interface constitutive law

The interface constitutive law will be presented within the framework of theory of plasticity. Let u_n and u_t denote normal and tangential relative displacement at interface, respectively. The interface in bonded beam will be under shear loading condition. Neglecting the dilatancy effect, we can write

$$u_n = 0, \qquad \dot{u}_t = \dot{u}_t^e + \dot{u}_t^p, \tag{9}$$

where $\dot{u}_t^e$ is reversible part of tangential slip rate and $\dot{u}_t^p$ is a irreversible part of the total slip rate.

The relation between interfacial shear stress τ and the reversible tangential slip is

$$\dot{u}_t^e = D_t\,\dot{\tau}, \tag{10}$$

where D_t is a compliance modulus.

The damage criteria is $F = 0$, where function F has the form

$$F(\tau, \delta_e) = |\tau| - t(\delta_e). \tag{11}$$

In the expression t is the interface shear strength and can decrease as damage progresses by means of increasing value of evolution parameter δ_e.

The rate of irreversible tangential slip is given by

$$\dot{u}_t^p = \dot{\lambda}\frac{\partial F}{\partial \tau}, \tag{12}$$

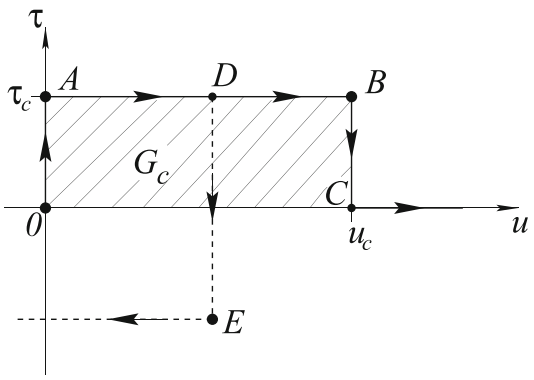


Fig. 4 Constitutive relation for the interface. Non-continuous degradation of mechanical properties

where λ is a plastic multiplier. Consequently we can write

$$\dot{\lambda} \geq 0, \quad F \leq 0, \quad \dot{\lambda} F = 0.$$

Upon substituting (11) into (12) one obtains

$$\dot{\delta}_t^p = \dot{\lambda} \text{sign}(\tau). \tag{13}$$

The rate of evolution equation of δ_e has the form

$$\dot{\delta}_e = |\dot{\delta}_t^p|. \tag{14}$$

For monotonic loading δ_e is the irreversible relative slip at the interface.

Function $t(\delta_e)$ will be chosen to simulate the degradation of mechanical strength at the interface. We propose

- Non-continuous degradation of interface strength

$$t(\delta_e) = \begin{cases} \tau_c & \delta_e \leq \delta_e^c \\ 0 & \delta_e > \delta_e^c \end{cases} \tag{15}$$

- Linear softening of mechanical properties at interafce

$$t(\delta_e) = \begin{cases} \tau_c - K\delta_e & \delta_e \leq \frac{\tau_c}{K} \\ 0 & \delta_e > \frac{\tau_c}{K} \end{cases} \tag{16}$$

We will assume that the interface is rigid until shear stress τ reaches critical value τ_c. The compliance modulus D_t equals to zero $D_t = 0$. For the beam debonding problem we have $u_t = u$. Constitutive relation for the interface defined by Eq. (15) is presented in Fig. 4. Figure 5 shows interface rigid plastic model with linear softening.

Formulation of the model is a special case of model presented in [95]. It could be derived from it by neglecting frictional effect and the normal traction acting on the joint. It can also be compared to formulation presented in [106], where crack patterns in thin layers under temperature loadings were analyzed. This phenomena was combined with thin layer debonding from the substrate. Similar approach was also used in [107] for analysis of combined debonding and segmentation cracking during cyclic loading of thin film. Numerical implementation of similar cohesive model with initially elastic interface is presented in [96]. It addresses debonding of 2D plate resting on a rigid substrate.

4 Non-continuous degradation of interface strength

The process of interface loading and the subsequent degradation of its mechanical properties will follow the constitutive equation presented in Fig. 4. Segment $0A$ denotes the rigid interface, segment AB is the interfacial plastic flow, segment CB is the debonding process. As seen in Fig. 4 we have discontinuous degradation of mechanical properties. The beam response to the loading consists of three stages.

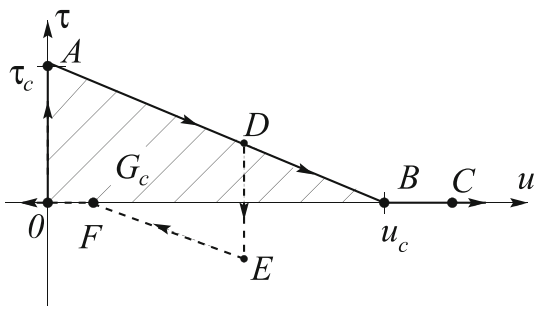


Fig. 5 Interface rigid plastic model with linear softening

4.1 Stage 1

During this stage there is no relative slip between upper and lower beams. We can write:

$$u_2 - u_1 = 0.$$

As a results we also obtain

$$u_2' - u_1' = 0,$$

and, by means of Eq. (7), we obtain formula for axial force N:

$$N(x) = -\frac{\lambda_2}{\lambda_1} M(x) = \frac{\lambda_2}{\lambda_1} T\,(L - x). \tag{17}$$

From Eq. (1) we can write the value of shear stress at the interface:

$$\tau(x) = \frac{\lambda_2}{\lambda_1} \frac{T}{b}, \tag{18}$$

and from Eq. (8) we obtain deflection of the cantilever beam:

$$w(x) = \lambda_2 \left(\frac{\lambda_2}{\lambda_1} - \frac{2}{j_1 + j_2} \right) \left(\frac{x^3}{6} - \frac{x^2}{2} L \right) T. \tag{19}$$

This function satisfies the boundary conditions $w(0) = w'(0) = 0$. The shear stress at the interface is constant along the entire cantilever beam, since the lateral force does not depend on location x. The interface reaches the critical value τ_c along the whole joint once the external loading force is equal to

$$T_p = \frac{\lambda_1}{\lambda_2} b\,\tau_c. \tag{20}$$

4.2 Stage 2

During the second loading stage the interface deforms plastically along the entire cantilever beam and the shear stress for every x is $\tau = \tau_c$. By integrating Eq. (1) with boundary condition $N(L) = 0$ we obtain formula for axial force:

$$N(x) = -b\,\tau_c\,(x - L). \tag{21}$$

By integrating (8) with boundary conditions $w(0) = w'(0) = 0$ we obtain the deflection line:

$$w(x) = \lambda_2 \left(b\,\tau_c - \frac{2T}{j_1 + j_2} \right) \left(\frac{x^3}{6} - \frac{x^2}{2} L \right). \tag{22}$$

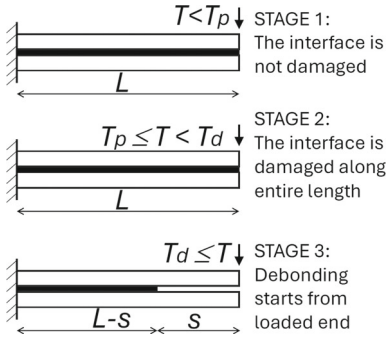


Fig. 6 Zones developed at the interface

Stage 2 will end when the relative displacement u at the interface reaches the critical value u_c. Debonding zone will start to develop from the loaded end of the cantilever beam. By integrating Eq. (7) with boundary condition $u(0) = 0$ we obtain formula for relative tangential displacement at the interface:

$$u(x) = (\lambda_1 \, b \, \tau_c - \lambda_2 \, T) \left(\frac{x^2}{2} - L \, x \right). \tag{23}$$

The above relation enables us to obtain value of external loading force T_d for which the debonding will be initiated at $x = L$. We simply have $u(x = L) = u_c$, and can write:

$$T_d = \frac{\lambda_1}{\lambda_2} \, b \, \tau_c + \frac{2 \, u_c}{\lambda_2 \, L^2} = T_p + \frac{2 \, u_c}{\lambda_2 \, L^2}. \tag{24}$$

4.3 Stage 3

During this stage we have a progressive debonding. There are two zones at the interface as presented in Fig. 6. They are plastic zone and, propagating from the loaded end, debonding zone. Let us denote by s the location of the transition point between the two zones. The shear stress at the interface within the delaminated region is $\tau = 0$. As a consequence the axial force in upper and lower beam is zero for $x \in < s, L >$. Within the plastic zone the shear stress at the interface is constant and equals τ_c. By integrating equilibrium Eq. (1), we obtain formula for the axial force within the plastic zone:

$$N(x, s) = -b \, \tau_c (x - s). \tag{25}$$

It satisfies the continuity condition at the transition point s: $N(s) = 0$. From now on, the value of s will be the parameter controlling the debonding process. All the internal forces and beam deflection will depend on s.

At the transition point with coordinate s we should satisfy the continuity condition: the relative displacement u at the interface for $x = s$ should be $u(s) = u_c$. This allows us to derive the value of the external loading force as a function of s. By integrating Eq. (7) with boundary condition $u(0) = 0$, we obtain:

$$u(x, s) = \lambda_1 \, b \, \tau_c \left(\frac{x^2}{2} - s \, x \right) + \lambda_2 \, T \left(L \, x - \frac{x^2}{2} \right).$$

To have $u(s) = u_c$, the value of T has to satisfy:

$$T(s) = \frac{\frac{1}{2} \lambda_1 \, b \, \tau_c \, s^2 + u_c}{\lambda_2 \, (L \, s - \frac{1}{2} s^2)}. \tag{26}$$

To obtain the cantilever deflection within the plastic zone we shall follow the same path as for the previous two stages—we will integrate formula (8). By making use of Eq. (25), we obtain function

$$w(x, s) = \lambda_2 \left[b \, \tau_c \left(\frac{x^3}{6} - \frac{x^2}{2} \, s \right) + \frac{T(s)(L \, x^2 - \frac{x^3}{3})}{j_1 + j_2} \right], \tag{27}$$

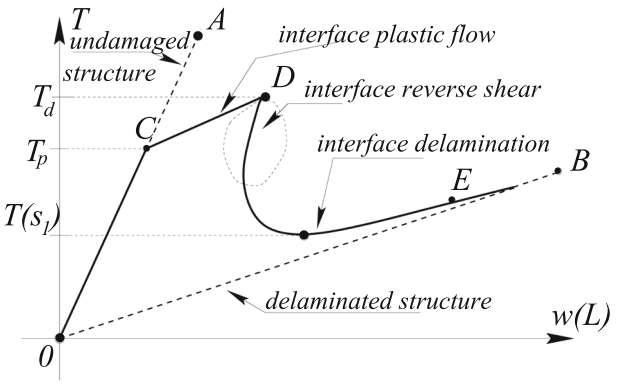


Fig. 7 The relation between external loading T and the displacement at the loaded end

satisfying the boundary conditions $w(0) = w'(0) = 0$. The above relation is valid for the plastic zone, namely for $x \in < 0, s >$.

The cantilever deflection within the debonded zone can be obtained by integrating Eq. (8) with force N equal to zero. Satisfying the continuity conditions $\lfloor w(s) \rceil = \lfloor w'(s) \rceil = 0$ at the transition point, we obtain the formula:

$$w(x, s) = \frac{\lambda_2 \, T(s)}{j_1 + j_2} \left(L \, x^2 - \frac{x^3}{6} \right) - \frac{1}{3} \lambda_2 \, b \, \tau_c \, s^2 \, x, \tag{28}$$

where $T(s)$ is given by Eq. (26). Function (28) is valid for $x \in < s, L >$.

Let us analyze the relation $T \sim w(L)$ for the debonding process. This dependence visualizes the degradation of mechanical properties of composite cantilever beam and transition from a structure consisting of three undamaged elements (two elastic beams and a rigid interface between them) to a structure consisting of two fully debonded beams. The relation between loading force T and displacement $w(L)$ under the loading force for undamaged structure is presented in Fig. 7 by segment OA. For a fully debonded structure it is presented by segment OB. The current analysis will show us how to move from line OA to line OB.

For force T lower than T_P, the behavior of the cantilever beam is simply Stage 1. The relation $T \sim w(L)$ for this particular stage is presented in Fig. 7 by segment OC lying on line OA. When T reaches T_p, a plastic zone starts to develop at the entire interface. The relation between T and $w(L)$ is still linear and given by formula (22), where we have to put $x = L$. It is represented in Fig. 7 by segment CD. Its length depends on the value of u_c, that is on the critical relative displacement at the interface. The higher the u_c value, the longer is the CD segment. When T reaches T_d we have a debonding zone developing at the interface and Stage 3 begins. We shall now focus closely on the $T \sim w(L)$ relation for this particular loading stage.

Let us examine how T changes as a function of s decreasing from L to zero. The derivative $\mathrm{d}T(s)/\mathrm{d}s$ is

$$\frac{\mathrm{d}T}{\mathrm{d}s} = \frac{\frac{1}{2} \lambda_1 \, b \, \tau_c \, s^2 \, L - u_c \, (L - s)}{\lambda_2 \, (L \, s - \frac{1}{2} s^2)^2} \tag{29}$$

and it is negative for $s \in (s_2, s_1)$, and non-negative otherwise. Values of s_1 and s_2 are given by

$$s_1 = \frac{\sqrt{u_c^2 + 2 \lambda_1 \, b \, \tau_c \, u_c \, L^2} - u_c}{\lambda_1 \, b \, \tau_c \, L}, \tag{30}$$

$$s_2 = \frac{-\sqrt{u_c^2 + 2 \lambda_1 \, b \, \tau_c \, u_c \, L^2} - u_c}{\lambda_1 \, b \, \tau_c \, L} < 0. \tag{31}$$

By having in mind that during the Stage 3, the value of s decreases from L to zero, we deduce that at the beginning of debonding process value of T shall decrease until s reaches s_1. For s lower than s_1, the value of T will start increasing again.

Let us examine the sign of derivative $w(x, s)$ with respect to s. By differentiating Eq. (28) with respect to s and putting $x = L$ and $s = L$ (beginning of debonding process) we have

$$\frac{\partial w(x = L, s = L)}{\partial s} > 0 \tag{32}$$

for every possible geometrical and mechanical parameters defining the cantilever beam. With s decreasing from L to zero, it simply means that beam deflection at the onset of debonding will decrease. The relation between force T and displacement $w(L)$ for Stage 3 is given by curve DE asymptotically approaching line OA. The inequality (32) means that always for the onset of debonding we have an abrupt decrease in the value of loading force T and displacement $w(L)$.

All these considerations were made by a silent assumption that the function $u(x, s)$ representing the relative displacement of the beams making the cantilever structure, will increase for s decreasing from L to zero. It means that the interfacial plasticity is connected with interfacial slip only in one direction. For this particular case, the interface relation is indeed given by $\tau = +\tau_c$, represented by line AB in Fig. 4. If that was not true, that is, the function $u(x, s)$ would decrease during the debonding process, we would have a reverse shear at the interface. The shear stress would be now $\tau = -\tau_c$ as shown in Fig. 4 by line EF. All the above considerations for Stage 3 were made for shear stress at the interface equal $\tau = \tau_c$, that is, we did not allow for reverse shear. As will be shown, this is not valid for the very offset of the debonding process.

In order for the interface in the plastic zone to be sheared only in one direction and to have $\tau = +\tau_c$, the following inequality should be satisfied:

$$\frac{\partial u(s, x)}{\partial s} \leq 0 \qquad x \in (0, s). \tag{33}$$

The derivative $u(x, s)$ with respect to s is

$$\frac{\partial u(x, s)}{\partial s} = x \left(-\frac{1}{2}\frac{\mathrm{d}T}{\mathrm{d}s}\lambda_2 x + \lambda_2 L \frac{\mathrm{d}T}{\mathrm{d}s} - \lambda_1 b \tau_c \right). \tag{34}$$

It is a quadratic trinomial with respect to x. In order to satisfy (33) for $x \in <0, s>$, the values of s has to be lower than $\tilde{s}$, where $\tilde{s}$ is a solution of the following equation:

$$\frac{\frac{1}{2}\lambda_1 b\tau_c \tilde{s}^2 L^2 - u_c(L - \tilde{s})L}{(L\tilde{s} - \frac{1}{2}\tilde{s}^2)^2} - \lambda_1 b\tau_c = 0. \tag{35}$$

By analyzing the above formula we see that $s_1 < \tilde{s} < L$, where s_1 is given by Eq. (30). It means that for s satisfying $\tilde{s} < s < L$, the interface is subjected to reverse shear.

It all leads to the conclusion that the derived equations for the Stage 3 of debonding process are not valid at its offset. They do not describe the reverse shear since the τ_c does not change the sign. The equations become valid when value of s is lower than $\tilde{s}$. For this particular phase we have $\tau = +\tau_c$.

The reverse shear is the effect of non-continuous constitutive relation for the interface. To omit the reverse shear we shall use now continuous degradation of mechanical properties at the interface.

5 Linear softening of mechanical properties at the interface

To describe the degradation of mechanical properties at the interface, we shall use the constitutive relation presented in Fig. 5. It consists of three stages of interface response: rigid (segment OA), plastic softening (segment AB) and debonding (segment BC). The cantilever loading process also consists of three stages.

5.1 Stage 1

For this particular loading stage the interface is rigid and forces and deformation are the same as for Stage 1 for the previous model. Equations (17), (18), (19) are still valid. For loading force reaching T_p given by (20), the interface becomes plastic along its entire length.

5.2 Stage 2

During this stage the entire interface is plastic. The constitutive relation between shear stress and relative displacement is

$$\tau(x) = -K\,u + \tau_c, \qquad \text{gdzie} \qquad K = \frac{\tau_c}{u_c}. \tag{36}$$

By differentiating the equilibrium Eq. (1) with respect to x we obtain

$$\frac{\mathrm{d}^2 N}{\mathrm{d}x^2} = -b\frac{\mathrm{d}\tau}{\mathrm{d}u}\frac{\mathrm{d}u}{\mathrm{d}x}.$$

Taking into account relations (7) and (36) we can write differential equation for axial force N:

$$N'' = -b\,K\,(\lambda_1\,N + \lambda_2\,M), \tag{37}$$

where $M = T(x - L)$ is the total bending moment at location x. By solving (37) we obtain

$$N(x) = C_1\,\cos(rx) + C_2\,\sin(rx) + \frac{\lambda_2}{\lambda_1}\,T\,(L - x) \tag{38}$$

where: $r = \sqrt{b\,K\,\lambda_1}$, and C_1, C_2 are integration constants. Equilibrium Eq. (1) allows us to write function $\tau(x)$ for shear stress at the interface:

$$\tau(x) = \frac{1}{b}\left[\frac{\lambda_2}{\lambda_1}T + C_1\,r\,\sin(rx) - C_2\,r\,\cos(rx)\right]. \tag{39}$$

By integrating (7) and using (38) we obtain function of relative displacement at the interface:

$$u(x) = \frac{\lambda_1}{r}[C_2\,\cos(rx) - C_1\,\sin(rx)] + C_3. \tag{40}$$

Integration constants C_1, C_2, C_3 and the force T can be obtained by enforcing following boundary conditions:

$$N(L) = 0, \qquad u(0) = 0, \qquad u(L) = u_L, \qquad \tau(L) = \tau_c(1 - \frac{u_L}{u_c}). \tag{41}$$

The parameter controlling the loading process will be the relative displacement at the interface u_L at location $x = L$. It increases from zero to the value $u_L = u_c$. For u_L higher than u_c we have a debonding zone propagating from the externally loaded end. By solving the set of Eq. (41) we obtain following functions:

- External loading force $T(u_L)$:

$$T(u_L) = T_p\,\frac{1 - \left(1 - \frac{u_L}{u_c}\right)\,\cos(Lr)}{1 - \cos(Lr)} \tag{42}$$

- Axial force N:

$$N(x, u_L) = \frac{r\,u_L}{\lambda_1}\,\frac{\sin[r(x - L)]}{1 - \cos(Lr)} + \frac{\lambda_2}{\lambda_1}T(u_L)(L - x) \tag{43}$$

- Relative displacement at the interface:

$$u(x, u_L) = u_L\,\frac{\sin\left(\frac{1}{2}rx\right)\,\sin\left[r(L - \frac{1}{2}\,x)\right]}{\sin^2\left(\frac{1}{2}L\,r\right)}. \tag{44}$$

By integrating Eq. (8) and taking into account (42), (43) and boundary conditions $w(L) = w'(L) = 0$ we obtain function for cantilever deflection:

$$w(x, u_L) = \lambda_2 \Bigg[\frac{\frac{u_L}{r} \sin[r(x-L)] + \frac{u_L}{r} \sin(rL) - u_L\, x\, \cos(rL)}{\lambda_1 [1 - \cos(rL)]} - \\ - T(u_L) \left(\frac{L\, x^2}{2} - \frac{x^3}{6} \right) \left(\frac{\lambda_2}{\lambda_1} - \frac{2}{j_1 + j_2} \right) \Bigg]. \tag{45}$$

The loading force $T(u_L)$ is given by Eq. (42).

For formulas (42), (43), (44), (45) to be valid, the following inequality should be satisfied:

$$\forall x \in <0, L> \qquad \frac{\partial u(x, u_L)}{\partial u_L} \geq 0,$$

meaning that the interface is sheared in one direction only. The above derivative is:

$$\frac{\partial u(x, u_L)}{\partial u_L} = \frac{\sin\left(\frac{1}{2} r x\right) \sin[r(L - \frac{1}{2} x)]}{\sin^2\left(\frac{1}{2} L\, r\right)}. \tag{46}$$

This function is non-negative for $x \in <0, L>$, provided that

$$rL \leq \pi \tag{47}$$

is satisfied. For rL greater than π, the derivative (46) for $x \in <0, L>$ is negative, meaning that we have a reverse shear at the interface. The constitutive relation is given by line EF, not AB, see Fig. 5. Equations (42)÷(45) are valid only when condition (47) is satisfied. In following part of the paper we shall not consider debonding process for which (47) is not satisfied. Reverse shear phenomena will be subject of separate research.

Let us examen formula (42). It is a linear function of u_L. Value of $T(u_L)$ for $u_L = u_c$ will be denoted by T_d and called debonding force. It starts the debonding process. We have three different situations:

- $T_d > T_p$—this inequality is true for rL satisfying the condition: $0 < rL < \pi/2$;
- $T(u_L) =$const meaning $T_d = T_p$. It is true for $rL = \pi/2$;
- $T_d < T_p$ meaning that during Stage 2 the force T is decreasing. This is true when $\pi/2 < rL \leq \pi$ is satisfied.

The greater is $r\,L$, the less durable to external loading is the structure. The interface model with linear softening allows us to describe a big spectrum of structural responses. It is valid for situations without reverse shear at the interface.

5.3 Stage 3

During Stage 3 we have a debonding process at the interface. There are two zones at the interface: plastic and debonded, propagating from the loaded end as presented in Fig. 6. The transition point between them has coordinate s. It will be the parameter controlling the beam degradation process at this stage. It should be stated that the debonding process can be beneficial for the structure. If the reverse shear did not happen during Stage 2 (meaning that condition (47) is satisfied), for sure it will not happen right now.

The shear stress at the debonded zone is $\tau = 0$, meaning that the axial force in the upper and lower beam is zero in this zone. The lateral force, the interfacial shear stress τ and the relative displacement at the interface u are given by Eqs. (38), (39), (40), respectively. The integration constants C_1, C_2, C_3 and force T as a function of s can be obtained by satisfying the boundary conditions:

$$N(s) = 0, \qquad \tau(s) = 0, \qquad u(0) = 0, \qquad u(s) = u_c.$$

We have

$$T(s) = \frac{r^2\, u_c}{\lambda_2[1 - \cos(rs) + r(L-s)\,\sin(rs)]}, \tag{48}$$

$$N(x,s) = -\frac{T(s)\,\lambda_2}{r\,\lambda_1}[r(L-s)\,\cos[r(s-x)] + \sin[r(s-x)] + \\ + \frac{\lambda_2}{\lambda_1}\,T(s)(L-x). \tag{49}$$

The cantilever deflection within the plastic zone can be derived by integrating (8). It results in

$$w(x,s) = \lambda_2\Bigg[\frac{T(s)}{r}\,\frac{\lambda_2}{\lambda_1}\Bigg[\frac{s-L}{r}\cos[r(x-s)] - \frac{s-L}{r}\cos(rs) + \\ + x(L-s)\,\sin(rs) + \frac{\sin[r(x-s)]}{r^2} + \frac{\sin(rs)}{r^2} - \frac{x}{r}\cos(rs)\Bigg] - \\ - T(s)\left(\frac{Lx^2}{2} - \frac{x^3}{6}\right)\left(\frac{\lambda_2}{\lambda_1} - \frac{2}{j_1+j_2}\right)\Bigg]. \tag{50}$$

This function satisfies the boundary conditions $w'(0) = w(0) = 0$. The cantilever deflection within the debonded zone can be obtained by integrating (8) for $N = 0$. By satisfying continuity conditions $\lfloor w(s) \rceil = \lfloor w'(s) \rceil = 0$ at the transition point between plastic and delamination zone, we obtain:

$$w(x,s) = \frac{2\lambda_2\,T}{j_1+j_2}\left(\frac{s^2}{2}\,x - L\,s\,x + \frac{1}{2}\,L\,x^2 - \frac{x^3}{6} + \frac{1}{2}\,L\,s^2 - \frac{1}{3}\,s^3\right) + \\ + f_1(s)(x-s) + f_2(s), \tag{51}$$

where:

$$f_1(s) = \lambda_2\left(\frac{T(s)\,\lambda_2}{r\,\lambda_1}\left[(L-s)\sin(rs) + \frac{1}{r} - \frac{\cos(rs)}{r}\right] - \\ - T(s)\left(L\,s - \frac{s^2}{2}\right)\left(\frac{\lambda_2}{\lambda_1} - \frac{2}{j_1+j_2}\right)\right),$$

$$f_2(s) = \lambda_2\left(\frac{T(s)\,\lambda_2}{r\,\lambda_1}\left[\frac{s-L}{r} - \frac{2s-L}{r}\cos(rs) + s(L-s)\,\sin(rs) + \\ + \frac{\sin(rs)}{r^2}\right] - T(s)\left(\frac{s^2}{2}\,L - \frac{s^3}{6}\right)\left(\frac{\lambda_2}{\lambda_1} - \frac{2}{j_1+j_2}\right)\right).$$

Function $T(s)$ is given by (48).

6 Results

In this section we shall present results obtained for two interface constitutive models. We shall analyze how the deflection of the loaded end $w(L)$ and the loading force T changes when the debonding progresses. The results will be presented in non-dimensional coordinates. The dimensionless force $\tilde{T}$ is defined by

$$\tilde{T} = \frac{T}{T_p},$$

where T_p is given by Eq. (20). This is the value of the external force that plasticizes the interface and ends Stage 1 in the loading process. The dimensionless displacement $\tilde{w}$ of the loaded end is given by

$$\tilde{w}(L) = \frac{w(L)}{w_p},$$

where:

$$w_p = \frac{1}{3}\left(\frac{2\lambda_1}{j_1 + j_2} - \lambda_2\right) b\tau_c L^3$$

is the deflection at coordinate L at the end of Stage 1 and can be derived from Eq. (19) for $x = L$ and $T = T_p$. The reason for using such a normalization of force and displacement is that w_p and T_p are identical for both interface constitutive models. They do not depend on the model character but only on the critical shear stress τ_c. At the end of Stage 1 of loading process we have $\tilde{T} = \tilde{T}_p = 1$, $\tilde{w}(L) = \tilde{w}_p(L) = 1$, regardless of constitutive equation for the interface.

Let us introduce the following dimensionless parameters:

$$\alpha = \frac{4u_c}{\tau_c b L^2[2\lambda_1 - (j_1 + j_2)\lambda_2]}, \tag{52}$$

$$\beta = \frac{2u_c}{\tau_c b L^2 \lambda_1}. \tag{53}$$

They allow to present relation $\tilde{T} \sim \tilde{w}(L)$ for both constitutive models.

6.1 Non-continues degradation of mechanical properties

During Stage 2 of the loading process we have a plastic slip at the interface. This process continues until the relative displacement of the beams reaches critical value u_c and the dimensionless debonding force satisfies

$$\tilde{T}_d = 1 + \beta. \tag{54}$$

Corresponding dimensionless displacement of the loaded end is

$$\tilde{w}_d(L) = 1 + \alpha. \tag{55}$$

During Stage 3 of the loading process we have the debonding propagating at the interface. The dimensionless force $\tilde{T}$ can be obtained from (26). By making use of parameters α and β, we can write

$$\tilde{T}(\xi) = \frac{\xi}{2 - \xi} + \frac{\beta}{(2 - \xi)\xi}, \tag{56}$$

where $\xi = s/L$. Value of ξ changes from unity to zero and defines the length of non-debonded zone. In similar fashion we can write the dimensionless deflection of the loaded end:

$$\tilde{w}_L(\xi) = \frac{\alpha}{(2 - \xi)\xi} + \frac{\alpha}{\beta}\frac{\xi}{2 - \xi} + \left(1 - \frac{\alpha}{\beta}\right)\xi^2. \tag{57}$$

This formula was obtained from Eq. (28).

6.2 Linear degradation of mechanical properties at the interface

During Stage 2 we have a degradation process taking place at the interface. It continues until the relative slip of the beams reaches the critical value u_c. For this moment the dimensionless loading force $\tilde{T}_d$ is given by

$$\tilde{T}_d = \frac{1}{1 - \cos\sqrt{\frac{2}{\beta}}}, \tag{58}$$

and the dimensionless deflection $\tilde{w}_d$ of the loaded end becomes

$$\tilde{w}_d = 1 + \frac{\cos\sqrt{\frac{2}{\beta}}}{1 - \cos\sqrt{\frac{2}{\beta}}} + \frac{3}{2}(\alpha - \beta)\frac{\sqrt{\frac{\beta}{2}}\sin\sqrt{\frac{2}{\beta}} - \cos\sqrt{\frac{2}{\beta}}}{1 - \cos\sqrt{\frac{2}{\beta}}}. \tag{59}$$

During Stage 3 we have a debonded zone propagating at the interface. The force $\tilde{T}$ can be obtained from Eq. (48) and is now given by

$$\tilde{T}(\xi) = \frac{1}{1 - \cos\left(\sqrt{\frac{2}{\beta}}\xi\right) + \sqrt{\frac{2}{\beta}}(1-\xi)\sin\left(\sqrt{\frac{2}{\beta}}\xi\right)}. \tag{60}$$

Identically as before, parameter $\xi = s/L$ denotes the dimensionless length of non-delaminated zone. The dimensionless deflection $\tilde{w}_L$ at the loaded end is a following function of ξ:

$$\begin{aligned}\tilde{w}_L(\xi) = &\frac{2\alpha - 2(\alpha-\beta)\xi(3 - 3\xi + \xi^2)}{2\beta\left[1 - \cos\left(\sqrt{\frac{2}{\beta}}\xi\right) + \sqrt{\frac{2}{\beta}}(1-\xi)\sin\left(\sqrt{\frac{2}{\beta}}\xi\right)\right]} + \\ &+ \frac{3(\alpha-\beta)\left\{\left[\sqrt{\frac{\beta}{2}} + \sqrt{\frac{2}{\beta}}(1-\xi)\right]\sin\left(\sqrt{\frac{2}{\beta}}\xi\right) - \xi\cos\left(\sqrt{\frac{2}{\beta}}\xi\right)\right\}}{2\left[1 - \cos\left(\sqrt{\frac{2}{\beta}}\xi\right) + \sqrt{\frac{2}{\beta}}(1-\xi)\sin\left(\sqrt{\frac{2}{\beta}}\xi\right)\right]}.\end{aligned} \tag{61}$$

6.3 Model comparison

It has been shown that two dimensionless parameters α and β can define the whole debonding process, regardless of the used constitutive equation. In particular, they define values of $\tilde{T}_d$ and $\tilde{w}_d(L)$ for dimensionless loading and corresponding dimensionless displacement. In addition, they define the post-critical structural response given by Eqs. (56), (57) or (60), (61) respectively for two interface models.

Parameters α and β cannot be totaly independent. They have to satisfy the inequality:

$$\alpha > \beta, \tag{62}$$

resulting directly from Eqs. (52) and (53). In addition, for the linear degradation model, the condition $rL < \pi$ requires that

$$\beta \geq \frac{2}{\pi^2} \approx 0.2026. \tag{63}$$

Figure 8 presents the relation between force $\tilde{T}$ and displacement $\tilde{w}$ for constant value of parameter β and different values of α. In Fig. 9 the same relation was shown for constant α and different β. What we see is a difference in results for the beginning of debonding process. The reason for this is following. Parameters α and β are defined in the same fashion for both interface models. The same α and the same β for both models mean the same critical relative displacement u_c at the interface in both cases. The corresponding energy G_c needed to damage unit area of the the interface are $\tau_c u_c$ and $(\tau_c u_c)/2$, respectively for non-continuous and linear softening.

To have the same value of G_c for both constitutive models we should have

$$u_c^{linear} = 2u_c^{nonlinear},$$

where u_c^{linear} and $u_c^{nonlinear}$ are critical relative displacements at the interface, respectively for linear and non-continuous softening. We should make a difference between introduced parameters α and β by stating that $\alpha^{nonlinear}$ and $\beta^{nonlinear}$ are for non-continuous softening and α^{linear} and β^{linear} are for linear softening. The equality of energy G_c for both cases means

$$\frac{1}{2}\alpha^{linear} = \alpha^{nonlinear} = \alpha, \tag{64}$$

$$\frac{1}{2}\beta^{linear} = \beta^{nonlinear} = \beta, \tag{65}$$

where α and β are given by Eqs. (52) and (53). Figure 10 presents the load versus displacement plots for different values of parameter $\alpha = \alpha^{nonlinear} = \alpha^{linear}/2$ and constant value of $\beta = \beta^{nonlinear} = \beta^{linear}/2$. In Fig. 11

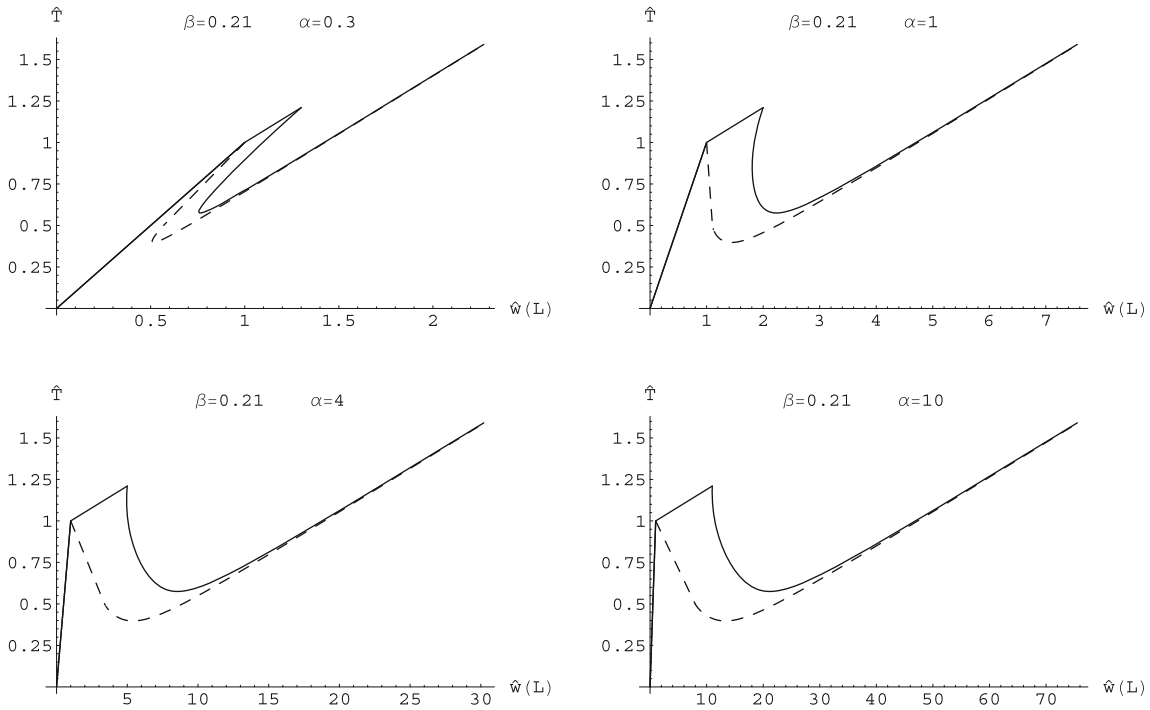


Fig. 8 The dimensionless force $\tilde{T}$ versus dimensionless displacement $\tilde{w}(L)$. Continuous line—non-linear degradation of interface mechanical properties, dashed line—linear softening. Identical critical displacement u_c

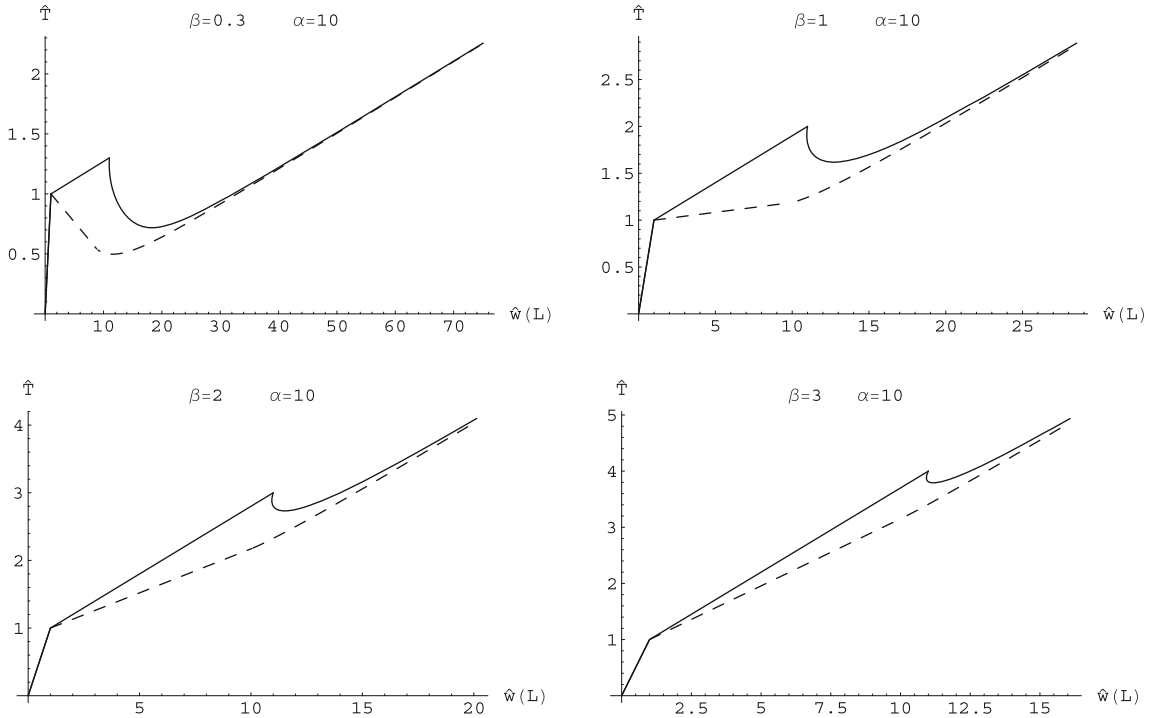


Fig. 9 The dimensionless force $\tilde{T}$ versus dimensionless displacement $\tilde{w}(L)$. Continuous line—non-linear degradation of interface mechanical properties, dashed line—linear softening. Identical critical displacement u_c

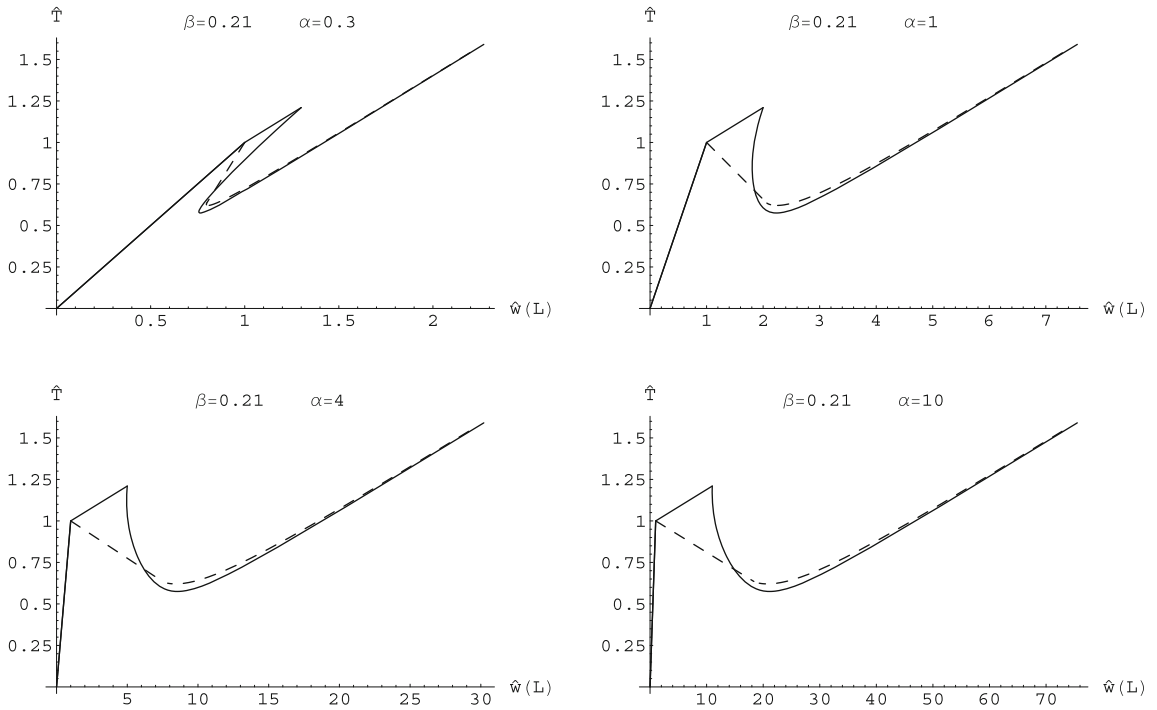


Fig. 10 The dimensionless force $\tilde{T}$ versus dimensionless displacement $\tilde{w}(L)$. Continuous line—non-linear degradation of interface mechanical properties, dashed line—linear softening. Identical critical energy G_c

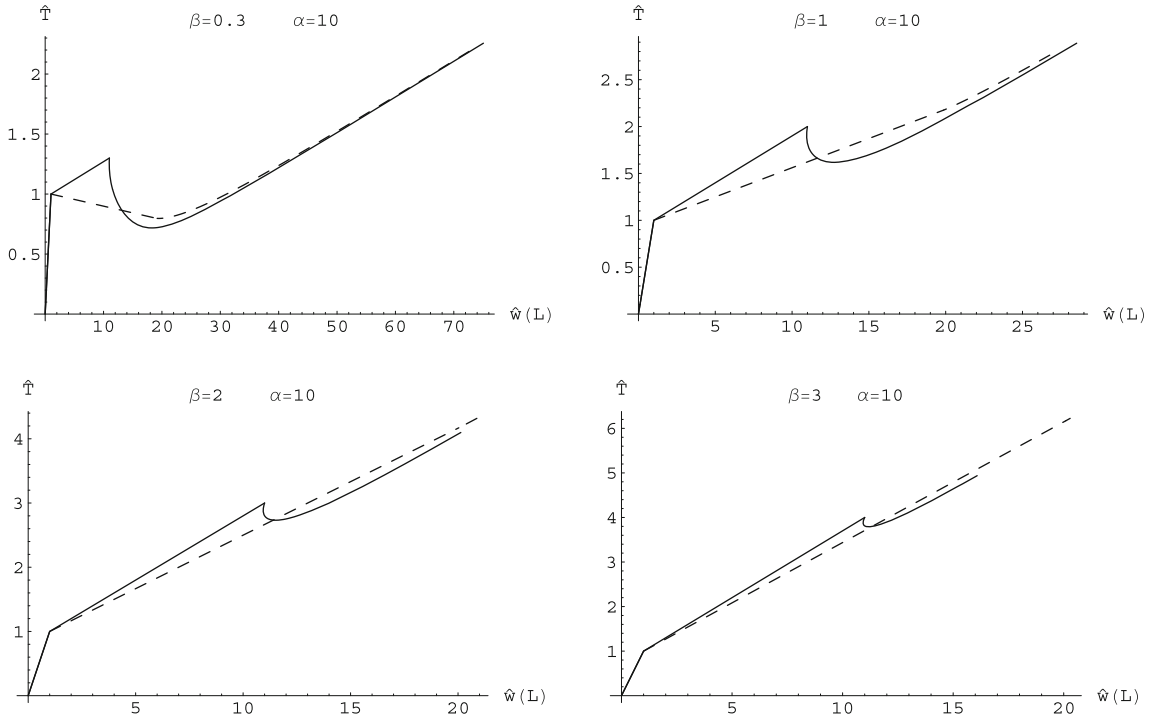


Fig. 11 The dimensionless force $\tilde{T}$ versus dimensionless displacement $\tilde{w}(L)$. Continuous line—non-linear degradation of interface mechanical properties, dashed line—linear softening. Identical critical energy G_c

we have a constant value of $\alpha = \alpha^{nonlinear} = \alpha^{linear}/2$ and different values of $\beta = \beta^{nonlinear} = \beta^{linear}/2$. The equilibrium paths for both models are now closer than before, when the same value of u_c was used regardless of interface constitutive relation.

Obtained results can be compared with results presented in [95,96], where cohesive zone model including linear softening allowed to obtain snap through and snap back responses in the relation between loading force and resulting displacement for a fiber pull out from a matrix or a plate sheared along a substrate. The choice of parameter governing the overall response was the length of debonded zone increasing monotonically. This lead to quasi-static solutions. Similar to the present results, type of response depended on the value of softening modulus, with steeper softening slope resulting in snap back and more horizontal softening leading to snap through. In the present formulation we obtain similar situation, with smaller values of dimensional parameter α for linear softening providing snap back in the load–displacement relation. For non-continuous degradation of mechanical properties at the interface we always have snap back response. This is the impact of discontinuity points in cohesive zone model. The papers [95,96] distinguish between initially rigid and elastic interface, followed by a softening branch in the cohesive zone formulation. Both approaches allowed to obtain snap back character of structural response, with interfacial elasticity allowing to generate quasi-static load–displacement loops. In the present formulation we have only rigid-softening interface and it is not possible to obtain the complex response shown in paper [96].

7 Conclusions

The study provides a comprehensive analytical model that improves the understanding of debonding processes in composite cantilever beams loaded by a point force. Two constitutive equations for the interface were used to describe quasi-static response without any dynamic loadings. The model with non-continuous interface softening is characterized by a non-stable equilibrium path with inverse shear at the interface. The model with continuous, linear degradation provides a more complex response and can cover a stable transition from an undamaged to a fully damaged structure. It can also depict an abrupt decrease in the loading force related to interfacial damage. The ability of the proposed formulation to predict the quasi-static equilibrium paths and snap-back responses in force and displacement highlights the importance of the interface layer mechanical properties. The fully analytical formulation of the bonded beams model allows for straightforward handling of snap-back. Obtained results are functions of length of debonded zone $L - s$ and can be traced as the parameter s decreases from L to zero. Thus, snap-back is easily obtained when examining how the loading force and the beam tip displacement change as functions of s. The research underscores the critical role of the interface layer in maintaining the structural integrity of composite beams. The cohesive zone model used in this study effectively simulates the degradation process, demonstrating how changes in the interface layer strength can significantly impact the beam overall performance. The proposed analytical approach offers a valuable tool for structural engineers. It enables more accurate predictions of debonding behavior in composite materials, which can lead to improved design and analysis of composite structures, enhancing their reliability and safety. The model delineates three distinct stages of interface degradation—no relative slip, plastic deformation, and progressive debonding. These stages provide insights into the beam response to loading conditions, offering a detailed understanding of the debonding process. The findings of this study open a way for future research, particularly in refining the cohesive zone models and exploring their applicability to different composite configurations and loading scenarios. Further studies could also investigate the impact of varying interface properties on the structural behavior of composite beams.

Another relevance of the presented results is that the analytical solution can be a reference to numerical treatment of complex cases where snap-back or snap-through is expected. The analysis clarifies the character of instability points and provides a quasi-static solution of progressive debonding. A dynamic analysis would provide more insight into failure development. It would be interesting to combine the proposed model with limit load design allowing for elastic-ideal plastic beams. This would allow us to examine interplay between interfacial debonding process and plastic collapse of the beams.

References

1. Malikan, M., Eremeyev, V.A.: A new hyperbolic-polynomial higher-order elasticity theory for mechanics of thick FGM beams with imperfection in the material composition. Compos. Struct. **249**, 112486 (2020)
2. Aßmus, M., Naumenko, K., Ochsner, A., Eremeyev, V.A., Altenbach, H.: A generalized framework towards structural mechanics of three-layered composite structures. Tech. Mech. **39**(2), 202–219 (2019)
3. Abali, B.E., Vazic, B., Newell, P.: Influence of microstructure on size effect for metamaterials applied in composite structures. Mech. Res. Commun. **122**, 103877 (2022)
4. Spagnuolo, M., Franciosi, P., dell'Isola, F.: A Green operator-based elastic modeling for two-phase pantographic-inspired bi-continuous materials. Int. J. Solids Struct. **188**, 282–308 (2020)
5. Contrafatto, L., Cuomo, M., Greco, L.: Meso-scale simulation of concrete multiaxial behaviour. Eur. J. Environ. Civ. Eng. **21**(7–8), 896–911 (2017)
6. Alessandroni, S., Andreaus, U., dell'Isola, F., Porfiri, M.: Piezo-electromechanical (PEM) Kirchhoff–Love plates. Eur. J. Mech. A/Solids **23**(4), 689–702 (2004)
7. Maurini, C., Pouget, J., dell'Isola, F.: Extension of the Euler–Bernoulli model of piezoelectric laminates to include 3D effects via a mixed approach. Comput. Struct. **84**(22–23), 1438–1458 (2006)
8. Darleux, R., Lossouarn, B., Giorgio, I., dell'Isola, F., Deü, J.-F.: Electrical analogs of curved beams and application to piezoelectric network damping. Math. Mech. Solids **27**(4), 578–601 (2022)
9. Olive, M., Auffray, N.: Symmetry classes in piezoelectricity from second-order symmetries. Math. Mech. Complex Syst. **9**(1), 77–105 (2021)
10. Malikan, M., Eremeyev, V.A.: On a flexomagnetic behavior of composite structures. Int. J. Eng. Sci. **175**, 103671 (2022)
11. Ko, K.Y., Solyaev, Y.: Explicit benchmark solution for topology optimization of variable-thickness plates. Math. Mech. Complex Syst. **11**(3), 381–392 (2023)
12. Giorgio, I.: Lattice shells composed of two families of curved Kirchhoff rods: an archetypal example, topology optimization of a cycloidal metamaterial. Continuum. Mech. Thermodyn. **33**(4), 1063–1082 (2021)
13. Giorgio, I., Ciallella, A., Scerrato, D.: A study about the impact of the topological arrangement of fibers on fiber-reinforced composites: some guidelines aiming at the development of new ultra-stiff and ultra-soft metamaterials. Int. J. Solids Struct. **203**, 73–83 (2020)
14. Desmorat, B., Spagnuolo, M., Turco, E.: Stiffness optimization in nonlinear pantographic structures. Math. Mech. Solids **25**(12), 2252–2262 (2020)
15. Shekarchizadeh, N., Abali, B.E., Barchiesi, E., Bersani, A.M.: Inverse analysis of metamaterials and parameter determination by means of an automatized optimization problem. ZAMM-Zeitschrift für Angewandte Mathematik und Mechanik **101**(8), e202000277 (2021)
16. Özen, A., Auhl, D., Völlmecke, C., Kiendl, J., Abali, B.E.: Optimization of manufacturing parameters and tensile specimen geometry for fused deposition modeling (FDM) 3D-printed PETG. Materials **14**(10), 2556 (2021)
17. Tošić, N., Aidarov, S., de la Fuente, A.: Systematic review on the creep of fiber-reinforced concrete. Materials **13**(22), 5098 (2020)
18. Giorgio, I.: A variational formulation for one-dimensional linear thermoviscoelasticity. Math. Mech. Complex Syst. **9**(4), 397–412 (2022)
19. Giorgio, I., Placidi, L.: A variational formulation for three-dimensional linear thermoelasticity with 'thermal inertia'. Meccanica 1–12 (2024)
20. Szlachetka, O., Giorgio, I.: Heat conduction in multi-component step-wise FGMs. Continuum Mech. Thermodyn. 1–19 (2024)
21. Abali, B.E., Vorel, J., Wan-Wendner, R.: Thermo-mechano-chemical modeling and computation of thermosetting polymers used in post-installed fastening systems in concrete structures. Continuum Mech. Thermodyn. **35**(3), 971–989 (2023)
22. Fabbrocino, F., Funari, M.F., Greco, F., Lonetti, P., Luciano, R., Penna, R.: Dynamic crack growth based on moving mesh method. Compos. B Eng. **174**, 107053 (2019)
23. Funari, M.F., Spadea, S., Fabbrocino, F., Luciano, R.: A moving interface finite element formulation to predict dynamic edge debonding in FRP-strengthened concrete beams in service conditions. Fibers **8**(6), 42 (2020)
24. Turco, E., Barchiesi, E.: Kinematically triggered nonlinear vibrations of hencky-type pantographic sheets. Math. Mech. Complex Syst. **9**(3), 311–335 (2022)
25. Eugster, S.R.: Numerical analysis of nonlinear wave propagation in a pantographic sheet. Math. Mech. Complex Syst. **9**(3), 293–310 (2022)
26. Ciallella, A., Giorgio, I., Eugster, S.R., Rizzi, N.L., dell'Isola, F.: Generalized beam model for the analysis of wave propagation with a symmetric pattern of deformation in planar pantographic sheets. Wave Motion **113**, 102986 (2022)
27. Giorgio, I., Della Corte, A., dell'Isola, F.: Dynamics of 1D nonlinear pantographic continua. Nonlinear Dyn. **88**(1), 21–31 (2017)
28. Abali, B.E.: Revealing the physical insight of a length-scale parameter in metamaterials by exploiting the variational formulation. Continuum Mech. Thermodyn. **31**(4), 885–894 (2019)
29. Alibert, J.-J., Seppecher, P., dell'Isola, F.: Truss modular beams with deformation energy depending on higher displacement gradients. Math. Mech. Solids **8**(1), 51–73 (2003)
30. dell'Isola, F., Andreaus, U., Placidi, L.: At the origins and in the vanguard of peridynamics, non-local and higher-gradient continuum mechanics: an underestimated and still topical contribution of Gabrio Piola. Math. Mech. Solids **20**(8), 887–928 (2015)
31. Turco, E., Barchiesi, E., Giorgio, I., dell'Isola, F.: A Lagrangian hencky-type non-linear model suitable for metamaterials design of shearable and extensible slender deformable bodies alternative to Timoshenko theory. Int. J. Non-Linear Mech. **123**, 103481 (2020)
32. Turco, E., Barchiesi, E., dell'Isola, F.: In-plane dynamic buckling of duoskelion beam-like structures: discrete modeling and numerical results. Math. Mech. Solids **27**(7), 1164–1184 (2022)

33. Barchiesi, E., dell'Isola, F., Laudato, M., Placidi, L., Seppecher, P.: A 1D continuum model for beams with pantographic microstructure: asymptotic micro-macro identification and numerical results. Adv. Mech. Microstruct. Media Struct. 43–74 (2018)
34. Barchiesi, E., Eugster, S.R., dell'Isola, F., Hild, F.: Large in-plane elastic deformations of bi-pantographic fabrics: asymptotic homogenization and experimental validation. Math. Mech. Solids **25**(3), 739–767 (2020)
35. Newmark, N.M.: Test and analysis of composite beam with incomplete interaction. Proc. Soc. Exp. Stress Anal. **9**(1), 75–92 (1951)
36. Granholm, H.: On composite beams and columns with special regard to nailed timber structures. Trans **88** (1949)
37. Pleshkov, P.: Theoretical studies of composite wood structures. Soviet Union (in Russian) (1952)
38. Goodman, J.R., Popov, E.P.: Layered beam systems with interlayer slip. J. Struct. Div. **94**(11), 2535–2548 (1968)
39. Murakami, H.: A laminated beam theory with interlayer slip. J. Appl. Mech. **51**, 551–559 (1984)
40. Rao, K., Ghosh, B.: Imperfectly bonded unsymmetric laminated beam. J .Eng. Mech. Div. **106**(4), 685–697 (1980)
41. Fazio, P., Hussein, R., Ha, K.H.: Sandwich beam-columns with interlayer slips. J .Eng. Mech. Div. **108**(2), 354–366 (1982)
42. Giorgio, I., Scerrato, D.: Multi-scale concrete model with rate-dependent internal friction. Eur. J. Environ. Civ. Eng. **21**(7–8), 821–839 (2017)
43. Ciallella, A., Scerrato, D., Spagnuolo, M., Giorgio, I.: A continuum model based on Rayleigh dissipation functions to describe a Coulomb-type constitutive law for internal friction in woven fabrics. Z. Angew. Math. Phys. **73**(5), 209 (2022)
44. Ciallella, A., Pasquali, D., Gołaszewski, M., D'Annibale, F., Giorgio, I.: A rate-independent internal friction to describe the hysteretic behavior of pantographic structures under cyclic loads. Mech. Res. Commun. **116**, 103761 (2021)
45. Cuomo, M., Contrafatto, L., Greco, L.: A cohesive interface model with degrading friction coefficient. Math. Mech. Complex Syst. **12**(2), 113–133 (2024)
46. Ponomarev, D.: A generalised time-evolution model for contact problems with wear and its analysis. Math. Mech. Complex Syst. **10**(3), 279–319 (2022)
47. Barchiesi, E., Hamila, N.: Maximum mechano-damage power release-based phase-field modeling of mass diffusion in damaging deformable solids. Z. Angew. Math. Phys. **73**(1), 35 (2022)
48. Scrofani, A., Barchiesi, E., Chiaia, B., Misra, A., Placidi, L.: Fluid diffusion related aging effect in a concrete dam modeled as a Timoshenko beam. Math. Mech. Complex Syst. **11**(2), 313–334 (2023)
49. Biolzi, L., Ghittoni, C., Fedele, R., Rosati, G.: Experimental and theoretical issues in FRP-concrete bonding. Constr. Build. Mater. **41**, 182–190 (2013)
50. Fedele, R., Milani, G.: Three-dimensional effects induced by FRP-from-masonry delamination. Compos. Struct. **93**(7), 1819–1831 (2011)
51. Bertolesi, E., Milani, G., Fedele, R.: Fast and reliable non-linear heterogeneous FE approach for the analysis of FRP-reinforced masonry arches. Compos. B Eng. **88**, 189–200 (2016)
52. Fedele, R., Milani, G.: Assessment of bonding stresses between FRP sheets and masonry pillars during delamination tests. Compos. B Eng. **43**(4), 1999–2011 (2012)
53. Dell'Isola, F., Volkov, I.A., Igumnov, L.A., Eugster, S.R., Litvinchuk, S.Y., Kazakov, D.A., Gorohov, V.A., Abali, B.E.: Estimating fatigue related damage in alloys under block-type non-symmetrical low-cycle loading. New Achievements in Continuum Mechanics and Thermodynamics: A Tribute to Wolfgang H. Müller, pp. 81–92 (2019)
54. Turco, E., Barchiesi, E., dell'Isola, F.: A numerical investigation on impulse-induced nonlinear longitudinal waves in pantographic beams. Math. Mech. Solids **27**(1), 22–48 (2022)
55. Placidi, L., Timofeev, D., Maksimov, V., Barchiesi, E., Ciallella, A., Misra, A., Dell'Isola, F.: Micro-mechano-morphology-informed continuum damage modeling with intrinsic 2nd gradient (pantographic) grain-grain interactions. Int. J. Solids Struct. **254**, 111880 (2022)
56. Placidi, L., Barchiesi, E., dell'Isola, F., Maksimov, V., Misra, A., Rezaei, N., Scrofani, A., Timofeev, D.: On a hemi-variational formulation for a 2D elasto-plastic-damage strain gradient solid with granular microstructure. Math. Eng. **5**, 1–24 (2022)
57. Placidi, L., dell'Isola, F., Kandalaft, A., Luciano, R., Majorana, C., Misra, A.: A granular micromechanic-based model for ultra high performance fiber-reinforced concrete (UHP FRC). Int. J. Solids Struct. **297**, 112844 (2024)
58. Placidi, L., Barchiesi, E., Misra, A.: A strain gradient variational approach to damage: a comparison with damage gradient models and numerical results. Math. Mech. Complex Syst. **6**(2), 77–100 (2018)
59. Abali, B.E., Klunker, A., Barchiesi, E., Placidi, L.: A novel phase-field approach to brittle damage mechanics of gradient metamaterials combining action formalism and history variable. ZAMM-Zeitschrift für Angewandte Mathematik und Mechanik **101**(9), e202000289 (2021)
60. Thompson, E.G., Goodman, J.R., Vanderbilt, M.D.: Finite element analysis of layered wood systems. J. Struct. Div. **101**(12), 2659–2672 (1975)
61. Cheung, M.S., Akhras, G., Li, W.: Combined boundary element/finite strip analysis of bridges. J. Struct. Eng. **120**(3), 716–727 (1994)
62. Hu, C., Hartley, G.A.: Elastic analysis of thin plates with beam supports. Eng. Anal. Boundary Elem. **13**(3), 229–238 (1994)
63. Kukreti, A., Cheraghi, E.: Analysis procedure for stiffened plate systems using an energy approach. Comput. Struct. **46**(4), 649–657 (1993)
64. Sapountzakis, E.J., Katsikadelis, J.T.: Interface forces in composite steel-concrete structure. Int. J. Solids Struct. **37**(32), 4455–4472 (2000)
65. Schulte, J., Dittmann, M., Eugster, S., Hesch, S., Reinicke, T., dell'Isola, F., Hesch, C.: Isogeometric analysis of fiber reinforced composites using Kirchhoff–Love shell elements. Comput. Methods Appl. Mech. Eng. **362**, 112845 (2020)
66. Greco, L., Castello, D., Cuomo, M.: An objective and accurate G1-conforming mixed Bézier FE-formulation for Kirchhoff–Love rods. Math. Mech. Solids **29**(4), 645–685 (2024)
67. Greco, L., Cammarata, A., Castello, D., Cuomo, M.: An objective FE-formulation for Cosserat rods based on the spherical Bézier interpolation. Comput. Methods Appl. Mech. Eng. **425**, 116947 (2024)

68. Baroudi, D., Giorgio, I., Battista, A., Turco, E., Igumnov, L.A.: Nonlinear dynamics of uniformly loaded elastica: experimental and numerical evidence of motion around curled stable equilibrium configurations. ZAMM-Zeitschrift für Angewandte Mathematik und Mechanik **99**(7), e201800121 (2019)
69. Giorgio, I.: A discrete formulation of Kirchhoff rods in large-motion dynamics. Math. Mech. Solids **25**(5), 1081–1100 (2020)
70. Turco, E., Barchiesi, E.: Equilibrium paths of Hencky pantographic beams in a three-point bending problem. Math. Mech. Complex Syst. **7**(4), 287–310 (2019)
71. Giorgio, I., Del Vescovo, D.: Energy-based trajectory tracking and vibration control for multilink highly flexible manipulators. Math. Mech. Complex Syst. **7**(2), 159–174 (2019)
72. Giorgio, I., Del Vescovo, D.: Non-linear lumped-parameter modeling of planar multi-link manipulators with highly flexible arms. Robotics **7**(4), 60 (2018)
73. Turco, E.: Modeling of three-dimensional beam nonlinear vibrations generalizing Hencky's ideas. Math. Mech. Solids **27**(10), 1950–1973 (2022)
74. Turco, E., dell'Isola, F., Misra, A.: A nonlinear Lagrangian particle model for grains assemblies including grain relative rotations. Int. J. Numer. Anal. Meth. Geomech. **43**(5), 1051–1079 (2019)
75. Berezovski, A., Giorgio, I., Della Corte, A.: Interfaces in micromorphic materials: wave transmission and reflection with numerical simulations. Math. Mech. Solids **21**(1), 37–51 (2016)
76. dell'Isola, F., Romano, A.: On the derivation of thermomechanical balance equations for continuous systems with a nonmaterial interface. Int. J. Eng. Sci. **25**(11–12), 1459–1468 (1987)
77. Dell'Isola, F., Kosinski, W.: Deduction of thermodynamic balance laws for bidimensional nonmaterial directed continua modelling interphase layers. Arch. Mech. 27 (1993)
78. Oehlers, D.J., Sved, G.: Composite beams with limited-slip-capacity shear connectors. J. Struct. Eng. **121**(6), 932–938 (1995)
79. Nguyen, N.T., Oehlers, D.J., Bradford, M.A.: A rational model for the degree of interaction in composite beams with flexible shear connectors. J. Struct. Mech. **26**(2), 175–194 (1998)
80. de Moura, M., de Morais, A.: Equivalent crack based analyses of ENF and ELS tests. Eng. Fruct. Mech. **75**, 2584–2596 (2008)
81. Bui, V., Marechel, E., Nguyen-Dan, H.: Imperfect interlaminar interfaces in laminated composites: delamination with the R-curve effect. Compos. Sci. Technol. **60**, 2619–2630 (2000)
82. Dourado, N., de Moura, M., de Morais, A., Pereira, A.: Bilinear approximations to the mode II delamination cohesive law using an inverse method. Mech. Mater. **49**, 42–50 (2012)
83. Giuliese, G., Palazzetti, R., Moroni, F., Zucchelli, A., Pirondi, A.: Cohesive zone modelling of delamination response of a composite laminate with interleaved nylon 6,6 nanofibres. Compos. B **78**, 384–392 (2015)
84. Moroni, F., Palazzetti, R., Zucchelli, A., Pirondi, A.: A numerical investigation on the interlaminar strength of nanomodified composite interfaces. Compos. B **55**, 635–641 (2013)
85. Blackman, B., Kinloch, A., Paraschi, M.: The determination of the mode II adhesive fracture resistance, G_{IIC}, of structural adhesive joints: an effective crack length approach. Eng. Fract. Mech. **72**(6), 877–897 (2005)
86. Blackman, B., Brunner, A., Williams, J.: Mode II fracture testing of composites: a new look at an old problem. Eng. Fract. Mech. **73**(16), 2443–2455 (2006)
87. Wang, C., Vassilopoulos, A.P., Keller, T.: Numerical investigation of two-dimensional Mode-II delamination in composite laminates. Compos. A Appl. Sci. Manuf. **179**, 108012 (2024)
88. Solis, A., Barbero, E., Sanchez-Saez, S.: Analysis of the influence of ply-orientation in delamination progression in composites laminates using the serial/parallel mixing theory. Compos. Sci. Technol. **211**, 108847 (2021)
89. Pereira, A., de Moris, A.: Mode ii interlaminar fracture of glass/epoxy multidirectional laminates. Compos. A **35**, 265–272 (2004)
90. de Moris, A., Pereira, A.: Application of the effective crack method to mode I and mode II interlaminar fracture of carbon/epoxy unidirectional laminates. Compos. A **38**, 785–794 (2007)
91. de Moris, A.: Novel cohesive beam model for the End-Notched Flexure (ENF) specimen. Eng. Fract. Mech. **78**, 3017–3029 (2011)
92. Cao, T., Zhao, L., Wang, L., Wang, K., Gong, Y., Zhang, J.: An efficient semi-analytical method to extract the mode II bridging-traction law in ENF tests directly from the experimental load displacement data. Compos. Struct. **285**, 115229 (2022)
93. Heidari-Rarani, M., Ghasemi, A.: Appropriate shape of cohesive zone model for delamination propagation in ENF specimens with R-curve effects. Theoret. Appl. Fract. Mech. **90**, 174–181 (2017)
94. Shahverdi, M., Vassilopoulos, A.P., Keller, T.: Mixed-mode quasi-static failure criteria for adhesively-bonded pultruded GFRP joints. Compos. A Appl. Sci. Manuf. **59**, 45–56 (2014)
95. Mróz, Z., Białas, M.: A simplified analysis of interface failure under compressive normal stress and monotonic or cyclic shear loading. Int. J. Numer. Anal. Methods Geomech. **29**(4), 337–368 (2005)
96. Białas, M., Mróz, Z.: Modelling of progressive interface failure under combined normal compression and shear stress. Int. J. Solids Struct. **42**(15), 4436–4437 (2005)
97. Soize, C.: An overview on uncertainty quantification and probabilistic learning on manifolds in multiscale mechanics of materials. Math. Mech. Complex Syst. **11**(1), 87–174 (2023)
98. La Valle, G., Abali, B.E., Falsone, G., Soize, C.: Sensitivity of a homogeneous and isotropic second-gradient continuum model for particle-based materials with respect to uncertainties. ZAMM-Zeitschrift für Angewandte Mathematik und Mechanik **103**(10), e202300068 (2023)
99. Barenblatt, G.: The mathemtical theory of equilibrium cracks in brittle fracture. Adv. Appl. Mech. **7**, 55–129 (1962)
100. Dugdale, D.: Yielding of steel sheets containing slits. J. Mech. Phys. Solids **8**, 100–104 (1960)
101. Camacho, G., Ortiz, M.: Computational modelling of impact damage in brittle materials. Int. J. Solids Struct. **33**(20–22), 2899–2938 (1996)

102. Needleman, A.: An analysis of tensile decohesion along an interface. J. Mech. Phys. Solids **38**(3), 289–324 (1990)
103. Moës, N., Belytschko, T.: Extended finite element method for cohesive crack growth. Eng. Fract. Mech. **69**(7), 813–833 (2002)
104. Williams, J., Hadavinia, H.: Analytical solutions for cohesive zone models. J. Mech. Phys. Solids **50**(4), 809–825 (2002)
105. Oehlers, D., Coughlan, C.: The shear stiffness of stud shear connections in composite beams. J. Constr. Steel Res. **6**(4), 273–284 (1986)
106. Białas, M., Mróz, Z.: Crack patterns in thin layers under temperature loading. Part I: monotonic loading. Eng. Fract. Mech. **73**, 917–938 (2006)
107. Białas, M., Mróz, Z.: Crack patterns in thin layers under temperature loading. Part II: cyclic loading. Eng. Fract. Mech. 73, 939–952 (2006)

Publisher's Note Springer Nature remains neutral with regard to jurisdictional claims in published maps and institutional affiliations.

Springer Nature or its licensor (e.g. a society or other partner) holds exclusive rights to this article under a publishing agreement with the author(s) or other rightsholder(s); author self-archiving of the accepted manuscript version of this article is solely governed by the terms of such publishing agreement and applicable law.

Conclusions

In the proposed study, we introduce a Timoshenko beam model enhanced with a micro-crack sliding descriptor, offering a robust and efficient framework for characterizing the mechanical behavior of cement-based materials. This model is distinguished by its computational efficiency and effectiveness, enabling precise evaluation of material strength and dissipative behavior. By incorporating a variable that represents the relative sliding of micro-cracks within the material, the model effectively captures additional dissipative mechanisms that contribute to energy loss during loading and unloading cycles. To demonstrate the model efficacy, we employed finite element method-based numerical simulations using COMSOL Multiphysics. These simulations successfully replicated experimental tests, revealing the impact of various parameters on the mechanical response, including energy dissipation and the behavior of kinematic descriptors such as longitudinal and transverse displacement, cross-sectional orientation, and relative sliding at micro-cracks. A comprehensive parametric study was conducted to examine the influence of varying frictional force parameters on energy dissipation. The findings indicated a non-linear relationship between these parameters and dissipated energy, with an optimal value of frictional force maximizing energy dissipation. The model predictions show strong agreement with experimental behaviors observed in flexural and compression tests of cement-based materials, offering preliminary validation of its capability to accurately capture the complex mechanical response of these materials under loading and unloading conditions. The insights derived from this study have significant implications for the design and optimiza-

tion of cement-based structures, particularly in applications where energy dissipation and mechanical resistance are critical, such as in seismic environments. By accurately modeling the dissipation mechanisms within the material, engineers can enhance the resilience and durability of such structures.

Future research should aim to refine the model by integrating additional complexities, such as material property heterogeneities and multiaxial loading conditions. Moreover, further experimental validation across a broader range of test configurations and material compositions would enhance the model's applicability and robustness. The study introduces a novel contribution by incorporating the friction term in the dissipation based on P. R. Dahl's model for dry friction in solids. In our case, the friction force arises from partial compression in some parts of the cross-section caused by bending deformation during the flexural test. This compression leads to the closure of microcracks, forcing the opposite faces to come into contact and causing a sliding displacement between them. This friction term evolves over time and describes an elastoplastic response, expanding the range of phenomena observed in the system using a 1D micromorphic continuum model. The simulations presented in this work illustrate some characteristics of plastic behavior, while other descriptors not directly influenced by the inner friction contribution appear to align with previously reported predictions. The model and analysis provided in this study could be valuable to researchers in the field of dissipation mechanisms for cementitious materials, particularly in adjusting control parameters, such as the evolution law of the friction force, to quantify the amount of aggregates/fillers needed in a mixture to achieve desired mechanical properties. The approach in this work could be a simplified tool for the initial assessment of aspects like energy dissipation and the mechanical response reliability for earthquake-proof concrete. However, it is essential to note that an experimental campaign is necessary to validate the proposed model and provide insights for further assessment. The knowledge gained from the proposed model could lead to an experimental testing procedure to assess the connection between friction and the mechanical properties of cementitious materials in the context examined.

List of Publications

Publications list

- Aretusi, G., Cardillo, C., Salvatori, A., Bednarczyk, E., & Fedele, R. (2024). A simple extension of Timoshenko beam model to describe dissipation in cementitious elements. *Zeitschrift für angewandte Mathematik und Physik*, **75**(5), 166.

- Aretusi, G., Cardillo, C., Terranova, L. M., & Bednarczyk, E. (2024). A dissipation model for concrete based on an enhanced Timoshenko beam. *Networks and Heterogeneous Media*, **19**(2), 700–723.

- Terranova, L. M., Cardillo, C., & Aretusi, G (2025) An enhanced beam model incorporating a hysteresis-based solid friction damping mechanism for cementitious materials. *Continuum Mechanics and Thermodynamics*, **37**, 2

- Scrofani, A., Aretusi, G., Salvatori, A., et al. (2025) Non-linear effects in seismic waves in high energy earthquakes: a two dimensional analysis for non homogeneous isotropic media with a view towards the study of the 2009 L'Aquila earthquake. *Mathematics and Mechanics of Solids*.

- Bialas, M. & Aretusi, G. (2025) An analytical model for delamination behavior in composite cantilever beams under point loads. *Continuum Mechanics and Thermodynamics*, **37**, 4

Tesi redatta con il sostegno finanziario del programma

FSE-REACT-EU, PON “Ricerca e Innovazione” 2014-2020 (D.M. 1061/2021)

Asse IV “Istruzione e ricerca per il recupero – REACT-EU”

Azione IV.4 “Dottorati e Contratti di ricerca su tematiche dell'innovazione”

